The Dissertation Committee for Maureen Anne LeVoir Walton Certifies that this is the approved version of the following dissertation:

TECTONIC AND SEDIMENTARY PROCESSES OF THE SOUTHEAST ALASKA MARGIN

Committee:

Sean P. S. Gulick, Supervisor

Gail L. Christeson

Peter J. Haeussler

Brian K. Horton

David C. Mohrig

TECTONIC AND SEDIMENTARY PROCESSES OF THE SOUTHEAST ALASKA MARGIN

by

Maureen Anne LeVoir Walton, B.A.

Dissertation

Presented to the Faculty of the Graduate School of

The University of Texas at Austin

in Partial Fulfillment

of the Requirements

for the Degree of

Doctor of Philosophy

The University of Texas at Austin

May 2016

Dedication

To my teachers through the years, who inspired and equipped me.

Acknowledgements

I would not have been able to complete this dissertation without the help and support of many wonderful and dedicated people. First and foremost, I thank my adviser, Sean Gulick. He is simply the best. Sean is forever positive, excited, and energetic, his enthusiasm contagious and inspiring. He truly prioritizes his students; he was always there when I needed him, while still allowing me to learn on my own. Sean's guidance, high standards, and timely, detailed feedback were vital to my success. My overwhelmingly positive experience at UT has been in huge part thanks to Sean; I am so lucky to have learned from and to know such an incredible person and scientist.

Each of my committee members has taken an avid interest in my work and provided meaningful feedback over the years. Gail Christeson has dedicated a lot of her time working with me on various aspects of seismic processing and has always valued my input and treated me as a colleague. Peter Haeussler has been an honor and a pleasure to work with – an expert in Alaska geology, he has given important suggestions on my work and is always quick to respond and eager to participate in the surrounding discussion. Brian Horton and David Mohrig have each provided timely and relevant feedback on my research, writing, and presentations despite their packed schedules. I will always remember and be grateful that I'm able to knock on their doors at any moment and be greeted with a smile and "sure, come on in."

Several other scientists have played an important role. Bobby Reece has actually played many roles, including mentor, peer, secondary adviser, big brother, and friend. His encouragement, criticism, feedback, and advice have been invaluable to my development as a scientist and as a person. Emily Roland has been so incredibly generous with her time and resources, always prepared, patient, and willing to help. Jake Walter has perfectly filled

the void of Emily's physical absence here at UTIG and has been a valuable collaborator. Harm Van Avendonk, despite being only tangentially involved in my work, has consistently given me detailed and useful comments on my writing. Lindsay Worthington was the first person to get me excited about the prospect of coming to UT to work with Sean, which I will never forget. Danny Brothers dedicated a lot of his valuable time to the next stage of my career at the USGS, and has already made me feel so welcome there. And of course, Karl Mueller and Barry Eakins got me interested in all this stuff in the first place at CU.

The technical and administrative staff at UTIG have made my life a whole lot easier over the years. Thanks to: Philip Guerrero, who has not only been a great friend of mine, but an indispensable student resource we would all be lost without; computer guru Mark Wiederspahn, without whom nothing would be accomplished, and Kevin Johnson, whom UTIG will miss greatly; Steffen Saustrup, for saving me hours of seismic-related troubles; Anatoly Mironov and John Gerboc, for their contribution to my OBS work; Judy Sansom, for solving everyone's funding issues with ease; Rosalind Gamble, for ensuring I never go hungry at meetings; Marcy Davis and Dan Duncan, for their easy smiles; and Nancy Hard, for all her help and positive attitude over the years.

My friends at UT have been a huge part of my support system. There are really too many to name, but for starters: Sebastian Ramirez, John Swartz, Kaustubh Thirumalai, Johnathon Osmond, and Bud Davis have always been there when I needed a laugh, a break, advice, or some good old-fashioned gossip. Marina Frederik has been the most considerate office mate anyone could ever ask for. My past JSG friends – particularly Julie Ditkof, Jessi Kopp, Christine O'Neill, Mark Duncan, Sarah Coyle, and Jacqui Maleski – were (and are) a joy to spend time with; I am sad that our time together in Austin was so short.

All my non-UT friends have kept me grounded and have given me some (very important) non-geo perspective. Again, there are too many to name, but most importantly thanks to: Sara Morrey, who has been the best and most loyal friend of all time – I am so happy she decided to come on this Austin adventure with me; Kevin Flake, for always being willing to be silly; Sheila V, who has kept our Skype dates and chats going strong; Nicholas Britt and Lindsey Shoemaker, who are always up for the latest faire, festival, and food- and drink-related debauchery; Priya Mukherjee, a fast friend and great listener; and Chris Deatrick, for never flaking (and never being late).

My family – old and new – has been a constant source of support and encouragement, despite their unfamiliarity with my field. They are endlessly proud of me, bragging about me to their own friends and colleagues, framing my old posters, and asking lots of questions. Special thanks to each and every Walton, who have welcomed me to their family with open arms.

Finally, and perhaps most importantly, my husband, David, has been with me at every turn, easily adapting to and enjoying the twists, moves, and challenges of our lives without complaint. He is my anchor, and our adventures are only beginning.

TECTONIC AND SEDIMENTARY PROCESSES OF THE SOUTHEAST ALASKA MARGIN

Maureen Anne LeVoir Walton, Ph.D.

The University of Texas at Austin, 2016

Supervisor: Sean P. S. Gulick

Strike-slip tectonics dominate the southeast Alaska margin. The Queen Charlotte-Fairweather Fault transform system extends ~1200 km from southern Canada north to Yakutat Bay, Alaska, accommodating nearly 4.5 cm/yr of dextral offset between the Pacific and North American plates. This dissertation aims to better characterize the transform plate boundary by examining the accommodation of oblique transpression, crustal structure, seismogenic faults, and tectonic influence on regional sedimentary processes. We address fundamental tectonic questions utilizing a suite of geophysical data including multichannel seismic (MCS) reflection, bathymetry, magnetics, gravity, and earthquake data. A 2011 MCS survey reveals subsurface channel deposits related to the development of the deep-sea Baranof sedimentary fan in the Gulf of Alaska. We find that Baranof Fan channels have avulsed consistently southward, affected by the changing position of channel heads relative to sediment sources along the shelf edge due to strike-slip motion along the Queen Charlotte Fault (QCF). Baranof Fan sediments sit atop a flexural depression in the Pacific crust near the QCF, which developed between ~6 Ma and ~2 Ma. We interpret the flexure to be an artifact of oblique convergence along the southern QCF, preserved by sedimentary loading in part from the Baranof Fan. ~150 km of the QCF near the Pacific flexural depression ruptured in January 2013, producing a M_w 7.5 earthquake near Craig, Alaska.

A tomographic inversion of Craig aftershock data reveals a low velocity zone on the Pacific side of the plate boundary at seismogenic depths, which may indicate the contrast of a warm, young Pacific crust along the older, colder North American crust. These results have relevance for rupture directionality and future seismic hazard along the QCF. Finally, we revisit seismic hazard associated with the 10 September 1899 Mw 8.2 earthquake at the northern termination of the transform system near Yakutat Bay, Alaska. We quantify uncertainty on coseismic uplift measurements and integrate various geophysical data, including a 2012 MCS survey, to provide an updated fault map and tectonic model of the Yakutat Bay region. Our results support a subduction-related rupture of the 10 September event with limited slip along the transpressive termination of the Fairweather Fault.

Table of Contents

List of Tables

List of Figures

Chapter 1: Introduction

The topic of this dissertation addresses tectonic and sedimentary processes along the tectonic plate margin of southeast Alaska. The studies included here were motivated by a desire to address fundamental questions related to the nature of the Queen Charlotte-Fairweather Fault and processes affected by that tectonic system. The Queen Charlotte-Fairweather Fault represents the plate boundary along southeast Alaska and western Canada for a total onshore/offshore length of ~1200 km, and accommodates nearly 45 mm/yr of dextral offset (Elliott et al., 2010). The Fairweather Fault (FF) represents the northern, primarily onshore extension of the offshore Queen Charlotte Fault (QCF) to the south. Despite active seismicity and several significant earthquakes over the last century, little is known about the geometry, crustal structure, and geohazards along the QCF, in part because of its remote offshore location. This dissertation provides new information about the Queen Charlotte-Fairweather system including its effect on regional sedimentary systems (Chapter 2), crustal deformation for the past ~6 Ma (Chapter 3), crustal architecture and its effects on seismicity (Chapter 4), and relevance to large-scale, regional earthquake hazards (Chapter 5).

Each chapter of this dissertation focuses on some aspect of strike-slip motion along the Queen Charlotte-Fairweather Fault in an effort to better characterize the system and associated hazards. The QCF is a unique transform plate boundary separating young (<20 Ma) Pacific oceanic crust from older, colder Pennsylvanian- to Neoproterozoic-age North American continental crust. The crustal structure is important when considering earthquake tectonics, as the rheology and thermal properties can control rupture depth, directionality, and magnitude of earthquake ruptures. The strike-slip system is slightly transpressive along strike, particularly south of 53.2° N, where convergence reaches rates of up to 20 mm/yr

(Hyndman and Hamilton, 1993). The transpressive nature of the fault has led to regionally heterogeneous accommodation of convergence which has affected crustal structure and seismicity. High rates of offset (~44 mm/yr) along the QCF also affect seismicity and other regional features, including the deposition of one of the largest deep-sea sedimentary fans in the world, the Baranof Fan. The FF to the north, accommodating offsets similar to the QCF, plays a major role in seismic hazard near Yakutat Bay, Alaska. The FF intersects with faults associated with the Yakutat subduction zone near Yakutat Bay, where a pair of large earthquakes occurred in September 1899 (M_w 8.1 and 8.2).

The remote, little-studied Queen Charlotte-Fairweather system provides a key target for first-order data collection, observation, and interpretation. I utilize multi-disciplinary, geophysically focused approaches to study the QCF and FF at the offshore plate boundary between the North American and Pacific plates. The primary data used throughout the studies presented in this dissertation are multichannel seismic reflection (MCS) data, much of which has been collected and processed for the studies presented here (see Appendix A for complete MCS data summary). In addition to MCS data, bathymetry, topography, sidescan sonar, and earthquake data inform my interpretations. Three separate field expeditions have contributed new data to this work, which I integrate with previously published data, results, and hypotheses.

Each chapter in this dissertation acts as a standalone study connected by the common theme of the southeast Alaska transform plate boundary (Fig. 1.1). In Chapter 2, I present new data from the 2011 MGL1109 MCS survey in the Gulf of Alaska, which covers regions of the deep sea subsurface. I use the high-resolution data to describe the deep-sea sedimentary deposits of the Baranof Fan, mapping sedimentary channel-levee deposits on the deep seafloor and connecting channel avulsions to strike-slip motion along the QCF. This finding adds significantly to the current state of knowledge about the

development of the Baranof Fan. This chapter was published in *Geosphere* in 2014 (Walton et al., 2014). My co-authors and committee members contributed assistance in collecting and processing the 2011 data as well as feedback on interpretations and writing. Seismic interpretations, figures, and writing for Chapter 2 are all my own, and include updates made during the draft and peer-review process. Co-authors outside my committee who contributed to this chapter include Dr. Robert Reece (Texas A&M University), Dr. Ginger Barth (U.S. Geological Survey), and Dr. Harm Van Avendonk (University of Texas Institute for Geophysics).

In Chapter 3, I take a closer look at legacy MCS data available along the QCF in light of the recent M_w 7.8 and M_w 7.5 events along the QCF in 2012 and 2013, respectively. The data reveal an interesting pattern of downwarping in the Pacific crust which we connect to past transpressional convergence along the QCF beginning at ~6 Ma. This chapter was published in the *Bulletin of the Seismological Society of America* in 2015 (Walton et al., 2015). My co-authors and committee members contributed useful feedback and suggestions for this work, but all seismic interpretations, figures, and writing are otherwise my own. Co-authors outside my committee who assisted me with this chapter include Dr. Emily Roland (University of Washington) and Dr. Anne Tréhu (Oregon State University). Some additional updates were also made during the peer-review process.

In chapter 4, I examine the crustal architecture along the QCF in the region of the 2013 Craig, Alaska event using aftershocks detected by a rapid-response ocean-bottom seismometer (OBS) deployment. A tomographic inversion of the OBS data indicates slower Pacific velocities exist in the study area, which has implications for the Craig event's rupture mechanics and future earthquake hazards in general. Dr. Emily Roland, Assistant Professor at the University of Washington, planned the OBS deployment and assisted greatly in the preparation of data. Dr. Jake Walter, Research Associate at the

University of Texas, helped to prepare the OBS data for local use at the University of Texas Institute for Geophysics (UTIG) and offered insights into inversion strategy. A University of Texas undergraduate student, Peter Dotray, picked earthquake arrival times in the aftershock data catalog. I completed inversion testing and earthquake relocations myself, and settled on final parameters independently. I wrote the chapter with feedback from the aforementioned collaborators and committee members. I generated all figures myself with input from my co-authors, committee members, and colleagues. At the time of this writing, efforts are ongoing to submit and publish Chapter 4 in a peer-reviewed journal.

In Chapter 5, I discuss the northern extension of the QCF, the FF, and how splays of the FF may have played a role in the Yakutat Bay earthquakes of 1899. I also discuss how the strike-slip system may link and potentially interact with the Yakutat subduction system. Dr. Sean Gulick and Dr. Peter Haeussler (committee members), Steffen Saustrup (seismic technician at UTIG), and Julie Zurbuchen (former University of Texas undergraduate student) assisted with the collection and processing of 2012 seismic reflection data discussed in the chapter. I generated all tables, figures, and writing for Chapter 5 myself with feedback from the aforementioned collaborators and other committee members. At the time of this writing, I hope to submit Chapter 5 to a peer-reviewed journal for publication in the near future.

Ultimately, each chapter of this dissertation answers questions about transform motion, deformation, fault structure, and seismicity along the QCF and FF systems. The dissertation overall addresses overarching goals of ocean exploration, making first-order observations of a seismogenic system, with relevant results for local and global study of strike-slip plate boundaries. The broad geohazard implications of this work will benefit hazard assessment for local communities along the entirety of the Queen Charlotte-

Fairweather system and provides a foundation on which to build future research in Alaska and around other seismogenic systems.

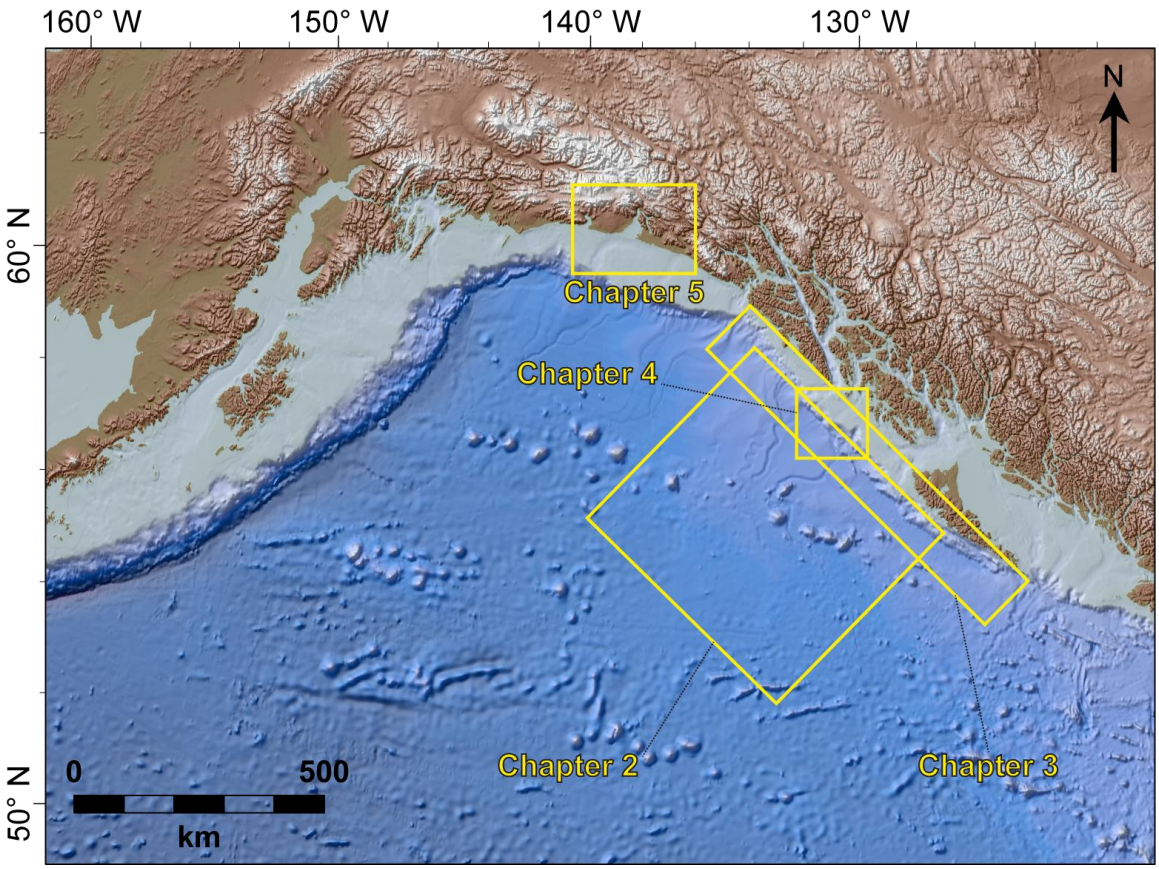

Figure 1.1. Regional overview of chapter study regions.

Chapter 2: Dynamic response to strike-slip tectonic control on the deposition and evolution of the Baranof Fan, Gulf of Alaska[1]

ABSTRACT

The Baranof Fan is one of three large deep-sea fans in the Gulf of Alaska, and is a key component in understanding largescale erosion and sedimentation patterns for southeast Alaska and western Canada. We integrate new and existing seismic reflection profiles to provide new constraints on the Baranof Fan area, geometry, volume, and channel development. We estimate the fan's area and total sediment volume to be ~323,000 km^2 and ~301,000 km^3, respectively, making it among the largest deep-sea fans in the world. We show that the Baranof Fan consists of channel-levee deposits from at least three distinct aggradational channel systems: the currently active Horizon and Mukluk channels, and the waning system we call the Baranof Channel. The oldest sedimentary deposits are in the northern fan, and the youngest deposits at the fan's southern extent; in addition, the channels seem to avulse southward consistently through time. We suggest that Baranof Fan sediment is sourced from the Coast Mountains in southeastern Alaska, transported offshore most recently via fjord to glacial sea valley conduits. Because of the northwestward translation of the Pacific Plate past sediment sources on the North American Plate along the Queen Charlotte strike-slip fault, we suggest that new channel formation, channel beheadings, and southward-migrating channel avulsions have been influenced by regional tectonics. Using a simplified tectonic reconstruction assuming a constant Pacific Plate motion along the QCF of 44 mm/yr, we estimate that, at earliest, Baranof Fan deposition initiated ca. 7 Ma.

[1] Walton, M. A. L., S. P. S. Gulick, R. S. Reece, G. A. Barth, G. L. Christeson, and H. J. A. Van Avendonk (2014), Dynamic response to strike-slip tectonic control on the deposition and evolution of the Baranof Fan, Gulf of Alaska, *Geosphere*, *10*(4), 680-691.

2.1 INTRODUCTION

The influence of tectonics on sedimentary processes has been studied in a wide variety of contexts and scientific disciplines, including tectonic geomorphology, basin modeling, and climate-tectonic interactions. Here we focus on the influence of regional plate tectonic motion on the deposition and evolution of a deep-sea fan, separated from its sediment supply by a strike-slip fault. Our study of the Baranof Fan in the Gulf of Alaska addresses questions about large-scale sedimentation along the margin, and the Baranof Fan serves as a natural laboratory for examining the influence of strike-slip tectonics on deep-sea fan sedimentation patterns. There are few instances of large-scale strike-slip tectonics influencing deep-sea sedimentation in the modern world, but there is evidence for the process in the geologic past. For example, the Zodiac Fan, the largest of the Gulf of Alaska deep-sea fans, is located along the Aleutian Trench, hundreds of kilometers removed from its sediment supply (Stevenson et al., 1983). In this study we show that the Baranof Fan is a good example illustrating the extent to which plate motion can influence deposition of large-scale sedimentary fans.

Sedimentary fans, including elements such as channels, overbank deposits, lobes, and avulsions, have been studied at length (e.g., Mutti and Normark, 1991; Piper and Normark, 2001). Many publications discuss sediment distribution mechanisms such as turbidity currents and shelf canyon systems (e.g., Normark and Carlson, 2003; Piper and Normark, 2009) and how they are related to the broad range of downslope deposits (Normark and Piper, 1991; Piper and Normark, 2009). Early and substantial analysis of sedimentary distribution systems and associated deposits has helped to inform our analysis of the Baranof Fan, which has not been examined recently (Steven son and Embley, 1987).

In this study we redefine the Baranof Fan boundaries, area, volume, and depositional controls, and provide new constraints on its age and evolutionary history.

Through use of two-dimensional (2D) seismic reflection and multibeam bathymetry data, we suggest a tectonic influence on Baranof Fan deposition, including progressive northwest to southeast channel avulsions and strike-slip–driven translation of shelf point sources along the fan's landward edge. We also show the paleopathway of the previously unstudied Baranof Channel, describe its influence in Baranof Fan evolution, and suggest the near-future formation of a new channel at the Dixon Entrance.

2.2 REGIONAL SETTING

2.2.1 Deep-sea fans

In addition to the Baranof Fan, the other two deep-sea fans in the Gulf of Alaska (Fig. 2.1) are the late Oligocene Zodiac Fan, located along the Aleutian Islands (Stevenson et al., 1983), and the younger Pliocene–Pleistocene Surveyor Fan to the northwest, which remains active (Reece et al., 2011). The Baranof Fan is similar in area and volume to the other two Gulf of Alaska deep-sea fans (Stevenson and Embley, 1987). The Gulf of Alaska fans have had both fluvial and glacial inputs; the Zodiac Fan predates Pleistocene glaciation in North America, but the Surveyor and Baranof Fans have transitioned to become primarily glacially fed (e.g., von Huene and Kulm, 1973; Stevenson and Embley, 1987; Dobson et al., 1998; Reece et al., 2011).

Baranof Fan sediment derives predominantly from the Coast Mountains along the southeast Alaska margin (Plafker et al., 1994). Rivers and glacial streams erode the mountains near the coastline; the associated fluvial or glacial systems then carry the eroded sediment out to the shelf edge, where turbidity flows distribute the sediment to the deep seafloor via channel-levee environments (e.g., Ness and Kulm, 1973; Manley and Flood, 1988; Dowdeswell et al., 1996; Lopez, 2001). Currently the main conduits for sediment transport across the continental shelf to the Baranof Fan are glacial sea valleys adjacent to

the Dixon Entrance and Chatham Strait, as well as a shelf canyon between these sea valleys (Fig. 2.2). The sea valleys, or shelf-crossing troughs, are ~30-km-wide features representing the pathways of recent glacial advances (Carlson et al., 1982, 1996). Slope canyon systems associated with the channel heads and sea valleys are largely absent; rather, sediments are transported downslope via gully systems (Steven son and Embley, 1987; Normark and Carlson, 2003).

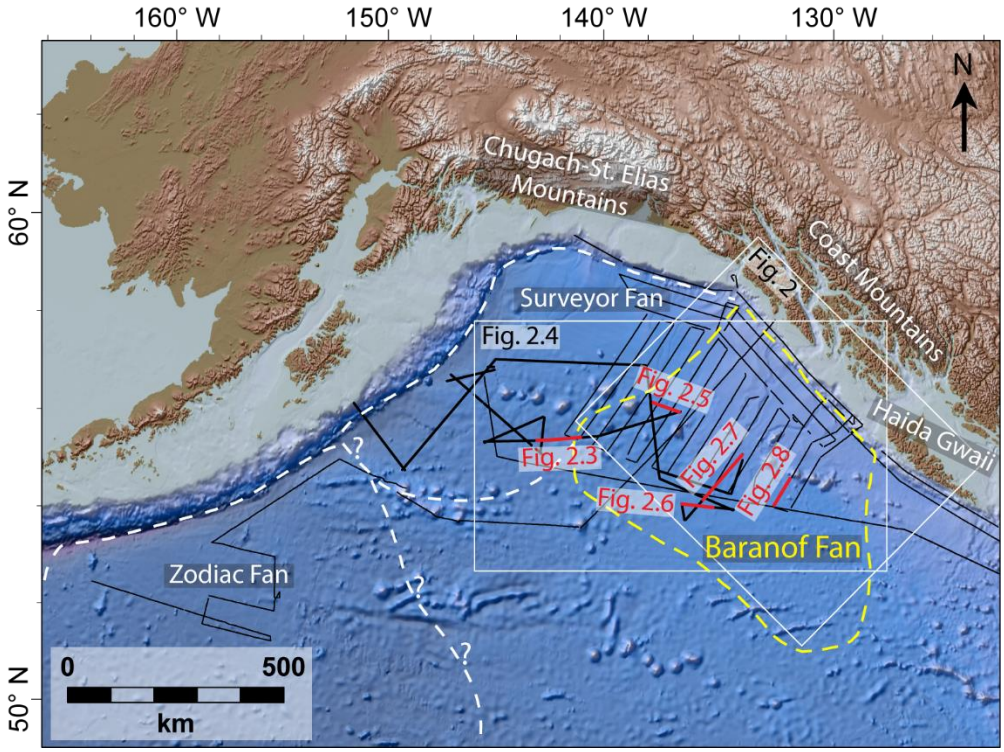

Figure 2.1. Baranof Fan study area. Background ETOPO1 bathymetric map (Amante and Eakins, 2009) is overlaid by Gulf of Alaska two-dimensional (2D) seismic data coverage (black, bold black, and red lines). The yellow dashed line outlines the Baranof Fan area on the seafloor; white dashed lines outline the Surveyor and Zodiac Fans. Bold black trackline shows 2011 seismic survey MGL1109. Red indicates 2D seismic transects used in this study.

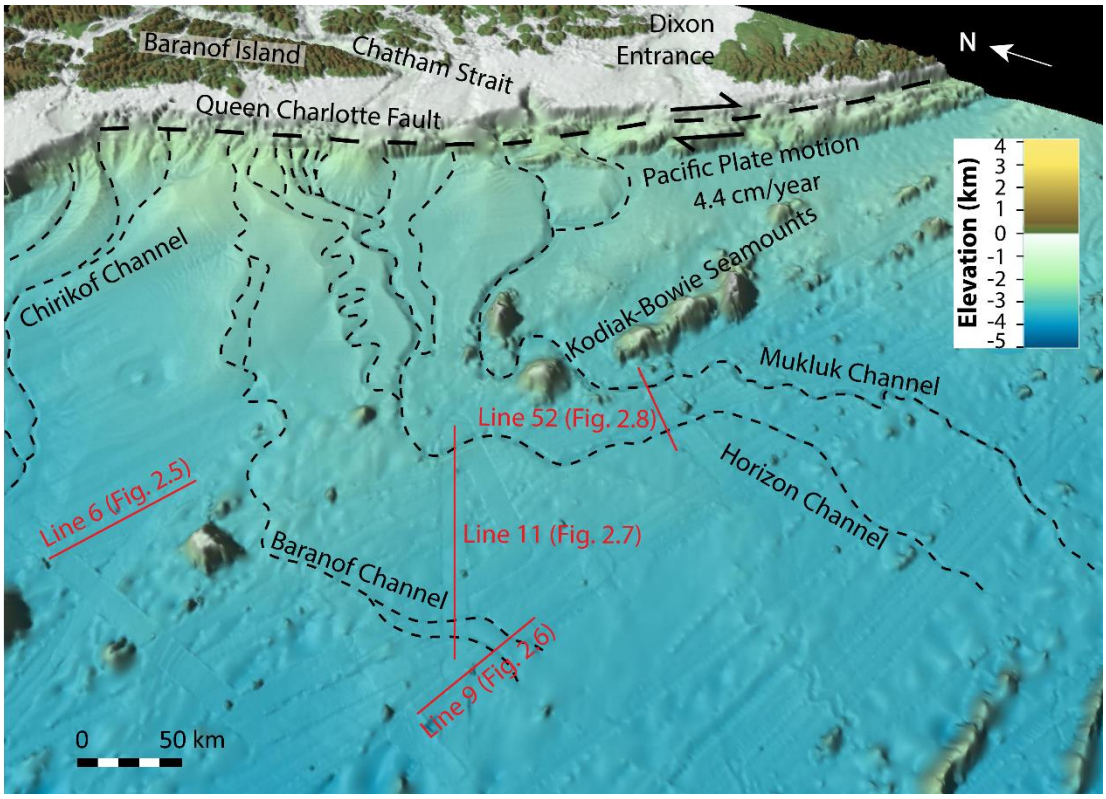

Figure 2.2. Bathymetric three-dimensional perspective image of the Baranof Fan. Image depicts major channels (the Baranof, Horizon, and Mukluk channels) and two-dimensional seismic transects used in this study (red). See Figure 2.1 for location. Bathymetry data include MGL1109 and U.S. Geological Survey Extended Continental Shelf multibeam data merged with ETOPO1 data. The Mukluk and Horizon channels are the only channels considered to be active today. This figure also highlights the locations of the NW-striking dextral Queen Charlotte Fault, the Kodiak-Bowie Seamount Chain, and Chatham Strait and the Dixon Entrance, two major conduits for glacial sediment input to the Baranof Fan.

2.2.2 Tectonic and climatic setting

The Baranof Fan overlies the Tufts Abyssal Plain and its channels weave through the ~1000-km-long Kodiak-Bowie Seamount Chain, which dominates both the seafloor (Fig. 2.2) and the subsurface in the Baranof Fan area (Morley et al., 1972). These volcanic edifices typically are 2–3 km above the surrounding crystalline basement and are thought to have been generated by a hotspot at the Pacific–North America–Juan de Fuca triple

junction to the southeast (Silver et al., 1974). Smaller seamounts in the chain are buried by sediment but are still clearly visible in the subsurface seismic data.

During the Baranof Fan evolution since the late Miocene, depositional processes have been influenced by the 44 mm/yr right-lateral motion of the Pacific plate relative to North America (Elliott et al., 2010). Northwestward motion of the Pacific plate along North America is accommodated by the Queen Charlotte Fault, a strike-slip fault located along the southeastern margin of Alaska, linking with the Fairweather Fault to the northwest (von Huene et al., 1979; Carlson et al., 1988). The Pacific plate's changing position relative to sediment sources on North America has caused both disruptions to sediment supply and evoked the creation of new channel systems in the Baranof Fan's history (Bruns et al., 1984; Stevenson and Embley, 1987; Dobson et al., 1998).

As a late Miocene high-latitude fan, the Baranof Fan system has likely been influenced by glacial cycles, which typically correspond with periods of higher sedimentation (e.g., Vorren et al., 1989, 1991). There is evidence for post-Miocene global cooling (Mathews and Rouse, 1963) as well as several glaciation events that likely had a strong influence on fan sedimentation. Glacial periods in the northern Pacific include an alpine and tidewater glaciation event ca. 5.5 Ma (Lagoe et al., 1993), hemisphere-scale glacial intensification at 2.56 Ma (Lagoe et al., 1993; Raymo, 1994; Farley et al., 2001), and a transition to ~100,000 yr glacial-interglacial cycles following the mid-Pleistocene transition at 0.7–1.2 Ma (Clark et al., 2006; Berger et al., 2008). In particular, intensification of glaciation ca. 2.6 Ma may have spurred isostatic uplift in the Coast Mountains (Farley et al., 2001) that was a positive feedback for increased glacial erosion rates during this period.

2.2.3 Channels

The Horizon and Mukluk channels (Fig. 2.2) are two of the longest deep-sea channels in the Gulf of Alaska and the most notable morphological features of the modern Baranof Fan. Merged bathymetry data from this study indicate that the total length of the Horizon Channel is ~800 km, and that of the Mukluk Channel is ~750 km. Both channels persist nearly 500 km onto the Gulf of Alaska abyssal plain from the shelf edge. Analysis of new seismic data shows channel-fill deposits of 2–7 km width, commonly composed of several smaller kilometer-scale channels characterized by high-amplitude reflections (e.g., Deptuck et al., 2003) and arranged in channel complexes. These channel complexes are so named because they represent a collection or complex of smaller channel deposits (Abreu et al., 2003) that have formed via different phases of fill (Deptuck et al., 2003).

The Horizon and Mukluk channels are the principle modern depositional pathways for Baranof Fan sediment. Previous work acknowledged the existence of a third, unnamed channel system north of the Horizon and Mukluk channels (Stevenson and Embley, 1987), though the extent of its influence was previously unpublished. We provide new constraints on this third system and propose that it be named the Baranof Channel. Sediment in the channels is carried downslope by turbidity currents and deposited in the lower gradient basin, a process typical of submarine fans (Piper and Normark, 2001, 2009). Herein we analyze downslope processes and present data showing that the channels appear to have evolved in a manner typical of many submarine fans, with lobe switching and avulsion events (Damuth and Flood, 1983; Manley and Flood, 1988). We consider the crust on which the sediment is deposited, the longevity of exposure to sediment sources, tectonic controls on sediment supply, and regional controls on sediment supply such as glaciation events; these are all important factors when developing a conceptual framework for sedimentation processes (Mutti and Normark, 1987).

2.3 DATA

2.3.1 2D Seismic reflection

The primary seismic data used in this study are from a June 2011 high-resolution data set collected aboard the R/V Marcus G. Langseth (the MGL1109 cruise); the data were acquired by the University of Texas Institute for Geophysics (UTIG) and the U.S. Geological Survey (USGS) as part of the U.S. Extended Continental Shelf (ECS) project, which is aimed at determining the full extent of the U.S. continental shelf maritime zone. The MGL1109 cruise collected 3260 km of multichannel seismic (MCS) data in 17 profiles. Data were acquired using an 8 km streamer towed at 9 m depth with 636 channels spaced at 12.5 m. The source was a 6600 in^3 36-airgun array, with 50 m shot spacing for most MCS profiles and 150 m spacing for two MCS lines coincident with ocean-bottom seismometer (OBS) stations. Common depth point (CDP) spacing is 6.25 m with a maximum fold of ~80. The data sampling rate was 2 ms, and record length was 16 s. The reflection data were processed to poststack time migration using Paradigm's FOCUS software (www.pdgm.com/solutions/seismic-processing-and-imaging/seismic-processing) utilizing the following processing flow: SEG-D convert, geometry definition, trace editing, 3-7–100-125 Hz bandpass filter, multichannel gap deconvolution, CDP sort, velocity analysis, spherical divergence correction, water-bottom mute, normal moveout (NMO) correction, stretch mute, trace balancing, stack, and F/K migration (using constant 1500 m/s velocity). See Appendix B for further survey and processing details.

Other seismic data sets used for Baranof Fan analysis include earlier seismic reflection profiles, including USGS surveys S679GA (1979), L681NP (1981), and F789EG (1989). Survey F789EG was collected as part of GLORIA (Geological Long-Range Inclined Asdic), a survey conducted by the USGS and the Institute of Oceanographic Sciences (now the University of Southampton National Oceanography Centre) in an effort

to better define the U.S. exclusive economic zone (EEZ) (EEZSCAN Scientific Staff, 1991). GLORIA surveys primarily aimed to obtain sidescan sonar coverage of the Gulf of Alaska, but 2-channel, single-airgun seismic data were also collected and these data have good coverage over the Baranof Fan. Processing of survey F789EG included trace editing and balancing, muting, and bandpass filtering (Reece et al., 2011). Surveys S679GA and L681NP are older (1979 and 1981, respectively), deep-water 2D USGS seismic surveys.

2.3.2 Bathymetry

Bathymetry data in the Baranof Fan region include MGL1109 multibeam acquired coincident with the seismic data lines, and a high-resolution (~100 m^2) multibeam survey collected as a part of the U.S. ECS project (Gardner et al., 2006) that covers much of the southeast Alaska continental margin. The MGL1109 multibeam data were processed by UTIG and USGS using the CARIS HIPS and SIPS (www.caris.com/products/hips-sips/) software package. The MGL1109 and ECS multibeam data have been merged with the ~1 km^2-resolution ETOPO1 global bathymetry grid (Amante and Eakins, 2009), provided by the National Oceanic and Atmospheric Administration (NOAA) National Geophysical Data Center. The integrated bathymetric data are displayed in Figure 2.2.

2.4 METHODS

2.4.1 Regional surfaces

After processing MGL1109 MCS data, we imported all 2D lines into Halliburton's Landmark OpenWorks (www.landmarksoftware.com) interpretation software; we completed the bulk of the seismic interpretation using the DecisionSpace Desktop module. We gridded bathymetry data using the Generic Mapping Tools (GMT) software package (www.soest.hawaii.edu/gmt), rendered the data using ESRI ArcGIS mapping software

(www.esri.com/software/arcgis), and imported the rendered data into DecisionSpace Desktop to be used in conjunction with the seismic 2D lines.

We mapped regional seismic unconformities in DecisionSpace Desktop, including the seafloor and oceanic basement. In addition to seafloor and basement, a regional stratigraphic downlap surface we call the Base Baranof horizon is observed as a mappable, high-amplitude seismic reflector throughout new MGL1109 and older USGS seismic transects (e.g., Fig. 2.3). Channels observable below the Base Baranof surface are generally smaller and less developed than channels above the surface, suggesting that channels above the surface dominated deposition of the fan (hence the name Base Baranof).

We gridded the seafloor, basement, and Base Baranof surfaces on a 0.01° grid (block size ~1 km^2) using GMT and visualized the result with Quality Positioning Services BV (QPS) Fledermaus software. From these grids, we generated two-way traveltime (TWTT) thickness grids: one for the thickness between the seafloor and the Base Baranof surface (Fig. 2.4a) and the other for the thickness between the seafloor and oceanic basement (Fig. 2.4b). Over the fan area, we calculated sediment volume both between the Base Baranof surface to the seafloor as well as between the mapped basement to the seafloor using these TWTT isopach grids. In areas where sediment thickness could not be picked or interpolated because of sparse data coverage, we calculated an average thickness in TWTT from existing grid cells (~650 ms) and used this value to then calculate sediment volume.

There are no core data to constrain seismic velocities in the Baranof Fan, though stacking velocities derived from MGL1109 seismic reflection processing are well constrained. In order to simplify the calculation and account for the fact that MGL1109 data only cover more distal areas of the fan, we applied a constant sediment velocity of 2000 m/s to convert sediment thickness from TWTT to meters and thereby estimate

sediment volume. The average acoustic sediment velocity of 2000 m/s is the same value that Reece et al. (2011) used for the adjacent Surveyor Fan, the value derived from Deep Sea Drilling Project Leg 178 cores (von Huene and Kulm, 1973) located within the Surveyor Fan. The 2000 m/s value is also consistent with preliminary MGL1109 OBS velocity models in the Baranof Fan (Reece et al., 2012).

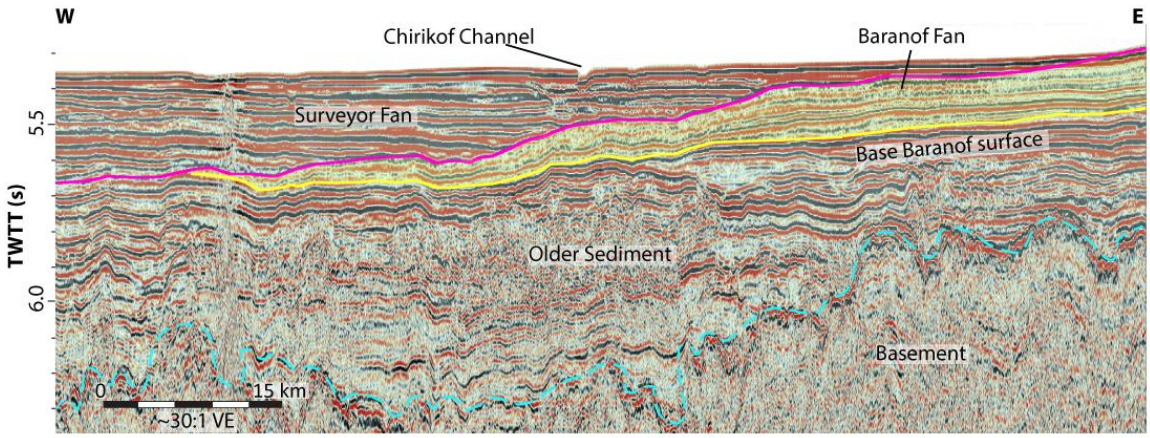

Figure 2.3. Two-dimensional seismic reflection profile MGL1109 Line 5. Section shows Baranof Fan sediment at its northwest extent pinching out beneath Surveyor Fan sediment (line location is shown in Fig. 2.1). TWTT—two-way traveltime. The basement horizon is outlined by the light blue dashed line, the Base Baranof horizon is denoted by the yellow line, and the boundary between the Surveyor and Baranof Fans is marked by the pink line. Note that the Baranof Fan area estimate (shown in Fig. 2.1 and described in the text) only includes the seafloor extent of the Baranof Fan; it does not include the extent of the Baranof Fan sediment pinching out beneath the Surveyor Fan as shown here, as this package is less constrained. VE—vertical exaggeration.

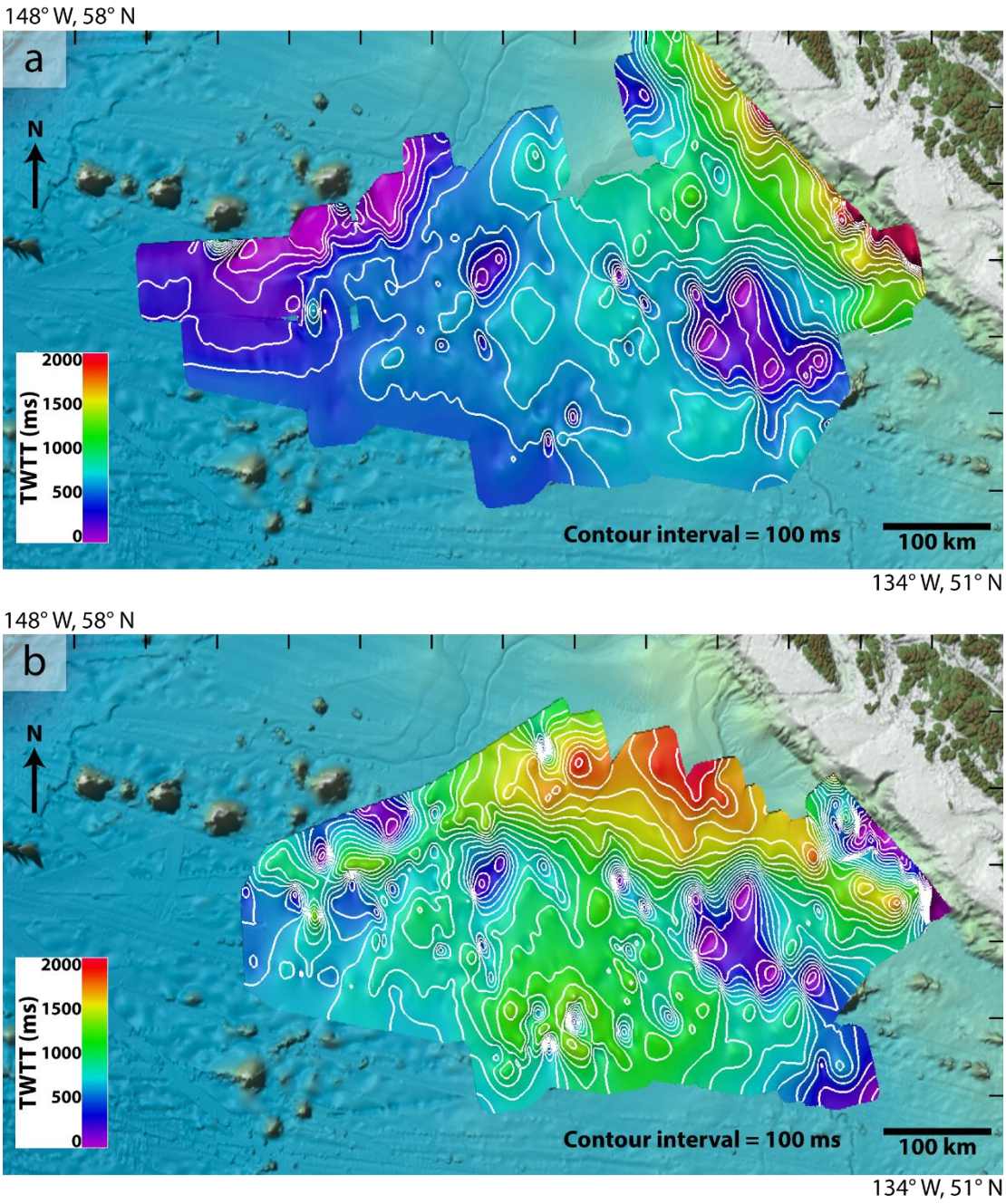

Figure 2.4. Map of gridded sediment thickness maps in two-way traveltime (TWTT). (a) The interval between the Base Baranof regional surface and the seafloor. (b) The interval between basement and the seafloor. Grids are based on picks of the basement, Base Baranof, and seafloor surfaces in available two-dimensional seismic reflection data. Contour interval is 100 ms. Assuming constant seismic velocity of 2000 m/s, thickness in meters matches the thickness values given in ms. Seamounts appear as zero sediment thickness

and some anomalies exist near the shelf and/or grid edges where data are sparse or lesser quality. Latitude/longitude coordinates are assumed to be at the corners of the figures. See Figure 2.1 for complete figure location outline.

2.4.2 Channel-levee systems

Channel complex deposits were mapped along with modern seafloor channel deposits and smaller (~1 km) channelized features. The locations of these channels relative to modern seafloor channel pathways were used to assist in interpreting paleopathways and channel avulsions. We interpret levee deposits as lenses of sediment built up by overbank sediment adjacent to the channel complex deposits.

We identify and map 2–3 levee overbank deposits for each channel complex deposit, mapping surfaces on the basis of high seismic reflectivity, regional continuity, and/or discontinuous stratigraphy. The uppermost levee reflector was mapped for each channel complex, representing the latest stage of active channel deposition. These surfaces were then correlated across 2D seismic reflection lines and assigned relative ages based on their stratigraphic relationships. Levee relationships with parent channels also allowed interpretation and interpolation of paleochannel pathways. In this manner we were able to determine a relative temporal sequence of channel-levee deposits and thereby construct a history of channel avulsions within the fan (Figs. 5–8).

2.4.3 Tectonic reconstruction

Five distinct channel pathways (and associated levees for each) were mapped throughout the subsurface fan, in addition to the Horizon and Mukluk channels on the modern seafloor. Utilizing the principle of superposition and assigning relative ages to the channel-levee systems, we were able to determine a sequence of channel avulsions through time. In order to visualize the changing position of the channels relative to sediment sources onshore, we built a simplified tectonic reconstruction (Fig. 2.9; see supplementary files for

a video showing finer temporal resolution). The reconstruction and subsurface channel relationships together allowed us to estimate the approximate timing of channel initiation, avulsion, and beheading (Fig. 2.9). Given the lack of age data, the reconstruction model was built primarily as a qualitative visualization tool rather than a quantitative age constraint. We assume, for example, channels were initiated after passing major sediment pathways on the shelf such as Dixon Entrance sea valley and Chatham Strait, and were later beheaded when sediment supply across the shelf was cut off by Baranof Island (Fig. 2.2). We have some evidence that tidewater glaciers tend to reoccupy the same sea valleys (e.g. Zurbuchen et al., 2015), so the Dixon Entrance and Chatham Strait sea valleys have likely remained fixed since at least the Pleistocene.

To build the tectonic reconstruction model, we used the GPlates open-source software package (www.gplates.org), superimposing the channel reconstruction on the modern coastline and the tectonic plate boundary (represented by the Queen Charlotte Fault) in a reference framework where North America is fixed. We also included the Yakutat block and the Kodiak-Bowie Seamount Chain in the reconstruction, two tectonic features that have influenced channel initiation and morphology. The total reconstruction was built at a resolution of 0.5 m.y. and begins at 8 Ma. The plate boundary remained a dextral transform interface during this period (e.g., Atwater, 1970; Hyndman and Hamilton, 1993; Prims et al., 1997), so we assume constant plate direction, rate of motion, and fixed sediment input points in our reconstruction.

2.5 OBSERVATIONS AND INTERPRETATIONS

2.5.1 Fan extents

On the abyssal seafloor, the Baranof Fan is situated between the Surveyor Fan to the northwest and the Scott-Moresby sedimentary system to the southeast (Mammerickx

and Winterer, 1970; Morley et al., 1972; Stevenson and Embley, 1987). The relationship between the Baranof Fan and the Scott-Moresby Fan is poorly constrained, but we are able to provide new insight into the relationship between the Baranof and Surveyor Fans using new data from the MGL1109 survey. The intersection of the Baranof Fan with the Surveyor Fan is apparent at the Baranof Fan's northwestern edge in three seismic data transects, including two of the new MGL1109 MCS transects (Fig. 2.3). The Surveyor Fan overlies the Baranof Fan, separated by a sedimentary unconformity with Surveyor sediment onlapping eroded Baranof sediment (Fig. 2.3). The Baranof Fan sediment pinches out in the subsurface beneath Surveyor sediment, meaning that the Surveyor Fan is younger than the Baranof Fan in this area. The Chirikof channel is clearly visible in the seafloor of the Surveyor Fan (Fig. 2.3), showing that it is entirely distinct from Baranof Fan channel systems. Truncations of Baranof Fan reflectors into the Baranof-Surveyor boundary are visible as well (Fig. 2.3). The boundary between the two fans is also visible due to a difference in seismic facies; acoustic amplitudes in the Surveyor Fan are generally higher as opposed to the lower amplitude Baranof reflectors. We interpolated the boundary between transects where it is visible and thereby constrain the northwestern and northern edges of the Baranof Fan.

The unconformity between the Baranof and Surveyor Fans (Fig. 2.3) suggests erosion of the Baranof Fan before or at the time of Surveyor Fan deposition. Because of this erosional relationship, it is difficult to assign an age to this surface, though we can say that Surveyor sediment is, at the oldest, equivalent to the age of Baranof Fan erosion here. Much of the Surveyor sediment has been deposited since 1 Ma (Reece et al., 2011), suggesting that the Baranof Fan's northern region, which we interpret as being the oldest lobe of the fan, is >1 Ma. The younger southern part of the Baranof Fan, however, could be equivalent in age to the Surveyor Fan.

Because the acoustic facies of the Surveyor Fan are higher amplitude than the more transparent Baranof Fan reflectors (Fig. 2.3), we suggest that the fans consist of different sediment types and therefore possibly derive from different sediment sources on the shelf. Where much of the sediment in the Baranof Fan is sourced from the Coast Mountains, Surveyor Fan sediment has largely and most recently been supplied by glacial erosion in the Chugach–St. Elias orogen (Fig. 2.1; Reece et al., 2011). This difference may be in part because of the geometry of the Yakutat block, an oceanic plateau and microplate (Christeson et al., 2010; Worthington et al., 2012) that has translated northward along North America, essentially transcurrent with the Pacific plate, over the past 20 m.y. (Plafker, 1987). We interpret that the Yakutat block essentially acted to separate sediment source regions for the more recent (~7 m.y.) history of the Baranof and the Surveyor Fans, affecting the natural development of drainage network evolution, with the Baranof Fan forming in the wake of the passing Yakutat block. In the Surveyor Fan, tidewater glaciation events transported sediments from their source across the wide shelf, locally formed by the Yakutat block, to the deep-sea fan (Reece et al., 2011). The separation of fan sediment sources due to the Yakutat block was suggested by Stevenson and Embley (1987) and our observations of fan seismic facies and regional tectonics support this interpretation.

Seafloor channels visible in new merged bathymetry data assist in defining more distal Baranof Fan boundaries and channel morphology. Major deep-sea channels are visible in bathymetric data as much as 500 km from the shelf edge. In the very distal fan, the Horizon and Mukluk channels terminate into a series of abyssal ridges (Fig. 2.2), interpreted to be at the Baranof Fan's southern edge and a part of the most distal lobe. A third, sinuous channel is observable in the distal bathymetry (Fig. 2.2), though we cannot constrain its existence with available geophysical data and therefore do not include it in the discussion. Because the channel is proximal to other channel systems in the Baranof Fan,

however, it is included in area and volume estimates for the fan. Close to the shelf where seismic data are sparse or of poor quality, fan extents are interpreted in between Baranof Fan channels and channels of neighboring systems, the Surveyor Fan's Chirikof channel (Reece et al., 2011) and the Scott-Moresby channels to the south and southeast (Mammerickx and Winterer, 1970; Morley et al., 1972).

The fan boundaries we observe in the available bathymetry and 2D seismic data, or otherwise based on interpolation between data points, give us a new estimate of 323,000 km^2 for the area of the Baranof Fan. The area estimate is likely a minimum because data are sparse at the more distal edges of the fan, and as it only includes seafloor extents, the estimate does not include sediment pinching out beneath the Surveyor Fan (Fig. 2.3). The wide shape of the fan is affected by the presence of the Kodiak-Bowie Seamount Chain, which obstructs sediment pathways to the deep seafloor (Fig. 2.1).

2.5.2 Fan volume

Small channel deposits exist below the regionally mapped Base Baranof surface (Fig. 2.3), but channel complex deposits above the surface are much larger; therefore, we interpret the surface as representing the onset of organized Baranof Fan deposition. Sediment below this reflector likely represents some combination of smaller scale channelization and pelagic and hemipelagic sedimentary processes, prior to initiation of large, organized channel systems. Because of this, the gridded Base Baranof horizon can be thought of as an approximation of the paleoseafloor at the onset of major channel formation within the fan. Using a fan area of 323,000 km^2 and isopach grids generated from the regional seafloor, Base Baranof, and basement surfaces (Fig. 2.4), we calculate a sedimentary volume of 209,000 km^3 for the seafloor–Base of Baranof isopach (Fig. 2.4a) and a volume of 301,000 km^3 for the entire sediment column within the fan (seafloor–

basement; Fig. 2.4b). These new estimates for Baranof Fan volume are both larger than the previous estimate of 200,000 km^3 (Stevenson and Embley, 1987). We reiterate that these values are minimum estimates as they do not include Baranof sediment that pinches out beneath the Surveyor Fan. This is because Baranof sediment beneath the Surveyor Fan is only constrained along three 2D seismic transects and depends on the accuracy of fan boundaries, which may be in doubt due to a lack of sufficient geophysical data coverage in the distal Baranof Fan. Given these new size estimates, we show that the Baranof Fan is comparable in size to the Mississippi Fan, and therefore among the largest deep-sea sedimentary fans in the world (Barnes and Normark, 1985; Sømme et al., 2009).

2.5.3 Channel avulsions and lobe switching

Subsurface sediment consists primarily of large channel-levee systems that are mostly buried by recent sedimentation. Channels appear as U- or V-shaped unconformities in the seismic reflection data, with shoulder-shaped, convex-up levee deposits on either side. These channel complexes and channel-levee systems are thought to have been deposited via typical downslope processes such as turbidity currents (e.g., Ness and Kulm, 1973; Stevenson and Embley, 1987; Dowdeswell et al., 1996; Mohrig and Marr, 2003). The majority of subsurface and surficial channel complex deposits are 2–7 km wide (e.g., Figs. 2.5 and 2.6), containing channel fill from several iterations of smaller channels (~1 km width). In many cases, overbank deposition due to thick overflow of turbidity currents causes 1-km-wavelength sediment waves within the levees (e.g., Normark et al., 2002; Posamentier, 2003; Babonneau et al., 2012) that are visible in 2D seismic and bathymetry throughout the fan (e.g., Fig. 2.5). Sediment waves have been observed in several deep-sea fans throughout the world, including the Indus, Amazon, and Monterey Fans (Normark et al., 2002; Fildani et al., 2006). Many levees we observe are also asymmetric, with the

higher side of the overbank occurring on the western sides of the channels (Figs. 2.6 and 2.7); this asymmetry is likely due to the ocean currents from the counterclockwise Gulf of Alaska Gyre (Rea and Snoeckx, 1995; Bart et al., 1999; Keevil et al., 2006) or possibly Coriolis force (e.g., Cossu and Wells, 2010). In seismic images, channel-levee systems appear to be dominantly aggradational, with some erosional transitions (e.g., Fig. 2.6), similar to channels observed in the Amazon and Surveyor Fans (e.g., Ness and Kulm, 1973; Damuth and Flood, 1983; Manley and Flood, 1988; Reece et al., 2011).

A notable pattern within the Baranof Fan is that the oldest channel-levee deposits are in the northwestern fan, and deposits become progressively younger to the southeast. In addition to the well-mapped Horizon and Mukluk channel systems, there is at least one and possibly two additional channel systems visible in subsurface seismic data near the northern extent of the Baranof Fan. The oldest channel-levee deposits (which we call "oldest Baranof deposits") were difficult to interpret due to data quality; only one new seismic line crosses that region (Fig. 2.5) and the Kodiak-Bowie Seamount Chain reduces our confidence in correlating reflectors among seismic lines. The oldest Baranof deposits cannot be connected to other known channel systems (i.e., the Baranof, Horizon, and Mukluk) in the fan. The lack of correlation between the oldest Baranof deposits and other known systems could be due to poor seismic data quality, or because the oldest Baranof deposits are a part of a separate channel system. Regardless, because the oldest Baranof deposits are now buried under ~0.25 km of sediment (Fig. 2.5) and also topped by Surveyor Fan sediment at their northern extent, we are confident that this is the oldest channel system in the Baranof Fan, now beheaded and inactive.

The next oldest channel system (which we call the Baranof Channel), directly south of the oldest Baranof deposits, can be mapped clearly in new 2D seismic data (Figs. 6 and 7) and is visible in high-resolution bathymetry data nearest to the shelf and on the older,

abyssal seafloor (Fig. 2.2). Although the Baranof Channel has a modern seafloor expression, the seafloor channels are less than half the width of previous iterations of the channel, and sediment has nearly aggraded to the top in some places (Fig. 2.7). For this reason, we interpret the Baranof Channel to be recently beheaded after passing Chatham Strait and therefore waning in deposition.

The Baranof Channel has been discussed in literature as a possible third channel system in addition to the Horizon and Mukluk channel systems (Stevenson and Embley, 1987). Our results support the existence of the Baranof Channel as a third, distinct channel system. The Baranof Channel is similar in scale, at ~700 km length, and in subsurface character to the ancestral Horizon and Mukluk Channel deposits. In addition, the Baranof Channel system appears to be the principle routing system for approximately half of the sediment deposited in the northern and western parts of the fan. In the 2D seismic data, we map two distinct buried channel complexes that appear to feed into the same levee overbank deposits, suggesting that these channels were separate systems active at the same time for at least a portion of their history (Fig. 2.7). We interpret one of these buried channels to be an early iteration of the Baranof Channel, currently inactive as it is buried by ~100–200 m of sediment. The other buried channel's uppermost levee reflector can be traced to the base of the modern Horizon Channel (Fig. 2.7), which we interpret to be an avulsion of the Horizon Channel; therefore, we interpret this buried channel complex to be a paleo–Horizon Channel (see Fig. 2.9 for reconstruction).

The traces of the two youngest channels, the Horizon and Mukluk channels, are largely constrained by bathymetric data, especially in the distal Baranof Fan where seismic data are sparse. Both of these channels have subparallel seafloor pathways as they curve through the Kodiak-Bowie Seamount Chain, terminating into a series of abyssal ridges among the Patton-Murray Seamount Chain (Fig. 2.2), seemingly blocked by the

topography. The Horizon and Mukluk channels are ~800 and 750 km in length, respectively, and persist nearly 500 km from the shelf edge onto the abyssal seafloor. The relationship of the modern Horizon Channel to the modern Mukluk Channel is observable in 2D seismic data from the more proximal fan (Fig. 2.8). The Mukluk Channel fill extends deeper into the sediment than the modern Horizon Channel fill, which might suggest that it is older than the Horizon Channel. We do not map an avulsion of the Mukluk Channel, however, whereas the Horizon Channel has undergone at least one avulsion (Fig. 2.7). We therefore propose that the Mukluk Channel is younger than the Horizon Channel, though we cannot be certain due to relatively poor data quality and coverage over the Mukluk Channel.

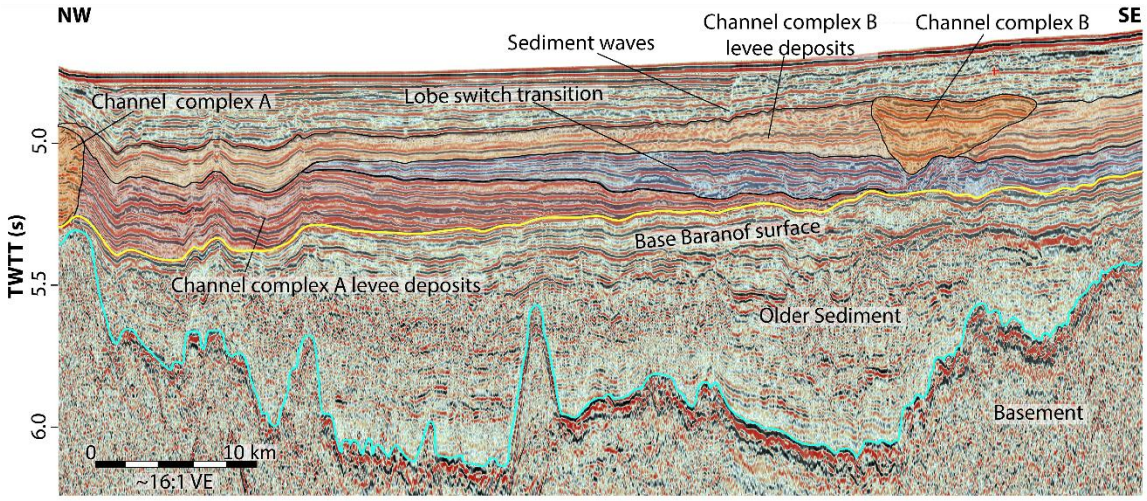

Figure 2.5. Two-dimensional seismic reflection profile MGL1109 Line 6. Section depicts the oldest mapped lobe switch within the Baranof Fan. TWTT—two-way traveltime; VE—vertical exaggeration. This figure highlights channel and levee deposits associated with the avulsion. Line location is shown in Figure 2.1.

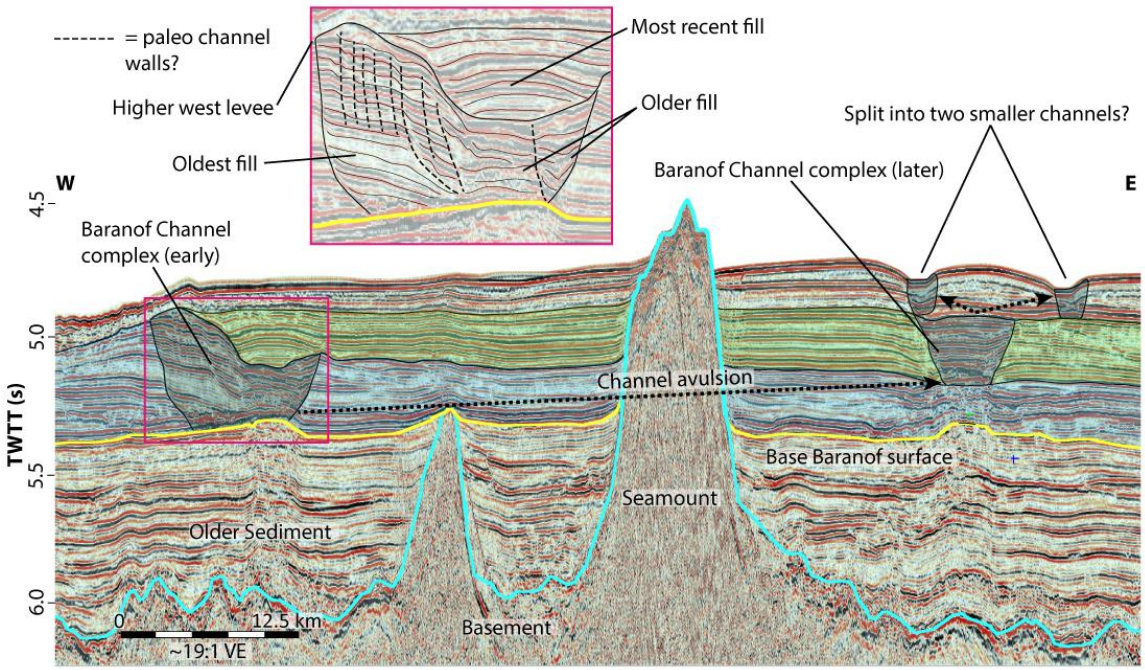

Figure 2.6. Two-dimensional seismic reflection profile MGL1109 Line 9. Section shows an avulsion of the paleo–Baranof Channel. TWTT—two-way traveltime; VE—vertical exaggeration. Levee deposits associated with each iteration of the Baranof Channel are highlighted in blue and green. Inset shows a line-drawing interpretation of stratigraphic relationships within the early, now buried, Baranof Channel complex (location is indicated by a pink box). Most recent channel fill of the early Baranof Channel may be derived from the later iteration of the Baranof Channel. Line location is shown in Figure 2.1.

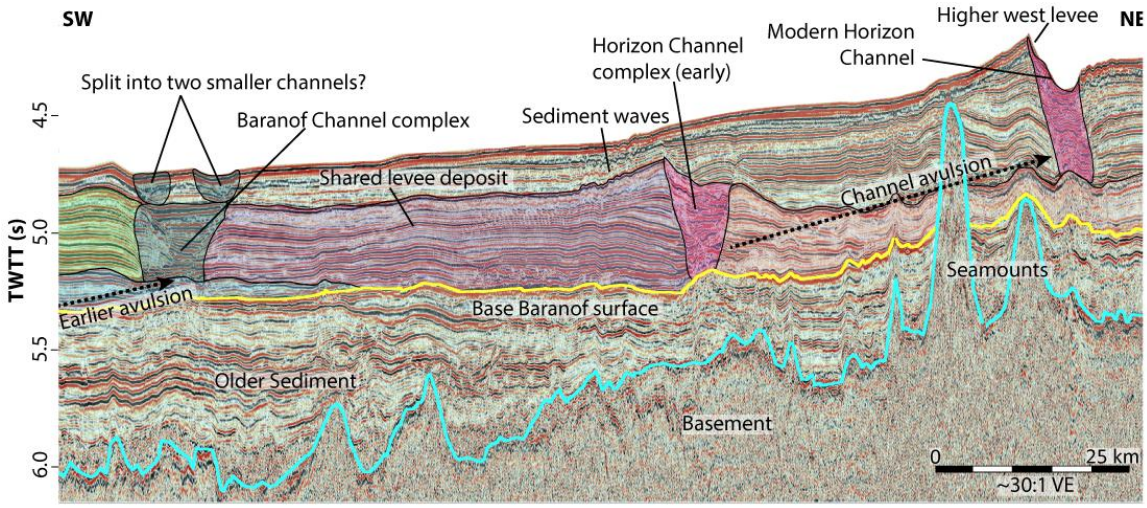

Figure 2.7. Two-dimensional seismic reflection profile MGL1109 Line 11. Section shows the subsurface, paleorelationship between the Baranof Channel and the paleo–Horizon Channel, as well as the Horizon Channel's latest avulsion to its current position on the modern seafloor. TWTT— two-way traveltime; VE—vertical exaggeration. Line location is shown in Figure 2.1.

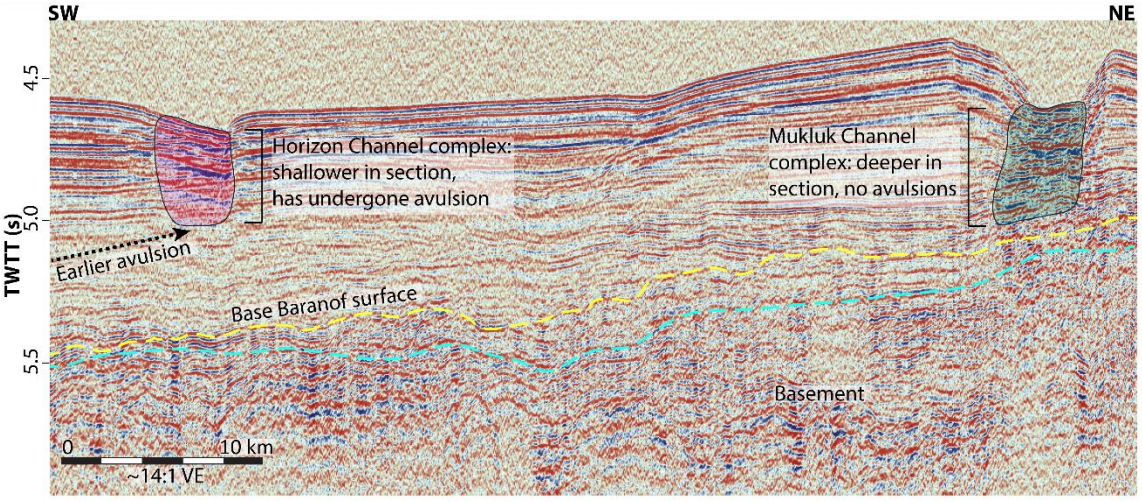

Figure 2.8. U.S. Geological Survey two-dimensional seismic profile (Line 52 from survey F789EG). Section shows the relationship between the modern Horizon Channel and the modern Mukluk Channel. The Mukluk Channel fill extends deeper into the subsurface than the modern Horizon Channel fill, but does not appear to have undergone an avulsion, as the Horizon Channel has. TWTT— two-way traveltime; VE—vertical exaggeration. Line location is shown in Figure 2.1.

2.5.4 Depositional history

We interpret the Baranof Fan to be a reactive system as described by Covault et al. (2010, 2013), with high sediment flux (interpreted based on large fan volume and glacial interaction) allowing for external tectonic forcing to be visible in the sediment record. Our observation of consistently southward-avulsing channels and channel-levee deposits younging southward suggests that the development of sediment pathways was influenced by the translation of the Pacific plate past sediment point sources on the shelf, such as the bathymetrically imaged glacial sea valleys or shelf-crossing troughs (Carlson et al., 1982, 1996; Vorren and Laberg, 1997). The sequence of channel system formations and beheadings supports this tectonics-driven depositional pattern in the fan, as the oldest channel systems in the north are now beheaded and the youngest (Mukluk) channel is the farthest south. This interpretation supports similar results from previous studies (Stevenson and Embley, 1987; Dobson et al., 1998).

Because of the lack of age control, there is still a question of when deposition of the Baranof Fan initiated and how quickly its channel systems developed. The timing of initiation also implies a position of the Pacific plate relative to North America sediment sources, an important yet unconstrained factor to consider. We hypothesize that major channel systems formed only when adjacent to major sediment sources such as the Dixon Entrance (Fig. 2.2), and that sediment supply was cut off where pathways to the seafloor are blocked, namely, in the south at the Haida Gwaii Islands and in the north by Baranof Island (Fig. 2.2). We know that the oldest channel systems in the northern Baranof Fan, now beheaded, must have been active when they were adjacent to sediment sources between Haida Gwaii and Baranof Island. The timing of activation of the oldest channel systems, however, could vary. In a small-offset model, the Baranof Channel, possibly the oldest channel system in the fan, could have initiated when it was adjacent to the Chatham

Strait sea valley ~100 km southeast of its modern position, with the Horizon and Mukluk channels forming subsequently as they received sediment via a shelf canyon system and the Dixon Entrance, respectively. In a longer offset model, the Baranof Channel initiated when it reached the Dixon Entrance ~300 km southeast of its modern location, the other channels forming later as new parts of the Pacific plate became exposed to this sediment source.

Our observations favor a large-offset (~300 km) model, with the Baranof Channel initiating at the Dixon Entrance and the Horizon and Mukluk channels forming sequentially as they in turn reached the Dixon Entrance. A small-offset model requires a southward-sequential pattern of channel development despite the three channel systems being simultaneously exposed to shelf sediment pathways. Large-offset-aided sequential exposure seems more likely than simultaneous exposure given that the seismic reflection data clearly show southward-younging deposits in the subsurface, and channel avulsions filling available accommodation space in the south. In addition, a small-offset model implies a much smaller time frame for fan development (~2 m.y., assuming constant plate motion). The Surveyor Fan's Chirikof channel system is visible in the seafloor on top of older, northern Baranof Fan sediment (Fig. 2.3). A small-offset model suggests full development and beheading of the Baranof Channel system as well as formation of the young Chirikof channel system over the past ~2 m.y., less likely than a large-offset solution that allows more time for Baranof Channel evolution and more realistic deep-sea sedimentation rates.

Based on a large-offset model, we provide an approximate age for the onset of Baranof Fan deposition using tectonic reconstruction, despite lack of age constraints from cores. Our tectonic model is constrained using previous regional analysis. Dextral strike-slip motion has dominated the Pacific–North America plate boundary along the Queen

Charlotte Fault for the past ~20 m.y. (Atwater, 1970; Hyndman and Hamilton, 1993); a discrete clockwise rotation in the Pacific plate motion vector ca. 6 Ma (Doubrovine and Tarduno, 2008) caused oblique convergence along the southern fault (Hyndman and Hamilton 1993). Today, the Queen Charlotte Fault is seismically active and has undergone large strike-slip and some oblique-thrust events (Lay et al., 2013).

Our tectonic reconstruction assists with visualization of channel formation, avulsions, and beheadings through the Baranof Fan's history (Fig. 2.9; see also supplementary video). We superimposed the reconstruction on the modern coastline to best emphasize the plate offset and create a frame of reference. We also include the outline of the full extent of the Yakutat block, which has translated north along with the Pacific plate for the past ~20 m.y. and is currently undergoing flat-slab subduction beneath North America (Eberhart-Philips et al., 2006). We use recent GPS measurements from Elliott et al. (2010) to provide a relative dextral offset rate of 44 mm/yr between the Pacific and North American plates. Assuming a constant 44 mm/yr rate and that sedimentary deposition initiated when the northernmost channels (the oldest Baranof deposits) were at the southernmost sedimentary source (the Dixon Entrance), the 300-km-long shift of the northernmost (now buried) channel from the south end of the Dixon Entrance to its modern position must have taken ~7 m.y. This calculation means that the oldest sedimentary deposits in the Baranof Fan are late Miocene, which is consistent with the 12 Ma basement rock underlying the fan sediment (Berggren et al., 1985). The timing of channel formation and beheading is based strictly on location relative to sea valleys on the shelf, with channels initiating as they pass the Dixon Entrance and beheading after passing Chatham Strait.

Although sediment pathways south of the Dixon Entrance are blocked by Haida Gwaii (Fig. 2.1), we acknowledge that the Queen Charlotte Sound south of Haida Gwaii may also have served as a source for older sediment in the Baranof Fan early in its history

(Yorath, 1987), providing a very-long-offset model possibility. However, the now-distal Baranof Fan may have been at the Queen Charlotte Sound ca. 12–14 Ma, and cut off from sediment sources until ca. 7 Ma as it passed by Haida Gwaii. The age of the basement beneath the proximal Baranof Fan is only 12 Ma, making a very long offset model unlikely; however, older sediment beneath the Base Baranof surface in the more distal fan may derive from the Queen Charlotte Sound if it is older than ca. 7 Ma.

Assuming that deposition of the Baranof Fan occurred over the past ~7 m.y., overlapping with several major periods of Northern Hemisphere cooling (including the Pleistocene Epoch beginning ca. 2.6 Ma), glacial events must have influenced sedimentation. The Surveyor Fan, north of the Baranof Fan, has been strongly influenced by periods of glaciation throughout its depositional history (Reece et al., 2011). Without the necessary core data to better constrain the ages of the sedimentary deposits in the Baranof Fan, however, it is not possible to match channel formation events or periods of accelerated deposition to specific glacial periods. Given the high latitude, the glaciation of the area, and the dynamic capability of glaciers to carry massive amounts of sediment (e.g., Dowdeswell et al., 1996; Reece et al., 2011), we think that glaciation over the past 7 m.y. has likely had a significant influence on the sedimentation rates and flux to the Baranof Fan, particularly since glacial intensification and increased uplift of the Coast Mountains and the St. Elias orogen ca. 2.56 Ma (Farley et al., 2001; Enkelmann et al., 2009).

It is interesting that there is no new channel forming at the mouth of the Dixon Entrance, despite the Mukluk Channel having passed it by; however, we hypothesize that there is either a channel poised to form at the mouth of the Dixon Entrance sea valley, or that all of the sediment in the area is still being funneled to the Mukluk Channel. The lack of new channel supports the idea that the Baranof Fan is a sea-level lowstand fan system,

and that perhaps a new channel may form at the Dixon Entrance during a near-term lowstand event.

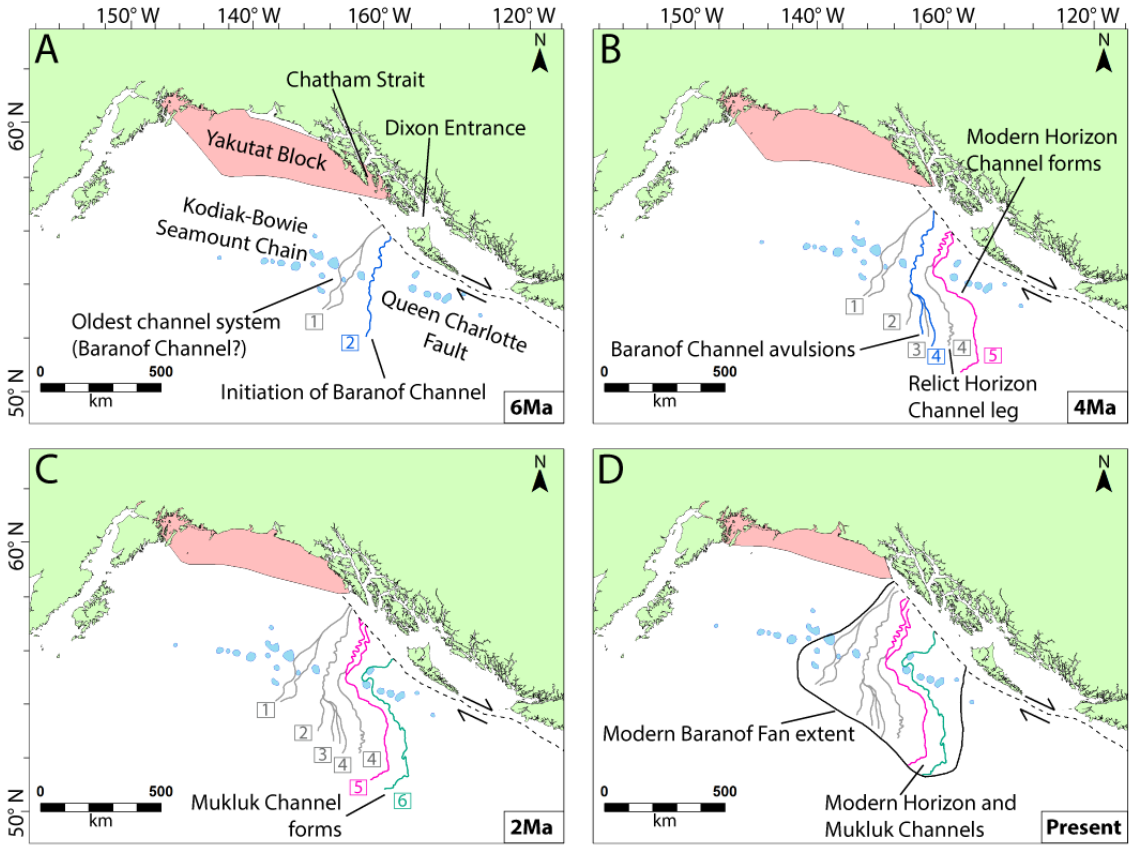

Figure 2.9. Simplified plate boundary reconstruction of the evolution of the Baranof Fan. Images show snapshots in time of channel formation, avulsion, and beheading as the Pacific plate moves past sediment sources on the shelf. Pink is the Yakutat block, green is land, and blue is the Kodiak-Bowie Seamount Chain. Active channels are shown in color; beheaded channels are shown in gray. Reconstruction uses the modern coastline and plate boundary (represented by the Queen Charlotte Fault) for reference. See supplementary files for a video at finer temporal resolution.

2.5.5 Similar systems

In both scale and downslope channel-levee dynamics, the Baranof Fan is similar to lower latitude fluvial fans like the Amazon Fan (Damuth and Flood, 1983; Manley and Flood, 1988; Lopez, 2001), though its high latitude, glacial valleys on the shelf, and thick sediment near the shelf edge would suggest a component of glacial influence (Carlson et al., 1982; Dowdeswell et al., 1996; Laberg and Vorren, 1996). The Gulf of Alaska deep-sea fans differ from high-latitude sedimentary deposits observed elsewhere (e.g., Norway, Greenland), however, which are typically referred to as trough-mouth fans (TMFs) (Vorren et al., 1989). The Gulf of Alaska fans have well-developed channel distributary systems similar to river-fed fans (e.g., Damuth and Flood, 1983), whereas TMFs tend to be composed of debris flow lobes (Vorren et al., 1989; Laberg and Vorren, 1996; Vorren and Laberg, 1997); in addition, the Gulf of Alaska fans are as much as 1–2 orders of magnitude larger than most TMFs. The Baranof Fan may have had sedimentary inputs from both fluvial and glacial sources, though there is evidence for more recent glaciation on the seaward shelf edge.

As a young deep-sea fan that matured quickly, the Baranof Fan provides a unique opportunity to observe a deep-sea fan in its early stages prior to full maturation and complexification – a rarity in deep-sea fan systems (e.g. Damuth and Flood, 1983; Clift et al., 2001). Though the Baranof Fan has few, if any, modern analogues at a similar scale, we find similar sedimentary processes when comparing it to smaller scale fan systems affected by strike-slip motion. There is evidence that strike-slip motion along the San Andreas fault in southern California, a fault similar in scale and offset to the Queen Charlotte Fault (Carlson et al., 1988), has caused sequential lobe switching in adjacent fans such as the Monterey Fan (e.g., Normark, 1998). The upper Monterey Fan, which consists of channel-levee systems similar to the Baranof Fan, and has undergone shifts in sediment

source and channel geometry due to tectonic influence (Normark, 1998; Fildani and Normark, 2004). However, both the volume of the upper turbidite sequence in the Monterey Fan (~100 km^3) and the time required to deposit it (500 k.y.) are several orders of magnitude smaller than those of the Baranof Fan.

2.6 CONCLUSIONS

Based on our interpretation of seismic and bathymetry data, we provide new constraints on the depositional history of the Baranof Fan. Mapping of bathymetry, channel deposits, and regional seismic horizons provide estimates of the area, shape, and volume of the Baranof Fan; the estimated area of the fan is 323,000 km^2, with a total estimated sediment volume of 301,000 km^3. Organized fan deposition comprises a sediment volume of 209,000 km^3 above the regionally mapped Base Baranof downlap surface. These size constraints are larger than previous estimates (Stevenson and Embley, 1987), making the Baranof similar in size to the Mississippi Fan. The intersection of the Baranof Fan with the Surveyor Fan to the north helps define the northern extent of the Baranof Fan. In this area, the Baranof Fan is older than the Surveyor Fan; much of the Surveyor Fan was deposited in the past 1 m.y., implying that this oldest lobe of the Baranof Fan is at least 1 m.y. old.

The Horizon and Mukluk channels are ~800 and ~750 km in length, respectively, curving sharply to the south at the Kodiak-Bowie Seamount Chain, creating a wider rather than longer fan shape. There is strong evidence for one or two now extinct or recently beheaded channel systems north of, and older than, the modern Horizon Channel system. We identify one of these as the Baranof Channel system in seismic data, observing it as a major channel-levee system distinct from the Horizon and Mukluk systems. It is difficult to map individual channel deposits in the sparse and lower quality seismic data in the northernmost fan, so it is unclear if the oldest Baranof deposits (Fig. 2.5) represent an early

phase of the Baranof Channel system, or if there was actually a fourth channel system, older than all of the other known channel systems.

We observe that the relative ages of channel-levee deposits in the Baranof Fan are consistently younger southward. Based on this observation, we conclude that channel avulsion, formation, and beheadings have progressed from north to south within the fan over the past ~7 m.y. Given the northwestern motion of the Pacific plate relative to sediment sources on the North American Plate, it is likely that this tectonic motion has been the dominant influence on channel development throughout the Baranof Fan history.

Chapter 3: Basement and regional structure along strike of the Queen Charlotte Fault in the context of modern and historical earthquake ruptures[2]

ABSTRACT

The Queen Charlotte Fault (QCF) is a NW-striking, dextral transform system located offshore of southeastern Alaska and western Canada, accommodating ~44 mm/yr of relative motion between the Pacific and North American plates. Oblique convergence along the fault increases southward, and how this convergence is accommodated is still debated. Using seismic reflection data, we interpret offshore basement structure, faulting, and stratigraphic relationships to provide a geological context for two recent earthquakes: a M_w 7.5 strike-slip event near Craig, Alaska, and a M_w 7.8 thrust event near Haida Gwaii, Canada. We map downwarped Pacific oceanic crust near 54° N, between the two rupture zones. Observed downwarping decreases to the north and south of 54° N, parallel to the strike of the QCF. Bending of the Pacific Plate here may have initiated with increased convergence rates due to a plate motion change at ~6 Ma. Tectonic reconstruction implies convergence-driven Pacific Plate flexure, beginning at 6 Ma south of a 10° bend in the QCF (which is currently at 53.2° N) and lasting until the plate translated past the bend by ~2 Ma. Normal-faulted approximately late Miocene sediment above the deep flexural depression at 54° N, topped by relatively undeformed Pleistocene and younger sediment, supports this model. Aftershocks of the Haida Gwaii event indicate a tensile stress regime, suggesting present-day plate flexure and underthrusting, which is also consistent with reconstruction of past conditions. We thus favor a Pacific Plate underthrusting model to

[2] Walton, M. A. L., S. P. S. Gulick, P. J. Haeussler, E. Roland, and A. M. Tréhu (2015), Basement and regional structure along strike of the Queen Charlotte Fault in the context of modern and historical earthquake ruptures, *Bull. Seismol. Soc. Am.*, *105*(2b).

initiate flexure and accommodation space for sediment loading. In addition, mapped structures indicate two possible fault segment boundaries along the QCF at 53.2° N and at 56° N.

3.1 INTRODUCTION

Offshore of southeast Alaska and western British Columbia, the ~750 km long NW-striking Queen Charlotte Fault (QCF) is the principle Pacific–North America plate boundary fault, accommodating relative dextral offset of 44 mm/yr (Fig. 3.1; Elliott et al., 2010). The fault is obliquely convergent along strike, with maximum convergence south of a bend in the QCF at 53.2° N. The northern QCF strikes at 338° (Rohr et al., 2000) and offshore of southeastern Alaska becomes the Fairweather Fault, resulting in a 1200-km-long onshore/offshore right-lateral transform zone (Fig. 3.1; Fletcher and Freymueller, 2003). The junction of the Queen Charlotte, Fairweather, and Transition faults is located at the southeastern tip of the Yakutat block, an oceanic plateau and microplate (Fig. 3.1; Gulick et al., 2007; Christeson et al., 2010). The southern boundary of the QCF is marked by the complex Pacific–North American–Explorer triple junction off the coast of southern British Columbia (Fig. 3.1; Rohr and Furlong, 1995; Rohr, 2015). South of 53.2° N, near Haida Gwaii, the strike of the QCF is 328°, a ~10° departure from the northern QCF, creating oblique convergence between the plates and a structural regime similar to a restraining bend along the southern QCF (Fig. 3.1; Rohr et al., 2000).

There have been several strike-slip earthquakes with a magnitude larger than 7 along the Queen Charlotte–Fairweather Fault system in the last century (Fig. 3.1). The earliest recorded large event was a magnitude 7.1 earthquake on the southeast QCF in 1927 (Tobin and Sykes, 1968). In 1949, the largest recorded earthquake in Canada occurred when an estimated 470 km long section (Rogers, 1986) of the southern and central QCF

slipped to produce a M_s 8.1 earthquake (Sykes, 1971). The extent of the 1949 rupture area is debated and poorly constrained due to difficulties in interpreting the aftershock sequence and disagreement with surface-wave directivity analysis. A study by Bostwick (1984) proposes two models for the 1949 event: a longer, bilateral rupture model based on aftershocks and a shorter, northward-propagating rupture based on surface-wave directivity (see Fig. 3 from Tréhu et al. (2015) for a summary of different rupture models for the 1949 event). Recent Global Positioning System (GPS) analysis of seismicity supports the latter, shorter rupture model for the 1949 event (Ding et al., 2015). Subsequent to the 1949 event, a M_s 7.9 earthquake in 1958 ruptured 280 km of the Fairweather Fault (Tocher, 1960; Plafker et al., 1978), and a M_s 7.6 earthquake ruptured near Sitka in 1972 along the central QCF (Schell and Ruff, 1989).

Two recent large earthquakes have brought increased interest to the fault structure along the QCF. On 28 October 2012, a M_w 7.8 earthquake occurred just offshore and south of Moresby Island, Canada (southern Haida Gwaii; Fig. 3.1). This earthquake (the Haida Gwaii earthquake) occurred on a thrust fault with some oblique slip, striking north-northwest ~320° and dipping ~18.5° to the east; it ruptured ~150 km of a fault at 14 km depth, with an average ~3.3 m of slip (James et al., 2013; Lay et al., 2013; U.S. Geological Survey [USGS]). On 5 January 2013 and 330 km northwest of the Haida Gwaii epicenter, a M_w 7.5 event occurred 95 km west of Craig, Alaska (Fig. 3.1). The Craig earthquake demonstrated significantly different source properties, with a right-lateral strike-slip mechanism. This event ruptured a ~150 km segment of the QCF, striking 335°on a subvertical fault plane dipping 63° to the east. Maximum slip was estimated at 7–8 m (from USGS). The Craig earthquake is similar in mechanism and magnitude to many of the historic strike-slip events along the QCF. The Haida Gwaii event was exceptional because it was significantly larger in moment magnitude than other thrust events along the

transpressional southern QCF system (Ristau et al., 2007; Rabinovich et al., 2008). It was followed by normal-mechanism aftershocks within the Pacific Plate, likely generated from bending of the Pacific Plate in response to underthrusting (Lay et al., 2013; Kao et al., 2015).

Because of active seismicity and its similarity to other large-scale strike-slip systems, study of the QCF system is important for assessing the hazard to communities located near the fault, as well as for better understanding of ocean-continental transform systems. The QCF system is comparable to the San Andreas in terms of length and moment release (e.g., Carlson et al., 1988; Freymueller et al., 1999), yet it has been much less studied. In this investigation, we compile and analyze publicly available marine geophysical data to provide regional-scale interpretations of crustal and fault structure along the entire strike of the QCF system. Specifically, we map areas of basement flexure, buried offshore normal faulting, and modern fault geometry. We observe downwarping of the Pacific Plate north of 53.2° N and suggest that this flexure is a remnant of, and evidence for, past convergence south of 53.2° N. By putting earthquake ruptures along the margin into the context of our observations, we also provide evidence for two possible fault segment boundaries along the QCF: one at 53.2° N and the other at 56° N.

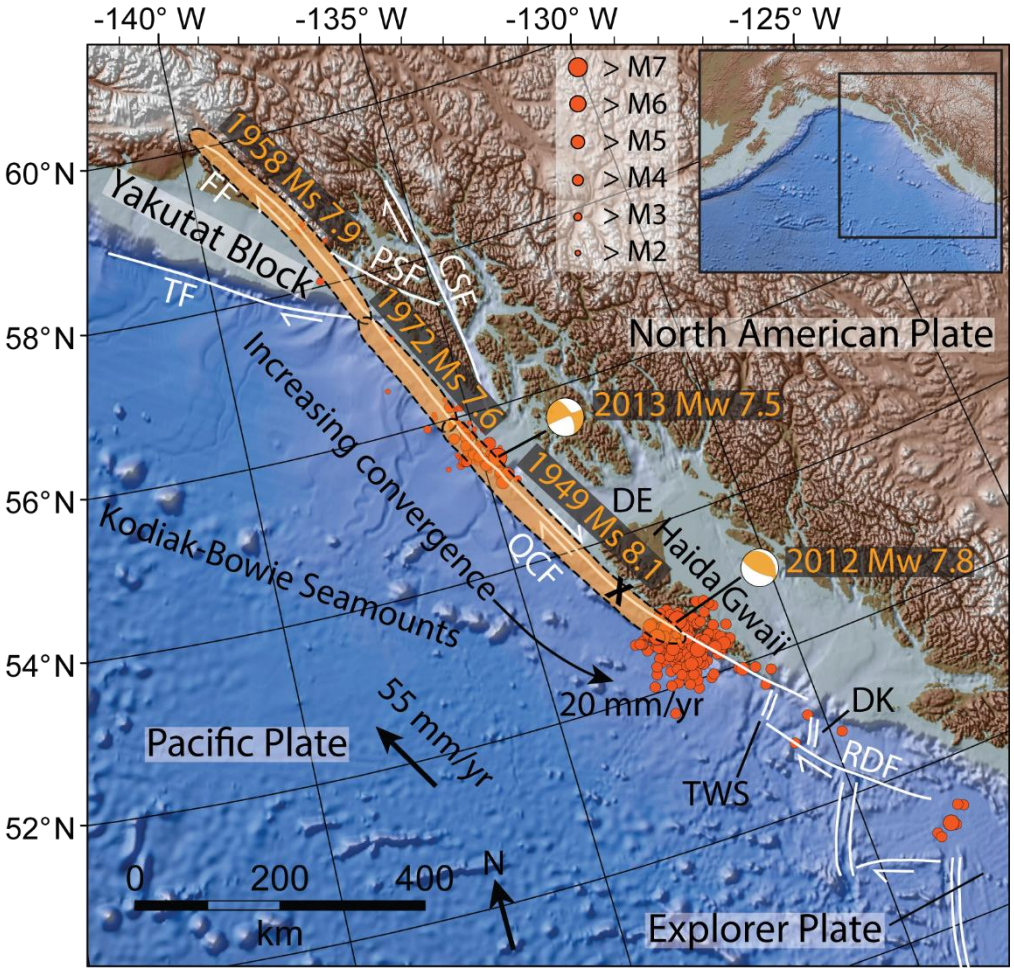

Figure 3.1. Map of the regional tectonic setting of the Queen Charlotte Fault (QCF). The inset shows regional location and major fault traces. Plate motion vector from MORVEL (DeMets et al., 2010). Because of the angle of the Pacific Plate vector and the geometry of the QCF, convergence along the fault increases to the south. The bold X on the QCF marks a 10° change in strike of the QCF at 53.2° N, south of which is an obliquely convergent segment of the QCF undergoing convergence rates up to ~20 mm/yr. The QCF is bounded to the north by the Yakutat block and to the south by the Explorer triple junction. Rupture zones defined by aftershocks for major historic earthquakes along the margin are indicated by dashed black outlines (Plafker et al., 1994). Aftershocks (circles) and focal mechanisms for the 2013 M_w 7.5 Craig earthquake and the 2012 M_w 7.8 Haida Gwaii earthquake are also included, along with a magnitude scale for aftershocks (derived from the Global Centroid Moment Tensor catalog; Ekström et al., 2012). DE, Dixon Entrance; TWS, Tuzo Wilson Seamounts; DK, Dellwood Knolls; RDF, Revere-Dellwood Fault; TF, Transition Fault; FF, Fairweather Fault; PSF, Peril Strait Fault; CSF, Chatham Strait Fault.

3.2 QUEEN CHARLOTTE FAULT GEOMETRY AND CONVERGENCE

The QCF system has had a varied history prior to the current phase of Pacific–North America plate motion. The system began at the time of a major plate reorganization in the Pacific at ~50 Ma (Haeussler et al., 2003). After oblique extension from ~36 to 20 Ma (Hyndman and Hamilton, 1993; Morozov et al., 1998), a plate motion change at 20 Ma resulted in the Yakutat block beginning to travel with the Pacific Plate (Hyndman and Hamilton, 1993). This event is generally interpreted as the beginning of strike-slip motion on the QCF (Atwater, 1970; Carlson et al., 1988), and it has remained a strike-slip fault since 20 Ma (Crouch et al., 1984). Oblique convergence along the QCF is thought to have begun in the late Miocene or early Pliocene due to a small change in Pacific Plate motion. The exact timing of the change is debated (e.g., von Huene et al., 1979; Hyndman and Hamilton, 1993; Wilson, 2002; Smith et al., 2003); recent modeling places the change at 6 Ma (Doubrovine and Tarduno, 2008), the age we assume for this study. The geometry of the QCF is important when considering local restraining and releasing bends; today, oblique convergence is highest along the QCF south of a restraining right step at 53.2° N (Fig. 3.1). Based on structural analysis, Tréhu et al. (2015) suggest that the change in strike of the QCF at 53.2° N significantly affects the response of the Pacific Plate upper crust and overlying sediments to transpression, with pure shear dominant to the south and simple shear dominant to the north. The results of this study are consistent with this idea.

The Haida Gwaii earthquake can be explained by oblique convergence along the southern QCF where the convergent component is 15–20 mm/yr as predicted by MORVEL (DeMets et al., 2010; Tréhu et al., 2015). A maximum 100–120 km of convergence based on a 20 mm/yr rate must have been accommodated along the QCF over the last 5–6 Ma (Crouch et al., 1984; Hyndman and Hamilton, 1993). Many questions still exist concerning

lithospheric and fault structure of the QCF and how shortening is accommodated in the crust, particularly along the southernmost QCF where the convergence rate is highest.

Convergence along the southern QCF, accommodated by underthrusting of the Pacific Plate beneath Haida Gwaii, has been proposed previously (e.g., Hyndman et al., 1982; Hyndman and Hamilton, 1993). Evidence for underthrusting includes the presence of the Queen Charlotte Trough west of Haida Gwaii, a sedimentary complex similar to an accretionary prism (the Queen Charlotte Terrace [QCT]), coastal uplift, heat flow measurements, and a dipping low-velocity anomaly at depth east of the QCF thought to represent oceanic crust (Bustin et al., 2007). These features are all consistent with incipient subduction. Models have also been proposed in which all convergence is accommodated by shortening via thrust faulting on either side of the QCF extending through the crust (Hyndman and Ellis, 1981; Rohr et al., 2000). This model requires at least 80 km of crustal shortening (assuming a 4 m.y. duration of 20 mm/yr convergence) over a width of 30–60 km within both the Pacific and North American plates (Crouch et al., 1984; Rohr et al., 2000), which is similar to the 14–72 km of transpression taken up along the San Andreas fault (Crouch et al., 1984). In the latter case, flexural modeling shows that the Queen Charlotte Trough could be explained by plate flexure due primarily to sediment loading on the Pacific Plate (Prims et al., 1997) and does not require an additional load from the Pacific Plate underthrusting the North American Plate east of the QCF (Harris and Chapman, 1994).

The source properties of the recent Haida Gwaii earthquake, as well as aftershock behavior and information on coseismic deformation, shed more light on convergence models for southern Haida Gwaii and support a model that incorporates underthrusting of the Pacific Plate (e.g., Lay et al., 2013; Nykolaishen et al., 2015). The Haida Gwaii mainshock hypocenter was located 7 km landward of the QCF main trace, at a depth

corresponding with the lower end of the seismogenic zone of an underthrust Pacific Plate (Kao et al., 2015). A tsunami with up to ~13 m runup also indicates a significant component of underthrusting and slip (Leonard and Bednarski, 2014). Normal-mechanism aftershocks in the Pacific Plate suggest plate bending and downdip extension, consistent with young subduction (Lay et al., 2013; Farahbod and Kao, 2015; Kao et al., 2015). GPS data and new thermal models are consistent with these interpretations, supporting a shallow megathrust event (Nykolaishen et al., 2015; Wang et al., 2015). Although these recent results strongly support underthrusting in the Haida Gwaii region, some amount of crustal shortening in the continental and/or oceanic plates has almost certainly taken place, given the complex fault patterns and deformation along strike of the QCF. The question of how much shortening versus underthrusting has taken place is a topic of ongoing debate and research.

In this study, we observe an inactive, buried flexural system north of Haida Gwaii and hypothesize that it is a remnant of a similar system currently observable to the south, suggesting that the now inactive system underwent convergence along the southern QCF before translating past it. We present a hybrid model that can accommodate elements of both underthrusting and crustal shortening, with Pacific Plate flexure initiated by underthrusting and preserved by sediment loading.

3.3 METHODS

3.3.1 Data

Seismic reflection data available through the USGS (Fig. 3.2) were used for the bulk of our interpretations. Two-dimensional USGS seismic surveys crossing offshore faults include L577EG (1977), L378EG (1978), S578EG (1978), S679GA (1979), and F789EG (1989). Each of these surveys was used in this study for mapping faults and

basement structure. S578EG (Carlson et al., 1985) was one of the original surveys used to map the QCF north of 56° N, and we compare our new mapping to these original results. Surveys L577EG and L378EG are high-resolution surveys employing a 24-channel streamer, with seismic lines crossing the QCF several times along strike, covering the northern half of Haida Gwaii and the Dixon Entrance. These two surveys were integral to this study, and several figures presented here display data from these surveys. Surveys S679GA and F789EG were used in this study, primarily for basement mapping. S679GA is a deep-water USGS survey that crosses the northern QCF. F789EG was shot as part of the Geological LOng-Range Inclined Asdic (GLORIA) project conducted by the USGS and the Institute of Oceanographic Sciences (now the Southampton Oceanography Center) in an effort to better define the United States exclusive economic zone. GLORIA surveys were primarily designed to obtain sidescan sonar data coverage of the Gulf of Alaska, but two-channel seismic reflection data were also collected (Bruns et al., 1992). Data are quite sparse along the southern QCF off of central Haida Gwaii; survey F789EG provides one of the few constraints on basement structure in this region, so data from other studies support interpretations here.

Academic survey EW9412, shot as a part of the ACCRETE project (e.g., Scheidhauer et al., 1999), is one of the better-quality marine seismic datasets crossing the QCF, with five 2D seismic reflection lines covering the area just north of Haida Gwaii at the Dixon Entrance (Fig. 3.2). The survey was collected aboard the R/V Maurice Ewing in 1994. Processing was completed by M. Scheidhauer (Scheidhauer, 1997; Scheidhauer et al., 1999). This survey was important for interpretation of faults and basement structure in the area, and examples of the EW9412 profiles are provided by Rohr et al. (2000) and Tréhu et al. (2015).

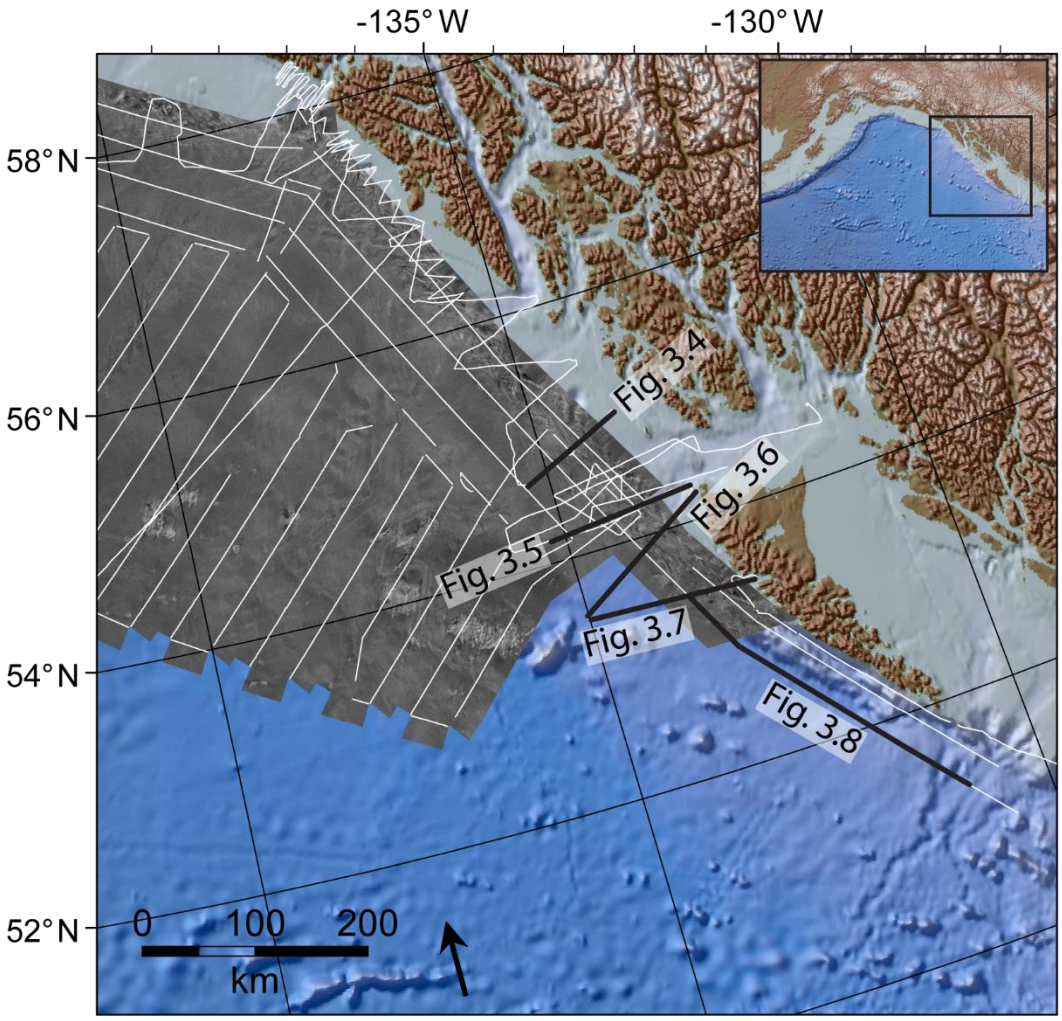

Figure 3.2. Data coverage map. Map shows ETOPO1 bathymetry as the background image (Amante and Eakins, 2009), GLORIA sidescan sonar data overlaid on top of the bathymetry, and U.S. Geological Survey (USGS) and academic 2D seismic reflection surveys that cross the QCF are displayed as white lines. Plotted surveys include USGS surveys L577EG, L378EG, S578EG, S679GA, and F789EG, and academic survey EW9412. For this study, basement and fault mapping were completed on lines from all surveys. Sections shown in other figures are highlighted with their figure numbers labeled. The inset shows regional location.

In addition to the coincident seismic data, GLORIA sidescan sonar data were used (Fig. 3.2) to map the seafloor trace of the QCF. The QCF has previously been mapped using the 50 m resolution GLORIA data (e.g., Bruns et al., 1992). In this study, the seafloor expression of the fault has been remapped using the GLORIA dataset and compared with fault-crossing seismic reflection data. In addition to the GLORIA data, there is high-resolution (~100 m^2) multibeam bathymetry coverage along the continental slope and rise of the northern and central QCF from the United Nations Commission Law of the Sea (UNCLOS; Gardner et al., 2006). Due to their lower resolution, these data are not quite as effective as the GLORIA data for mapping the QCF on the seafloor. The 100 m resolution UNCLOS data were merged with ETOPO1 1 arc-min global relief data (Amante and Eakins, 2009) and used primarily as a background map for reference. The southernmost QCF has new, high-resolution multibeam coverage and is discussed by Barrie et al. (2013) and Rohr (2015).

Gridded magnetic and gravity datasets also complement seismic reflection data and provide a regional picture of basement character and age. Gridded magnetic anomalies were acquired from the EMAG2 model, compiled by the National Geophysical Data Center (NGDC; Maus et al., 2009). These anomalies combined with isochron maps of Müller et al. (1997) provide age estimates for the Pacific basement adjacent to the QCF. Recently updated gridded gravity anomalies (Fig. 3.3) from Sandwell et al. (2013) also give insight into regional changes in sediment thickness and basement structure.

3.3.2 Analysis

The analysis presented here required mapping of the seafloor and subsurface geophysical data, and various techniques were used. The seafloor geometry of the QCF was visualized primarily using GLORIA sidescan data in Halliburton's Landmark

DecisionSpace Desktop software (www.landmark.solutions). This seafloor mapping was verified using available 2D seismic datasets. Comparing the sidescan sonar and seismic reflection data allowed characterization of the bathymetric expression and internal character of the QCF along strike.

In addition to faults, regional stratigraphic surfaces were mapped in the sediment offshore of Haida Gwaii and the Dixon Entrance using DecisionSpace Desktop. Two surfaces (SEAK1 and SEAK2) were mapped based on disconformities visible in seismic reflectors. Both surfaces exhibit onlap relationships. The surface of the Pacific basement rock, recognizable by high-amplitude, semicontinuous seismic reflectors, was also mapped. The Pacific basement surface was gridded and interpolated at 1 km resolution in DecisionSpace Desktop and exported to be analyzed in Esri's ArcGIS software (www.esri.com).

Gridded surfaces, including global gravity (Sandwell et al., 2013), magnetics (Maus et al., 2009), seafloor age (Müller et al., 1997), global bathymetry (Amante and Eakins, 2009), and depth to Pacific basement were compiled into ArcGIS. Gridded data were then analyzed and compared with new maps of the QCF (also exported from DecisionSpace Desktop), offshore faults, and historic earthquake rupture areas to supplement observations and interpretations. Gridded horizons interpreted on seismic data are displayed in two-way travel time (TWTT) instead of thickness for accuracy and consistency, as velocity information is not available for many of the 2D transects used in this study. Dips on faults and surfaces were calculated using a sediment velocity of 2000 m/s in the sediment column and 2200 m/s at the basement surface, similar to the sediment column value used by Walton et al. (2014) for the study of deep-sea Baranof Fan sediment.

In order to conceptually visualize the position of the Pacific Plate along the margin through time, a simplified plate reconstruction was also built in order to provide insight

into where the now-downwarped Pacific Plate was located along the margin during its 13 m.y. existence (age data from Müller et al., 1997). We used GPlates software (www.gplates.org) for the reconstruction, which is based on a tectonic model by Seton et al. (2012); however, we supplement interpretation of the reconstruction with more detailed information of the margin from recent studies (e.g., Doubrovine and Tarduno, 2008; DeMets et al., 2010; Elliott et al., 2010; Tréhu et al., 2015) that provide more local insight than the plate reconstruction on its own. We assume that the plate boundary remained fixed in time and space relative to North America. We also assume that the ~15° clockwise rotation of the local Pacific Plate motion vector occurred at 6 Ma, consistent with data from Doubrovine and Tarduno (2008), and that convergence rates and plate motion vectors remained constant since that time.

3.4 OBSERVATIONS

3.4.1 Faults

The QCF has been mapped in the past using GLORIA backscatter data and 2D seismic reflection profiles (von Huene et al., 1979; Carlson et al., 1985, 1988; Scheidhauer, 1997; Rohr et al., 2000). A new interpretation of the segment from ~53°–56° N, based on the EW9412 data, is discussed by Tréhu et al. (2015). Our updated maps (Fig. 3.3), generated using similar methods, were compared with a comprehensive fault database compiled by the Geological Society of America (Reed et al., 2005; Fig. 3.3). New mapping confirms the traces of major faults and splays along the QCF system as identified by the database, giving us confidence in the accuracy of the QCF's seafloor geometry.

Offshore Haida Gwaii, the QCF can be imaged within the slope sediment, which is commonly referred to as the QCT (e.g., Hyndman and Hamilton, 1993). The shallow manifestations of the QCF in this region change along strike and have been discussed in

several studies (e.g., Rohr et al., 2000; Tréhu et al., 2015). The QCT is composed of sediment and likely some crystalline rock as well; a refraction study by Dehler and Clowes (1988) detected ocean crustal velocities 4–5 km beneath the seafloor of the outer QCT. The morphology of the QCT is variable along strike, with the main trace of the QCF sometimes marked by half-grabens and other times by a narrow ridge (Rohr et al., 2000). Recent mapping on the QCF south of 53° N also indicates small pull-apart basins along strike (Barrie et al., 2013).

In the subsurface, the QCF is observable most often as a vertical discontinuity with small displacement on the seafloor and near-seafloor reflections (e.g., Fig. 3.4). Available seismic data often confirm the location of the QCF and assist in identifying splay faults, and we map the QCF confidently in the top ~1 s TWTT (~750 m) of sediment. Because of somewhat chaotic reflectivity and seafloor multiples, however, we cannot interpret the fault below a depth of ~750 m beneath the seafloor.

The strike of the QCF has several discrete changes; notably, a bend in the fault at 53.2° N marks a change in fault strike from ~328° (clockwise from north) south of 53.2° N near Haida Gwaii to a strike of ~338° north of the Dixon Entrance (e.g., Rohr et al., 2000; Tréhu et al., 2015). This bend causes the angle of convergence with the Pacific Plate to change from >15° near Haida Gwaii to ~5° north of 53.2° N (Tréhu et al., 2015).

The QCF is the dominant structural feature within the slope sediment. Farther offshore, however, there is a notable series of buried normal faults (e.g., Fig. 3.5), with a higher density of these faults seaward of the Dixon Entrance at 54° N. We observe a decrease of normal faults to the north and where seamounts are present at ~53° N. Dips on the faults are between 60° and 70° on average, with many continuing as deep as the top of Pacific basement, but none reaching the seafloor. Normal faults are buried beneath an onlap

surface (SEAK2) within the basin sediment, under 200–1000 m of sediment. The package of sediment above the normal faults thickens toward the coastline.

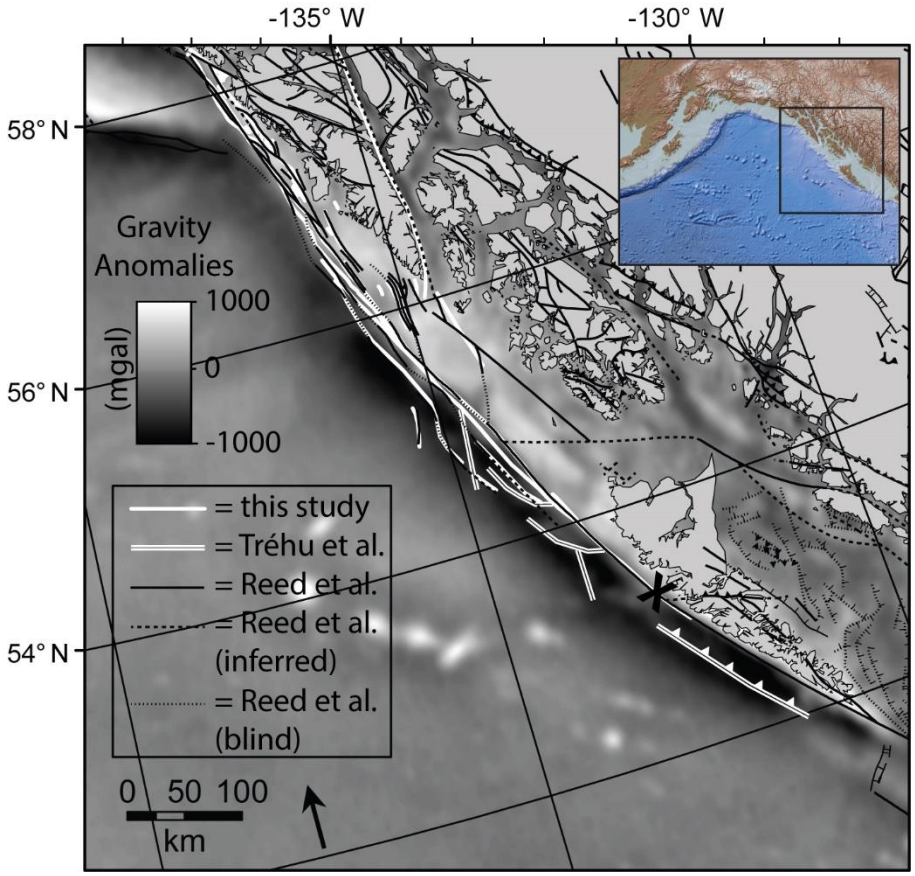

Figure 3.3. Grayscale gridded gravity anomalies. Anomalies are from Sandwell et al. (2013) with the modern coastline for reference. New Quaternary fault mapping from this study (thick white lines) and the faults proposed by Tréhu et al. (2015; double white lines) are also plotted, along with a compilation of previously mapped faults in the area (Reed et al., 2005; thinner black lines). Inferred faults from Reed et al. (2005) are plotted with black dashed lines and blind faults (Reed et al., 2005) with black stippled lines. Bold black X marks a change in strike along the QCF. New mapping from this study is based on USGS seismic reflection profiles and GLORIA data. Agreement between the new mapping and the Reed et al. (2005) database is good where USGS data exist. The inset shows regional location.

3.4.2 Pacific basement

The top of the igneous Pacific basement surface was mapped along seismic reflection profiles adjacent to and seaward of the QCF. The basement surface was only mappable beneath the deep seafloor, as high reflectivity in the slope sediment prevents imaging below ~1 km depth. Interpolation and extrapolation of basement picks up to ~50 km between and at the edges of seismic data transects offshore allow for visualization on a regional scale. Note that no picks were made beneath the slope sediment of the QCT.

Moving from north to south, the dip of the Pacific basement adjacent to the QCF changes significantly along strike (see Fig. 3.2 for line crossing locations). North of 55° N, the basement does not have a significant dip, but line L-3-78EG_951 crossing the QCF perpendicularly at 55° N shows the Pacific basement dipping toward North America at an angle of ~1.5° (Fig. 3.4). Landward dip increases southward (see line L577EG_03, Fig. 3.5), finally reaching an observed maximum dip of ~6°, with basement reaching an observed maximum depth of ~7.5 s TWTT (~8 km below sea level and ~5 km below seafloor), as shown on line L-5-77EG_02 (Fig. 3.6).

South of 54°, at which the strike of the QCF changes from 338° to 328°, the Pacific basement shallows dramatically and the dip toward the continent seems to decrease, as illustrated by seismic reflection profile L577EG_01 (Fig. 3.7). We also observe a nearly completely buried seamount in this area. South of the seamounts, the Pacific Plate basement deepens along central Haida Gwaii. This is constrained by only one seismic line (Fig. 3.8), but other studies have inferred crustal flexure here by looking at the bathymetry of the Queen Charlotte Trough (e.g., Chase and Tiffin, 1972), low-penetration seismic data (Davis and Seemann, 1981), and negative gravity anomalies (Rohr, 2015). South of this crustal deepening near Haida Gwaii, the basement shallows southward toward the Tuzo Wilson seamounts ~51.5° N (see transect F789EG_58, Fig. 3.8), where new ocean crust is

exposed at the seafloor (Carbotte et al., 1989; Rohr and Furlong, 1995). A 1 km resolution grid of basement picks (Fig. 3.9) illustrates the changing structure of the Pacific Plate along the QCF.

A plate tectonic reconstruction based on Seton et al. (2012) shows that downwarped crust at the QCF between 53.2° and 56° N was generated at the Juan de Fuca Ridge. The youngest (and most downwarped) of this crust, now forming a flexural depression at 54° N (near seismic line L577EG_02; see Fig. 3.6), was generated at the ridge ~13 Ma. After creation, this crust moved northward along the QCF until the ~15° clockwise rotation in Pacific Plate motion at 6 Ma (from Doubrovine and Tarduno, 2008). At 6 Ma, this crust was located ~250 km south of its current position assuming a 44 mm/yr rate of relative motion (Elliot et al., 2010), exposed to the higher convergence rates along the QCF south of ~53° N (which we assume to have been consistent since 6 Ma). At 4 Ma, the Explorer plate was generated south of the QCF (Botros and Johnson, 1988). Younger oceanic crust adjacent to the QCF would have continued to experience compression associated with oblique convergence south of the bend. Convergence and any associated downwarping would have continued until the crust translated north past the bend, and by 2 Ma, the now-flexed part of the Pacific Plate would have moved almost entirely past the zone of oblique convergence into a dominantly strike-slip regime.

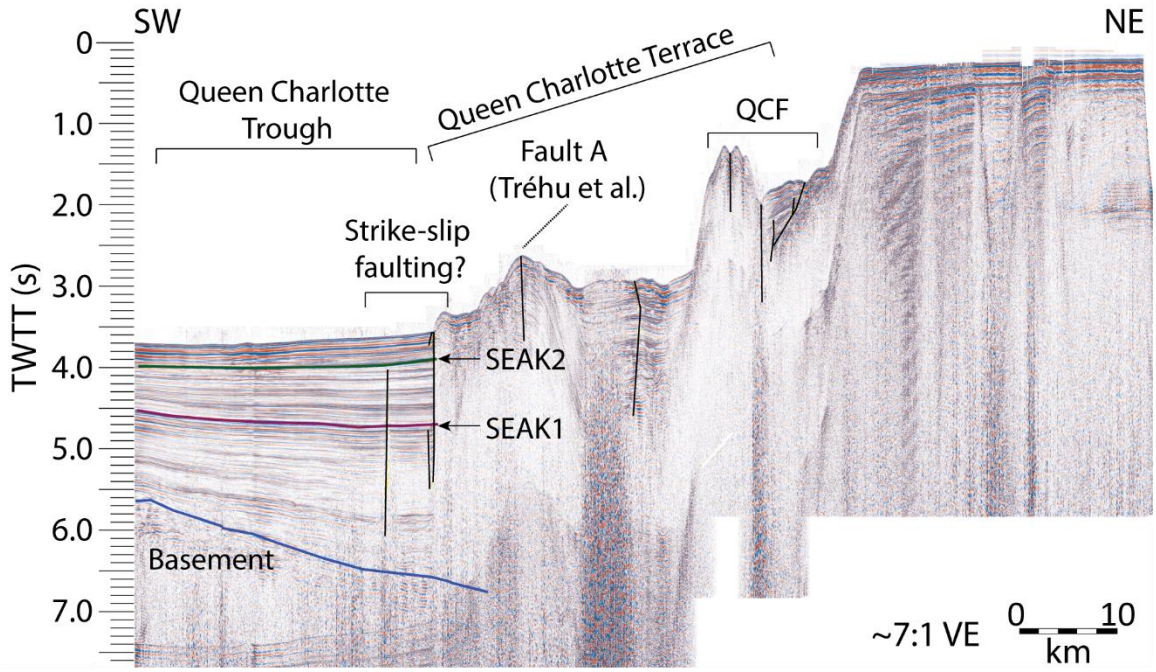

Figure 3.4. USGS seismic reflection profile L378EG_951. Line location shown on Fig. 3.2. The northernmost of the lines is shown in this study. The vertical axis shows depth in two-way travel time (TWTT). Basement, SEAK1, and SEAK2 horizons are plotted as thick lines along with strike-slip faulting and a fault from Tréhu et al. (2015; thinner subvertical lines). Location of the Queen Charlotte Terrace and Queen Charlotte Trough also highlighted – these deposits exist along the QCF throughout our study area. The top of the igneous oceanic basement here is dipping toward North America at ~1:5° in the profile, with near-vertical strike-slip faulting evident in the sediment atop the plate. Seismic lines here and in Figs. 3.5–3.7 are plotted on the same scale to give a sense of relative change along strike.

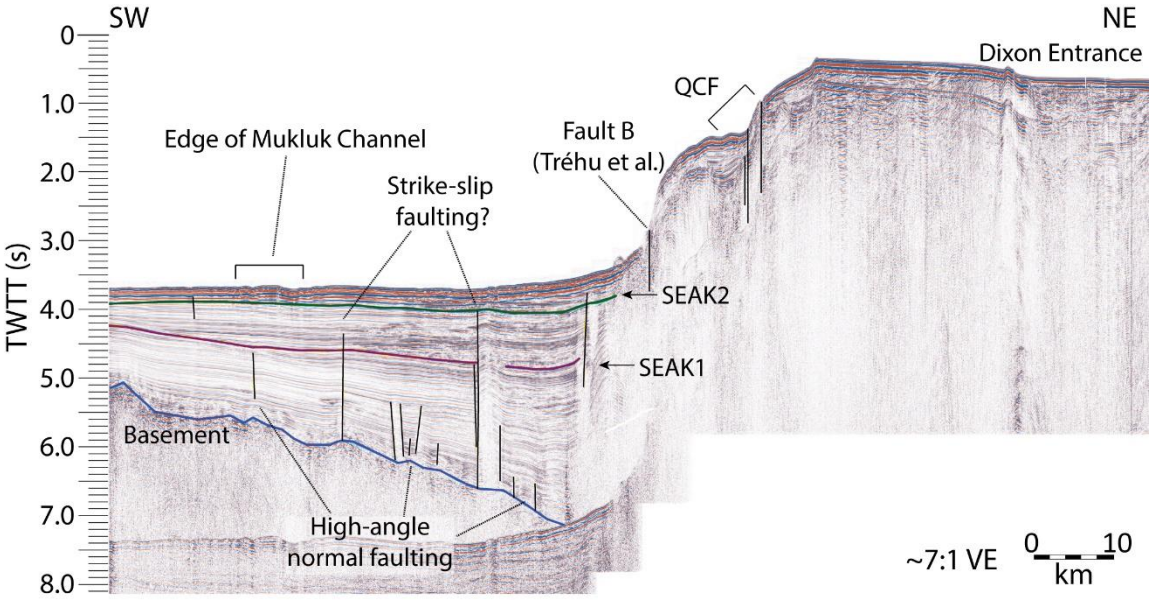

Figure 3.5. USGS seismic reflection profile L577EG_03. Line location shown in Fig. 3.2. The vertical axis shows depth in TWTT. Basement, SEAK1, and SEAK2 horizons are plotted as thick lines along with strike-slip faulting, normal faulting, and a fault from Tréhu et al. (2015; thinner subvertical lines). The oceanic basement is dipping more steeply here than in Fig. 3.4, with some normal faulting in the sediment atop the plate. On the seafloor and uppermost subsurface, the influence of the Mukluk Channel is visible as slightly disturbed, high-amplitude reflections.

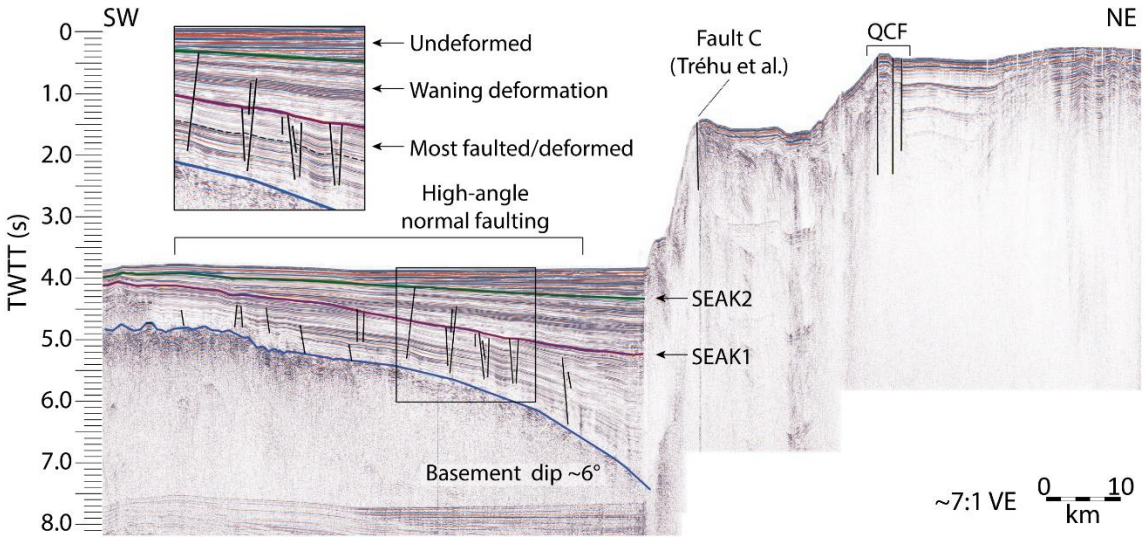

Figure 3.6. USGS seismic reflection profile L577EG_02. Line location shown in Fig. 3.2. This line is the closest to a 54° N crossing of the QCF is where we observe maximum flexure. The vertical axis shows depth in TWTT. Basement, SEAK1, and SEAK2 horizons are plotted as thick lines along with strike-slip faulting, normal faulting, and a fault from Tréhu et al. (2015; thinner subvertical lines). The top of the Pacific crust dips toward North America at about 6°, with high-density normal faulting in the sediment above the plate. The inset shows a closer view of the normal faulting and sedimentary relationships with interpretations. The dashed line in the inset indicates the onset of possible growth strata and therefore syntectonic sedimentary deposition.

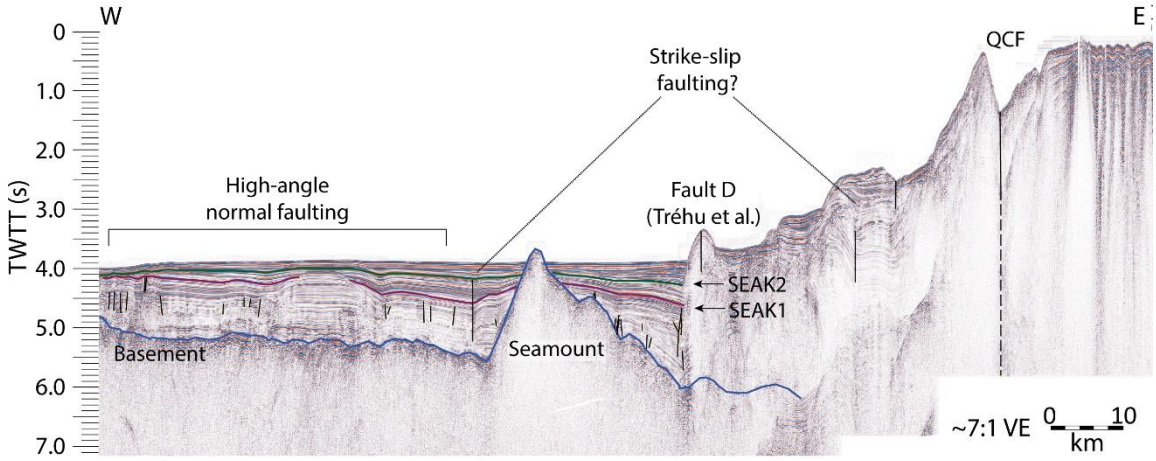

Figure 3.7. USGS seismic reflection profile L577EG_01. Line location shown in Fig. 3.2. This is the southernmost margin-orthogonal line is included in this study. The vertical axis shows depth in TWTT. Basement, SEAK1, and SEAK2 horizons are plotted as thick lines along with strike-slip faulting, normal faulting, and a fault from Tréhu et al. (2015; thinner subvertical lines). The top of the Pacific crust here is significantly shallower than lines located to the north of it, with a seamount visible in the subsurface as well.

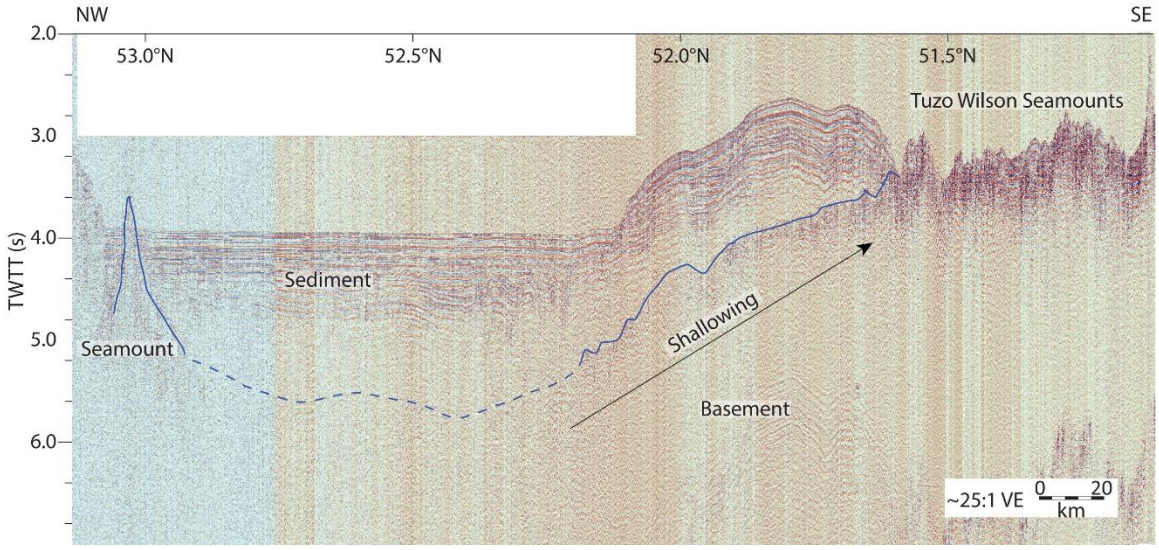

Figure 3.8. USGS seismic reflection profile F789EG_58. Line location shown on Fig. 3.2. This is a QCF strike-parallel line showing the basement crust shallowing southward to the Tuzo Wilson seamounts, where there is active volcanism and basaltic crust exposed at the seafloor. The basement horizon here is plotted as a thick line and is indicated with a dashed line where location is uncertain. The vertical axis shows depth in TWTT. Note that this seismic line is plotted on a different scale than the seismic data shown in Figures 3.4–3.7 in order to show a larger region.

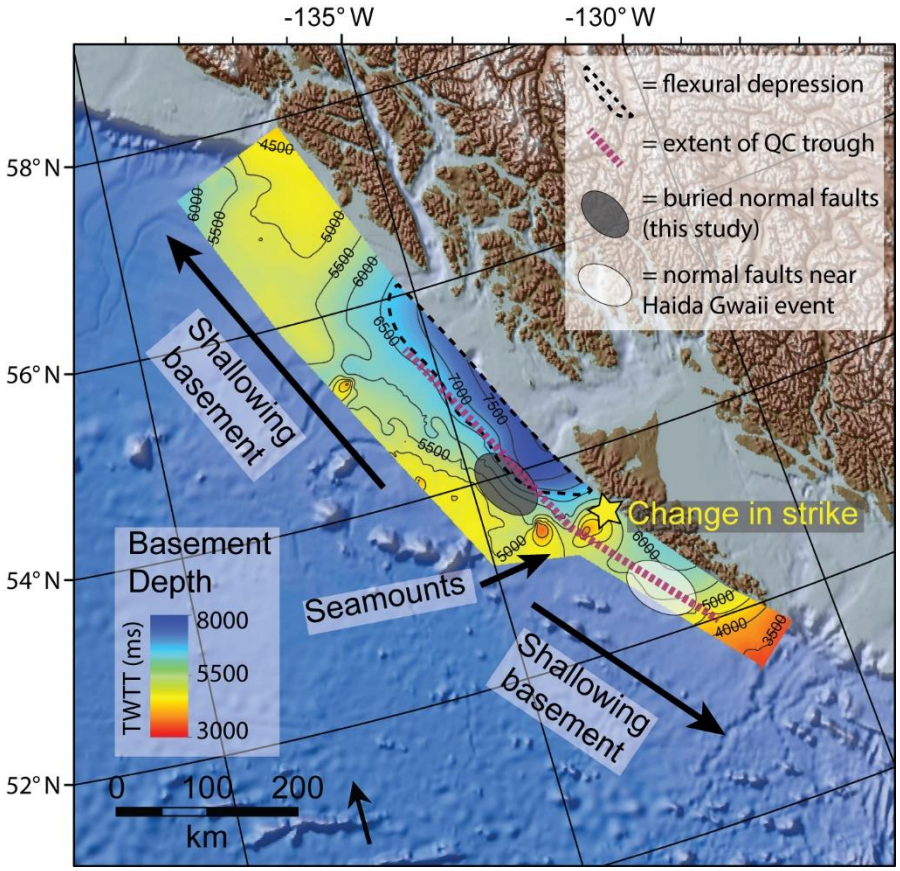

Figure 3.9. Gridded structure contour map showing depth to the top of the igneous basement crust. Grid is in TWTT depth with a contour interval of 500 ms. Picks are interpolated and extrapolated over distances as much as ~50 km from seismic reflection lines (Fig. 3.2). There are no picks beneath the Queen Charlotte Terrace. The area with the highest-density normal faults as mapped in this study is highlighted by a gray ellipse. The approximate area of Haida Gwaii normal fault aftershocks (derived from the Global Centroid Moment Tensor catalog; Ekström et al., 2012; see also Farahbod and Kao, 2015, and Kao et al., 2015) is denoted by a white ellipse. The extent of the Queen Charlotte Trough at the seafloor is also plotted by a thick dashed line. Interpretations indicate shallowing crust outward of apparent maximum flexure located at 54° N. The area of the figure covers the same region as Figure 3.2.

3.4.3 Gravity and magnetics

Interpreted magnetic anomalies (Fig. 3.10) define a Pacific Plate that decreases in age to the south, from 20 m.y. at the Yakutat block to 0 m.y. at the Explorer triple junction. The Aja fracture zone intersects the QCF at 56° N, which is coincident with the northern extent of the observed Pacific crustal flexure.

Gravity data (Fig. 3.3) exhibit local highs where seamounts are present and lows at the thick sedimentary deposits of the Queen Charlotte Trough and terrace. South of 56° N, areas immediately adjacent to the QCF are characterized by negative gravity anomalies. These gravity lows vanish at the southernmost QCF near the Explorer triple junction, where basement rock is very young, shallow, and not yet covered with sediment (Rohr, 2015).

3.4.4 Historic earthquake ruptures

The relationship between our structural analysis and earthquake events is shown in Figures 9 and 10. Apart from the segments that ruptured in the 2012 Haida Gwaii and 2013 Craig events, nearly the entire QCF ruptured between the northern M_s 7.6 event in 1972 and the southern M_s 8.1 event in 1949 (Fig. 3.1). The northern edge of the aftershock zone of the 5 January 2013 Craig event, at 56° N, correlates well with the boundary between the 1972 and 1949 event rupture zones. Aftershocks of the Craig strike-slip event overlap with the northernmost ~125 km of the rupture zone of the 1949 event (Plafker et al., 1994; Fig. 3.1), assuming the longer rupture model estimated from the 1949 aftershocks (Rogers, 1986). The northern extent of the Craig event's rupture zone is also adjacent to downwarped oceanic crust (Fig. 3.9) and thick sediment deposits indicated by negative gravity anomalies (Fig. 3.3), all of which appear to extend only to ~56° N.

The epicenter of the 28 October 2012 Haida Gwaii thrust event overlaps with the southern end of the 1949 strike-slip event's rupture zone (Fig. 3.1), although there are

several rupture models for the 1949 event that disagree about the geographic extent of the rupture (Bostwick, 1984; Rogers, 1986; Ding et al., 2015). Despite the extent of the 1949 aftershocks (Plafker et al., 1994; Fig. 3.1), a seismic gap in the Haida Gwaii region was predicted (Rogers, 1986; Bérubé et al., 1989). The entirety of the Haida Gwaii aftershock zone is just south of 53.2° N, where the strike of the QCF changes from 328° to 338° (Farahbod and Kao, 2015; Kao et al., 2015). Aftershocks of the Haida Gwaii event are primarily within the Pacific Plate, and the majority of the aftershocks have normal fault mechanisms (Lay et al., 2013; Kao et al., 2015).

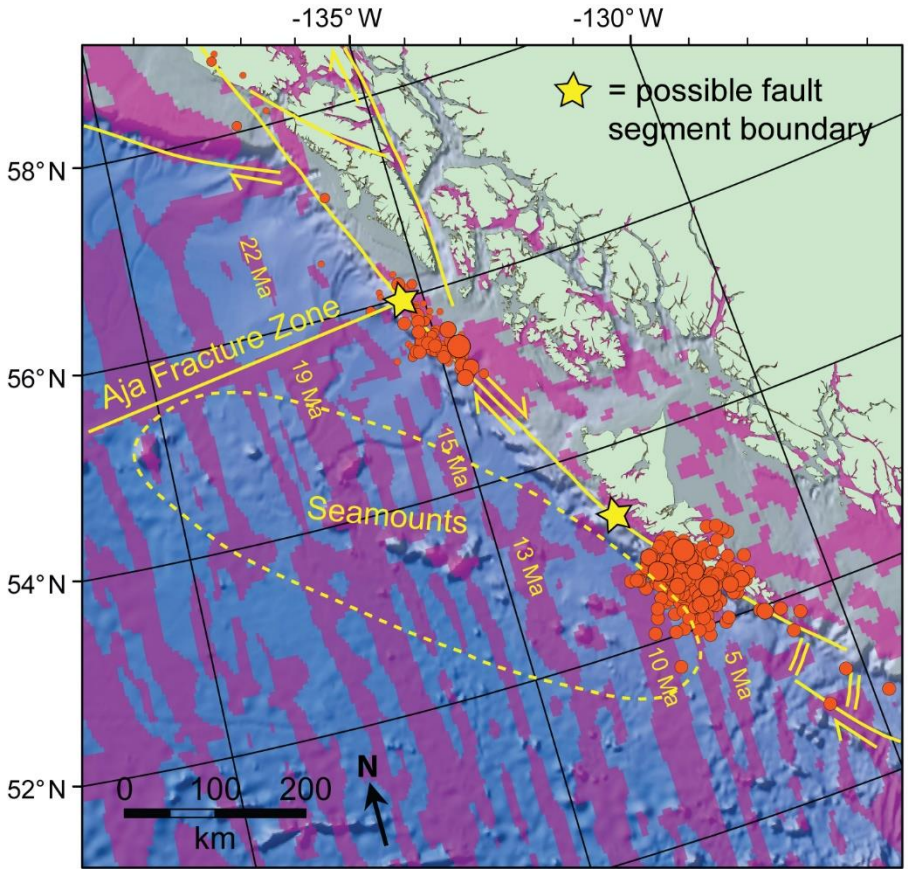

Figure 3.10. Bathymetry image overlaid by positive magnetic anomalies and the modern coastline. The Aja fracture zone, Kodiak–Bowie seamounts, simplified regional fault traces, and select ages of anomalies near the margin are shown on the map. Aftershocks of the Craig and Haida Gwaii earthquakes (northern and southern clusters of circles, respectively) are included for context (derived from the Global Centroid Moment Tensor catalog; Ekström et al., 2012). Two possible fault segment boundaries, one at 53.2° N and the other at 56° N, are denoted by stars. The area of the figure covers the same region as Figure 3.2.

3.5 INTERPRETATION AND DISCUSSION

The primary new observations made in this study are (1) the change in flexure of the Pacific Plate along strike on the QCF and (2) the distribution of normal faults in sediment overlying the Pacific crust offshore. We observe plate flexure along the central QCF between 53.2° and 56° N, with observed maximum downwarping at 54° N. This region is adjacent to a segment of the QCF characterized by strike-slip faulting, north of where oblique convergence occurs at rates reaching ~20 mm/yr. We observe normal faulting in the lithified sediment above the Pacific Plate within and seaward of the downwarped region, with the highest density of normal faults in the sediments observed where downwarping reaches a maximum. We incorporate these principle results into a model for how the Pacific Plate has evolved throughout the past 6 m.y. that has relevance for understanding of modern mechanisms of convergence being accommodated along the southern QCF in the location of the Haida Gwaii earthquake.

3.5.1 Faulting

The main trace of the QCF changes strike at 53.2° N (Fig. 3.3), based on observations of GLORIA backscatter. South of 53.2° N near central Haida Gwaii, the fault strikes at 328° and is characterized by transpression (Rohr et al., 2000; Tréhu et al., 2015). North of 53.2°, the QCF strikes 338° and is characterized by strike-slip faulting (Ristau et al., 2007) with far lower amounts of transpression (Tréhu et al., 2015). In addition to major splays such as the Chatham Strait Fault, the northern region also shows a number of minor splays within the QCT (Fig. 3.3). Tréhu et al. (2015) discuss reactivated faults in this northern region. Although the QCF is thought to have existed as a transform boundary for the last ~40–50 m.y. (e.g., Atwater, 1970; Crouch et al., 1984; Haeussler et al., 2003), the shift in Pacific Plate motion at 6 Ma (Doubrovine and Tarduno, 2008) leading to 15–20

mm/yr convergence along Haida Gwaii may have caused complexities in the fault. It is possible that splays in the northern QCF are very young, developing after this plate motion change at 6 Ma, as discussed by Tréhu et al. (2015). Tréhu et al. further suggest that the angle of convergence is a key factor controlling the response of the upper crust to transpression. South of the 53.2° N bend near Haida Gwaii, a convergence angle of >15° leads to accommodation of compression via a thickening of the upper crust and sediments (Mackie et al., 1989; Rohr et al., 2000) through thrust and reverse faulting and folding parallel to the QCF (pure shear). In the Tréhu et al. (2015) model, the decrease in the amount of convergence north of 53.2° N leads to deformation via splay faults oblique to the main fault (simple shear). They ultimately conclude that faults formed by thrusting south of 53.2° N are oriented at an angle favorable for accommodation of compression via simple shear, and that deformation is focused on those structures which are reactivated as wrench faults as the Pacific Plate moves around the bend in the QCF.

We confirm the presence of the QCF main trace, its splays, and the vertical fault plane suggesting strike-slip motion using available seismic reflection data along the entirety of its strike. The structure and dip of the QCF at depth, however, remain uncertain. For instance, we map a vertical QCF ~1 km beneath the seafloor near the rupture of the 2013 Craig earthquake, though the earthquake ruptured a fault plane dipping at 63°, with a hypocenter at ~10 km depth (USGS). The deep structure of the QCF and the plate interface is a particularly interesting question near the epicenter of the Haida Gwaii thrust earthquake of 2013. We infer a gently dipping Pacific Plate in the region of the Haida Gwaii event. The Haida Gwaii earthquake fits in well with this observation, as the mainshock ruptured a fault dipping 18.5° to the east at 14 km depth beneath the seafloor of the QCT (James et al., 2013; Lay et al., 2013; USGS). In addition, several recent studies based on seismicity, GPS observations of coseismic and postseismic motion, and thermal modeling (Farahbod

and Kao, 2015; Kao et al., 2015; Nykolaishen et al., 2015; Wang et al., 2015) support the Haida Gwaii event as a shallow megathrust on the Pacific–North America plate interface near the QCF.

We suggest there are two potential fault segment boundaries along the QCF. At 56° N, the boundary between the 1972 and 1949 rupture areas coincides with the intersection of the Aja fracture zone and the QCF (Fig. 3.10), which also marks a ~3 m.y. offset in Pacific Plate age. In addition, gridded Pacific basement traveltime picks indicate that flexure of the plate exists only south of 56° N, and gravity data indicate thicker sediment deposits there as well (Fig. 3.3). These structural differences across 56° N provide a lithospheric discontinuity that may impede earthquake rupture propagation (e.g., Wesnousky, 2006) and could explain the 56° N limit of the 2013 Craig event's aftershock zone.

The other possible fault segment boundary is located south near 53.2° N, at the bend in the QCF and where possible members of the Kodiak–Bowie seamounts are present (Fig. 3.10). Either or both may limit the extent of rupture during some earthquakes. Our observations also show that the Pacific Plate flexes downward sharply north of 53.2° N. Because of the change in strike of the QCF here, 53.2° N represents an abrupt transition in structural regimes along the QCF (Tréhu et al., 2015). Research has shown that fault steps and underthrust seamounts can limit rupture propagation via stress changes across them (King and Nábělek, 1985; Wesnousky, 2006; Wang and Bilek, 2011). Disturbed magnetic anomalies here correlate with and are likely related to the seamounts, though we cannot determine if any have been underthrust. The M_s 8.1 event of 1949 may have crossed this boundary according to some models, although surface-wave directivity suggests a rupture propagating northward of the 53.5° N epicenter (Bostwick, 1984; Rogers, 1986), leading to a possible seismic gap to the south. The 2012 Haida Gwaii rupture is located entirely

south of the structural transition across 53.2° N, though given its thrust mechanism, it does not seem to have ruptured the QCF proper. It is possible that the QCF here has yet to rupture in a large event, or that it has been accommodating strike-slip motion aseismically over time (Lay et al., 2013). We recognize that interpretations of segmentation are based on very few direct observations, and additional data and/or numerical modeling are needed to test whether these boundaries do indeed limit the extent of ruptures.

Aside from the changing structures along strike of the QCF, sedimentary deformation and unconformities offshore of the QCF provide insight into the timing of observed flexural deformation and support interpretations of the origin of the observed flexure (see the Crustal Flexure section for discussion). We observe normal faulting in the sediment just above the Pacific Plate where flexure occurs in the underlying crust (e.g., Fig. 3.6), suggesting that normal faulting is related to plate flexure here. We map three distinct sedimentary packages atop the Pacific Plate, separated by two onlap unconformities (SEAK1 and SEAK2). Normal faults appear exclusively in the lower two sediment packages and at a higher density where downwarping is greater (Fig. 3.6, inset). The lowermost package (basement-SEAK1) is the most deformed, with tilted layers, extensive normal faulting, and some possible growth strata in the upper part of the package and toward the shelf (Fig. 3.6, inset). These observations suggest faulting coincident with plate bending and later phases of syntectonic deposition or deformation. The middle package (SEAK1– SEAK2) exhibits gently dipping strata with a few normal faults extending into it, suggesting waning deformation during the deposition of these strata. The most recent sedimentation (SEAK2-seafloor) appears as high-amplitude, flat-lying, and undeformed layers (Fig. 3.6, inset), suggesting that extensional deformation is no longer active today. Without deep cores in the area, it is impossible to date mapped surfaces and faults, though other studies have interpreted the SEAK1 horizon as a Miocene–Pliocene

unconformity, identifiable by truncating reflectors and a change in interval velocity (Snavely et al., 1981; Scheidhauer, 1997; Tréhu et al., 2015).

3.5.2 Crustal flexure

The top of the igneous basement of the Pacific Plate dips landward toward the North American Plate between 53.2° and ~56° N (Fig. 3.9), reaching an observed maximum dip of~6° at~54° N (Fig. 3.6). The plate boundary here, however, has only ruptured in strike-slip earthquakes in recorded history. These observations and examination of plate reconstruction suggest that the crust characterized by flexure between 54° and 56° N was undergoing oblique convergence for 0–4 m.y. (between ~6 and ~2 Ma), before being translated north of the fault bend at 53.2° N. The Pacific Plate currently near 53.2° N would have been exposed to convergence for a longer period of time prior to translating past the obliquely convergent southern QCF, whereas lithosphere now located at 56° N would have passed the bend into a strike-slip regime more quickly and would have been exposed to convergence for less time. The plate reconstruction is consistent with observations of changing flexure along strike.

Analogous flexure may be occurring currently along the southern QCF (where the Haida Gwaii event occurred). A shallower crustal deepening here reaches ~5:5 s TWTT (~6 km depth), approximately 2 km shallower than the flexure we observe at 54° N (Fig. 3.8), and others have supported a dipping plate here using a variety of geophysical data (e.g., Chase and Tiffin, 1972; Davis and Seemann, 1981; Prims et al., 1997; Nykolaishen et al., 2015; Wang et al., 2015). Flexure between 54° and 56° N appears to be inactive based on observations of recent undisturbed sediment but seems active south of 53.2° N because of normal faulting in the Pacific Plate after the Haida Gwaii earthquake of 2012 (Lay et al., 2013). The aftershocks imply plate-bending faults from downwarping (Kao et

al., 2015), a common phenomenon observed at subduction zones (Masson, 1991). We interpret the buried normal faults in the sediment above the downwarped plate at 54° N to be the signature of similar events in the past when the plate was farther south.

To explain our observations, we support a Pacific Plate underthrusting model with flexure initiated by underthrusting and subsequently preserved by sediment loading in the trough and QCT. Figure 11 of this study and Figure 2 of Tréhu et al. (2015) show that the implied amount of underthrusting decreases gradually northward and southward of 53.2° N. An underthrusting model would explain the observed maximum in the apparent flexural depression of the Pacific Plate near 54° N, which is the segment of plate that has been exposed to pronounced convergence along the southern QCF for the longest period of time, as well as a northward-decreasing amount of flexure (Fig. 3.11). Some of the ~100–120 km of total predicted convergence since 6 Ma has undoubtedly been accommodated within the plates, though the ongoing question of how much is beyond the scope of this study.

The tectonic history of the margin is consistent with our interpretation; Figure 3.12 illustrates a conceptual model. The minimum age of the Pacific Plate at 54° N, where we observe apparent maximum flexure, is ~13 m.y. If we assume that flexure did indeed initiate with the onset of QCF convergence at ~6 Ma due to a combination of underthrusting and sediment loading as accommodation space was created, then we can say that the deformed sediment in the lowermost package (basement–SEAK1) was faulted concurrently with flexure (Fig. 3.12). Lesser amounts of late-stage deformation exist in the SEAK1-SEAK2 strata, with possible growth strata in the upper package potentially supporting syntectonic deposition (Fig. 3.6, inset). Thus, we interpret that much of the lowermost package was deposited between 13 and 6 Ma, with deformation initiating sometime after 6 Ma. This interpretation is consistent with that of Snavely et al. (1981),

stating that the SEAK1 unconformity represents the Miocene–Pliocene unconformity (~5.3 Ma).

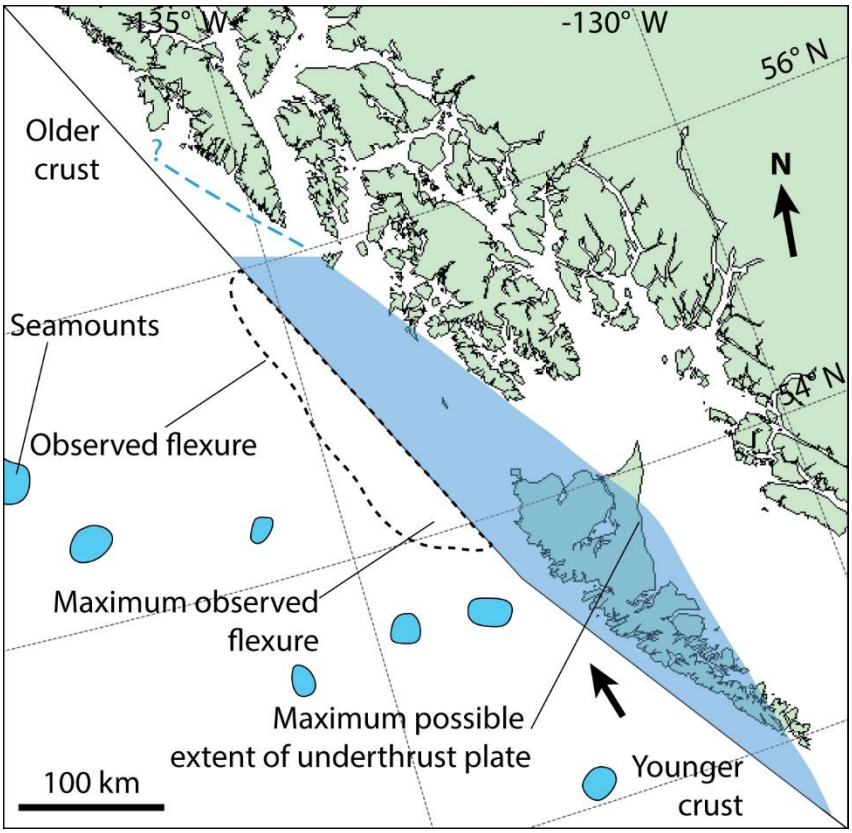

Figure 3.11. Schematic diagram of the maximum possible cumulative tectonic overlap between the Pacific and North American plates. Shaded region shows overlap due to convergence along the QCF from 6 Ma to present. The overlap presented here assumes pure underthrusting and does not show the effects of intraplate deformation or thickening, which could be significant; this figure does not represent our final model for convergence accommodation (see Fig. 3.12). The overlap was calculated based on modern MORVEL plate motion vectors (DeMets et al., 2010) and assumes a simplified QCF geometry that remains fixed to North America, a 20° angle of convergence with the Pacific Plate motion vector south of 53.2° N, a 5° angle of convergence north of 53.2° N, and a 2D plane of plate motion. The mapped region of flexure is shown as a dashed line to illuminate the relationship between convergence and flexure.

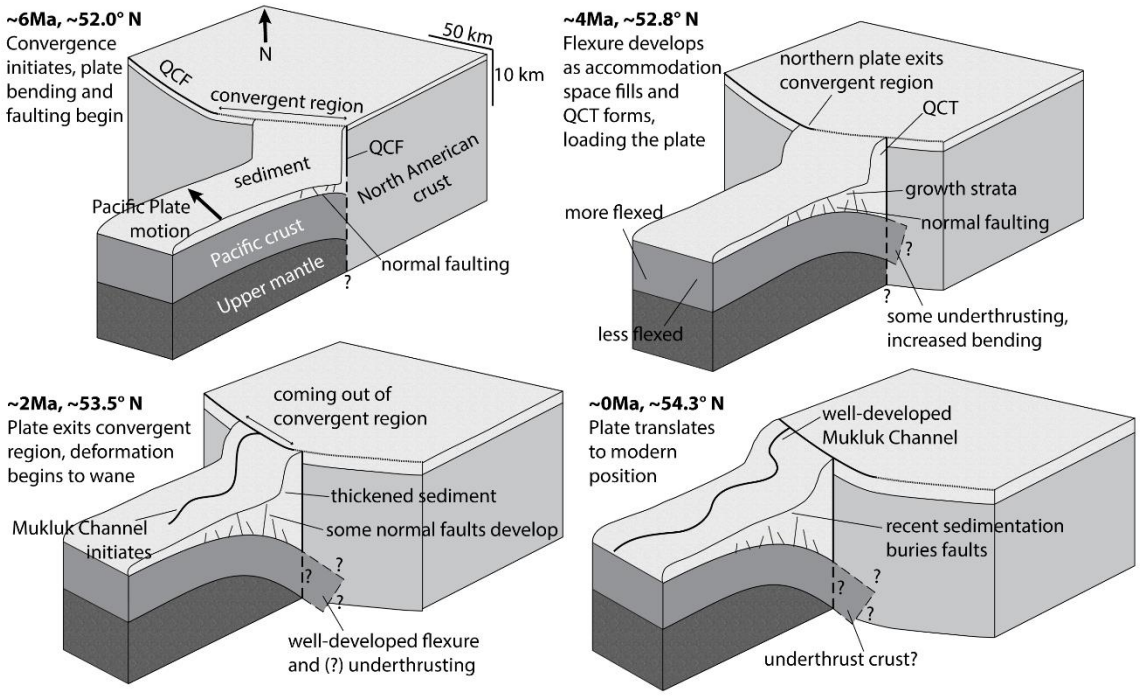

Figure 3.12. Development of the flexure and underthrusting of a piece of the Pacific Plate through time. Illustration begins at 6 Ma when convergence initiated along the southern QCF. Snapshots in time of the flexure and fault development until the plate translates to its modern position at ~54.3° N are shown.

After 6 Ma, convergence and strike-slip motion both continued until the flexed portion of the plate bypassed the more-convergent southern QCF by ~2 Ma, suggesting a period of diminishing deformation sometime between 6 and 2 Ma. The middle sedimentary package (SEAK1–SEAK2) is the least constrained in time, but smaller amounts of deformation via faulting and tilting support a waning deformation interpretation (Fig. 3.12). The SEAK1–SEAK2 package, then, must have been deposited and deformed beginning sometime after 6 Ma and ending at ~2 Ma. The relatively large thickness of this middle package could also indicate higher sedimentation rates during this period, some of which is perhaps related to the onset of northern hemisphere glaciation (Raymo, 1994). This timeline is consistent with interpretation of the onset of deposition in the Baranof deep-sea fan system, which is thought to have undergone more rapid deposition beginning at ~7 Ma and further intensification during the Pleistocene (Walton et al., 2014).

The uppermost sedimentary package (SEAK2–seafloor) is the least deformed and is marked by an increase in acoustic amplitude. Given the interpretation of the timing of the other sedimentary packages, the uppermost package was most likely deposited after 2 Ma (Fig. 3.12). We were able to match this package with deposits from the nearby Mukluk seachannel, which likely initiated sometime around the onset of northern hemisphere Pleistocene glaciation at ~2.58 Ma (Walton et al., 2014). The age of the Mukluk Channel is consistent with the interpretation of an upper sedimentary package age of ~2 m.y.

Although continued underthrusting north of 53.2° N is not thought to be occurring, despite a small (~5°) angle of oblique convergence (e.g., Tréhu et al., 2015), flexure of the Pacific Plate has been preserved after it translated into a strike-slip regime. This preservation of downwarping may be a combination of sediment loading and a portion of the Pacific Plate remaining pinned beneath North America, a remnant of past underthrusting. Our model assumes that flexure initiated at ~6 Ma, at which time

convergence along the southern QCF would have led to underthrusting and downwarping, resulting in creation of sedimentary accommodation space with the coincident formation of the Queen Charlotte Trough (Fig. 3.12). Sedimentary loading in the trough and tectonic thickening of the QCT contributed to flexure as convergence progressed, and this load continued to depress the Pacific Plate as it translated past the bend in the QCF into a strike-slip regime. Through flexural modeling, Prims et al. (1997, with a correction by Rohr et al., 2000) accounted for all of the observed plate flexure at ~54° N with sedimentary loading from the Queen Charlotte Terrace and Trough. Our observations are compatible with these models, though we suggest (based on diminishing flexure to the northward of 54° N) that underthrusting initiated the downwarping and creation of accommodation space necessary for accumulation of a sediment load. Although sedimentary and possible North America loading is our preferred interpretation to explain the preservation of flexure north of 53.2° N, we acknowledge the possibility that small amounts of convergence (~5° angle) north of 53.2° N may play a role in maintaining flexure as well.

Our model suggests that some amount of plate flexure should exist along portions of the Pacific Plate that have been exposed to convergence. The present day signature of plate flexure may be overprinted at the Kodiak–Bowie seamounts, as we observe crustal shallowing where the bathymetric high of the seamount chain crosses the Queen Charlotte Trough. A study by Harris and Chapman (1994) discusses the superimposed effects of the geodynamic influences of the Kodiak– Bowie seamounts and the sediment-filled trough, though their study only utilized gravity and bathymetry data; in this study, we include observations of seismic reflection profiles. The Kodiak–Bowie seamounts were likely emplaced on young, thin crust, suggesting formation at a spreading ridge (Turner et al., 1980; Harris and Chapman, 1994) that could generate a fairly wide swath of seamounts (Fig. 3.10). Though the age is unconstrained, we assume the seamount that we image in

the Queen Charlotte Trough (Fig. 3.7) was generated at a ridge and is similar in age to the surrounding crust; despite this, we do not observe obvious flexure here. It is possible that the locally thicker and more buoyant crust of the Kodiak–Bowie seamounts may have resisted underthrusting and/or blocked propagation of flexure to the south (e.g., Christeson et al., 2010; Worthington et al., 2012), though more likely it is simply an overprinting of flexure due to higher topography. We are unable to effectively image and assess flexure around the seamounts with the existing data coverage, however.

We recognize that our interpretation of flexural changes has little constraining data, and that uncertainties allow for alternative explanations. For instance, we assume a plate boundary that remains fixed to North America, but it is probable that the boundary has shifted some through time, directly affecting the amount of convergence along the QCF. It is also possible that downwarping is still somewhat active and that recent, rapid sedimentation of the Baranof Fan (Walton et al., 2014) has yet to be deformed. Our interpretation is most consistent with the available data, though it is not the only plausible model. Given the uncertainties, we highlight the need to acquire improved imaging along the QCF that could better test the model presented here.

3.6 CONCLUSIONS

Our observations put the Queen Charlotte Fault into a regional tectonic context that includes recent and historical earthquake ruptures. The QCF changes strike at 53.2° N, marking an important transition in fault structure and Pacific basement flexure. We propose a conceptual model of the tectonic evolution of the margin since the initiation of convergence along the QCF at 6 Ma. The main conclusions of this study of the QCF margin are as follows.

1. We observe landward Pacific Plate flexure north of 53.2° N, with an observed maximum dip of 6° in the oceanic basement at 54° N. North and south of here, the Pacific basement shoals along the continental margin. Buried normal faults in the overlying sediment suggest that the upper portion of the plate was extended during bending.
2. We hypothesize that there are two possible segment boundaries along the QCF: one at 56° N and the other at 53.2° N, at the bend in the QCF. Observed plate flexure ends at ~56° N, which marks the maximum extents of the 1949 and 1972 earthquakes and is consistent with the Craig event's aftershock zone (which also extends to ~56° N). We propose that the 56° N boundary is due to the presence of the Aja fracture zone's intersection with the QCF, which also marks an abrupt ~3 m.y. change of crustal age. The 53.2° N boundary is characterized by the bend in the QCF, the Kodiak–Bowie seamounts, and a reduction of Pacific Plate flexure south of the boundary, where the 2012 M_w 7.8 Haida Gwaii event occurred.
3. A tectonic reconstruction suggests that crust exhibiting flexure now located between 54° and 56° N was located along the southern QCF at the initiation of convergence there ~6 m.y. ago. We interpret the flexure between 54° and 56° N to be a result of past convergence and underthrusting along the obliquely convergent southern QCF, now inactive as the crust has translated past a bend in the QCF into a more strike-slip regime.
4. Normal faulting and stratigraphic unconformities above the Pacific Plate suggest that the trough generated by underthrusting was filled with sediment both concurrent with and after active plate flexure. We suggest that flexure was preserved after translation north of the bend in the QCF due to load from the trough sediment, the QCT, and/or the North American Plate itself.

5. The model supports the idea that the young Pacific crust along the southern QCF is flexing and beginning to underthrust adjacent to the margin of British Columbia today, and that the recent Haida Gwaii event was caused by these plate interactions. The observations of downwarping and normal faulting along the northern QCF may be a northern analog for the modern process occurring near Haida Gwaii. Better imaging of the QCF fault at the location of the recent Haida Gwaii rupture is required to conclusively define the fault boundaries at depth and to identify a possible thrust surface that may have accommodated seismogenic slip of the 2012 event.

Chapter 4: Seismic velocity and fault structure along the 2013 Craig, Alaska supershear rupture of the Queen Charlotte Fault

ABSTRACT

On 5 January 2013, the M_w 7.5 Craig, Alaska earthquake ruptured ~150 km of the Queen Charlotte Fault (QCF), a right-lateral strike-slip system separating the Pacific and North American plates. Regional shear wave analyses suggest this event was supershear, a seismic phenomenon where the rupture exceeds the shear wave speed of the material through which the rupture propagates. Here, we test whether supershear propagation was promoted by a bimaterial interface along the QCF, favoring northward-propagating rupture due to an elastically stiffer Pacific Plate at seismogenic depths. Less than four months after the mainshock, we deployed 8 ocean-bottom seismometers (OBS) as a part of a rapid-response effort and detected 2345 aftershocks during a 21-day period. The spatial distribution of aftershocks and our tomographic traveltime inversion for velocity structure surprisingly indicate a low-velocity (Vp and Vs) zone on the Pacific side of the plate boundary at 7.5-20 km depths. Crustal seismic velocities are as much as 20-30% slower than the North America side where the older, Paleozoic North American crust is seismically faster. Our results 1) support previous hypotheses that the base of the seismogenic zone along the QCF is closer to 15-20 km depth, similar to an oceanic strike-slip system, 2) suggest that at seismogenic depths, the fault zone is weaker than would otherwise be predicted, and 3) imply that rupture did not propagate in the theoretical preferred direction for supershear ruptures. Combining aftershock records with seismic reflection data, we also provide confirmation of a previously hypothesized active strand of the QCF within the Pacific Plate.

4.1 INTRODUCTION

The Queen Charlotte Fault (QCF), a NW-striking strike-slip fault stretching the length of western Canada and part of southeastern Alaska, is a right-lateral system representing the plate boundary between the Pacific and North America tectonic plates (Fig. 4.1). The northern end of the QCF is marked by an onshore-offshore transition to the Fairweather Fault, with the offshore length of the Fairweather-Queen Charlotte strike-slip system totaling ~800 km (Fig. 4.1). The QCF has ruptured in several great earthquakes (magnitude 7+) in the past century, including the M_w 8.1 Queen Charlotte earthquake of 1949 (Sykes, 1971; Bostwick, 1984; Rogers, 1986), the M_w 7.6 Sitka event of 1972 (Schell and Ruff, 1989; Doser and Rodriguez, 2011), and most recently, a pair of events – M_w 7.8 and M_w 7.5 – near Haida Gwaii, British Columbia in 2012 and Craig, Alaska in 2013, respectively (e.g. James et al., 2013; Lay et al., 2013; Yue et al., 2013; Aiken et al., 2015; Ding et al., 2015). Historical seismicity indicates that the QCF is a seismically active, locked fault system that ruptures periodically in major events, and is thus a significant hazard to communities in western Canada and southeastern Alaska. Although the QCF sustains events of comparable moment release to the San Andreas Fault (Carlson et al., 1988; Fletcher and Freymueller, 2003), much less is known about the QCF margin, in large part due to its location offshore.

In this study, we focus on the portion of the plate boundary closest to the M_w 7.5 Craig, Alaska event, which occurred on 05 January 2013 (Fig. 4.1). This event caused shaking in the nearby population centers of Craig (pop. ~1,250), Juneau (pop. ~32,660), and Sitka, Alaska (pop. ~9,000), among others (from USGS ShakeMap; Wald et al., 2005). Study of the Queen Charlotte Fault is relevant for anticipating earthquake and tsunami hazards to local communities and for better understanding ocean-continent strike-slip systems.

The 2013 Craig earthquake was a M_w 7.5 right-lateral strike-slip event that ruptured parallel to ~150 km of the mapped plate boundary (e.g. Aderhold and Abercrombie, 2015). Regional shear wave analysis was used to infer that the Craig rupture was supershear, in which the rupture propagation velocity exceeded the elastic shear wave velocity. Supershear rupture propagated northward at speeds of up to 5.5-6 km/s (Yue et al., 2013). Numerical models of unilateral supershear ruptures suggest that they generally occur along bimaterial interfaces, which is a condition of significant contrast in elastic properties across a fault (Shi and Ben-Zion, 2006; Ampuero and Ben-Zion, 2008; Ma and Beroza, 2008). Since supershear rupture velocities tend to occur in the direction of motion of the faster side of the fault (e.g. Xia et al., 2005), for the Craig event, supershear rupture propagation would be expected in the northward direction, if one assumes that Pacific Plate oceanic crust is stiffer at seismogenic depths (e.g. Yue et al., 2013).

Due to the offshore location of the QCF, little is known about the crustal material on either side. Some insights into the elastic properties are available from older, local-scale reflection and refraction studies (Shor, 1962; von Huene et al., 1979; Horn et al., 1984; Dehler and Clowes, 1988; Mackie et al., 1989; Rohr et al., 2000) and geologic mapping throughout southeast Alaska (e.g. Plafker et al., 1989). In this study, we 1) provide constraints on crustal material/velocities along the QCF, 2) assess whether the fault zone consists of a bimaterial interface, and 3) use the Craig aftershocks to better understand the seismogenic zone geometry. We address these goals with a dataset of Craig aftershocks from an array of 8 ocean-bottom seismometers (OBS; Fig. 4.1), using these data to invert for a coarse tomographic model of P- and S-wave velocity structure across the QCF in the region of the Craig earthquake. We provide the first modern information on the seismic velocity structure at an ocean-continental strike-slip system, shedding light onto the physical conditions along the QCF that may have influenced rupture of the Craig event.

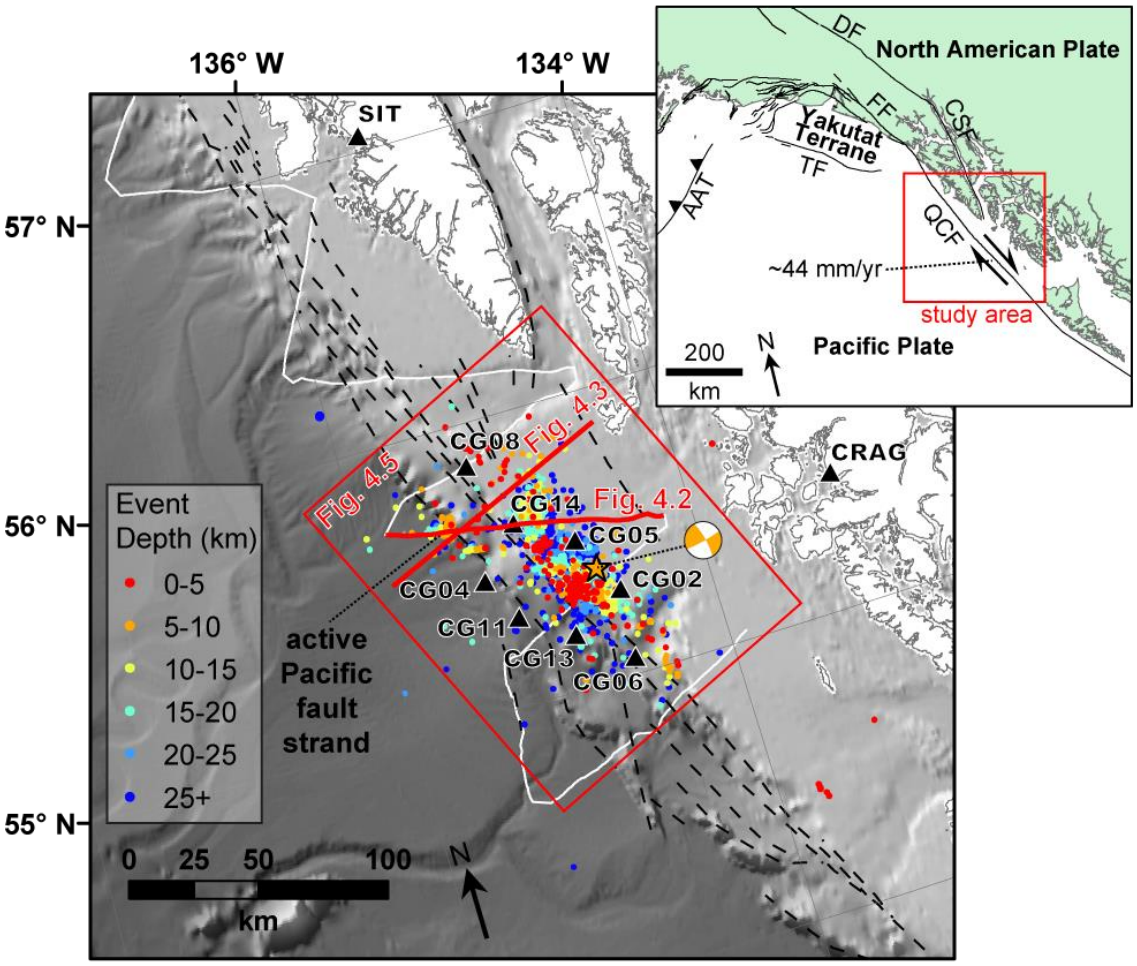

Figure 4.1. Map showing Craig earthquake area. Background shows grayscale bathymetry from Smith and Sandwell (1997) and the United Nations Commission on the Law of the Sea (UNCLOS; Gardner et al., 2006). 2345 aftershock epicenters used in this study are colored by depth (warm = shallow, cool = deep). Craig mainshock epicenter indicated by an orange star and focal mechanism. Labeled black triangles are the passive-source stations used in this study, including the 8 rapid-response OBS instruments. Dashed black lines are fault traces mapped by Walton et al. (2015), with a potentially active fault within the Pacific Plate labeled. White lines indicate the trackline of seismic reflection survey L378EG, with the locations of the profile in Fig. 4.2 and cross-section in Fig. 4.3 as red lines, and the location of Fig. 4.5 as a red box. Inset shows larger region and major tectonic features. Plate motion vector from Elliott et al. (2010). QCF – Queen Charlotte Fault. FF – Fairweather Fault. DF – Denali Fault. CSF – Chatham Strait Fault. TF – Transition Fault. AAT – Alaska-Aleutian Trench.

4.2 REGIONAL SETTING

As the plate boundary separating the Pacific and North American plates, the QCF accommodates ~44 mm/yr of offset between the Pacific and North American plates. To the north, the Fairweather Fault accommodates closer to ~5 cm/yr right-lateral offsets between North America and the Yakutat Terrane, a thick oceanic crustal plateau largely traveling with the Pacific Plate (Fig. 4.1; Gulick et al., 2007; Elliott et al., 2010; Christeson et al., 2010; Worthington et al., 2012). The southern end of the QCF is located at a triple junction associated with the Explorer Plate. There, the QCF meets the Revere-Dellwood Fault, another right-lateral strike-slip system, causing a "leaky transform" via extension (Rohr and Furlong, 1995; Rohr, 2015). The QCF has existed as a transform boundary for 50 m.y. and as a strike-slip fault for the past 20 m.y., since the Yakutat Terrane began traveling concurrently with the Pacific Plate (Atwater, 1970; Crouch et al., 1984; Carlson et al., 1988; Hyndman and Hamilton, 1993; Haeussler et al., 2003). Some form of transform motion has existed along the Queen Charlotte plate boundary since a major plate reorganization at 50 Ma (Haeussler et al., 2003). At 6 Ma, a slight clockwise shift in the vector of the Pacific Plate led to increased convergence along the QCF, particularly in the south (Doubrovine and Tarduno, 2008).

Morphologically, the QCF is a vertical fault residing within the Queen Charlotte Terrace, the deformed slope deposits between the North America shelf and Pacific basin (e.g. Rohr et al., 2000). The main trace of the QCF is visible on the seafloor in GLORIA sidescan sonar data (Bruns et al., 1992), but several major fault strands are evident in seismic reflection data within and south of our study area (e.g. Tréhu et al., 2015; Walton et al., 2015; Fig. 4.1, Fig. 4.2). Slight bends in the QCF lead to shifts in the degree of convergence along the fault, which likely contribute to variability in earthquake focal mechanisms (Tréhu et al., 2015). A 10° bend in the QCF at 53.2° N results in increased

convergence to the south, with a 15° angle of convergence between the plates and 15-20 mm/yr of shortening accommodated by Pacific underthrusting and intraplate crustal deformation (e.g. Hyndman and Hamilton, 1993; Tréhu et al., 2015). The northern QCF between 53.2° N and the Fairweather Fault is dominantly strike-slip, with lesser amounts of transpression from a smaller convergence angle of 5° (Tréhu et al., 2015).

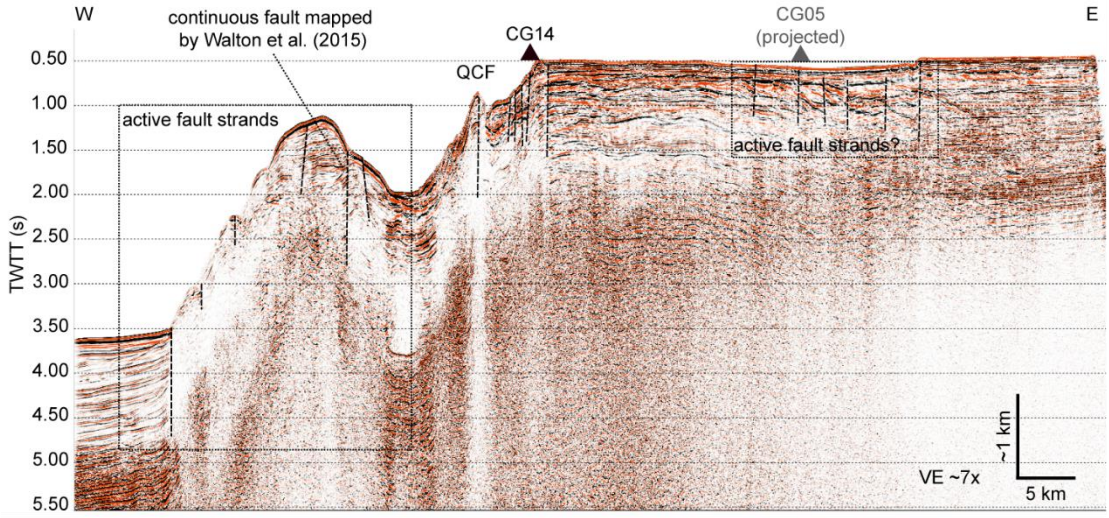

Figure 4.2. USGS 2D seismic reflection profile L378EG_954. Interpreted faults are indicated by dashed lines in the subsurface, with QCF and active fault strands labeled. The two nearest OBS instruments are plotted for context. Location shown in Fig. 4.1.

To the west of the QCF, the Pacific side of the QCF is geologically young, with age increasing northward from the Explorer triple junction to ~20 m.y. old crust near the Yakutat Terrane. There are thick sedimentary deposits overlying the Pacific crust due to the Baranof deep-sea fan system (Walton et al., 2014). The Pacific crust exhibits a topographic "trough" along the central QCF caused by past convergence (Chase and Tiffin, 1972; Walton et al., 2015). Downwarping of the Pacific Plate due to underthrusting likely led to increased accommodation space for sedimentary accumulation, introducing further

load onto the plate and preserving Pacific Plate flexure (Walton et al., 2015). The thickest sedimentary deposits are therefore atop the Pacific Plate nearest the QCF, within the Queen Charlotte Trough and the deformed Queen Charlotte Terrace slope sediments, along strike of nearly the entire QCF (e.g. Rohr et al., 2000; Tréhu et al., 2015; Fig. 4.2). Near the Craig event, the seismic velocities of the Pacific crust and sedimentary deposits are only constrained by a few local refraction profiles (von Huene et al., 1979), which show faster Pacific crustal velocities and confirm a thick sedimentary deposit within the Queen Charlotte Trough.

East of the QCF, the North American crust along the QCF is composed of a complex series of late Paleozoic accreted terranes, namely the Alexander and Wrangellia terranes (e.g. Plafker et al., 1989). Alexander Terrane outcrop exists nearest the QCF at Haida Gwaii, a group of islands located just to the south of the Craig event and on the North America side of the plate boundary; the islands are largely composed of exposed Wrangellia Terrane (e.g. Coney et al., 1980). These Alexander and Wrangellia terranes were contiguous by at least the mid-Pennsylvanian (Gardner et al., 1988) and were accreted to North America during the Mesozoic (Howell and McDougall, 1978). The two terranes, together often called the Insular Superterrane, consist of low-grade metamorphic rocks, felsic plutons, and Mesozoic basalt flows overlain by carbonate and chert (e.g. Coney et al., 1980; Plafker et al., 1989). Morozov et al. (1998) utilized rock-type velocity studies (e.g. Christensen and Mooney, 1995) to estimate compressional seismic wave velocities in the range of 5.7-6.0 km/s for the Insular Superterrane crust, with higher velocity estimates for plutons.

4.3 DATA AND METHODS

4.3.1 Aftershock data

A total of 12 OBS instruments from the University of Texas Institute for Geophysics (UTIG) instrument pool were deployed for this experiment; eight instruments were recovered and/or had usable data (Fig. 4.1). The instruments are short-period OBS typically used for offshore active-source experiments. The sensors have a natural frequency of 4 Hz and recorded for 21 days from 28 April 2013 through 19 May 2013, ~4 months after the mainshock. The array covered the southern ~100 km of the ~150 km Craig rupture with instruments spaced ~20 km apart. The OBS data were imported into an Antelope database (www.brtt.com/software) and interpreted using the Antelope software, along with data from several nearby land stations from the Alaska Earthquake Center (AEC) and National Earthquake Information Center (NEIC) (Fig. 4.1).

Using the continuous waveform data from the OBS instruments, we used Antelope software to auto-detect aftershock events with a STA/LTA detection algorithm. For our final models, we generated and used a catalog consisting of 222 aftershock events, each of which had at least 6 arrivals in the catalog. The 222 catalog events were rigorously examined with P and S arrivals re-picked manually in Antelope, using a filter of 3-15 Hz. We ran a network matched-filter technique (Meng et al., 2012; Walter et al., 2015), which cross-correlates each of the 222 events with continuous data; using this technique we were able to detect 2123 additional events for a total of 2345 events (Fig. 4.1, Fig. 4.3). We also analyzed many of the matched-filtered events individually. Phase data from event arrival times were exported from Antelope to be used in tomographic inversions. Our catalog has a larger number of events and covers a shorter time period than the Craig aftershock study by Holtkamp and Ruppert (2015), which found a 1785 events during ~5 months following the Craig mainshock.

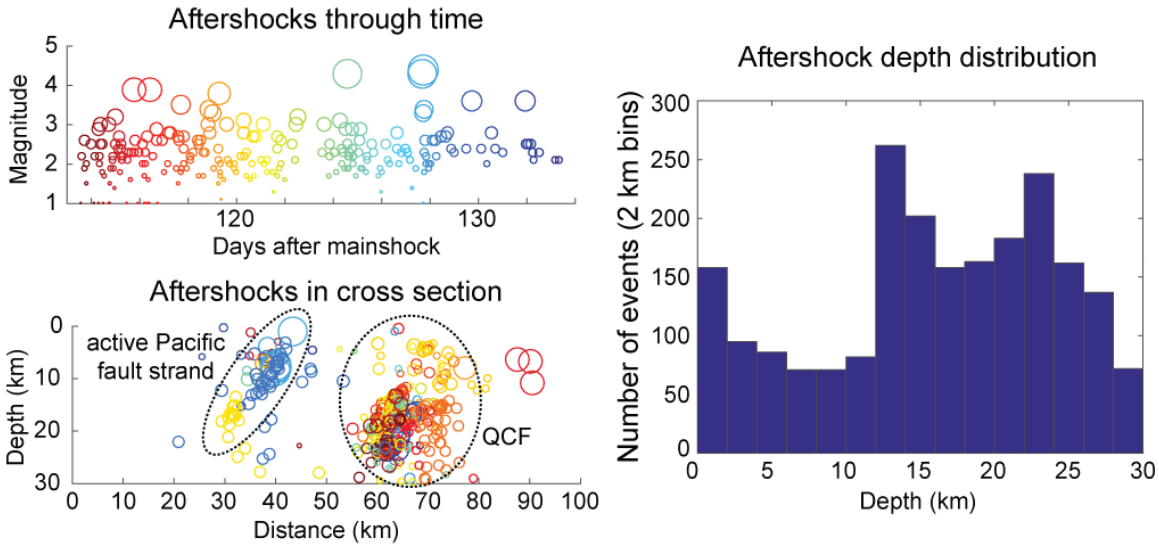

Figure 4.3. Plots showing spatial distribution of aftershocks used in this study. Top left plot shows the events used in this study through time, bottom left plot shows aftershocks within 15 km of a fault-normal cross-section (cross-section orientation shown in Fig. 4.1). Rainbow colors in left plots indicate date of deployment, size of circles scale with event magnitude. Histogram (right) shows depth distribution of all 2345 relocated aftershock events used in this study, with 2 km bins from 0-30 km depths.

4.3.2 Tomography

To solve for crustal velocities, we use a double-difference tomography method which iteratively attempts to minimize the residual between absolute and predicted arrival times by updating the relative location between pairs of earthquakes (Zhang and Thurber, 2003). The tomoDD software performs a joint inversion by using double-differencing to relocate event hypocenters, subsequently utilizing the relocated events to solve for 3D velocity structure at user-defined nodes. We use three types of data in the inversions: absolute P and S arrival times, catalog P and S differential arrival times, and cross-correlation P and S differential arrival times. We follow methodology similar to Froment et al. (2014) and McGuire et al. (2015).

TomoDD requires a user-defined starting velocity model which is then updated during the inversion. Our 1D starting Vp model (Appendix F.1, also see supplementary files) was based on von Huene et al. (1979), which provides a synthesized velocity model based on several smaller-scale refraction studies and gravity modeling. We used a constant Vp/Vs ratio of 1.73 to determine S-wave velocities. Our initial P- and S-wave velocity models are shown in Fig. 4.4 and Appendix F.1. We chose a 1D starting model to avoid introducing an additional variable of poorly constrained lateral heterogeneity, which could possibly influence the results. 1D starting velocity models are common in the type of analysis we employ here (Froment et al., 2014; McGuire et al., 2015).

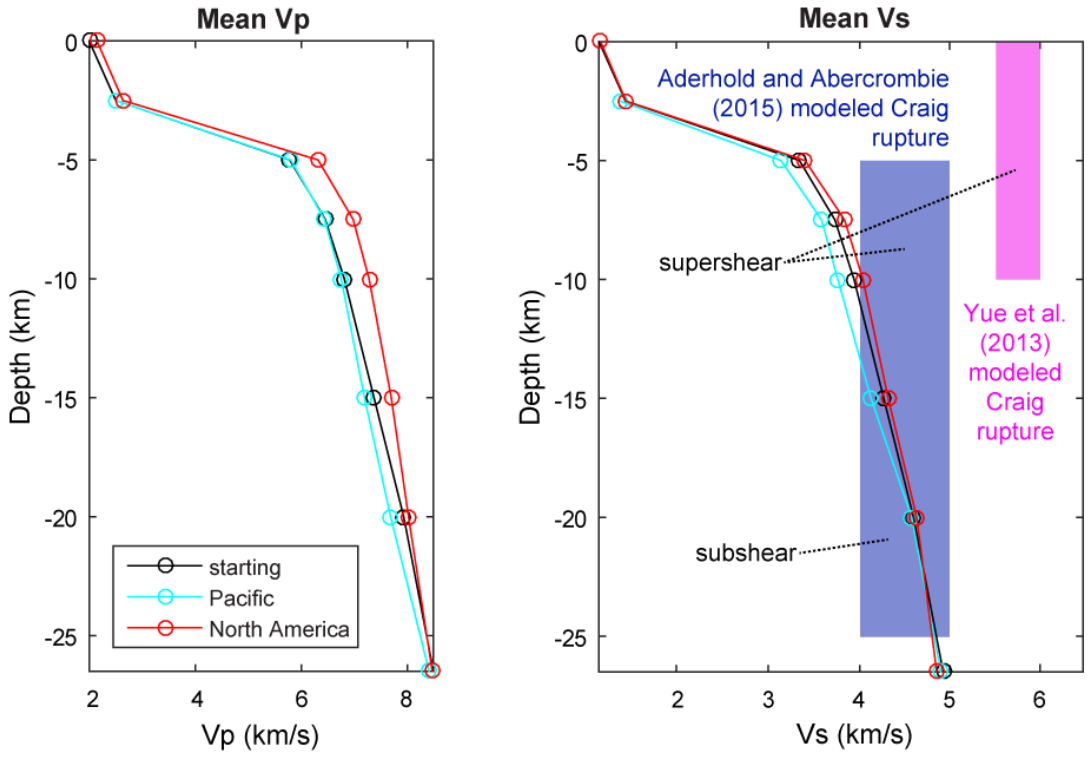

Figure 4.4. Depth vs. velocity for modeled Vp and Vs, showing the starting model based on von Huene et al. (1979) and modeled Pacific and North America velocities. Craig rupture models from Yue et al. (2013) and Aderhold and Abercrombie (2015) are overlaid on our Vs model. Averages only consider velocities at nodes where DWS>100 (the most reliable data points). Note that maximum variation is larger than the mean values shown here.

The seismic velocity model-space consists of horizontal spacing of 5 km in x and y directions centered directly over the OBS instrument array, with coarser spacing at the edges of the model. We began by inverting for P-wave velocity for catalog events only, gradually introducing cross-correlation events and S-wave arrivals as we gained confidence in our inversion strategy. Model node spacing, weighting, smoothing, and other inversion parameters were iteratively tested and ultimately chosen based on output of a geologically reasonable model with relatively low traveltime residuals (Table 4.1; also see supplementary files). In general, we assume that the catalog picks are more reliable than cross-correlation events and therefore weigh catalog P- and S-wave arrivals more heavily in the inversion (Table 4.1). Derivative Weight Sum (DWS) values at each node act as a proxy for ray coverage, and were used to determine the relative sampling of different areas of our model space and create data filters (Appendix H.1). Here we present Vp and Vs slices through the final tomography model at 5, 7.5, 10, 15, 20, and 26.5 km depths (Appendix G).

The number of events used in this study is low compared to similar studies (Froment et al., 2014; McGuire et al., 2015). Therefore, we do not attempt to resolve absolute velocities or highly localized velocity anomalies. Our principle goal is instead to address whether or not there is a significant velocity contrast or regional patterns in velocity structure, particularly across the QCF. Residuals in our study are also likely high for a tomographic model given the limited number of events and OBS stations (Appendix H.3). Despite the limitations of our dataset, resolution testing (Appendix H.2) confirms patterns of lateral variation detected by our model and thus we are confident that we provide new information about velocity contrasts along the first ~100 km of the Craig rupture at seismogenic depths.

Iteration	Cross-correlation data		Catalog data		Absolute/ Differential ratio	DWS threshold
	P-wave weight	S wave weight	P-wave weight	S wave weight		
1-10	0.3	0.3	0.6	0.6	1	0.2

Table 4.1. TomoDD relocation and velocity inversion parameters.

4.3.3 Complementary data

In addition to the OBS aftershock data described above, we utilized several supplementary geophysical datasets to inform our interpretations. GLORIA sidescan sonar data informs our interpretation of the seafloor trace of the QCF (Bruns et al., 1992; Walton et al., 2015). Legacy seismic reflection data were used for both subsurface mapping of QCF-related fault structures (see Walton et al., 2015 for detailed methods and surveys) and for interpretation of aftershock distribution at depth. One survey of note is USGS survey L378EG, which crosses the OBS array at several locations. We reprocessed line L378EG_954 for this study (Appendix E), implementing a post-stack time migration that provides further detail for structural interpretation. L378EG processing steps include geometry definition, trace editing, 5-8-60-70 tapered bandpass filter, v^2 gain, multichannel windowed deconvolution, velocity definition, stack, and F-K migration (see Appendix E for further details).

4.4 OBSERVATIONS

4.4.1 Aftershock distribution

In map view, most seismicity appears to align with the QCF main trace as mapped on the seafloor, with deeper seismicity slightly landward (Walton et al., 2015; Fig. 4.1). In cross-section, aftershocks indicate a near-vertical, planar feature that is likely the QCF itself (Fig. 4.3). There is a significant trend of seismicity off of the main trace and on the Pacific Plate side of the boundary (Fig. 4.1, Fig. 4.3), which dips steeply away from the main QCF trace. Seismic reflection data indicate the presence of several possible strike-slip fault strands in the region of the focused Pacific aftershocks (Fig. 4.2, Fig. 4.3). In depth, the 2345 aftershocks presented in this study occur dominantly at depths from 12-24 km (Fig. 4.3). There are also ~150 events at very shallow (0-2 km) depths (Fig. 4.3);

however, shallow events can be poorly constrained in depth due to near-horizontal take off angles. Aside from the aforementioned spatial distribution, we do not notice any significant correlation between time and aftershock occurrence (i.e., clusters of events), time and spatial distribution, or magnitude and location during the 21-day OBS deployment (Fig. 4.3). Holtkamp and Ruppert (2015) notice some temporal variation in a longer ~5 month aftershock catalog following the Craig event, namely clusters of events over very short time periods. We should note that our study time period occurred ~4 months after the Craig mainshock and only covers 21 days, limiting our ability to detect regional and temporal patterns of aftershock occurrence.

4.4.2 Velocity structure

Average Vp and Vs values constrained by the inversion vary no more than ~10% from the starting velocity models (Fig. 4.4). Velocities on both sides of the QCF consistently increase with depth throughout the model without the appearance of low-velocity zones (Fig. 4.4). Noticeable lateral variation in Vp and Vs at depth occurs from 7.5-20 km, with the largest lateral contrasts occurring at 10 and 15 km (Figs. 4.4, 4.5). These are likely crustal depths on at least the North America side and possibly also the Pacific side based on seismic reflection profiles (Fig. 4.2) and previous refraction models (e.g. Shor, 1962; von Huene et al., 1979), which show the depth of Mohorovičić discontinuity to be at ~26.5 km (North America) and up to ~13 km (Pacific). Slower Vp and Vs velocities appear dominantly on the Pacific side of the QCF and faster velocities on the North America side (Fig. 4.5). Absolute lateral variations in both Vp and Vs are ~1.5 km/s, leading to as much as ~30% total variation across the QCF in our output models. Even without an initial velocity contrast imposed, the modeled velocity contrast correlates

well with aftershock locations and the seafloor QCF fault geometry; we can project the QCF to depth assuming a vertical dip from seismic reflection data (Fig. 4.2).

Shallow (0-5 km) and deep (>20 km) tomography results exhibit the least amount of variation from the starting model (Appendix G). Shallow slices indicate locally fast or slow velocities around OBS instrument locations (generally on the North America and Pacific sides of the QCF, respectively), which lessen or are nonexistent at depths of 7.5 km and deeper (Appendix G). The hotspots may be an artifact of relatively high ray coverage near the stations at shallow depths (as indicated by DWS; Appendix H.1). Slices deeper than 20 km exhibit the least variation from the starting model (Appendix G), likely associated with reduced model resolution at these depths due to a lack of rays from shallower aftershocks (Appendix H.2; also see resolution testing section). Due to generally lower resolution and/or poor ray coverage in the shallow and deep portions of our model, we only consider depths of 7.5-20 km in our interpretations.

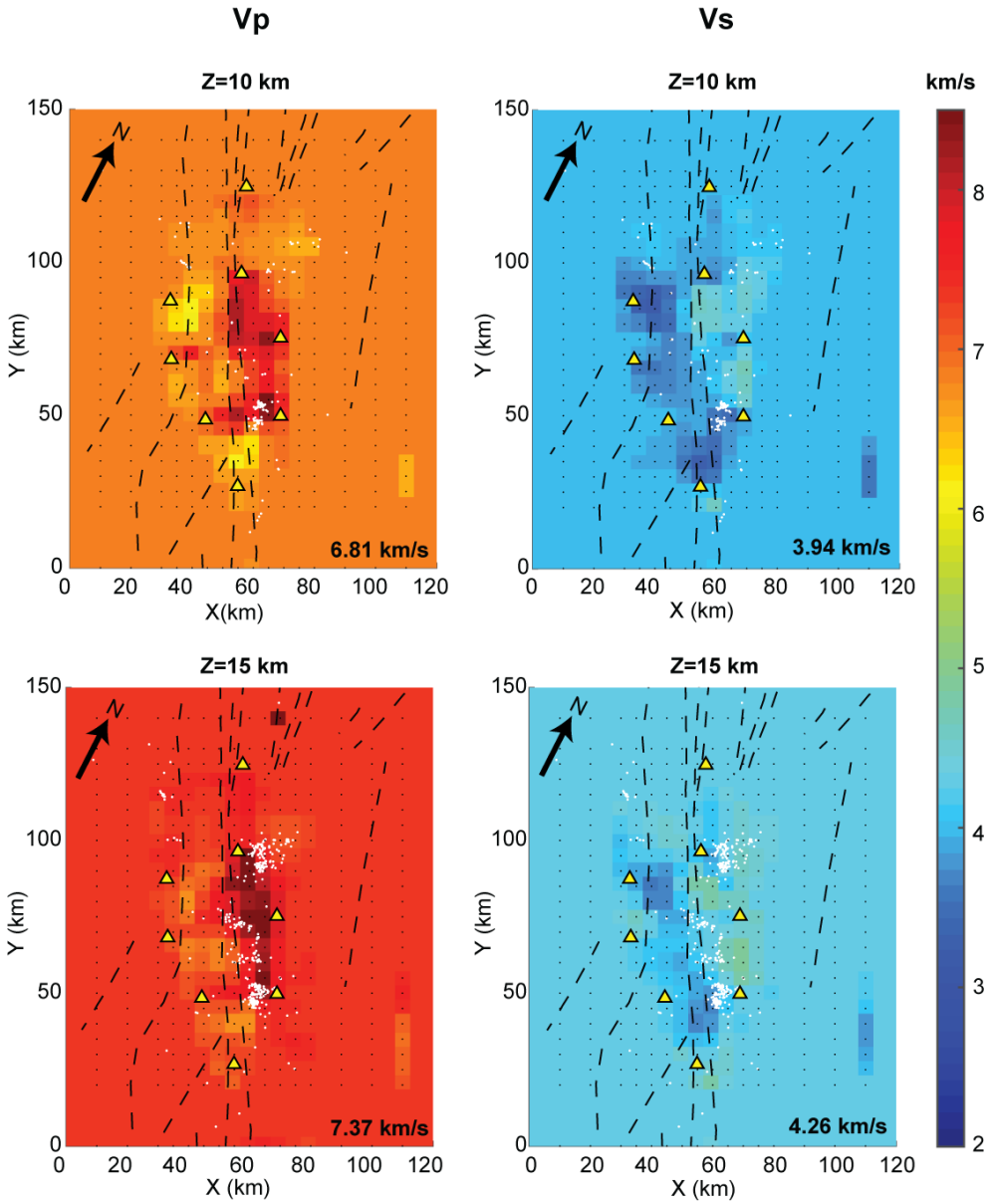

Figure 4.5. Vp (left) and Vs (right) tomography slices. Figure highlights 10 km (top) and 15 km (bottom) depths over the survey area (location shown in Fig. 4.1). Velocity data corresponding with DWS>20 are displayed and have not been interpolated, extrapolated, or otherwise filtered in these images. Starting 1D velocity model value (background) is indicated in the bottom right. Tomography data are overlaid by faults (Walton et al., 2015; black dashed lines), aftershock hypocenters within 2.5 km depth of the depth slice (white dots), user-defined nodes utilized in velocity inversion (small black dots), and OBS stations (yellow triangles).

4.4.3 Resolution testing

A resolution test, similar to a simplified checkerboard test (e.g. McGuire et al., 2015), was used to test our model's ability to resolve features of interest (Appendix H.2). Resolution testing of our final model was completed using modified tomoDD code and a synthetic velocity model based on values from our preferred output velocity model (Fig. 4.4). The synthetic velocity model was divided along a simplified QCF with velocities on either side of the fault defined by the median output velocity at that layer, leading to a ~10% contrast in P velocity and a ~5% contrast in S velocity across the QCF. Synthetic event travel times were generated using the synthetic velocity model; synthetic travel times were then used to re-run the inversion with preferred parameters. Without exception, the resolution test reproduces a contrast in velocities across the QCF with a faster North America at depths of 7.5-20 km (Appendix H.2). The contrast in the resolution test is more subtle than the contrast in our final preferred model; this could be due to the relatively small contrast chosen for the synthetic velocity model (i.e., real contrast is larger than 5-10%), or this could indicate the presence of regional heterogeneity which was not accounted for in the synthetic velocity model.

4.5 DISCUSSION

4.5.1 Implications of event distribution

The Craig hypocenter has been located at a depth of 9.8 ± 3.5 km by the U.S. Geological Survey (USGS; www.usgs.gov, last accessed January 2016); our catalog shows aftershocks significantly deeper than the mainshock hypocenter. Most aftershocks in our catalog occur at depths of 12-24 km, suggesting stick-slip fault behavior at depths greater than most continental strike-slip faults, which tend to have a maximum locking depth of ~10-15 km (e.g. Harris and Segall, 1987; Fletcher and Freymueller, 2003). Our results are

consistent with the finite-fault modeling of Aderhold and Abercrombie (2015) in which slip during the Craig event occurred in the zone between 5 and 25 km depths. Yue et al. (2013) also modeled a supershear Craig rupture, but only at depths less than 10 km. Our results supports the hypothesis of Rohr et al. (2000) and Aderhold and Abercrombie (2015) that the brittle-ductile transition along the QCF is thermally controlled like an oceanic strike-slip system, which is due to the mafic Pacific and mafic-intermediate North American crustal composition. The warm, ~15 Ma Pacific crust likely controls the maximum depth of brittle deformation. Heat flow measurements ~350 km to the south of our study area indicate that Pacific heat flow is nearly twice that of North America (86 and 47 mW/m^2, respectively; Hyndman et al., 1982), potentially supporting a deeper frictional transition that is controlled by thermal properties of the oceanic crust.

We use aftershocks to indicate active strands of the QCF (e.g. Lieser et al., 2014). The Craig aftershock distribution shows evidence for at least one major, active fault strand within the Pacific crust in the region of the Craig earthquake (Fig. 4.1), extending to a depth of at least ~20 km (Fig. 4.3). Seismic reflection data confirm the presence of offset sedimentary rocks near the Pacific seafloor along several faults in this area (Fig. 4.2). One of these Pacific faults has been interpreted on adjacent reflection profiles along the margin (Walton et al., 2015), and reflection data indicate that fault strand could be as long as ~200 km. The minimal sedimentary rock offsets and steep dip of the fault (Figs. 4.2, 4.3) would suggest a strike-slip or transpressive fault (Fig. 4.2). Holtkamp and Ruppert (2015) show Craig aftershocks in the Pacific Plate perhaps indicating the same fault. Holtkamp and Ruppert (2015)'s moment tensor solutions indicate a thrust focal mechanism for one of the Pacific events, supporting a transpressional structure and the apparent fault dip in our aftershock distribution (Fig. 4.3). The aftershock locations are insufficient to infer if or how this or other Pacific fault strand(s) relate to the QCF, and it is also unclear whether

this fault played a role in the Craig mainshock. The clear presence of off-axis aftershock locations on proposed faults, however, provides additional evidence that plate deformation is accommodated across a wide zone of deformation, and that various structural features (Fig. 4.1) may contribute to fault zone heterogeneity in the vicinity of the Craig rupture. We speculate that these observations of Pacific faulting may also suggest that strike-slip-related deformation is preferentially accommodated within the Pacific crust, possibly implying that the Pacific crust is weaker than North America (Tréhu et al., 2015).

4.5.2 Implications for velocity structure

Our tomography results support a seismically faster North America at depth, which is consistent with the deeper aftershock distribution. One of the primary observations of this study is the 20-30% Vp and Vs contrast across the QCF at seismogenic depths well-resolved by our dataset (7.5-20 km). The contrast in both Vp and Vs, most obvious in the 10-15 km depth range (Fig. 4.5), is unexpected in that the Pacific crust appears to be ~20-30% slower than the continental crust. We would expect mafic rocks, especially deeper gabbroic rocks, to be significantly (up to ~1 km/s) faster than granitic continental rocks at an equivalent depth (e.g. Christensen and Mooney, 1995).

We therefore revisit the crustal architecture of the North American Plate at this location to explain this unexpected velocity contrast. The Insular Superterrane makes up the North American crust here and contains higher-velocity rocks such as low-grade metamorphic rocks, felsic plutons, and basalts (e.g. Coney et al., 1980; Plafker et al., 1989). Rock type alone could suggest a seismically faster North America than has been previously presumed. Additionally, and somewhat independent of lithology, the ages of the crust that the QCF separates may contribute to changes in elastic properties within the crustal rocks of both plates. The North American crust at the site of the Craig earthquake is at least

Pennsylvanian age (Gardner et al., 1988), and some rocks south of Craig are as old as Neoproterozoic (Gehrels, 1990), so North American rocks are significantly older than the ~15 Ma oceanic crust here. Between lithology and age, it is certainly feasible that the North American crust is seismically faster (Vp and Vs) than the Pacific crust in our study area.

An alternative explanation for the lower Pacific velocities is that our model raypaths are sampling a broad deformational zone along the QCF, rather than competent crustal structure. It is possible that our model cannot resolve crustal velocities and is instead indicating a localized lithologic feature. The QCF cuts through the Queen Charlotte Terrace, which has been deformed by dextral shear and strike-slip faulting during the long history of the QCF (e.g. Rohr et al., 2000). In the region of the Craig earthquake, the Pacific crust was deformed and faulted with transpressional splays of the QCF as well as deeper plate-bending faults (Tréhu et al., 2015; Walton et al., 2015). If deformation favors the Pacific crust because it is inherently weaker, the deformed terrace and/or Pacific crust could have developed large damaged zones with increased porosities and therefore lower seismic velocities (particularly lower Vs), which could yield velocities up to 8% slower than the surrounding rock (Roland et al., 2012). S-waves appear to travel predominantly through the North America side of the plate boundary (as indicated by DWS; Appendix H.1) and Vp/Vs is higher on the Pacific side (Appendix G), both potentially supporting higher Pacific deformation and/or porosity.

The OBS network does not sample enough Pacific crust to be confident that absolute seismic velocities are similar to or lower than normal oceanic crustal velocities, which might provide a preferred explanation for the lower Pacific velocities zone. We do note, however, that Pacific Plate deformation appears to be limited to several discrete, mappable faults in seismic reflection and aftershock data (Fig. 4.1, Fig. 4.5; Walton et al., 2015) with more pervasive deformation within the Queen Charlotte Terrace. We model

lower Pacific velocities ~20 km beyond the QCF zone (Fig. 4.5), perhaps suggesting these velocities are more representative of Pacific lithologic velocities than deformation associated with the QCF.

Our results are ultimately limited by the size and quality of our dataset, so we acknowledge several anomalies and sources of uncertainty. Shallow tomography slices indicate very fast velocities near the OBS stations (Appendix G). These anomalies could be related to a relatively large number of shallow events that are poorly-resolved in depth, small static offsets for events near the stations, or limited ray coverage indicated by DWS (Appendix H.1). Additionally, OBS station clocks were dead when they were retrieved, and were adjusted using drift correction from another deployment of the same instruments. We examined teleseismic arrivals to calibrate potential clock errors, and have limited evidence from one detectable teleseismic arrival that station CG11 (possibly others) may require clock adjustment (Appendix F.3). We do not correct any station times, however, due to lack of firm constraints. Regardless of these limitations, we are able to resolve broad-scale results of our velocity model at 7.5-20 km depths (based on resolution tests; Appendix H.2), which are the depths most relevant for understanding the Craig seismogenic zone. Absolute model velocities are well within reasonable ranges for crystalline oceanic crust, continental crust, and mantle at these depths, giving us further confidence in our interpretations of regional velocity patterns.

4.5.3 Implications for supershear rupture

On the basis of regional S-wave observations, the Craig earthquake of 05 January 2013 was found to be a dominantly unilateral rupture, propagating northward at supershear velocities up to 5.5-6.0 km/s (Yue et al., 2013). Supershear ruptures have rarely been observed in actual earthquakes (Dunham and Archuleta, 2004), but have been effectively

modeled in numerical and physical studies (Xia et al., 2005; Shi and Ben-Zion, 2006; Ampuero and Ben-Zion, 2008). Experimental results indicate that supershear ruptures can occur at fault zones where there is a strong material contrast to either side of the fault. Based on numerical and physical experiments, the "preferred" slip direction for subshear ruptures ("normal" earthquakes) is in the direction of slip of the seismically slower material; supershear ruptures, however, tend to propagate in the "non-preferred" direction, or the direction of slip of the faster material (Xia et al., 2005). The Craig earthquake ruptured dominantly northward (Yue et al., 2013) slipping right-laterally between the Pacific crust to the west and North American crust to the east. Our results show a slower Pacific crust at seismogenic depths relative to the North American crust within the Craig rupture area (Fig. 4.5), which would indicate the Craig rupture propagated in the opposite direction than expected for a supershear rupture.

Although our results do show a considerable velocity contrast across the fault, it appears to be of the opposite sense one would assume for a north-propagating supershear rupture. A rupture propagating at 4 km/s within a depth range of 5-25 km, which is the preferred northward rupture model for Aderhold and Abercrombie (2015), would actually be propagating at sub-shear wave speeds for much of the seismogenic zone thickness based on our tomographic results (Figs. 4.4, 4.5). Thus, the possibility remains that the Craig event may have ruptured at a sub-shear propagation rate. The other possibility is that velocity contrast across the seismogenic zone is perhaps not the only factor that might contribute to supershear rupture. We note that the presence of active faults preferentially located on the Pacific side provides evidence beyond our tomographic models implying a weaker Pacific Plate. If supershear rupture indeed occurred, then less-understood factors such as fault-zone frictional properties, pore pressure variations, elastic properties of the fault zone outside the immediate study area, and other complexities could contribute to

supershear directionality. Some studies have also hypothesized and modeled supershear transients along geometrically smooth fault segments (Bouchon et al., 2010; Bruhat et al., 2016). We do not quantify the smoothness of the QCF here, but it is possible that a smoother fault to the north may have led to supershear rupture in that direction.

4.6 CONCLUSIONS

1. The majority of Craig aftershocks in our study occur between 12 and 24 km depth, implying that the fault zone is seismogenic at least to that depth and supporting previous hypotheses that elastic deformation along the QCF is thermally-controlled by mafic rheology.
2. Active seismicity in the Pacific Plate, as well as apparent dip of that seismicity, appears to suggest the presence of at least one active fault strand in the Pacific crust that is mappable in seismic reflection data, which is possibly accommodating transpressive stress.
3. In the vicinity of the 2013 Craig, Alaska earthquake, the Pacific Plate demonstrates P-and S-wave velocities that are up to 30% slower than the North America Plate at seismogenic depths. The variation in velocity across the fault is especially evident at the 10-15 km depth range, coincident with the best-resolved portions of our velocity model and the zone through which the mainshock ruptured.
4. The low-velocity zone on the Pacific side of the QCF is consistent with the presence of deformed, faulted rocks within the Pacific Plate or Queen Charlotte Terrace, but may also indicate a contrast in crustal lithologies, possibly associated with the Paleozoic-Mesozoic Insular Superterrane accreted to North America.
5. Our results show a slower Pacific crust to the west and faster North America to the east, yet the Craig supershear rupture propagated northward. These primary results

are contrary to supershear directionality theory and the hypothesis of Yue et al. (2013) that the northward supershear propagation was due to a bimaterial contrast of faster Pacific crust adjacent to a slower North American crust. We therefore speculate that there may be controls other than plate strength or seismic velocity that affect supershear rupture propagation. Within the framework of our tomographic results, however, we cannot eliminate the possibility that the Craig rupture speed was slower than the shear-wave speed of the seismogenic zone and thus may have ruptured subshear.

Chapter 5: Revisiting the 1899 earthquake series using integrative geophysical analysis in Yakutat Bay, Alaska

ABSTRACT

A series of large earthquakes in 1899 affected southeastern Alaska near Yakutat and Disenchantment Bays. The largest of the series, a M_w 8.2 event on 10 September 1899, generated 14.4 m of coseismic uplift in Yakutat Bay, the largest ever measured globally, and a 6 m tsunami. The complex fault systems near Yakutat Bay are poorly constrained, with limited insight on their roles in the 10 September event and modern hazard. In an effort to better characterize local fault structure, we collected and interpreted 153 km of high-resolution multichannel seismic (MCS) reflection profiles in Yakutat Bay in August 2012. We combine our MCS data with published GPS models, geologic uplift measurements, seismic reflection data, and thermochronology to constrain fault geometry and subsurface structure. Additionally, we assess older datasets for uncertainty and provide quantitative assessment of dataset reliability. Results include 1) an updated map of faults local to Yakutat Bay, 2) a conceptual structural model of these faults, and 3) a Coulomb stress model of the 4 September 1899 event. Together, our findings support a rupture related to Yakutat subduction for the 10 September 1899 event, with the majority of coseismic slip limited to the Esker Creek system on the northwest side of Yakutat Bay. This work provides an improved tectonic framework with which to understand regional hazard and recurrence of a similar event.

5.1 INTRODUCTION

The 1899 earthquake series in Yakutat Bay, Alaska includes two large events, a M_w 8.1 and M_w 8.2, which occurred on 4 and 10 September, respectively (Abe and Noguchi, 1983; Plafker and Thatcher, 2008). Termination of the Fairweather strike-slip system,

collision of the Yakutat Terrane (an oceanic plateau and microplate; Plafker, 1987; Christeson et al., 2010) with North America, and flat-slab subduction of the Yakutat Terrane beneath North America (Gulick et al., 2007; Worthington et al., 2012) lead to complex fault structures throughout the Yakutat-St. Elias region of Alaska and particularly near Yakutat Bay (Fig. 5.1). The earlier 4 September 1899 event likely relates to subduction of the Yakutat Terrane, as the epicenter relocation and strongest shaking are near the Pamplona Zone (Fig. 5.1), which is the modern Yakutat-North America subduction deformation front (Coffman et al., 1982; Doser, 2006; Worthington et al., 2010). Much less is known about the 10 September event, however. The epicenter has been located imprecisely to be near the Yakutat Bay region and the focal mechanism cannot be constrained with existing teleseismic data (Doser, 2006). Eyewitness reports of shaking and a 6 m tsunami, as well as coseismic uplift of over 14 m, locate the 10 September mainshock to be somewhere in the region of Yakutat Bay and/or its northern extension, Disenchantment Bay (Fig. 5.1; Tarr and Martin, 1912).

Understanding recurrence of an 1899-type event is important for hazard assessment, and it is also important to know how the 1899 events relate to the larger Alaska-Aleutian subduction history, notably the M_w 9.2 great Alaska earthquake of 1964. The 1964 event ruptured nearly 800 km of the eastern Aleutian megathrust (Plafker, 1969), including a portion of the Yakutat megathrust, the interface between the subducting Yakutat Terrane and overriding North America (e.g. Eberhart-Phillips et al., 2006; Finn et al., 2015). Recent paleoseismic evidence indicates that the eastern Aleutian and adjacent Yakutat plate boundaries as far east as the Pamplona Zone may have ruptured simultaneously ~900 and ~1500 years ago, generating a “super ‘64” event (Shennan et al., 2009). This scale of rupture would have a combined area 15% larger than the great Alaska earthquake (Shennan et al., 2009), leading to enormous shaking and tsunami hazards. A

rupture of this size would affect not only the local town of Yakutat (pop. ~650), but cities throughout south-central and southeastern Alaska. Furthermore, the paleoseismic event ~900 years ago is potentially the most recent time at which the Yakutat patch ruptured prior to 1899. Unless the 1899 events relieved ~800 years of accumulated stress, which would amount to some ~30 m of slip, assuming 37 mm/yr convergence (Elliott et al., 2013), some built-up stress remains. The 1964 rupture and tsunami have been studied extensively (e.g. Plafker, 1969; Shennan et al., 2009; Parsons et al., 2014; Finn et al., 2015; Haeussler et al., 2015), but the 1899 events are far less understood and equally critical for characterizing and forecasting large plate-boundary ruptures in Alaska.

The 1899 events occurred near the structural syntaxis between Yakutat subduction and the Fairweather strike-slip system. The 10 September event was likely due to Yakutat subduction and/or collision (e.g. Doser, 2006), but could also be related to strike-slip motion along the Fairweather Fault. If it was indeed a subduction event, the mechanics of the rupture are poorly understood. Did the rupture originate along the Yakutat megathrust or on shallower thrust fault systems? How much of the measured uplift was coseismic, and how much was postseismic? How did stress transfer to and between local fault systems where uplift was observed? Some of the foreland thrust fault systems in the remote Chugach-St. Elias Mountains have been mapped in geologic field studies (Bruhn et al., 2004; Chapman et al., 2012; Pavlis et al., 2012) and by using glacial ice flow patterns (Bruhn et al., 2012; Cotton et al., 2014). Faults more local to Yakutat Bay, which likely played a major role in the 10 September 1899 rupture, are the least constrained and generally inferred where mapped.

In our study, we aim to constrain regional fault geometry and structure in the Yakutat Bay region by compiling various geological and geophysical data, assessing each dataset for reliability, and providing updated fault maps based on our analysis. Available

data prior to this study include uplift measurements made in Yakutat Bay in 1905 (Tarr and Martin, 1912) and later (Plafker and Thatcher, 2008), GPS modeling (Elliott et al., 2010; Elliott et al., 2013), satellite imagery, bathymetric and topographic data (e.g. Amante and Eakins, 2009; Goff et al., 2012), thermochronology data (Enkelmann et al., 2015), and crustal-scale seismic reflection data from survey EW0408 (Gulick et al., 2004; Elmore et al., 2013). We also interpret new 2012 high-resolution multichannel seismic (MCS) reflection data (first published in Zurbuchen et al., 2015). We originally collected these MCS data in order to image Bay-crossing fault structures proposed by Plafker and Thatcher (2008) thought to potentially relate to the 10 September 1899 rupture. We examine the MCS data for active structures and evidence for long-term deformation. We supplement these data with the other available geophysical datasets to 1) provide a conceptual tectonic model and updated maps of faulting on the southeast side of Yakutat Bay, 2) evaluate previous hypotheses that the 10 September event was related to Yakutat subduction, 3) quantify error in previous models, 4) put our model into the context of the 1899 events using Coulomb stress models, and 5) highlight the risk of a similar, future event in the Yakutat region.

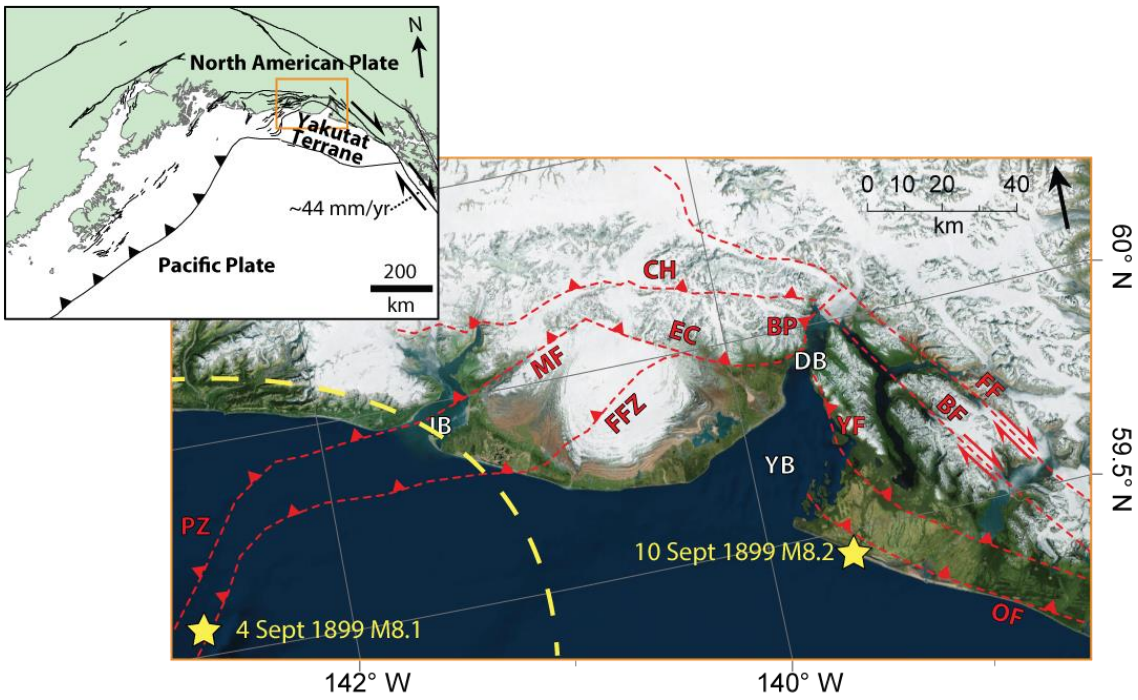

Figure 5.1. Location map showing Yakutat Bay and Icy Bay. Yellow stars indicate 4 and 10 September 1899 epicenter relocations by Doser (2006). Yellow dashed line indicates partial approximate error ellipse for the 4 September event; the ellipse for the 10 September event encompasses the figure (Doser, 2006). Major fault systems from Bruhn et al. (2012) are shown as dashed red lines. Inset shows larger region with tectonic plates and relative Pacific/North America velocity from Elliott et al. (2010). Inset faults modified from Quaternary Faults and Folds in Alaska database (Koehler et al., 2005). Orange box in inset indicates Fig. 1 location. IB – Icy Bay. YB – Yakutat Bay. DB – Disenchantment Bay. PZ – Pamplona Zone. MF – Malaspina Fault. CH – Chaix Hills Fault. FFZ – Foreland Fault Zone. EC – Esker Creek Fault. BP – Bancas Point Fault. FF – Fairweather Fault. BF – Boundary Fault. YF – Yakutat Fault. OF – Otmeloi Fault. Background imagery is an integrated Esri basemap that includes data from Esri, DigitalGlobe, GeoEye, Earthstar Geographics, CNES/Airbus DS, USDA, USGS, AEX, Getmapping, Aerogrid, IGN, IGP, swisstopo, and the GIS User Community.

5.2 REGIONAL SETTING

The geology of coastal southeastern Alaska consists of a number of fault-bounded accreted terranes, including the Insular Terrane, the Prince William Terrane, the Chugach Terrane, and the Yakutat Terrane, which is currently in the process of accreting to North America (Plafker et al., 1994). The terranes are generally composed of highly deformed deep-sea sedimentary rocks (Plafker et al., 1994). Formations in exposed rocks include the Cretaceous Yakutat Group, the Eocene Kultieth Formation, Oligocene-Miocene Poul Creek Formation, the Miocene-Pleistocene Yakataga Formation, and some volcanic Yakutat Terrane rocks (e.g. Chapman et al., 2012; van Avendonk et al., 2013). Rapid sedimentation due to active orogenesis and glacial erosion also leads to extensive cover of unconsolidated Pleistocene-Holocene sediments (Gulick et al., 2015). In Yakutat Bay and Disenchantment Bay (Fig. 5.1), up to ~500 m of the shallowest sediments have been deposited by the Hubbard and Malaspina glaciers during and since the early phase of the Little Ice Age (~1000 AD; Elmore et al., 2013; Zurbuchen et al., 2015). Because of glacial activity, sedimentation rates in Yakutat and Disenchantment bays approach and can even exceed ~1 m/yr (Goff et al., 2012).

The tectonic framework of southeastern Alaska tectonics are dominated by right-lateral strike-slip motion along the Queen Charlotte-Fairweather Fault. The Queen Charlotte Fault represents the plate boundary between the Pacific and North American plates along western Canada and southernmost southeast Alaska. The Queen Charlotte Fault links up with the largely onshore Fairweather Fault, which separates the Yakutat Terrane from North America (e.g. Chase and Tiffin, 1972; Carlson et al., 1988; Fig. 1). To the north, the Pacific Plate subducts beneath North America along the Alaska-Aleutian subduction zone. The Yakutat Terrane, an anomalously thick piece of oceanic crust

(Plafker, 1987; Christeson et al., 2010; Worthington et al., 2012), travels with the Pacific Plate and resides in the corner between subduction and strike-slip faulting (Fig. 5.1). The Yakutat Terrane is undergoing flat-slab subduction beneath North America due to its thickness and buoyancy (Gulick et al., 2007, Abers, 2008). The Yakutat Terrane is bounded by the Fairweather Fault to the northeast, the largely inactive Transition Fault to the southeast, and the Pamplona Zone subduction deformation front to the northwest (e.g. Pavlis et al., 2004; Gulick et al., 2007; Gulick et al., 2013). Thicker regions of the Yakutat Terrane are colliding with North America, causing active orogenesis in the Chugach-St. Elias Mountains, the highest coastal mountain range in the world (Berger et al., 2008; Enkelmann et al., 2009; Pavlis et al., 2012; Worthington et al., 2012).

The Yakutat Terrane plays an important role in understanding the 1899 events and regional fault structure. The 1899 earthquakes ruptured in the complexly-faulted vicinity of the syntaxis between subduction/collision of the Pamplona Zone and transpressive strike-slip along the Fairweather Fault (e.g. Chapman et al., 2012; Cotton et al., 2014). The Yakutat-North America subduction zone boundary essentially lies along the series of Pamplona Zone faults, with its northeastern edge at the Fairweather Fault system. Convergent stresses related to Yakutat subduction are accommodated locally in northwestern Yakutat Bay along the Esker Creek, Bancas Point, and Chaix Hills faults (Fig. 5.1). On the southeastern side of the bay, the Fairweather system accommodates major right-lateral offset of ~4.3 cm/yr (Elliott et al., 2010), with smaller amounts of transpressive motion along the Boundary and Yakutat faults (Fig. 5.1). The Fairweather Fault itself ends not far from Yakutat Bay, creating additional tectonic complexity associated with the termination of a major strike-slip fault (e.g. Bruhn et al., 2012). Proposed fault models in the area have been largely based on structural mapping north and west of Yakutat Bay (e.g. Chapman et al., 2012), with mapping and geophysical modeling

more local to Yakutat Bay by Plafker and Thatcher (2008) and Bruhn et al. (2012). Plafker and Thatcher (2008)'s model includes faults crossing Yakutat Bay and has been commonly employed (e.g. Shennan et al., 2009; Elliott et al., 2010; Enkelmann et al., 2010); we seek to verify and update this model. We primarily focus on better-defining the near-shore Esker Creek, Bancas Point, Yakutat, Boundary, and Otmeloi fault systems, which are critical to understanding the 1899 events and their relationship to Yakutat-North America subduction.

5.3 DATA

5.3.1 Uplift measurements

Two sets of historical geologic uplift measurements have been taken along the coastlines of Yakutat and Disenchantment Bays. The first set was measured by Tarr and Martin in 1905 (Tarr and Martin, 1912; Fig. 5.2a). Their robust set of measurements covers the northwest and southeast sides of Yakutat Bay, noting and photographing areas of both uplift and subsidence; their detailed report also includes interviews with local inhabitants and eyewitness accounts of earthquake shaking and the 10 September 1899 tsunami. In their field work, Tarr and Martin (1912) utilized common elevation markers including exposed barnacles, submerged trees, and uplifted beaches, sea caves, and sea cliffs. As their field work was completed shortly after the 1899 events, measured uplift was interpreted to be coseismic with the 1899 events.

The second set of uplift measurements were taken by Plafker and Thatcher (2008) in several field seasons between 1967 and 2000, in which they revisited many of Tarr and Martin's original sites and assessed the older measurements for accuracy (Fig. 5.2a). The majority of their field data were collected in 1973 and 1980; we assume their uplift measurements were taken in 1980 to match text in the discussion and air photo dates. Many

of Plafker and Thatcher (2008)'s measurements are similar to Tarr and Martin (1912), although they found that areas Tarr and Martin (1912) noted as tectonic-induced subsidence had actually subsided due to non-tectonic surficial slumping, perhaps induced by earthquake shaking.

5.3.2 Seismic reflection

In order to map offshore fault structures, a high-resolution seismic reflection survey was shot aboard the U.S. Geological Survey (USGS) R/V *Alaskan Gyre* in August 2012 (USGS survey 2012-602-FA; here we will refer to the survey as AG0812; see Fig. 5.2b). The survey targeted near-shore areas in Yakutat Bay and Disenchantment Bays which had not been imaged previously and had suspected faulting based on Plafker and Thatcher (2008). The AG0812 survey was funded through the USGS Earthquake Hazards External Grants Program. The MCS reflection data include ~153 km of 2D profiles shot using a Sercel mini-GI gun (15/15 in^3), which has a peak frequency of ~250 Hz, and a 24-channel, 100 m streamer with group spacing at 3.125 m. Vertical resolution of the data are 1-2 m and the total record length is 2 s. Processing presented here is to post-stack time migration. Further processing details can be found in Appendix C and in Zurbuchen et al. (2015), who first published the data as part of an analysis of Hubbard Glacier advance-retreat history and glacigenic sedimentary sequences.

In addition to the USGS AG0812 data, several other lower-resolution, deeper-penetrating seismic reflection datasets exist in Yakutat Bay, including a 2004 R/V Ewing survey (EW0408; see Gulick et al., 2007 for survey details), a 2008 R/V Langseth survey (MGL0814; see Worthington et al., 2010 for survey details), and a 1979 Western Geophysical survey (W1279EG; see Elmore et al., 2013 for survey details). These lower-resolution MCS surveys, particularly line 2101 from the EW0408 survey, were primarily

used for planning the AG0812 survey and to provide regional subsurface context for mapped structures and sedimentary deposits. We also utilize 2010 CHIRP envelope data collected aboard the R/V *Quest* in Russell Fiord.

5.3.3 Bathymetry and topography

Bathymetry and topography data exist near Yakutat Bay. Pre-1899 sounding data are available through the National Geophysical Data Center (NGDC; ngdc.noaa.gov). The 1892 survey (H02159) sparsely covers upper Yakutat Bay and lower Disenchantment Bay (Fig. 5.2c). High-resolution bathymetry data in Yakutat Bay is available from several sources and have been compiled and merged into a 50 m resolution grid (Fig. 5.2; Goff et al., 2012). Sources (described in detail in Goff et al., 2012) include multibeam bathymetry collected during survey EW0408. The merged bathymetry data have also been published by Elmore et al. (2013) and Zurbuchen et al. (2015). For onshore topographic observations, we utilize regional digital elevation data available through the NGDC as the integrated 1 arc-minute ETOPO1 global relief model (Amante and Eakins, 2009). Additionally, we use Landsat satellite imagery (landsat.usgs.gov) with 30 m resolution to inform our topographic interpretations at a higher resolution.

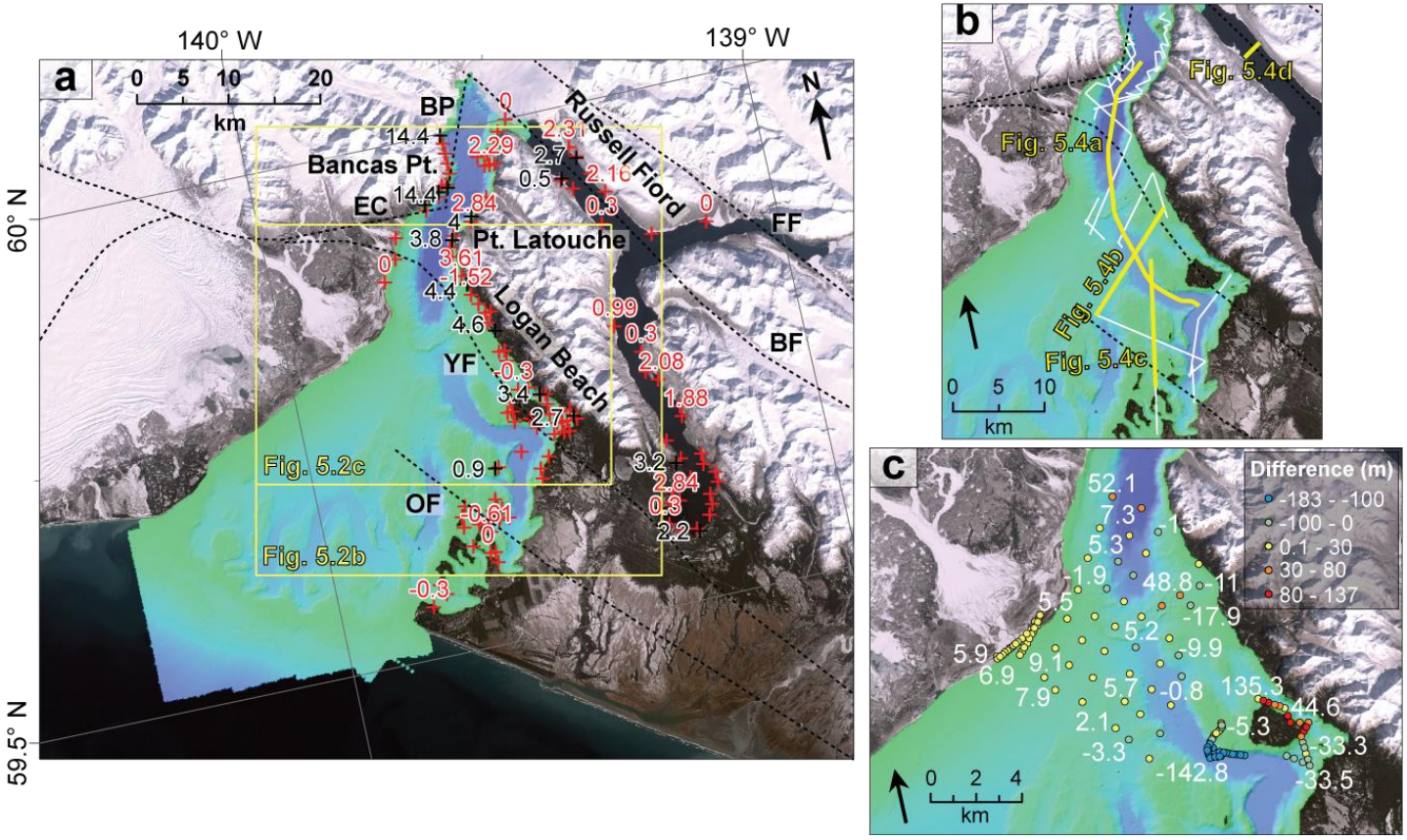

Figure 5.2. Maps of Yakutat Bay datasets used in this study.

Background imagery in each shows Yakutat Bay merged bathymetry (Goff et al., 2012) and Landsat satellite imagery. Black dashed lines in each figure are faults proposed by Plafker and Thatcher (2008). (a) Zoom of Yakutat Bay with select uplift measurements in meters by Tarr and Martin (1912; red) and Plafker and Thatcher (2008; black), with locations of Figs. 5.2b and 5.2c in yellow. (b) Depicts location of seismic survey AG0812 (white lines) with locations of seismic profiles shown in Fig. 5.4 highlighted in bold yellow. Note Fig. 5.4a is a line from survey EW0408, not AG0812. (c) Difference between 1892 bathymetric sounding data and merged bathymetry plotted as labeled, colored dots where 1892 data exist. Negative values indicate subsidence or erosion and positive values indicate uplift or deposition. EC – Esker Creek Fault. BP – Bancas Point Fault. FF – Fairweather Fault. BF – Boundary Fault. YF – Yakutat Fault. OF – Otmeloi Fault.

5.3.4 Complementary datasets

GPS data represent some of the more robust geophysical datasets available in the Yakutat Bay region. GPS data have been published recently by Larsen et al. (2004) and Elliott et al. (2010, 2013). Tectonic and glacial isostatic adjustment (GIA) models fit to GPS data by Elliott et al. (2010, 2013) inform our understanding of regional fault geometry and kinematics throughout southeastern Alaska. The southeastern Alaska GPS tectonic model is constrained by 102 stations (Elliott et al., 2010), and the south-central model is constrained by 65 stations (Elliott et al., 2013).

Notable in the GPS data is the large component of vertical uplift present throughout southeastern Alaska. Elliott et al. (2010, 2013) and others attributed the uplift to be due to GIA since the ice retreat at the end of the Little Ice Age (~1780 AD). Larsen et al. (2004) and Elliott et al. (2010) successfully modeled the effects of GIA, fitting it to the GPS data, in the region just southeast of Yakutat Bay where the effect is particularly significant. Uplift due to GIA reaches rates of 3 cm/year in places of former heavy ice coverage, particularly the Yakutat Ice Fields (Larsen et al., 2005). These uplift rates may significantly

affect measurement and/or interpretation of coseismic tectonic uplift in the region, and are important to consider when evaluating the reliability of geologic field observations.

Recent thermochronology results from Enkelmann et al. (2015) are also highly relevant to our study. Low-temperature thermochronology, including apatite and zircon ages, provide exhumation rates along fault systems around Yakutat Bay. They find exhumation to be between 1-5 mm/yr throughout the Yakutat Bay area. As exhumation rates are so high, they can be used as a proxy for active uplift and relative fault motion, so thermochronology results therefore support our interpretations of Yakutat Bay active fault structure and kinematics.

5.4 METHODS

Most analyses and data integration were completed using ESRI's ArcGIS Desktop software (www.esri.com). Seismic tracklines, bathymetry, topography, and satellite imagery were plotted alongside contoured GPS data from Elliott et al. (2010, 2013), uplift measurements (Tarr and Martin, 1912; Plafker and Thatcher, 2008), and previous fault models (Plafker and Thatcher, 2008; Bruhn et al., 2012). The combination of these data assisted with re-mapping of fault geometry. Coulomb modeling was completed using Coulomb 3.3 software available through the USGS (Toda et al., 2011).

Plafker and Thatcher (2008)'s fault model inferred one or more thrust faults crossing Yakutat Bay to explain 1899 coseismic uplift patterns. To test the hypothesis that there were major thrust systems crossing Yakutat Bay, we collected and analyzed seismic reflection data throughout Yakutat and Disenchantment Bays. Survey AG0812 MCS data were processed using Paradigm's Echos processing software and imported into Landmark's DecisionSpace Desktop (www.halliburton.com) for visualization and interpretation alongside previously-existing seismic reflection surveys, including MCS

data from EW0408, MGL0814, and W1279EG. Integrated bathymetric/topographic maps of the Yakutat region were also imported into DecisionSpace Desktop to assist with regional context and identification of potential offshore features. The 1892 bathymetric sounding survey is too coarse (~2 km) to provide meaningful gridded images, so we difference the 1892 data points with the Goff et al. (2012) merged bathymetry grid (dated 1978-2006) in ArcGIS to extract potential topographic response to the 1899 events (Fig. 5.2c).

In order to assess reliability of Plafker and Thatcher (2008)'s fault model, we re-visit their uplift measurements and attempt to quantify uncertainty, which has not been done previously. We also compare, point-by-point, published Plafker and Thatcher (2008) values with digitized Tarr and Martin (1912) data (Table 5.1). We assume that uplift data were collected in 1905 (Tarr and Martin, 1912) and in 1980 (Plafker and Thatcher, 2008), and note that GIA is one of the most significant topographic forcings in the region (Elliott et al., 2010). GIA must have affected Plafker and Thatcher's measurements in 1980, so for each data point published by Plafker and Thatcher (2008), we extract GIA uplift from Elliott et al. (2010) and calculate cumulative GIA from 1905-1980, assuming constant uplift rates (Table 5.1). 75 years of cumulative GIA should be close to the difference between Plafker and Thatcher (2008) and Tarr and Martin (1912)'s measurements, and thus is helpful in estimating uncertainty for Plafker and Thatcher (2008)'s uplift measurements. Plafker and Thatcher (2008)'s values were subtracted from this sum of Tarr and Martin (1912)'s measurements and 75 years cumulative GIA to derive GIA-related uncertainty in Plafker and Thatcher (2008)'s measurements.

Location	TM (1905) measured uplift (m)	PT (1980) measured uplift (m)	75 years GIA uplift (m)	Est. GIA uncertainty (m) for PT measurements, this study*	PT value with total est. uncertainty (m), this study
Bancas Pt	2.84 ± 0.3	2.8 ± 1	1.75 ± 0.16	1.8	2.8 ± 2.1
Bancas Pt	12.8 ± 0.3	14.4 ± 1	1.77 ± 0.16	0.2	14.4 ± 1
Bancas Pt	12.17 ± 0.3	14.4 ± 1	1.78 ± 0.16	0.4	14.4 ± 1.1
Bancas Pt	10.34 ± 0.3	14.4 ± 1	1.69 ± 0.16	2.4	14.4 ± 2.6
Bancas Pt**	14.4 ± 0.3	?	1.74 ± 0.16	?	?
Russell Fiord	0.48 ± 0.3	0.5 ± 1	1.89 ± 0.16	1.9	0.5 ± 2.1
Russell Fiord	2.74 ± 0.3	2.7 ± 1	1.91 ± 0.16	2.0	2.7 ± 2.2
South Russell	2.64 ± 0.3	3.2 ± 1	2.11 ± 0.16	1.5	3.2 ± 1.8
South Russell	2.24 ± 0.3	2.2 ± 1	2.08 ± 0.16	2.1	2.2 ± 2.4
Logan Beach	2.84 ± 0.6	4 ± 1	1.84 ± 0.16	0.7	4 ± 1.2
Logan Beach	3.81 ± 0.6	3.8 ± 1	1.81 ± 0.16	1.8	3.8 ± 2.1
Logan Beach	0.3 ± 0.6	4.4 ± 1	1.86 ± 0.16	2.2	4.4 ± 2.5
Logan Beach	0 ± 0.6	4.6 ± 1	1.92 ± 0.16	2.7	4.6 ± 2.9
Logan Beach	3.2 ± 0.6	3.4 ± 1	1.99 ± 0.16	1.8	3.4 ± 2.1
Logan Beach	2.72 ± 0.6	2.7 ± 1	2.03 ± 0.16	2.1	2.7 ± 2.3
In Bay	0.91 ± 0.3	0.9 ± 1	1.95 ± 0.16	2.0	0.9 ± 2.2

Table 5.1. Uplift measurements published by Tarr and Martin (1912) compared to Plafker and Thatcher (2008).

Final column includes total uncertainty estimates computed in this study (see text for details). *Estimated GIA uncertainty calculated by taking the absolute value of [TM measured uplift] + [75 years GIA uplift] – [PT measured uplift]. **Corresponding data point not published by Plafker and Thatcher (2008) for this Bancas Point location.

Total uncertainty estimates for Plafker and Thatcher (2008)'s measurements were calculated using a root of the sum of the squares method and include estimates of GIA uncertainty, 1 m measurement uncertainty, and cumulative GPS instrumental error. We assume that uncertainty in uplift due to measurement method, tools used, rugged terrane, relative sea level, and imprecise location of paleo-shorelines is on the order of ±1 m, likely a low-end estimate. We might consider the effects of sea level rise; however, this effect is on the order of ~10 cm from 1905-1980 (Church and White, 2011), and therefore is essentially negligible when discussing uplift on the scale of meters and GIA of ~2-3 cm/yr. When considering effects of GIA on uplift measurements and/or the relative reliability the GPS data, GPS instrument uncertainty is similarly small, amounting to a maximum of ~20 cm cumulative uncertainty over the 75 years in question (1905-1980); however, we do include average GPS instrumental error in our uncertainty calculations as it is a relatively straightforward parameter to calculate and include.

A simple Coulomb model of the 4 September 1899 event was generated to visualize potential stress loading of a rupture on the Yakutat-North America plate boundary interface (Fig. 5.3). We assume the 4 September event ruptured the offshore Yakutat-North America subduction interface to the Foreland Fault Zone, which represents the modern subduction deformation front. This model is consistent with the relocation of the 4 September event and with previous interpretations of the rupture (Doser, 2006; Plafker and Thatcher, 2008; Cotton et al., 2014). We assume the dip of the décollement to be 5° with rupture extending to 10 km depth, consistent with subduction interface faults modeled by Elliott et al. (2013).

Although both the area and slip during the actual event are poorly constrained, the preferred model we present here requires 6 m slip of the modeled area to generate a M_w 8.1 earthquake. Several iterations of varying geometries and slip parameters were tested with similar model output.

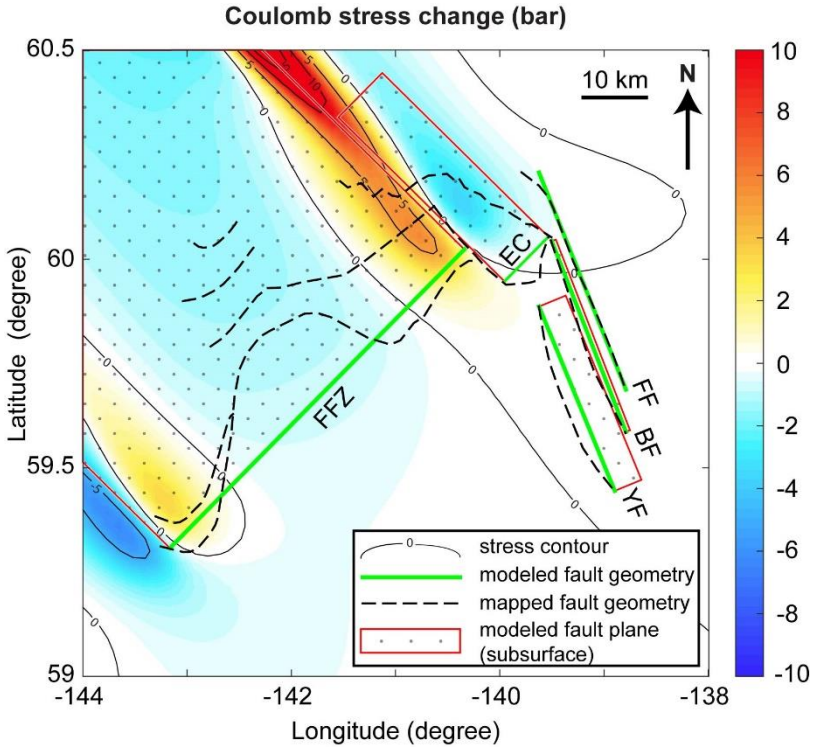

Figure 5.3. Coulomb stress model of the 4 September 1899 event. Figure area is slightly larger than the region shown in Fig. 5.1. Modeled event assumes a 4 September 1899 subduction rupture along the Yakutat-North America décollement with a M_w of 8.1. Modeled fault geometries (green) are simplified from surficial fault traces compiled for this study (black dashed). Subsurface fault planes (red outline, stippled interior) are based on parameters used by Elliott et al. (2010, 2013). Although this is our preferred model, slightly varying fault geometries consistently yield increased stress loading at the edges of 4 September rupture patch. FFZ – Foreland Fault Zone. EC – Esker Creek Fault. FF – Fairweather Fault. BF – Boundary Fault. YF – Yakutat Fault.

5.5 OBSERVATIONS

Our initial goal was to map bay-crossing fault structures associated with the Esker Creek and/or Bancas Point faults, Boundary Fault, Yakutat Fault, and Otmeloi Fault using offshore seismic reflection data. Line 2101 from survey EW9412, which runs down the length of Disenchantment Bay and along the eastern, sediment-filled glacial trough within Yakutat Bay (Fig. 5.4a), does not reveal any evidence of faulting and thus became the basis for the AG0812 survey design (Fig. 5.4b, 4c). Unexpectedly, none of the processed AG0812 data reveal any deep-seated, continuous, or deformational fault structures offsetting sediments within the upper several 100 m (Fig. 5.4b, 4c), despite crossing offshore fault structures proposed by Plafker and Thatcher (2008). Given onshore evidence for proposed faults (e.g. Elliott et al., 2010; Bruhn et al., 2012; Elliott et al., 2013), we would expect to see evidence for deep-seated and long-term deformation manifested as fold-and-thrust systems, growth strata, deformed mélange, and continuous, regionally-mappable, and linear or curvilinear fault geometries – none of which we observe in the MCS data.

Glacial sequences, erosional glacial channels, and chaotic moraine deposits dominate the stratigraphy throughout Yakutat and Disenchantment bays (Fig. 5.4), making it difficult in some areas to interpret tectonic features (an interpretation of glacial stratigraphy can be found in Zurbuchen et al., 2015). Therefore, it is possible that there are deeper blind thrusts, faults beneath glaciers, or faults within seismically-reflective glacial moraine deposits. We contend, however, that continuous offshore faults would inevitably cut across flat-lying glacial retreat sequences, which are abundant in the center of Yakutat and Disenchantment bays. Faulting-related offsets of seismic reflectors should be apparent in flat-lying sequences, especially in high-resolution data (Fig. 5.4). The AG0812 MCS data have a vertical resolution of 1-2 m and sedimentation rates in the bays are very high

(up to ~1 m/yr) due to the presence of the Hubbard tidewater glacier (Cowan et al., 1996; Goff et al., 2012). This rapid sediment accumulation provides a high-resolution sedimentary succession which, when coupled with the AG0812 high-resolution data, provides a subsurface record capable of resolving seismic reflectors with nearly annual temporal resolution. Given the high sedimentation rates, active faults may not necessarily reach the seafloor, but there should be clear evidence for long-term offset and/or growth strata in the subsurface, especially if any such faults ruptured in 1899.

The 1892 bathymetric sounding data provide a unique opportunity to examine and compare the offshore bathymetric expression prior to the historical 1899 earthquake events. The difference between the 1892 sounding and the Goff et al. (2012) merged bathymetry (Fig. 5.2c) reveals values ranging from -183 to 137 m, with negative values indicating subsidence or erosion and positive values indicating uplift or deposition. Regional patterns include a cluster of low values within a glacially carved channel, high values near Knight Island in southeastern Yakutat Bay, and generally higher values nearer to Hubbard Glacier's calving front. Low values in the channel might be attributed to the difficulty of older data to detect steep slopes, and high values near Knight Island are likely similarly anomalous due to the presence of land and/or mismatch between datasets. Other positive values are well within range of sedimentation in the bays over the last century, as we'd expect up to ~100 m of deposition since 1892. There are otherwise no regionally observable or linear trends in the differenced bathymetry data that might indicate offshore or bay-crossing faults, so differences therefore appear to be geomorphic and are not considered in our tectonic interpretations.

Lack of evidence for faults crossing Yakutat and Disenchantment bays led us to re-visit geologic uplift measurements measured by Tarr and Martin (1912) and Plafker and Thatcher (2008) (Fig. 5.2a, Table 5.1) and assess possible sources of error in these

measurements. In comparing the two datasets, several Plafker and Thatcher (2008) values, measured in ~1980, nearly exactly match Tarr and Martin (1912)'s values measured in 1905, where others are ~1-3 m higher. There is no appreciable geographic pattern indicating systematic error in the 1980 data. GIA uplift of 2-3 cm/yr gives insight into the uncertainty of Plafker and Thatcher (2008)'s measurements. We would expect all the 1980 measurements to be on the order of ~1-2 m higher than the 1905 measurements due to glacial unloading (Elliott et al., 2010; Table 5.1). We include GIA uncertainty in our calculations of 1-3 m total uncertainty on Plafker and Thatcher (2008)'s measurements (Table 5.1). Uncertainty of 1-3 m is significant especially in less-uplifted areas along Logan Beach and Russell Fiord. In light of these dataset comparisons and the general difficulty of measuring paleoseismic slip, particularly ~80 years later, we generally rely more heavily on the original measurements of Tarr and Martin (1912) as a truer indicator of 1899 coseismic motion.

5.5.1 Bancas Point (Esker Creek and Bancas Point faults)

Bancas Point is the site of the maximum 14.4 m of measured uplift interpreted to be coseismic with the 10 September 1899 event (Tarr and Martin, 1912; Fig. 5.2a, Table 5.1). The Esker Creek and Bancas Point faults run along the coastline of Disenchantment Bay north of Bancas Point, and are traceable as linear features at the hinges of a major topography change along the range front of the St. Elias Mountains (Fig. 5.1). Additionally, a deflection in a tongue of glacial ice near the head of Malaspina Glacier supports that the geometry of the fault is at or near the range front and beneath the glacial ice on land (Cotton et al., 2014). Some maps have inferred that the Esker Creek Fault continues to the east, crossing Yakutat Bay to connect with the Yakutat Fault south of Russell Fiord (Plafker and Thatcher, 2008). The AG0812 MCS data, however, do not indicate any evidence for major

thrust systems crossing Yakutat or Disenchantment bays (Figs. 5.4b, 5.4c). Given onshore observations of the Esker Creek system and the lack of faults crossing Yakutat Bay, we assume that the Esker Creek and/or Bancas Point faults exist entirely on land or very near the coastline.

The Esker Creek and Bancas Point faults appear to be active thrusts accommodating significant motion, as evidenced by 10.3-14.4 m of uplift during the 10 September 1899 event (Tarr and Martin, 1912). Evidence for this uplift includes a raised shoreline and sea cliff as well as dead, uplifted barnacles measured in 1905 (Tarr and Martin, 1912). Plafker and Thatcher (2008) corroborate the uplift at Bancas Point in ~1980, also measuring up to 14.4 m of uplift at several locations along Bancas Point (Fig. 5.2a, Table 5.1). The magnitude of the uplift and the presence of abundant dead barnacles in Tarr and Martin's 1905 dataset indicates a reliable measure of rapid uplift. Tarr and Martin (1912) observed dead barnacles at 80% of uplifted sites measured, and estimate the error on these sites to be no more than ~0.3 meters (Table 5.1). Additionally, GPS and thermochronology data support significant convergence and exhumation along the Esker Creek system, results which are consistent with rapid uplift during earthquake events (Elliott et al., 2013; Enkelmann et al., 2015).

5.5.2 Logan Beach (Yakutat Fault)

Plafker and Thatcher (2008) mapped the Yakutat Fault as a northwest-striking, shallowly dipping thrust fault running along Logan Beach, which represents a ~20 km stretch of coastline in southeastern Yakutat Bay, connecting across the Bay to the Esker Creek Fault (Fig. 5.2a). Despite expectations, we see no evidence for the Yakutat Fault offshore in AG0812 seismic data (Figs. 5.4b, 5.4c), so we return again to geologic uplift measurements. In 1905, Tarr and Martin measured little to no uplift along Logan Beach

except at Point Latouche, and even measured subsidence in some areas (Fig. 5.2a, Table 5.1). Upon revisiting the Tarr and Martin sites, Plafker and Thatcher (2008) observed ~3-5 m of uplift along the length of Logan Beach, re-classifying subsidence recorded by Tarr and Martin as non-tectonic slumping. Plafker and Thatcher (2008) also observed a linear near-shore "scarp" visible along Logan Beach from the air, now overgrown by trees. Below the "scarp" (and nearest the shore), all trees have been dated post-1899, suggesting rapid uplift of the beach and subsequent growth of the trees along the uplifted shore (Plafker and Thatcher, 2008).

Logan Beach is one area where Plafker and Thatcher (2008)'s measurements are significantly higher than those of Tarr and Martin (1912), some of which can be explained by GIA. We would expect ~2 m of GIA-related uplift to accumulate between measurements in 1905 and 1980 along Logan Beach (Table 5.1). GIA could account for ~half of the measured uplift at Plafker and Thatcher (2008) sites along Logan Beach. When including GIA in uncertainty estimates, we find that there may have been as little as ~0.3-2.8 m of actual coseismic or postseismic uplift along Logan Beach in 1899 (Table 5.1).

GPS and thermochronology data indicate that the Yakutat Fault is a steeply dipping reverse fault, which is different than Plafker and Thatcher (2008)'s shallowly dipping model. GPS data predicts an average of 0.5 ± 1.6 mm/yr of left-lateral strike-slip and 4.7 ± 0.9 mm/yr of convergence across the Yakutat Fault (modeled as the Foothills Fault; Elliott et al., 2010), which, as modeled, would be a thrust fault running along the coast of Logan Beach. Thermochronology indicates uplift of 2-3 mm/yr north of the Yakutat Fault, approaching rates of 3-5 mm/yr along the subduction-related Esker Creek Fault (Enkelmann et al., 2015), again supporting steeper thrust motion.

5.5.3 Russell Fiord (Boundary Fault)

The Boundary Fault has been mapped as a transpressive fault subparallel to the Fairweather Fault running through Russell Fiord (e.g. Plafker and Thatcher, 2008; Fig. 5.1). Morphologically, the Boundary Fault expression is as a linear-shaped fjord which continues to the southeast, which is evident in valley topography through the Fairweather Range (the southernmost range of the St. Elias Mountains) just south of Russell Fiord (Figs. 5.1, 5.2a). The Boundary Fault was imaged in a 2010 CHIRP line which crosses Russell Fiord orthogonally (Fig. 5.4d). Evidence for the Boundary Fault includes a notched seafloor and some potential growth strata in the shallow sediments (Fig. 5.4d), though the subsurface is difficult to interpret due to seismic artifacts. Sedimentation rates in Russell Fiord, though not quantified directly, are presumably lower than in Disenchantment Bay given the substantially lower amount of sediment in Russell Fiord (Fig. 5.4d). Lower sedimentation rates allow for better preservation of long-term tectonic deformation at or near the seafloor due to tectonic structures remaining less buried, so near-surface features could indicate tectonic deformation rather than sedimentary processes.

Tarr and Martin (1912) originally measured minor uplift in Russell Fiord, on the scale of ~0.5-2 m, with Plafker and Thatcher (2008) measuring similar values (Fig. 5.2a). In southern Russell Fiord, both Tarr and Martin and Plafker and Thatcher measured generally higher uplift values in the ~2-3 m range. Uplift values would suggest some amount of thrusting, but GPS modeling (Elliott et al., 2010) fits the Boundary Fault as a near-vertical fault with of 3.6 ± 1.4 mm/yr right-lateral strike-slip and 2.2 ± 1.5 mm/yr of convergence across it. The best-fit GPS model is significantly different than Plafker and Thatcher's original structural model, in which the Boundary Fault is a shallowly dipping thrust. Thermochronology data measure <1.5 mm/yr of exhumation along the Boundary Fault, around half that observed along the Yakutat Fault (Enkelmann et al., 2015).

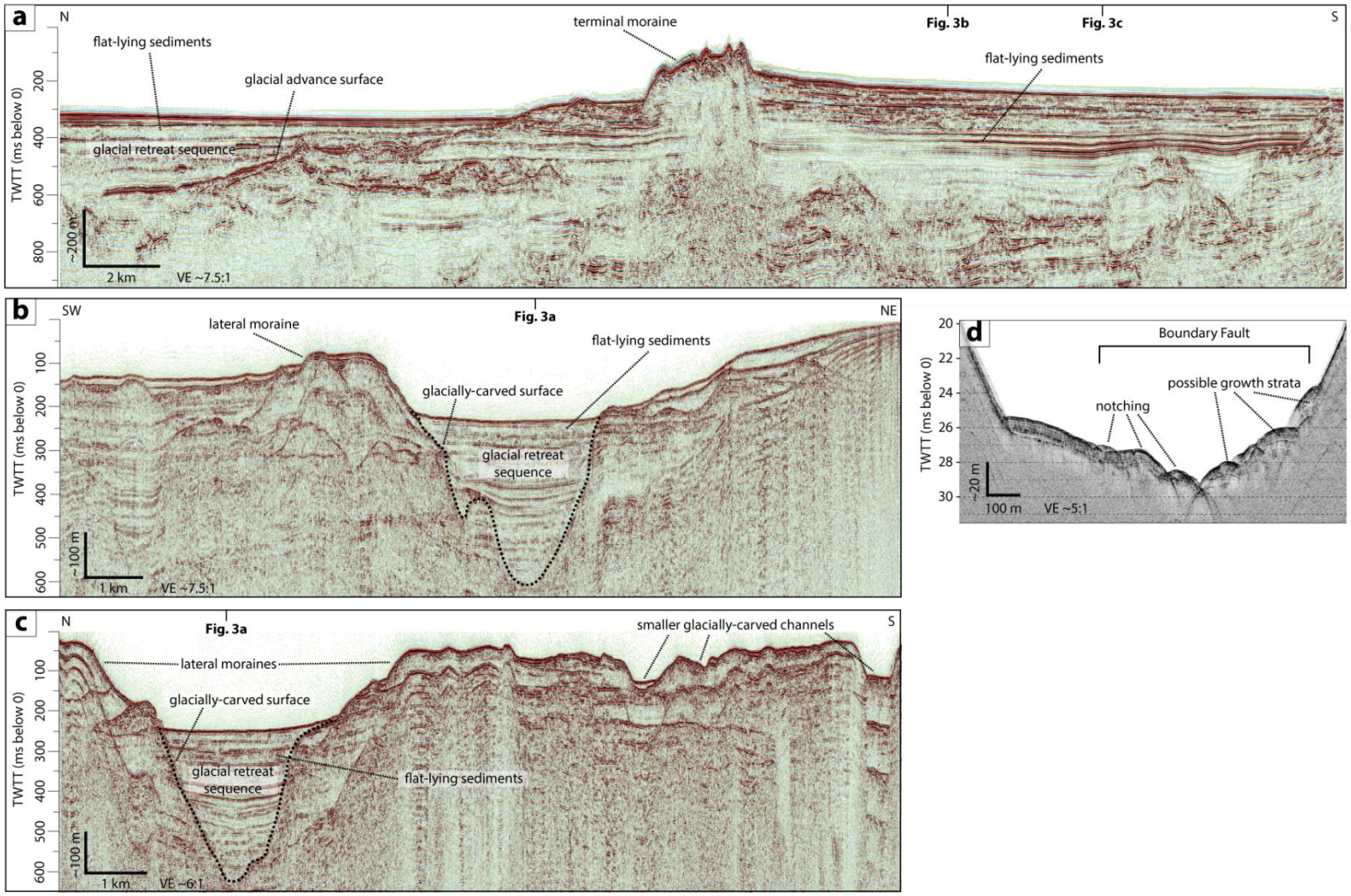

Figure 5.4. Four representative seismic profiles. See profile locations in Fig. 5.2c.

(a) Line 2101 from survey EW0408. The section exhibits glacial stratigraphy of a recent Hubbard Glacier advance and retreat but no major fault systems. (b) and (c) Profiles from survey AG0812 crossing locations of offshore faults proposed by Plafker and Thatcher (2008). Glacial deposits are observed, but again no major fault systems. (d) CHIRP profile from a 2010 R/V *Quest* survey crossing Russell Fiord, providing an image of the Boundary Fault.

5.5.4 Coulomb models

We model the 4 September 1899 event as slip along the Yakutat-North America décollement with geometric parameters chosen to be consistent with previously published values (Doser, 2006; Elliott et al., 2013). Even with iterations of several geometries, models consistently indicate stress loading at the edges of the 4 September rupture patch (Fig. 5.3). The largest stress change occurs on the northeast side of the rupture, well within the Yakutat-North America subduction zone and downdip of the Esker Creek and Chaix Hills systems (Fig. 5.3). These results are consistent with Coulomb models described in Cotton et al. (2014).

5.6 DISCUSSION

Our observations lead to an updated, simplified map of fault geometry in Yakutat Bay (Fig. 5.5), an improved conceptual structural model, and a refined understanding of how local fault structures relate to the 1899 events. The updated map (Fig. 5.5) represents our best understanding of fault geometry local to Yakutat Bay given this compilation of new and previously acquired geophysical data, and is consistent with recent studies (Elliott et al., 2013; Cotton et al., 2014; Enkelmann et al., 2015). We have also compiled our observations with those of previous studies into a table (Table 5.2) and conclude which structures we believe to be active and potentially important for the 1899 events and future geohazard assessment.

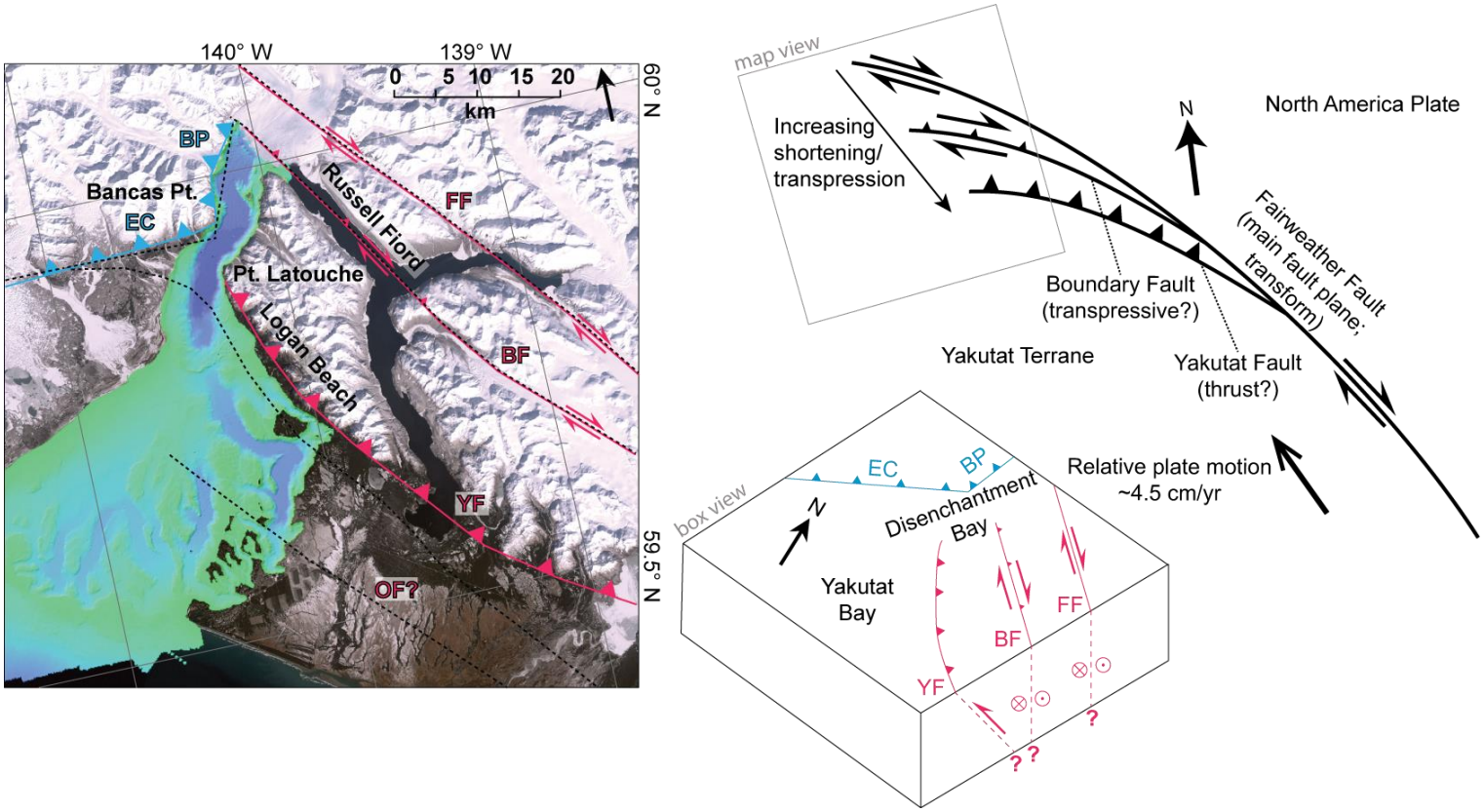

Figure 5.5. Final fault geometry map and conceptual structural models for the Yakutat Bay region. Map (left) includes fault traces compiled and mapped in this study (color) alongside original Plafker and Thatcher traces (black dash). Map area and background imagery are similar to those of Fig. 5.2. Block diagram indicates proposed subsurface fault geometry on the southeastern side of Yakutat and Disenchantment bays. Upper right schematic diagram indicates a cartoon of proposed kinematics for a strain-partitioning, transpressional horsetail splay structure associated with the termination of the Fairweather strike-slip fault. BP – Bancas Point Fault. EC – Esker Creek Fault. FF – Fairweather Fault. BF – Boundary Fault. YF – Yakutat Fault. OF – Otmeloi Fault.

Fault	Constrained by/rationale for displacement	References
Fairweather transform	M7.9 event of 1958	Doser (2010)
	Geodetic modeling	***Elliott et al. (2010)***
	Offshore seismic crossings	***Gulick et al. (2007)***
	Topographic expression	***See Fig. 5***
Boundary transform (?)	Uplift measured following M8.2 event of 10 Sept 1899	Plafker and Thatcher (2008)
	Exhumation rates from thermochronology	***Enkelmann et al. (2015)***
	Geodetic modeling	***Elliott et al. (2010)***
	Imaged in 2010 CHIRP data	***See Fig. 4d***
	Topographic expression	***See Fig. 5***
Yakutat oblique thrust (?)	Uplift measured following M8.2 event of 10 Sept 1899	Tarr and Martin (1912); Plafker and Thatcher (2008)
	Exhumation rates from thermochronology	***Enkelmann et al. (2015)***
~~Otmeloi thrust~~	~~Deformation following M8.2 event of 10 Sept 1899~~	~~Tarr and Martin (1912);~~ ~~Plafker and Thatcher (2008)~~
	Little to no reliable evidence observed	
Esker Creek and Bancas Pt. thrusts	M8.1 event on 10 Sept 1899 caused a linear north-south shoreline, as well as ~10m (Esker) and ~9m (Bancas) uplift across Disenchantment Bay coseismic with the 10 Sept 1899 event	Plafker and Thatcher (2008)
	Dextral offset subglacier drainage valley	Cotton et al. (2014)
Foreland Fault Zone	Geodetic modeling	Elliott et al. (2013)
	Uplift of a beach berm ca. 1899 (tentative correlation)	Bruhn and Shennan (personal commun.)
Malaspina Fault	Geodetic modeling	Elliott et al. (2013)
	Aftershocks of M7.4 Saint Elias earthquake of 1972	Savage et al. (1986); Estabrook et al. (1992)
	Offshore seismic crossings	***Worthington et al. (2010)***

Table 5.2. Quaternary faults in the Yakutat Bay region and rationale for historical displacement. Table has been modified from Bruhn et al. (2012). Bold italics indicate data or lines of evidence added, compiled, and considered during this study. Strikethrough indicates lack of constraints.

5.6.1 Fault geometry and structure

All lines of evidence suggest that fault systems on the northwestern side of Yakutat Bay are onshore, active, and steeply dipping thrusts accommodating convergence similar to rates experienced by other areas of the Yakutat subduction system. As we do not observe the Esker Creek, Bancas Point, and Chaix Hills thrust systems offshore in Yakutat Bay, we presume they are primarily onshore near the bay, connecting with the offshore Yakutat-North America subduction zone via the Foreland Fault Zone and/or Malaspina Fault. GPS modeling supports thrust motion across the offshore Malaspina Fault and Foreland Fault Zone, indicating ~37 mm/yr of contractional stress across the zone with each fault accommodating convergence of up to ~15 mm/yr (Elliott et al., 2013). This stress must somehow transfer onshore to Yakutat Bay, as recent thermochronology data support rapid exhumation (3-5 mm/yr) along the Esker Creek and Chaix Hills faults (Enkelmann et al., 2015). We infer the Esker Creek Fault's onshore presence at a topographic hinge, which also suggests significant thrust motion (Fig. 5.5). Geologic measurements along the Esker Creek and Bancas Point faults more local to Yakutat Bay (Tarr and Martin, 1912; Plafker and Thatcher, 2008) also exhibit compelling evidence for rapid and significant coseismic uplift with the 10 September 1899 event (Table 5.1). Although likely connected to the Yakutat subduction system, the Esker Creek and Bancas Point faults might be better identified as thin-skinned faults associated with terrane accretion rather than subduction (Chapman et al., 2012); regardless, they appear to relate to and partially accommodate Yakutat Terrane motion. Our results are consistent with extensive geologic mapping by Chapman et al. (2012) which supports the Esker Creek and Chaix Hills faults as major onshore thrust systems; we do not modify these results aside from contributing new observations that the Esker Creek and Chaix Hills systems likely exist exclusively onshore.

In southeastern Yakutat Bay, the Fairweather Fault has a clear topographic signature (Fig. 5.5) and a fairly straightforward ~44 mm/yr of dextral strike-slip offset (Elliott et al., 2010). Combined observations suggest an oblique, strike-slip Boundary Fault with some coseismic or postseismic slip in 1899. The Boundary Fault, like the Fairweather Fault, has a clear topographic signature (Fig. 5.5), but lacks the major elevation change observed along the Esker Creek and Yakutat thrusts. CHIRP data support the presence of the Boundary Fault within Russell Fiord (Fig. 5.4d), but the data do not constrain the dip or sense of motion across the fault. Tarr and Martin (1912) uplift measurements show ~0.5-2.7 m of rapid uplift following the 1899 events in upper Russell Fiord, suggesting a thrust fault running through Russell Fiord with a hanging wall to the northeast (Fig. 5.2a, Table 5.1). Thermochronology data (Enkelmann et al., 2015) indicate lower rates of exhumation (<1.5 mm/yr) across the Boundary Fault than across the Yakutat and Esker Creek faults, suggesting a smaller thrust component. In GPS models, the Boundary Fault has a near-vertical dip and accommodates oblique, though primarily dextral, motion (Elliott et al., 2010).

The Yakutat Fault is more likely a steeply dipping thrust fault running along the range front from southern Russell Fiord and along Logan Beach (Fig. 5.5), entirely onshore or near-shore as we do not observe any evidence for the Yakutat Fault offshore. The Yakutat Fault is modeled as a vertical plane in GPS models, but it is almost completely convergent, suggesting reverse motion (Elliott et al., 2010). Thermochronology data support more rapid exhumation along the Yakutat Fault (2-3 mm/yr) than along the Boundary Fault, again supporting a thrust interpretation (Enkelmann et al., 2015). Both Tarr and Martin (1912) and Plafker and Thatcher (2008) note uplift (2.2-3.2 m) at southern Russell Fiord (Fig. 5.2a, Table 5.1), which would be affected by motion on a northeast-dipping Yakutat Fault. Interestingly, Tarr and Martin (1912) observe little to no uplift along

central Logan Beach, which disagrees with Plafker and Thatcher (2008)'s data (Table 5.1). The sandy Logan Beach shoreline is surely much more difficult to measure than the rocky coastlines of Bancas Point featuring plenty of exposed barnacles, perhaps affecting Tarr and Martin (1912)'s measurements. The delineation Plafker and Thatcher (2008) observe in onshore trees along Logan Beach, beneath which exist only trees younger than 1899, is a strong piece of evidence suggesting at least some amount of rapid uplift around 1899. Plafker and Thatcher (2008)'s values still exhibit relatively large uncertainty due to GIA, so we propose that there were smaller amounts (~2 m) of coseismic or postseismic motion in southeastern Yakutat Bay along the Yakutat Fault around the time of the 1899 events.

The Otmeloi Fault, the final fault along the southeastern side of Yakutat Bay proposed by Plafker and Thatcher (2008), has no obvious topographic signature and the only reported uplift data is well within the uncertainty caused by GIA. The Otmeloi Fault is also not required to fit GPS models (Elliott et al., 2010), and thermochronology data do not indicate any tectonic deformation along the inferred Otmeloi Fault trace (Enkelmann et al., 2015). Therefore, we suggest that the Otmeloi Fault does not exist (Table 5.2).

In general, geophysical data support the existence of significant strike-slip motion along the Fairweather Fault, transpression along the Boundary Fault, and convergence along the Yakutat Fault. The Fairweather Fault terminates just northwest of Yakutat Bay, and strike-slip systems commonly exhibit interesting and often complex splay behavior at their endpoints (e.g. Woodcock and Fischer, 1986; Cunningham and Mann, 2007). Given our combined observations, we suggest that the termination of the Fairweather Fault is accompanied by regional-scale strike-slip transpression similar to a horsetail structure (e.g. Woodcock and Fisher, 1986; Cunningham and Mann, 2007), also similar to the one-sided flower structure described by Enkelmann et al. (2015). In this conceptual model, the Boundary and Yakutat faults are splays of the Fairweather Fault, accommodating

increasing transpression moving southward in a strain-partitioning fashion. Thus, in our model, the Fairweather Fault is a vertical strike-slip fault with purely strike-slip motion, the Boundary Fault is vertical or near-vertical transpressional splay, and the Yakutat Fault is a northeast-dipping high-angle thrust accommodating convergence (Fig. 5.5).

5.6.2 Relevance for 1899 events

We have developed an updated fault model of Yakutat Bay using offshore seismic observations and integration with other geophysical datasets (Fig. 5.5). So how then does can this model assist with our understanding of the 1899 events and future hazard? Can we understand which faults likely slipped coseismically with the 10 September event? Can our fault model help us understand rupture dynamics and future geohazards? We now have an improved tectonic framework with which to approach these problems.

If the earlier 4 September 1899 event was indeed related to subduction of the Yakutat Terrane and ruptured faults within the offshore Pamplona Zone faults and/or the Yakutat décollement, it may have loaded onshore faults related to the same subduction system (e.g. Malaspina, Esker Creek). We test this hypothesis with a simplified Coulomb model of the 4 September 1899 event (Fig. 5.3). The Coulomb model indicates elevated stress at the edges of the 4 September rupture patch, particularly at the northeast edge closest to the Esker Creek system (Fig. 5.3), suggesting loading of the Yakutat-North America interface near Yakutat Bay following the 4 September event. Results suggest the 10 September 1899 event was a Yakutat subduction event, perhaps originating on a deeper thrust or the décollement itself with stress transferring to Yakutat Bay via the Malaspina Fault and/or Foreland Fault Zone systems. Deeper slip might have propagated to the surface along the steeper Esker Creek and/or Bancas Point faults, causing ~14 m of coseismic uplift and a ~6 m tsunami.

The Bancas Point Fault featured the largest slip during the 10 September 1899 event, but smaller amounts of slip (~0.5-4 m) on the southeastern side of the bays appears to be legitimate. The 4 September Coulomb model does not indicate stress loading on the southeast side of the bays. Therefore, the 10 September event was likely primarily responsible for loading or simultaneously rupturing the southeastern faults (namely the Yakutat and Boundary faults). It is possible that the 10 September 1899 event was a multi-fault rupture, or that faults on the southeast side of Yakutat Bay (e.g. Boundary, Yakutat faults) slipped post-seismically due to stress loading by movement on the Esker Creek and/or Bancas Point thrusts. Lack of relatively large events following the 10 September event in the historical record may favor a multi-fault rupture model for the 10 September event.

The magnitudes of the main 1899 events – M_w 8.1 and 8.2, respectively – are quite large, but within the range of large subduction events (e.g. Ammon et al., 2005; Hayes, 2011). The 14.4 m of coseismic uplift, however, is the largest ever measured. The 10 September 1899 event would require smaller slip over a large area or larger slip or a smaller area to achieve an 8.2 magnitude (e.g. Wells and Coppersmith, 1994). 14.4 m is likely a minimum estimate of slip as it was observed as uplift on the surface. Even if the 14.4 m is a maximum slip, though, it would be large enough to generate a magnitude 8+ event (Wells and Coppersmith, 1994). The observed 14.4 m of slip may thus imply the 10 September event slipped a larger amount over a smaller area to generate the M_w 8.2 earthquake. The 14.4 m of uplift on the surface also suggests that the 10 September event likely featured shallow locked faults, allowing for a velocity-weakening rupture and for slip to accelerate as it propagated to the surface. Updip-accelerating slip also occurred along Japan Trench during the Tohoku-Oki event of 2011 (e.g. Ammon et al., 2011; Hayes, 2011).

There is significant risk of 1899 earthquake recurrence in the near future. If we assume convergence of ~37 mm/yr across the deformation front from GPS models (Elliott et al., 2013), over 4 m of stress has accumulated since 1899 – enough to cause a magnitude 6.5+ event (Wells and Coppersmith, 1994). Additionally, the 1899 events may not have achieved a total stress drop, so there may be even more than 4 m accumulated stress. The last recorded Yakutat subduction event was ~900 years ago (Shennan et al., 2009). Assuming 37 mm/yr of constant stress accumulation since 900 years ago, there would have been ~30 m of built-up stress by 1899. The 10 September 1899 event may have slipped 14.4 m of that built-up stress, meaning there could be as much as ~15 m of stress left over. Adding this to the ~4 m of stress that has built up since 1899, the Yakutat-North America plate boundary could be poised to slip as much as ~19 m, potentially leading to a magnitude 7+ 1899-type earthquake (Wells and Coppersmith, 1994).

Multiple lines of evidence support the existence of major Yakutat Bay fault systems completely onshore, near-shore, or as blind thrusts. In that case, then, why was there such a big tsunami? Eyewitnesses reported a tsunami with ~6 m wave height at the base of Hubbard Glacier, and field observations support up to 12 m of tsunami runup (Tarr and Martin, 1912). Effects of the tsunami may have stretched beyond Yakutat Bay along the coast of western North America, with possible seiching as far south as Lake Chelan, Washington (Coffman et al., 1982). This tsunami, then, may have been a fairly significant event, though regional evidence for the tsunami is quite limited; it is also possible that this was a local event, perhaps in that case due to the submarine landslide/slumping events noted by Plafker and Thatcher (2008) and originally misinterpreted by Tarr and Martin (1912) as tectonic subsidence. Our preferred hypothesis, however, is that the tsunami was generated by simply uplifting the coast, which may have caused sufficient water

displacement, or that coseismic slip on deepwater thrust systems (like the Malaspina Fault or Foreland Fault Zone) generated the tsunami.

There are many remaining questions, especially related to current hazard in Yakutat Bay. More data are required to adequately understand and map local thrust fault systems. An obvious target is to examine the onshore-offshore connections between the offshore Malaspina Fault and Foreland Fault Zone systems and the onshore Esker Creek Fault. Understanding the geometry, character, and recent offsets along the Malaspina Fault and Foreland Fault Zone will assist with linking offshore deformation structures related to subduction to onshore-offshore structures in and around Yakutat and Icy Bay, thus improving understanding of the possibility of recurrence of an 1899-type event.

5.7 CONCLUSIONS

1) We quantify error on interpreted coseismic uplift measurements for the Plafker and Thatcher (2008) dataset, finding between 1-3 m of estimated uncertainty. Uplift related to GIA may have influenced some measurements by Plafker and Thatcher (2008), and therefore we rely more heavily on the 1905 measurements taken by Tarr and Martin (1912) to inform our interpretations
2) There are no major active fault systems located crossing Yakutat Bay; this finding suggests that the Esker Creek, Bancas Point, and Yakutat faults exist entirely onshore, near-shore, or are blind thrusts. We provide an updated map of fault geometry based primarily on evidence from seismic reflection and topographic changes.
3) Dextral transpression likely dominates in southeastern Yakutat Bay with a strain-partitioning, horsetail-type termination of the Fairweather strike-slip fault. Convergence dominates in the northwest, where the majority of the 10 September

1899 slip occurred. This finding supports the presence of an eastern structural syntaxis, a transition between Yakutat subduction/collision and Fairweather strike-slip motion.

4) Coulomb modeling of the 4 September 1899 confirms stress changes at the edges of the slip patch, potentially loading the Yakutat-North America interface downdip of the Esker Creek and Chaix Hills faults. This supports a subduction-dominated rupture for the larger 10 September 1899 event, with slip propagating to the surface locally along the Esker Creek and Bancas Point thrusts.
5) Coseismic slip during the 10 Sept 1899 event on the southeast side of the Bay seems to be minimal. The 10 September 1899 event may have been a multi-fault rupture, or slip on the southeast side of the Bay may have been postseismic.

Chapter 6: Conclusions

Scientifically, I am excited by the prospect of studying remote environments, making first-order scientific discoveries, and science with societal relevance. Thus far, my research has focused on regional-scale tectonics and geohazards in offshore environments. I employ the use of geophysical data to study tectonic systems, and have gained expertise in the acquisition, processing, and interpretation of multiple types of marine geophysical data. Aside from my experience with modern data, I am also intrigued by integrating older legacy data with newer data, viewing it with a modern lens. This dissertation presents interpretations of geophysical data new and old and focuses on the Pacific-North America plate boundary offshore of southeast Alaska, a little-studied but highly active transform environment. Here, I address fundamental questions about the Queen Charlotte-Fairweather system from end to end, exploring the geometry, plate boundary architecture, strike-slip kinematics, earthquake hazards, and linked sedimentary systems along strike.

The main conclusion of Chapter 2, which explores the origin and development of the Baranof deep-sea sedimentary fan, is that the southward-migrating channel avulsions are a function of strike-slip motion of the Pacific Plate along the Queen Charlotte Fault (QCF). Chapter 3 hypothesizes that increased convergence along the QCF starting at ~6 Ma may have caused Pacific underthrusting beneath North America and concurrent Pacific downwarping. This downwarping now appears to be inactive, but has been preserved by sedimentary loading. Chapter 4 takes a closer look at the crustal material on either side of the QCF at the site of the 5 January 2013 M_w 7.5 Craig, Alaska earthquake; results suggest that the seismogenic zone is deeper than usual for a continental boundary and support a contrast of cold, seismically-fast North American crust with warmer, weaker Pacific crust across the QCF. Chapter 5 examines the northern continuation of the QCF and Fairweather

Fault (FF) transform system near Yakutat Bay, at the site of the M_w 8.2 earthquake of 10 September 1899. Chapter 5 shows that the southeast side of Yakutat Bay is dominated by transpressional strike-slip and supports a Yakutat subduction model for the two largest 1899 events.

The work presented in this dissertation provides answers to key questions about the nature of the southeast Alaska transform plate boundary at many locations along strike, characterizing the nature of the crust, seismicity, and coupling with other regional tectonic and sedimentary systems. My results add to overall understanding of the local QCF and FF systems and to strike-slip systems in general, and are relevant to geohazard and resource assessment. Maps and products from these chapters are being integrated into regional fault maps (the Quaternary Fault and Fold database; Appendix I), which will assist in hazard prediction and mitigation regionally, and have contributed to the U.S. Extended Continental Shelf (ECS) Project (e.g. Appendix J). Chapters 2 and 3 have been published in peer-reviewed literature, contributing to interdisciplinary scientific discussion on earthquake hazards in southeast Alaska, with plans to publish chapters 4 and 5.

I have chosen to study Alaska tectonics because of the dynamic systems that exist there, and because of the exciting possibility of new discovery. The QCF-FF system, in particular, is an ideal location for first-order science due to its remote, largely offshore location, limited population centers, and propensity to rupture in large earthquakes. The offshore QCF is often simplified and depicted as a single fault strand accommodating plate motion along western Canada and along southeastern Alaska; this is simply not the case, and my work helps to quantify the QCF's complexity. In this dissertation, for example, I show evidence for seismically active strands related to the QCF and suggest that the crustal rheology along the fault may be different than previously hypothesized. Fault complexity, crustal architecture, and fault geometry are all integral components of earthquake rupture

dynamics; my results can therefore potentially assist with local hazard prediction and understanding of the QCF-FF seismogenic system on the whole.

One thing that stood out to me in the course of my graduate work is the need for new, high-quality geophysical data at all scales over active tectonic systems. This certainly applies in my field area of southeast Alaska, but also among tectonic systems globally. Much of the work I present here is ultimately speculative interpretation or informed hypotheses based on relatively sparse data and/or limited observations; however, even interpretation of sparse data adds new knowledge to the field of tectonics and regional hazard in southeast Alaska today. Still, it is vitally important to continue to collect new, high-resolution, and high-coverage geophysical data over active tectonic systems, which will bring us closer to understanding seismogenic systems in Alaska and worldwide. There is a desperate need in geoscience for improved understanding of regional tectonics, interdisciplinary cooperation and research, and public support of large-scale scientific endeavors. As I begin my career in research, I hope that future public science funding allows for continuous support of in-depth, multidisciplinary study of and data collection over seismogenic systems across the planet.

This dissertation provides a solid foundation on which to propose future local work or continue global study in the broad areas of strike-slip tectonics, geohazards, and large-scale structural and tectonic interpretations. Going forward, I will continue research in geohazards with a funded research expedition to Icy Bay, Alaska where we will collect high-resolution seismic data in an effort to better understand the onshore-offshore connections between the Pamplona deformation front and the Malaspina and Esker Creek thrust systems onshore, which likely slipped during the 1899 earthquakes. From there I will continue to study strike-slip motion and geohazards along the San Andreas Fault system offshore of Los Angeles, California in the California Continental Borderland. Farther down

the road, I also hope to continue research in Alaska; it remains one of the most active, dynamic, and undiscovered regions in the world today.

Appendix A: Summary of seismic reflection surveys

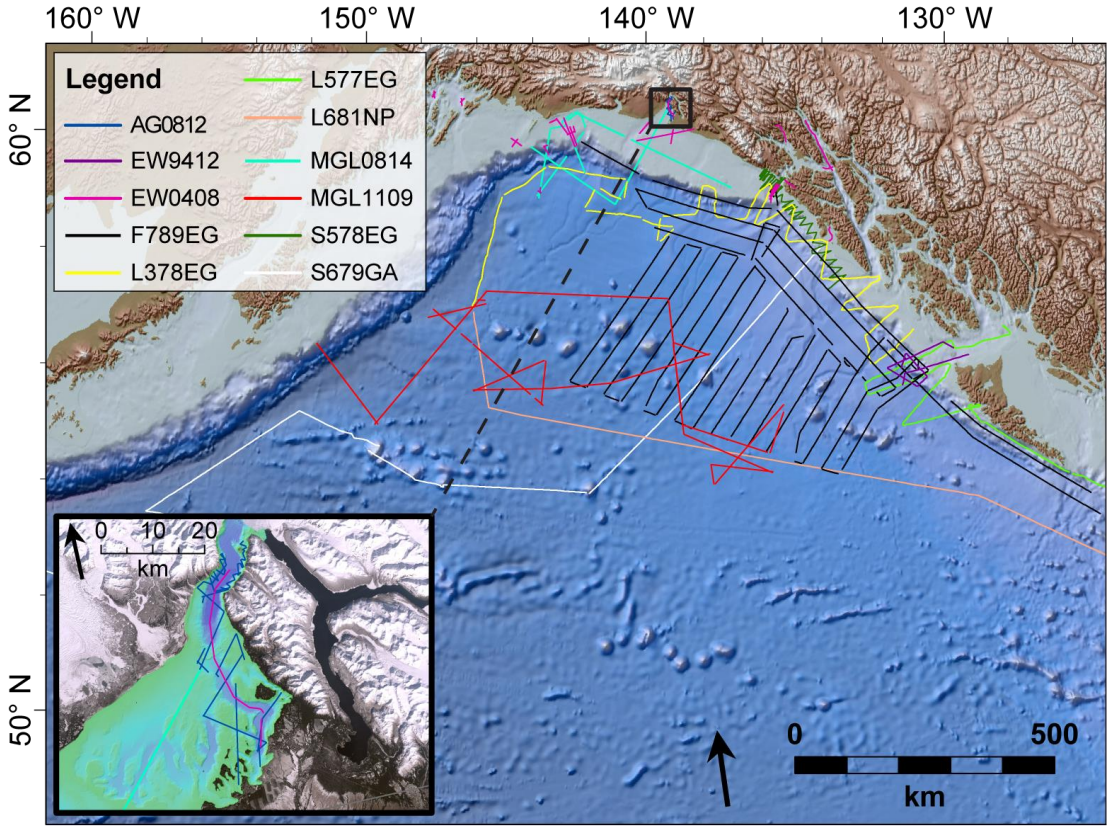

Figure A.1. Map showing 2D seismic reflection surveys used in this dissertation. Inset shows zoom of Yakutat Bay region. Black box on main figure indicates location of inset.

Cruise ID	Year	Vessel	Project	Institution(s)	Chief Scientist(s)
L577EG	1977	R/V *Samuel P. Lee*		USGS	Parke Snavely
L378EG	1978	R/V *Samuel P. Lee*		USGS	Terry Bruns
S578EG	1978	*Sea Sounder*		USGS	George Plafker, Paul Carlson
S679GA, S679NP	1979	*Sea Sounder*		USGS	Bill Menard, Dave Scholl, Tracy Vallier
L681NP	1981	R/V *Samuel P. Lee*		USGS	Andy Stevenson
F789EG, F789GA	1989	M/V *Farnella*	Geological Long-Range Inclined Asdic (GLORIA)	USGS	Terry Bruns, Andy Stevenson
EW9412	1994	R/V *Maurice Ewing*	ACCRETE	LDEO	John Diebold
EW0408	2004	R/V *Maurice Ewing*	IODP site survey	Oregon State Univ., Univ. Florida	Alan Mix, John Jaeger
MGL0814	2008	R/V *Marcus G. Langseth*	ST. Elias Erosion and tectonics Project (STEEP)	UTIG, USGS	Sean Gulick, Gail Christeson
MGL1109, L0911GA	2011	R/V *Marcus G. Langseth*	U.S. Extended Continental Shelf (ECS) Project	UTIG, USGS	Sean Gulick, Ginger Barth
AG0812, 2012-602-FA	2012	R/V *Alaskan Gyre*	National Earthquake Hazards Reduction Program (NEHRP)	UTIG, USGS	Sean Gulick

Table A.1. Details of 2D seismic reflection surveys used in this dissertation.

Appendix B: Summary of MGL1109 processing

This appendix summarizes the basic MCS processing flow used for survey MGL1109 completed at UTIG. Data were processed to post-stack time migration at sea and later improved with velocity analysis at finer intervals, hand-picked mutes, and prestack processing of Line 15. This appendix includes the original at-sea processing cookbook along with representative code and screenshots from final processing steps. MGL1109 data files can be found in /disk/staff/sean/alaska/MGL1109 as of 4/28/2016.

B.1 AT-SEA PROCESSING

Set-up:

- Open Focus
    - pgver epos3
    - focus
- Open project (GOALLOS)
    - Select line (make sure you get the right one!)
    - PID is at the top of session manager
    - Open jobs in production window

1) Get data: AK_segdget.csh line# 1st reel last reel
2) Convert segd format into Focus format: AK_segdin.csh line#
3) Move original .segd files from here: /mnt/focus1_data/SEGD/
   To here: /mnt/focus2_data/segd_completed/
4) Define line geometry: AK_geometry.csh line# 1st shot
5) Initial stack: AK_brutestack.csh line#
    a. Pick seafloor (make sure num/caps locks are off). Pick -> horizons. Event: sf, Attribute: time.

6) Run this: AK_segyout.csh line #
    a. Kill bad channels
7) Deconvolution: AK_decon.csh line #
    a. View data from job (production) window or session manager. Make sure correct line is selected.
    b. To look at bad channels, look at shots file.
    c. Zoom in and find possible bad areas. Press play on “view data window” to check for bad channel consistency or channel noise.
    d. Display -> headers and amplitudes, click header and add “channel.”
    e. Press “play” to cycle through shots and find consistently bad channels.
    f. Make note and edit in job window.
    g. Interactive run (running man) or batch job (red right arrow: submit job)
8) Sort: AK_sort.csh line#
9) Define velocities: AK_veldef.csh line#
    a. Stop sign and display on last step.
    b. Check compute coherency.
    c. Make a pick or two.
    d. Apply NMO.
    e. Parameters -> Global options. Put “Number of Ensembles to use to form Supergather” up to maximum and increase contours.
    f. Functions -> check “Form supergather”
    g. Pick velocities.
    h. As a check, from “Session Manager” under “Tools” click “Velocities” and check the interactive velocity display for flatness.
10) Final stack: AK_velstack.csh line#

11) Migrate: AK_fkmig.csh line#

B.2 GEOMETRY DEFINITION

```
>> LOS_09_marine.dat
*JOB    GOALOS  LOS_09
*CALL   DUMIN
*CALL   MARINE  2336    636     636     176     12.5    50
915
*END
```

B.3 PREPROCESSING AND DECONVOLUTION

```
>> LOS_09_decon.dat
*JOB    GOALOS  LOS_09
*CALL   DSIN
LABEL   LOS_09.shots
*CALL   PROFILE LOS_09  636     6.25    999999          0000636
*CALL   HEADPUT WBT             INTEGER
ATTRI   CDP     TIME    SF      LOS_09  CDP
*CALL   EDIT    shot    chan
SEL     1       99999   KILL
484     608
*CALL   FILTER  shot                    MINIMUM
KEYDEF  1
BAND                41
      15000   3       7       100     125
*CALL   GAIN    SHOT
```

```
SPHDIV 1      0      2
*CALL   STATIC  WBT    REMOVE  -100
*CALL   MCDECON       offset                  ACROSS
11
KEYDEF  1      176    8172
GAP    81           40
100    2100   2200   3600   0      15000  1      15000
*CALL   STATIC  WBT          -100
*CALL   FILTER  shot                   MINIMUM
KEYDEF  1
BAND                41
      15000  3      7      100    125
*CALL   DSOUT   OVERWRT             0      15000
LABEL   dec_LOS_09.shots
*END
```

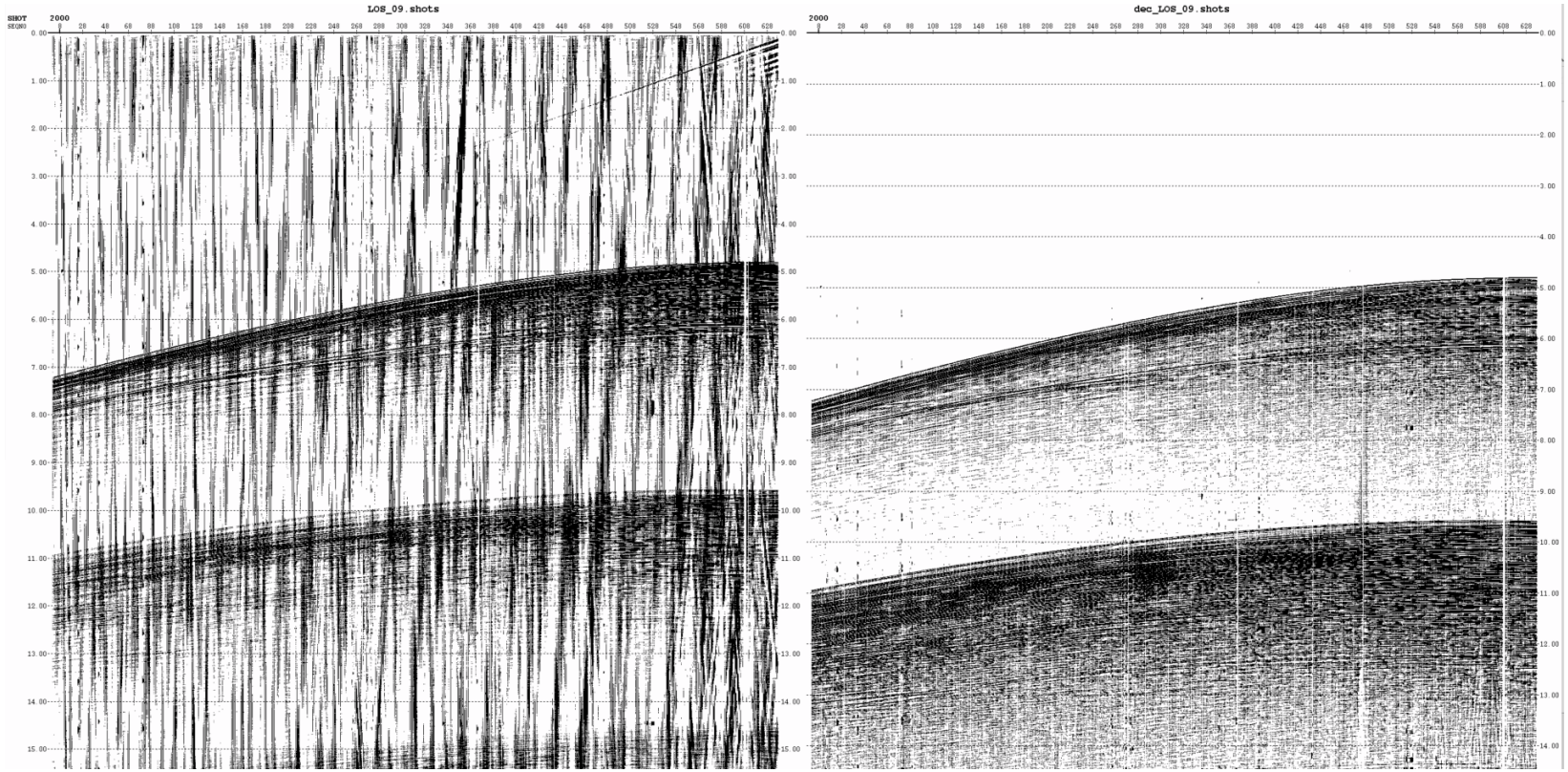

Figure B.1. Shot gather before and after preprocessing (left and right, respectively). Pre-processing includes trace editing, bandpass filtering, spherical divergence correction, and multichannel deconvolution. Vertical axis is in two-way travel time (TWTT).

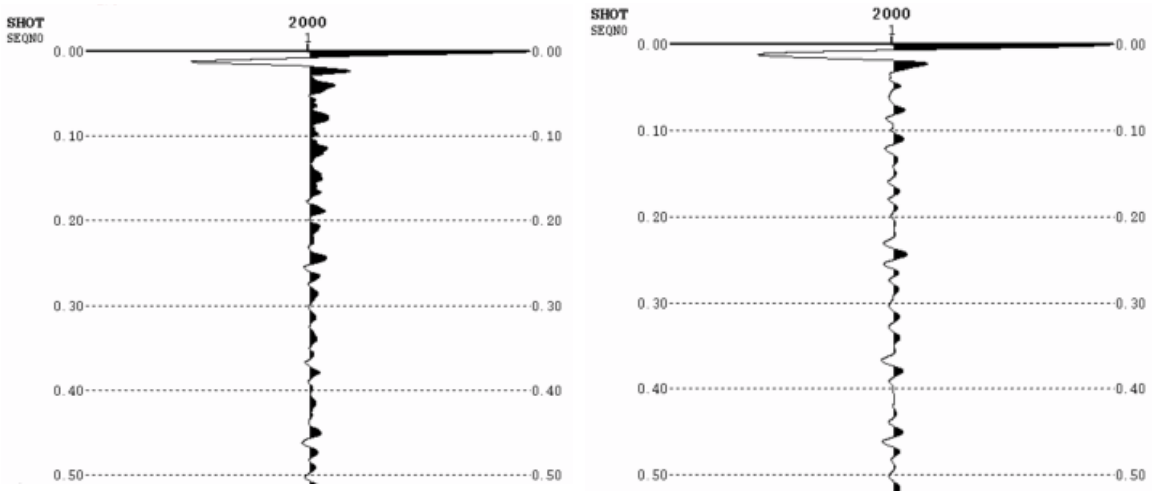

Figure B.2. Auto-correlation function of a shot gather before and after preprocessing and deconvolution (left and right, respectively). Vertical axis is in TWTT.

B.4 VELOCITY ANALYSIS

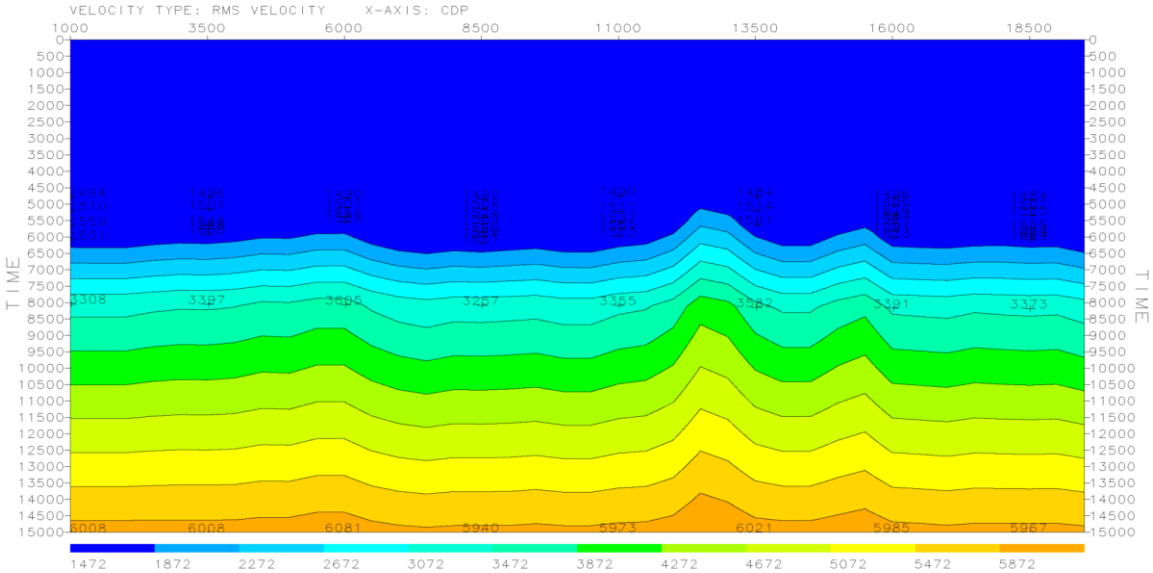

Figure B.3. Root mean square (RMS) velocity model for Line 9. Velocities are in m/s. CDP spacing is 6.25 m.

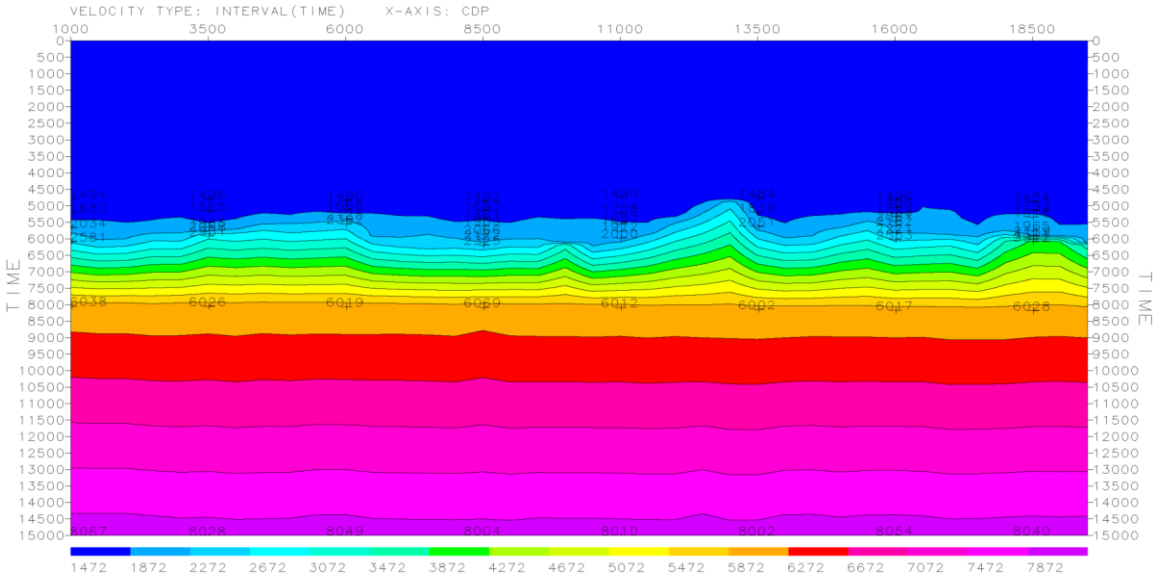

Figure B.4. Interval velocity model for Line 9. Velocities are in m/s. CDP spacing is 6.25 m.

B.5 STACKS

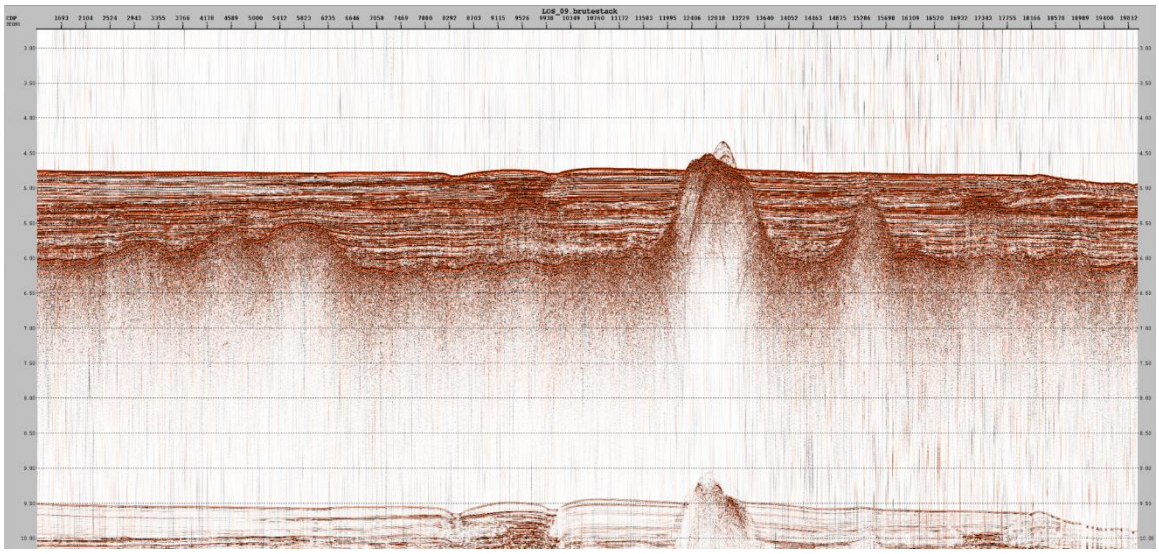

Figure B.5. Brutestack of Line 9 before processing. Vertical axis is in TWTT. CDP spacing is 6.25 m. No automatic gain control (AGC) scaling has been applied in this image.

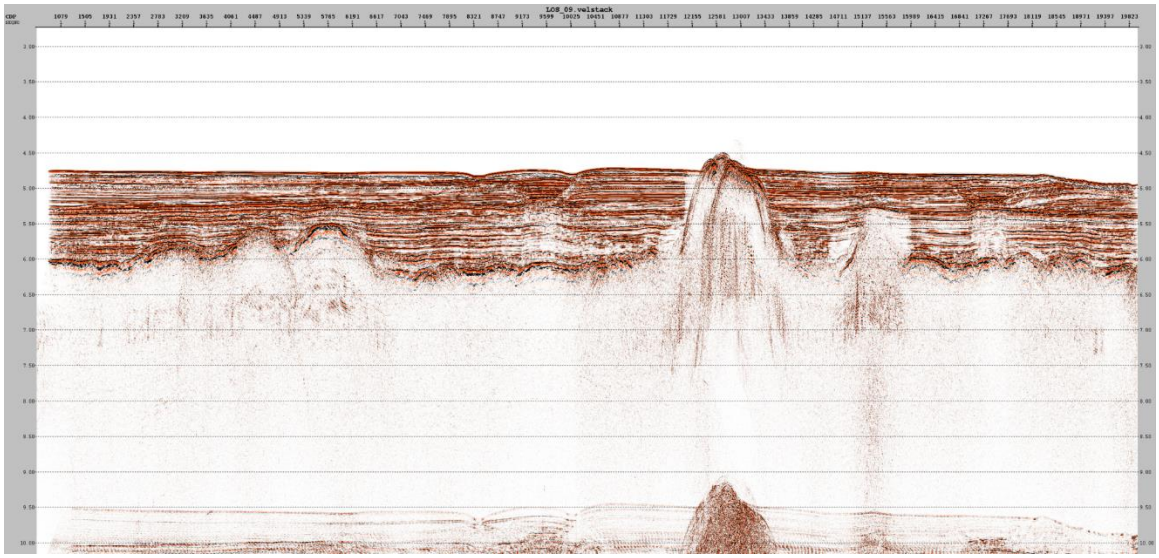

Figure B.6. Stack of Line 9 after preprocessing, sorting, and normal moveout (NMO) correction. Vertical axis is in TWTT. CDP spacing is 6.25 m. No AGC scaling has been applied in this image.

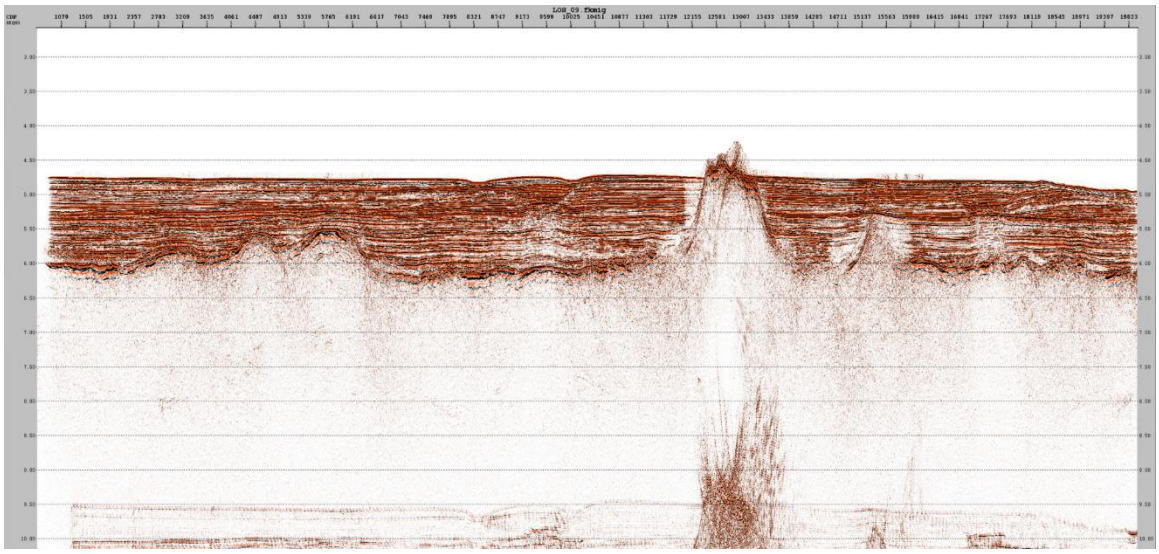

Figure B.7. Poststack time migration of Line 9. Processing features a frequency-wavenumber (FK) migration. Vertical axis is in TWTT. CDP spacing is 6.25 m. No AGC scaling has been applied in this image.

B.6 LINE 15 PRESTACK PROCESSING TEST

After full post-stack processing:

- **Step 1:** Migrate CMP gathers (*note that this job also includes PRADMUS multiple reduction which seems to work well with the other multiple reduction that's been done)
    - JOB: LOS_15_prestack_mal.dat
    - INPUT CDP FILE: dec_LOS_15_supp_smac.cdps
    - VELOCITY MODEL: Use VELRSR surrounding the PRADMUS module and VELSMTH in MIGTX and the NMO following that. VELRSR contains our best picked RMS velocities, and VELSMTH is the smoothed version of VELRSR. Note that we are using unreduced velocities, as these yielded the best result after testing several reduced velocity models.
    - OUTPUT FILES: (3 parts) LOS_15_prestack.migtx_0-15.5k, LOS_15_prestack.migtx_16-26k, LOS_15_prestack.migtx_25.5-32k
    - STATUS (as of 3/9/2016): All migrations have finished and CDP database files remain in GOALOS Echos project.
- **Step 2:** Re-pick velocities on migrated CDPs
    - JOB: LOS_15_veldef_prestack_mal.dat
    - INPUT FILES: output CDP files from step 1 (LOS_15_prestack.migtx_0-16.5k, LOS_15_prestack.migtx_16-26k, LOS_15_prestack.migtx_25.5-32k)
    - VELOCITY MODEL: Update the VELPRSTK model. This is essentially a copy of the VELRSR model for which you will update existing velocities using the new, migrated CDP gathers. After this step is complete, the VELPRSTK model should contain the best velocity information for the line.

- STATUS (as of 5/7/2013): CDPs 20,000-22,000 are the only updated velocities in the VELPRSTK model, completed as an individual project for the seismic processing class. Note: pay close attention to model "seams" here, especially as the Moho velocity was updated because it was too fast.

- **Step 3:** Stack the migrated gathers
  - JOB: LOS_15_velstack_prestack_mal.dat
  - STATUS (as of 5/7/2013): Currently, only stacks of the test area exist (20,000-22,000 CDPs). The best stack of the test area is LOS_15_prestack**test**.migtxstack_run3.
- **Step 4:** Splice the three stacked sections together
  - (5/7/2013) This job has not been yet created, but LOS_15_splice.dat job can be used as a template for splicing together the three stacks.

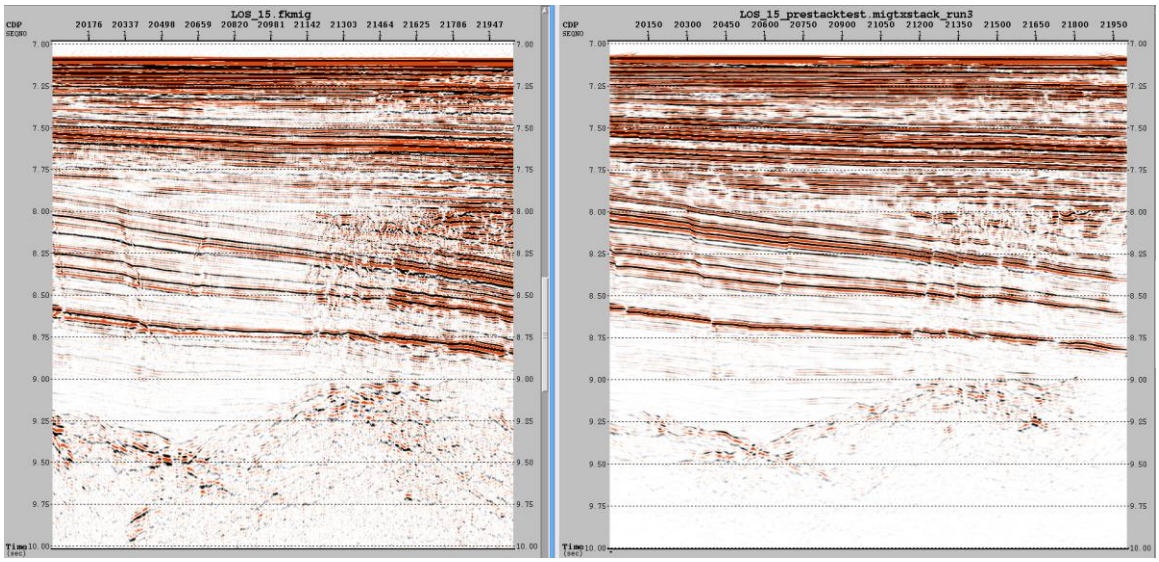

Figure B.8. Before and after prestack test images of Line 15. Images show CDPS 20,000-22,000, a zoom within the trench wedge sediments. Left image shows poststack time migration, right image shows prestack time migration. CDP spacing is 6.25 m, vertical axis is in TWTT.

Appendix C: Summary of AG0812 processing

AG0812 processing was completed at sea and then improved on at UTIG. Primary improvements from at-sea processing (completed by Julie Zurbuchen and Maureen Walton) includes velocity analysis at finer intervals and more sophisticated preprocessing. We generally followed the seismic processing cookbook used by UTIG's MG&G Field Course as we used the UTIG seismic equipment for acquisition. Parts of that cookbook are reproduced here along with representative code, notes, and screenshots. All data have been processed to poststack time migration as of 3/9/2016. Data files are located in /disk/staff/sean/alaska/YakBay2012 as of 4/28/2016.

C.1 GEOMETRY DEFINITION

Shots were taken every 5-8 seconds with navigation recorded separately. Several steps are required to generate and a shot-based navigation file and calculate geometry. First, produce a shot-based navigation file – Steffen Saustrup developed code to accomplish this for the UTIG seismic system. Run the following scripts to clean up shot data, navigation data, and finally generate a shot-based navigation file. The first two scripts generate new files with the suffix "fix" which will then be merged into the final navigation (.nav) file.

```
>> logfix.csh line.log
>> gpsfix.csh date.txt
>> mcsnavdist linename firstshot lastshot line.fix date.fix line.nav
```

After segy data have been imported into Echos, you must define the source and receiver geometry in Focus/Echos and calculate CDP numbers (binned at 3.125 m spacing). For the AG0812 survey, we also account for the unique geometry of the setup onboard the R/V *Alaskan Gyre* in the geometry job. See the survey setup and geometry job code below (1205_geometry.dat).

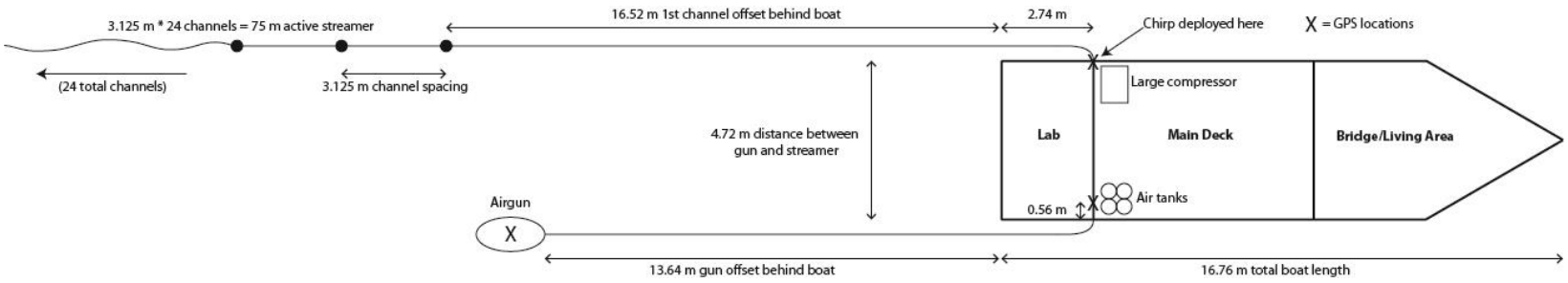

Figure C.1. Schematic diagram of the AG0812 survey setup.

```
>> 1205_geometry.dat
*JOB    YAKUTAT 1205
*CALL   DUMIN          2000
*CALL   LINE
LOCN    1
REPEAT  15000   3.12
CDP     12      15000   0             1
*CALL   PATTERN 24      YES
SPREAD  24      1       -2.88   -3.125
*CALL   SOURCE
SHOT    1417    24      0             24      24
REPEAT  2000    5       0             5
*END
```

Following geometry definition in Echos, update the geometry spreadsheet to account for dynamically changing distances due to time-based shots.

- Under Utilities, pull up the Spreadsheet.
- Along the left side, click on Shot to display the shotpoint spreadsheet.
- Under Functions, select Input Text File.
- Choose your *.nav file from the nav directory.
- Change “First Line” to “2” to skip the first line of your file.
- On the left side, click “Shot number” and then highlight the columns containing shot in your file. Allow room for at least 5 digits.
- On the left side, click “Station location” and then highlight the columns containing station at the far right of your file. Allow for at least 6 digits.

- Do the same for “Pattern Origin” and select the same columns as for Station.
- Click “Fill” and the correct values should be entered into your spreadsheet.
- Under Functions, select “Calculate X,Y”.
- Under “File”, select “Save All to Database” and then exit the spreadsheet.
- Under “2D Tools”, display your Geometry.

C.2 PREPROCESSING

Preprocessing steps include a Butterworth filter, an offset header calculation accounting for survey geometry, and spherical divergence gain. Note that a deconvolution was not performed due to the use a mini-GI gun, which reduces or eliminates the need for source deconvolution. After testing a multichannel deconvolution we opted to not use one in order to best preserve the original data. Also note that CDP sorting into 3.125 m bins occurs in a separate job.

```
>> 1205_preproc.dat
*JOB    YAKUTAT 1205
*CALL   DSIN
LABEL   1205.shots
FILEID  0000400500a00bc1.000000.00000001
PKEYLST
1417    2496
*CALL   SCALE   -1
*CALL   FILTER  SHOT                    ZERO
BUTTER
      1500    40      2       500     2
*CALL   PROFILE         1               10
```

```
*CALL   HDRMATH
HCPOW   OFFSET  2       OFFSET
HCADD   OFFSET  22.3    OFFSET
HSQRT   OFFSET  OFFSET
*CALL   GAIN    SHOT
SPHDIV
0       1500    100     1800    300     2000    500     2200
1000    2800    1500    3200    2000    3500
#*CALL   MCDECON        CHAN
24
KEYDEF  1       1       24
GAP     80              8
0       300     0       300     0       1000    0       1000
*CALL   BALANCE
*CALL   DSOUT   OVERWRT
LABEL   1205.PREPROCESSED.SHOTS
*END
```

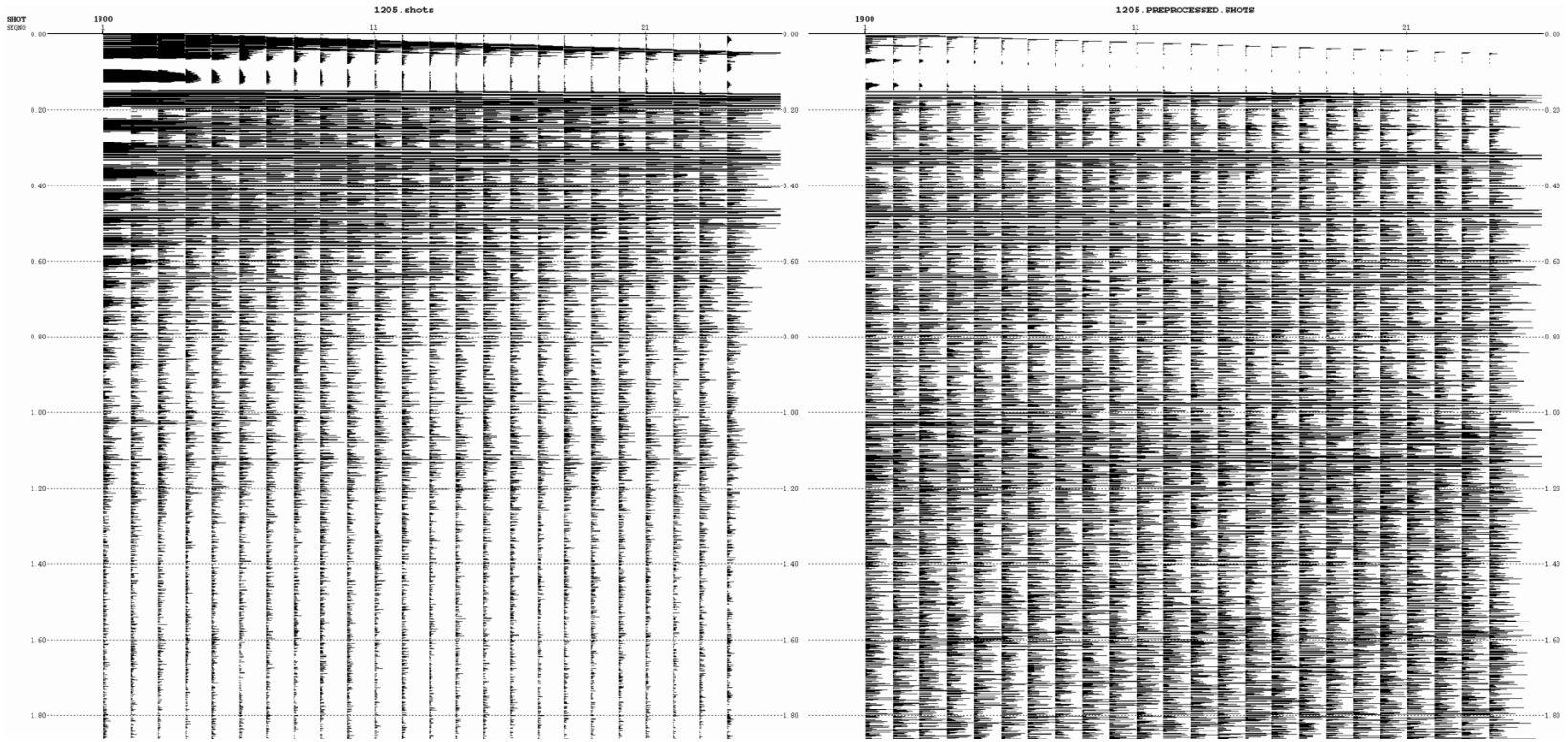

Figure C.2. Shot gather prior before and after preprocessing (left and right, respectively). Vertical axis is in two-way travel time (TWTT).

C.3 VELOCITY ANALYSIS

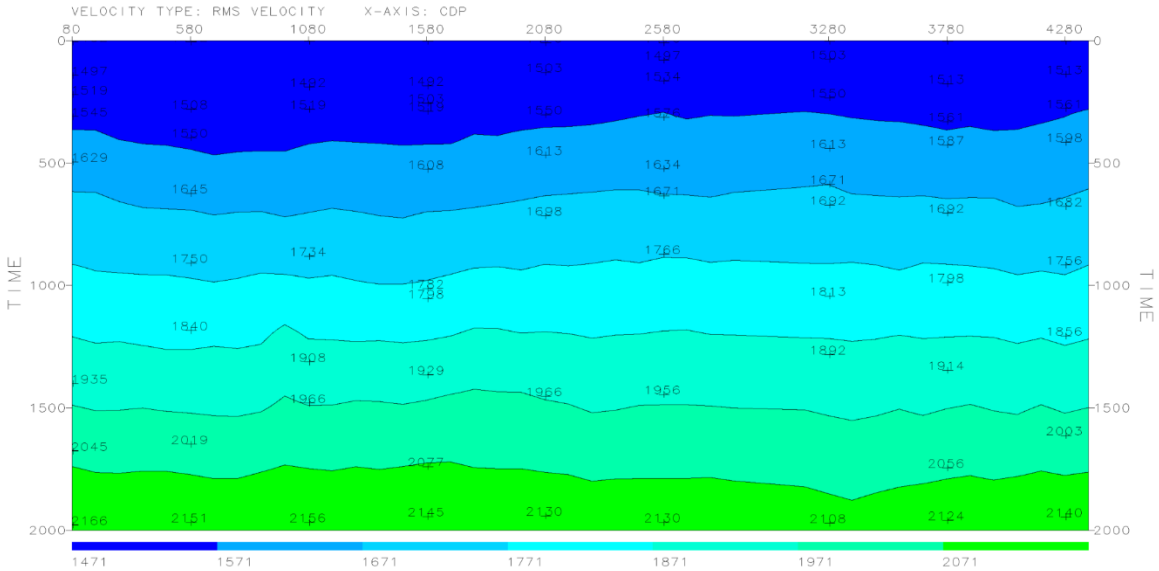

Figure C.3. Root mean square (RMS) velocity model for Line 1205. Velocities are in m/s. CDP spacing is 3.125 m.

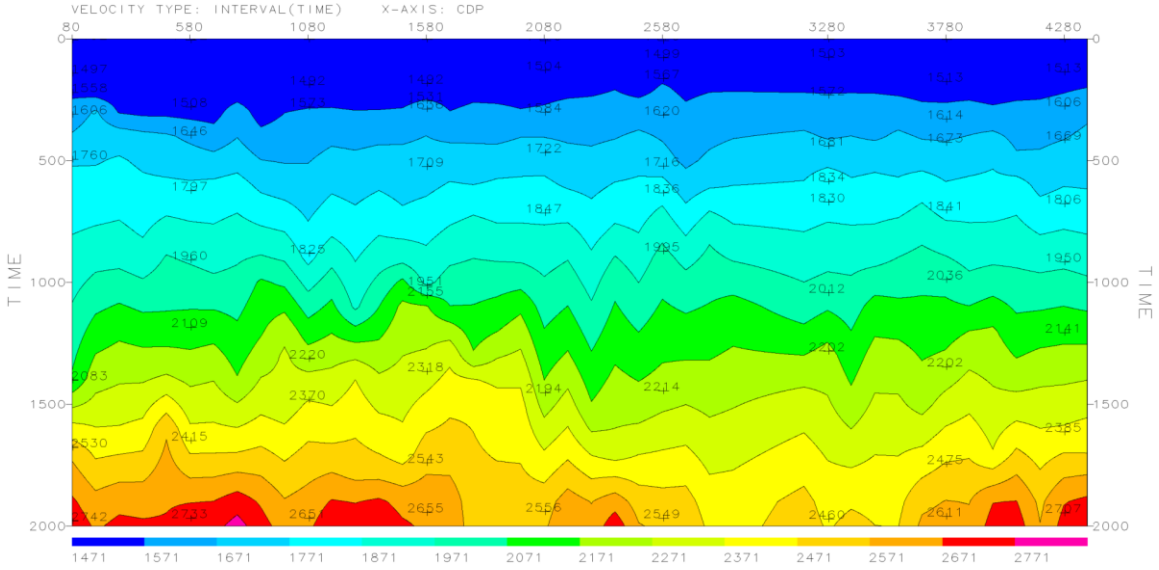

Figure C.4. Interval velocity model for Line 1205. Velocities are in m/s. CDP spacing is 3.125 m.

C.4 STACKS

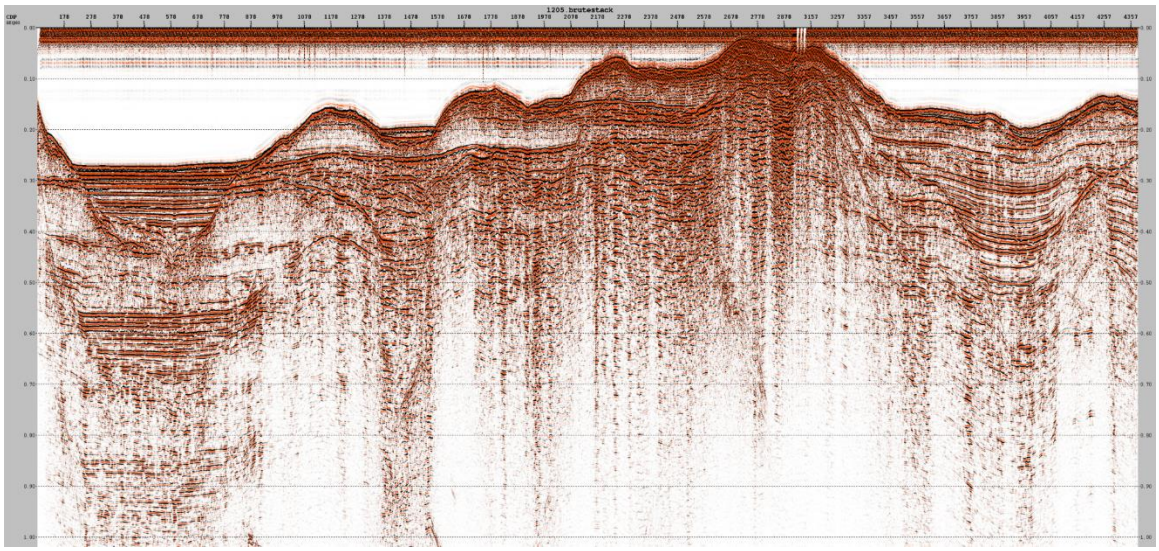

Figure C.5. Brutestack of Line 1205 before processing. Vertical axis is in TWTT. CDP spacing is 3.125 m. No automatic gain control (AGC) scaling has been applied in this image.

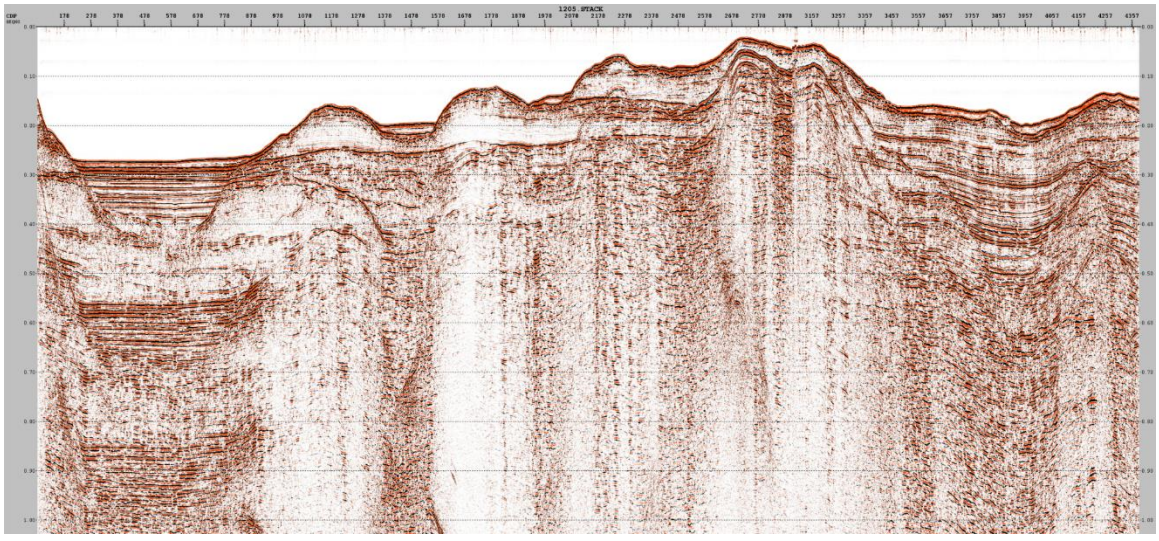

Figure C.6. Stack of Line 1205 after preprocessing, sorting, and normal moveout (NMO) correction. Vertical axis is in TWTT. CDP spacing is 6.25 m. No AGC scaling has been applied in this image.

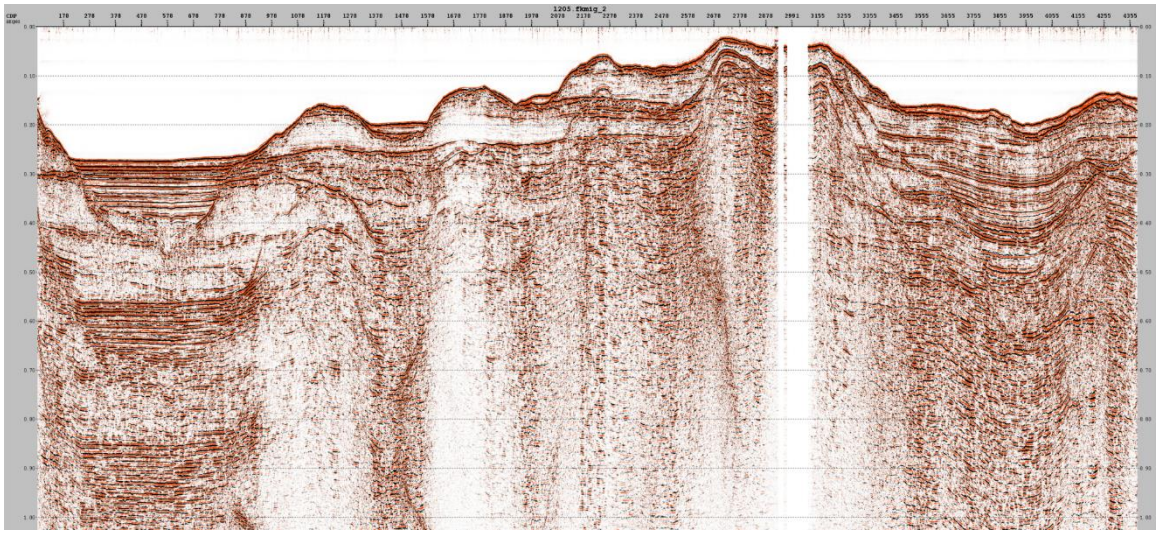

Figure C.7. Poststack time migration of Line 1205. Processing features a frequency-wavenumber (FK) migration. Vertical axis is in TWTT. CDP spacing is 3.125 m. No AGC scaling has been applied in this image.

Appendix D: EW9412 prestack processing

D.1 PROCESSING COOKBOOK

Line 1250 of survey EW9412 has been processed to prestack time migration by Maureen Walton at UTIG using the procedures detailed below. Processing of the other fault-orthogonal line, 1262, has been started; the cookbook below was written for processing 1262. The processing steps detailed below have been completed for line 1250, with results and future work described in section D.2. Information is current as of 3/9/2016.

File locations:

Raw segy (format R0): /disk/staff/sean/alaska/ew9412/segy_raw

Navigation (including calculated distances):

/disk/staff/sean/alaska/ew9412/nav/utig

UTIG-processed segy: /disk/staff/sean/alaska/ew9412/segy_processed/malw

Trehu-processed segy:

/disk/staff/sean/alaska/ew9412/segy_processed/stacks_Trehu

Echos jobs: /disk/staff/sean/alaska/ew9412/JOBS

Echos project name: ew9412

Survey parameters:

Source volume: 8400 in^3

Source pressure: 2000 psi

Source depth: 6 m

Shot interval: 20 s (about ~50)

# of channels: 224

Near channel #: 224

Distance to near channel: 245 m

Group spacing: 12.5 m

Active streamer length: 2800 m

Total streamer length: 3050 m

Streamer tow depth: 8 m

Original sample interval: 2 ms

Record length: 16.5 s

Max fold: ~60 (when binned at 12.5 m)

High frequency: ~125 Hz

Line 1262 parameters:

Shots: 21817-24519

Stations before sort (spacing 12.5 m… will be close to CDP values): 1-11368

Processing steps below are listed by job name. Bold items indicate modules and/or jobs that need to be modified and run for line 1262. Note there may be unanticipated Focus to Echos conversion issues.

1. 1262_echos_segyin.dat
   - Import raw segy (raw data in R0 format)
   - Resamp to 4 ms
2. 1262_echos_marine.dat
   - Navigation data has been processed to calculate distance and station information based on fortran code from Steffen (see /disk/staff/sean/alaska/ew9412/nav/distcalc.xlsx)

- Use MARINE module for geometry definition
- Update Echos spreadsheet with distance information using nav file (1262_distcalc_utig.nav):

Under Utilities, pull up the Spreadsheet.

Along the left side, click on Shot to display the shotpoint spreadsheet.

Under Functions, select Input Text File.

- Choose your *.nav file from the ../nav/utig/* directory.
- Change “First Line” to “2” to skip the first line of your file.
- On the left side, click “Shot number” and then highlight the columns containing shot in your file. Allow room for at least 5 digits.
- On the left side, click “Station location” and then highlight the columns containing station at the far right of your file. Allow for at least 6 digits.
- Do the same for “Pattern Origin” and select the same columns as for Station.
- Click "Fill" and the correct values should be entered into your spreadsheet.
- Under Functions, select “Calculate X,Y”.
- Under “File”, select “Save current to database”.

Update CDP spacing to be every 12.5 m rather than 6.25 to bin more traces.

Again, in Spreadsheet (Utilities -> Spreadsheet)…

- Along the left side, click on CDP to display the CDP spreadsheet.
- Parameters -> CDP/Station parameters -> number of CDPs per station to 1.0.
- Under Functions, click “Create CDPs”.
- CDP X values should update to be spaced at 12.5 m.

Sample of navigation data

(/disk/staff/sean/alaska/ew9412/nav/utig/1262_distcalc_utig.nav):

ew9412_1262	shot	ddlat	ddlon	line	?	?shot?
totdist	station					
1994+263:04:55:44.6	21817	54.512160	-132.936685	1262	376.4	7983
0.000000	1					
1994+263:04:56:05.0	21818	54.512515	-132.937182	1262	376.5	7984
50.909657	4					
1994+263:04:56:25.3	21819	54.512862	-132.937682	1262	376	7985
101.240465	8					
1994+263:04:56:45.2	21820	54.513202	-132.938172	1262	375.5	7986
150.587166	12					
1994+263:04:57:05.4	21821	54.513547	-132.938678	1262	375.1	7987
201.053913	16					
1994+263:04:57:25.6	21822	54.513887	-132.939202	1262	375.1	7988
251.809423	20					

3. 1262_echos_brutestack.dat****job has been modified and run****
    - You'll only need this for picking the seafloor and comparison to a crude image.
    - DSIN: nearest 10 channels of raw shots
    - PROFILE
    - FILTER: Bandpass filter (8-14-80-100)
    - SORT: CDP order
    - VFNDEF: Define a VEL1500 velocity model

- NMO: Apply the VEL1500 velocity model
- STACK: Maxfold = 5
- DSOUT: 1262.BRUTE

4. **Pick seafloor on the brutestack.**
   - **Select 1262.BRUTE in View Data.**
   - **Pick -> Horizons. Make a new event called: SF with attribute: TIME**
   - **Pick the seafloor on the stack.**

5. **1262_echos_preproc.dat**
   - DSIN: Input raw shots
   - **EDIT: Trace editing (be sure to check on this and modify… chan 195 and shot 101 were bad for 1250)**
   - **FILTER: Bandpass filter (8-14-80-100 was good for 1250)**
   - HDRMATH: Adds SOFFSET into the headers (not there originally for some reason)
   - PROFILE: shouldn't need to modify
   - GAIN: Spherical divergence, start with t^2. This will just be for visualization with 1st-round velocity picking, you'll come back to do a better spherical divergence gain later.
   - HEADPUT: puts SF water-bottom time (WBT) value into the CDP headers
   - STATIC: flattens seafloor to -100 ms for prep input into decon
   - **MCDECON: multichannel, changing-windows decon. This is pretty involved – Line 1250 employs two windows designed for shallow and deep**

deconvolution, re-iterated for changing topography. A deconvolution cookbook written by Ryan Lester describes the method in detail.

- STATIC: shifts seafloor back to normal.
- SORT: re-sort into CDPs by increasing offset.
- DSOUT: Outputs processed, sorted CDPs (1262.CDPS_DEC)

*Note that SMAC multiple reduction would normally be run at this point. SMAC was tested extensively and it doesn't seem to like the oddly-spaced offsets caused by binning at 12.5 m. If SMAC is desired, re-run processing at default 6.25 m bins and use template job 1250_echos_smac.

6. **1262_echos_veldef.dat**
   - **DSIN: Input SMAC CDPs, select how often you'd like to pick (set at 50 for now)**
   - FILTER: Harsher bandpass filter for better visualization (15-20-60-70)
   - AGC: 1000 ms AGC… can change if you'd like
   - **VELDEF: The software distinguishes between RMS and stacking velocities. The default function type here is stacking, which should be fine. Rename vfunc file, and picks will save to the database.**

7. **1262_echos_prestack.dat**
   - **DSIN: Input preprocessed CDPs. May want to start with a smaller test set (~1000 CDPs) to see how well it's working, as the prestack migration takes a while to run. Even a small subset will most likely need to run overnight.**

- REGLO: Gets traces ready for parabolic radon transform… shouldn't need to modify
- UNIFORM: Gets traces ready for parabolic radon transform… shouldn't need to modify
- **NMO: Apply NMO – input best velocity model name here.**
- **RADNPAR: Identification of seafloor multiples using a parabolic radon transform. Check the min/max moveout and band filter settings here.**
- RADNPAR: Inverse subtraction of the previous identification of seafloor multiples – probably won't need to modify.
- **NMO: Remove previously applied NMO – input best velocity model name here.**
- **MIGTX: This performs the Kirchoff prestack migration. Insert the best velocity model name here. You can also play with the DIPLIM and VSCALE parameters, the values already there worked well with line 1250. Note that MIGTX performs NMO as a part of the processing, (hence the need to input a velocity model).**
- **NMO: Removes the NMO applied in the MIGTX module – input best velocity model name here.**
- DSOUT: Output migrated CDPs (1262.CDPS_PRESTACK)

8. Brutestack and pick new SF

- Once you've migrated the full section, the newly-migrated section will have a slightly different seafloor, especially in steeper areas, hence the need to re-pick the seafloor.

- **Run 1262_echos_brutestack.dat and input the migrated CDPs. It will look messy as the new CDPs haven't been cleaned up yet (you'll do this in the next step).**
- **Pick a new seafloor (attribute: TIME) with a new name, like SF_MIG. You'll use this for muting in the future.**

9. **1262_echos_prestack_stack.dat**
   - **DSIN: Input migrated CDPs.**
   - GAIN: Remove t^2 spherical divergence gain from the preproc job.
   - **GAIN: Add better v^2t spherical divergence using the best velocities – input vfunc model name.**
   - HEADPUT: Put the info from the new SF_MIG horizon into the headers to replace the old WBT header. Shouldn't need to modify, as long as you named it SF_MIG.
   - **NMO: Apply NMO – input best velocity model name here.**
   - **MUTE (commented): This is where you can put hand-picked mutes, if any.**
   - **MUTE: 35% stretch mute (tested on 1250, works well) applied using the best velocity model (input name here).**
   - **FILTER: This is a time-varying filter, will almost certainly need to be modified. A good time-varying filter will tease out structures at appropriate depth-varying resolutions.**
   - **FILTER (commented): In lieu of the time-varying filter in the previous module, you can use this simpler filter option instead.**
   - **BALANCE (commented, optional): Trace balancing wasn't necessary for line 1250.**

- STACK: Simple stack of CDP traces, no need to modify.
- **AGC (commented, optional): This can be easily implemented later, so you can decide whether you'd like it here or not. Window currently set at 500 ms.**
- MUTE: Water-bottom mute. Shouldn't need to be modified.
- DSOUT: Output stack (1262.STACK_PRESTACK).

10. Re-pick vels (iterative velocity picking)

- **There are several ways to do this, you can use Echos or GeoDepth. Input the migrated CDPs and modify the velocities from the previous velocity model. A cookbook written by Ryan Lester describes a method for picking residuals in GeoDepth.**

11. Re-run 1262_echos_prestack

- **Be sure to modify the job with the name of the new velocity model from step 11. This job shouldn't need to be modified otherwise. It will take some time to run.**

12. Re-run 1262_echos_prestack_stack

- **Input the latest set of CDPs (from step 12).**
- **Modify the job for GAIN, NMO, and MUTE to include the name of the latest, best velocity model.**
- **The resulting stack is your final output.**

D.2 RESULTS AND FUTURE WORK

Line 1250 of survey EW9412 has been completely processed to prestack time migration (Fig. D.1). Results show improved imaging of fault structures in the sediments atop the Pacific basement and within the Queen Charlotte Terrace. Future improvements include implementing a more robust multiple reduction, improving the time-varying filter, and residual velocity analysis using GeoDepth. Line 1262 has been imported into Echos and the geometry has been calculated as of 3/9/2016 with additional prestack processing in progress.

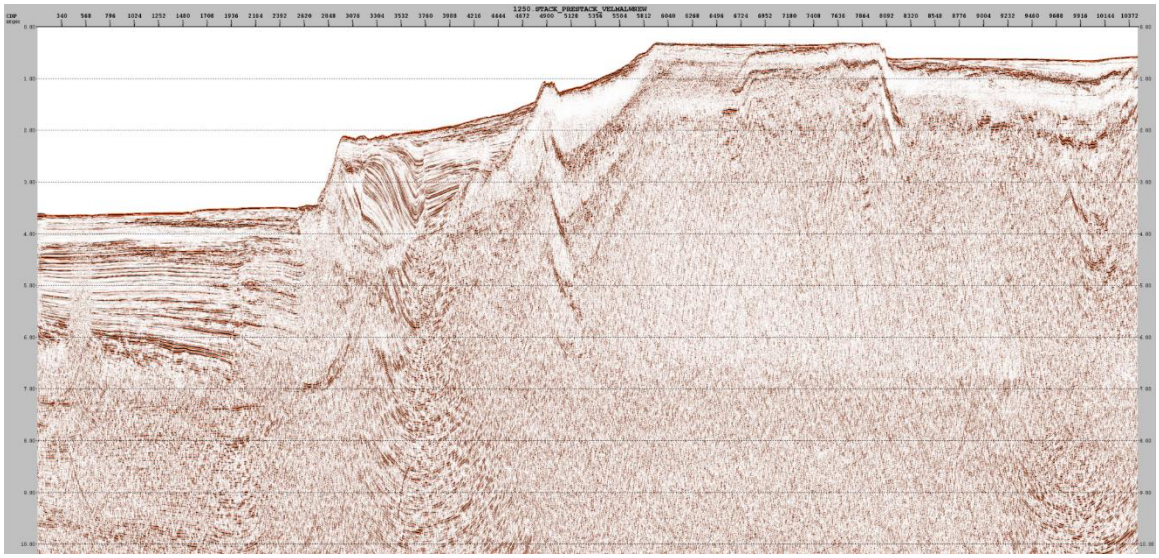

Figure D.1. Prestack time migration of Line 1250. Vertical axis is in TWTT. CDP spacing is 12.5 m. A 1000 ms automatic gain control (AGC) has been applied.

Appendix E: L378EG processing

E.1 PROCESSING COOKBOOK

Line 954 of survey L378EG has been processed to poststack time migration by Maureen Walton at UTIG in an effort to improve the legacy data using modern processing techniques. Processing of additional lines in the survey is in progress with work being completed by Maureen Walton and Ray Sliter (USGS). The processing steps detailed below are steps that have been completed for Line 954; cookbook includes some notes and trace editing specific to line 954. Cookbook is current as of 3/9/2016. All data files are located on the UTIG network in /disk/staff/sean/alaska/l378eg as of 4/28/2016.

Survey parameters (Bruns, 1982; Bruns et al., 1987)

5 airgun array, 1326 in^3, 1900 PSI

2400 m streamer

24 channels (near #24)

268 m near offset according to headers (270 calculated from shot data)

100 m group spacing

Shot spacing 50 m

24-fold

2 ms sample rate, resampled to 4 ms during demultiplexing

Maximum 11 second record length

954_segyin.dat

- DSIN: SPRINT format (determined by trial and error), 4 ms sample interval, 10s record length (verified in SeiSee)
- 954-1: shots 282-470

    - Does not match shots with same values in 954-2
    - Do not use
- 954-2: shots 260-2005
    - Seems to be main file
    - Needs editing: Bad shots, changes in seafloor time
- 952-3: shots 2140-2379 (needs editing)
    - GPS nav file indicates this is a part of the 954 line with a gap in shots between 2005 and 2140
    - Will process as separate 954a line

954_marine.dat

- GPS navigation comes in 3 files: 954.nav, 954a.nav, 954b.nav (.nav files derived from original USGS file named l-3-78-eg.410_051). 954 is simply a concatenation 954a and 954b.
- Navigation has shots 40-1972 and 2146-2356 concatenated. Sample rate in nav is 10 shots.
- Use MARINE geometry model. Use near offset = 268, which is the value from the headers.

954_traceedit.dat

- DSIN: 954-2.SHOTS
- EDIT (1st module): Edit entire shot ensembles, use KILL unless OMIT noted, both RANGE and NORANGE
    - Bad shots: 256 (OMIT), 287, 386, 428, 446, 479, 576, 590, 608, 689, 773, 779, 782, 786, 819, 824, 884, 901, 959, 1041, 1050, 1051, 1073, 1172, 1207,

1231, 1273, 1294, 1321, 1402, 1571, 1591, 1626, 1670, 1691, 1718, 1719, 1731-1734, 1746-1752, 1754, 1768-1787, 1819, 1906, and 1970

- EDIT (2nd module): KILL bad channels, these appear to be bad shots at first glance, but you can see the bad channel and other good data with trace scaling (vs. section scaling)
    - Bad chans [shot-chan]: 261-1, 275-1, 387-14, 429-20, 436-21, 465-3, 510-11, 517-12, 767-8, 849-14, 1146-1, 1194-1, 1216-2, 1646-8, 1652-1, 1680-4, 1697-2
- DSOUT: 954-2.SHOTS_EDIT
- Note: SPKCHK can find and kill bad chans automatically – use for future lines

  *CALL SPKCHK 1 7000 0 YES

  Check on killed chans: awk '/SPIKE/ { getline; print $0 }' 956spkchk.log > 956chan_kill.log
- Note: shots shouldn't even need to be omitted if they're blank – do this in the future

954_static.dat

- Note: 154 ms static shift found in header tsa. There is too much white space, must be removed for multiples to come in at the right time. Use/check for this and future lines.
- Change in seafloor time between 1362 and 1560 (missing 1s of shallowest data)
    - DSIN: 954-2.SHOTS_EDIT, ENSEMBLE shots 260-1361
    - DSOUT: NEW 954-2.SHOTS_EDIT_SHIFT
    - DSIN: SHOTS_EDIT, ENSEMBLE shots 1362-1560
    - HDRMATH: add 0s into headers labeled as STATIC, because the STATIC module will add the shift to an existing header value. Since we want a

constant shift of 1000, we need to add 1000 to 0 first, and therefore we need to insert 0s into the headers somehow.

  - STATIC: STATIC (header label for 0s), APPLY, 1000, TIME
  - DSOUT: APPEND, 954-2.SHOTS_EDIT_SHIFT

- Change in SF time between 1561 and 1652 (back to normal, can see direct wave)
  - DSIN: SHOTS_EDIT, ENSEMBLE shots 1561-1652
  - Comment HDRMATH and STATIC
  - DSOUT: APPEND, 954-2.SHOTS_EDIT_SHIFT
- Change in SF time between 1653 and 1767 (missing shallowest 1s data)
  - DSIN: SHOTS_EDIT, ENSEMBLE shots 1653-1767
  - HDRMATH: add 0s to headers
  - STATIC: STATIC (header label for 0s), APPLY, 1000, TIME
  - DSOUT: APPEND, 954-2.SHOTS_EDIT_SHIFT
- Change in SF time between 1768-1867 (missing 2s shallow data, note 1768-1787 all bad shots)
  - DSIN: SHOTS_EDIT, ENSEMBLE shots 1768-1867
  - HDRMATH: add 0s to headers
  - STATIC: STATIC (header label for 0s), APPLY, 2000, TIME
  - DSOUT: APPEND, 954-2.SHOTS_EDIT_SHIFT
- Change in SF time between 1868 and 2005 (missing 1 more s shallow time, total of 3s missing)
  - DSIN: SHOTS_EDIT, ENSEMBLE shots 1868-2005
  - HDRMATH: add 0s to headers
  - STATIC: STATIC (header label for 0s), APPLY, 3000, TIME
  - DSOUT: APPEND, 954-2.SHOTS_EDIT_SHIFT

954_brutestack.dat

- DSIN: SUBGTHR CHAN 23-24, input *.SHOTS_EDIT_SHIFT
- PROFILE: 24, 99999, 0, SHOT
- FILTER: 5-10-60-70 bandpass
- SORT: 5, CDP (the CDP is key here, otherwise won't stack properly)
- STACK
- DSOUT: 954-2.BRUTE

Pick seafloor

- On brutestack
- Event: SF; Attribute: TIME
- Note missing shots cause disruptions in SF time within terrace

954_preproc.dat

- DSIN: 954-2.SHOTS_EDIT_SHIFT
- FILTER: 5-8-60-70 bandpass
- PROFILE: 2668 inline radial distance
- GAIN: t^2
- HEADPUT: SF horizon as WBT
- STATIC: hang data from flattened SF in prep for decon
- MCDECON: multichannel gap deconvolution with two windows (shallow and deep), 5 applications for changing topography and/or basement structure. Example parameters:

  *KEYDEF 260 1 24

*GAP 40 7 [shallow decon]

TDS1 TDE1 TDS2 TDE2 TAS1 TAE1 TAS2 TAE2

1300 2000 100 800 1200 1400 0 200 [T**1 and T**2 for near/far offset times seem reversed because 1 is far channel, so start with T**1 = far offset times]

[TD** are design windows, TA** are application windows]

*GAP 60 30 [deep decon]

TDS1 TDE1 TDS2 TDE2 TAS1 TAE1 TAS2 TAE2

1400 5200 200 4000 2000 10000 800 10000

[repeat KEYDEF, GAP, GAP sequence at SHOT values where there are significant topography and/or basement structure changes]

- STATIC: Shift seafloor back to normal
- SORT: CDP order
- DSOUT: 954-2.CDPS

954_veldef.dat

- DSIN: 954-2.CDPS, groups of 3, intervals of 50
- FILTER: 8-12-50-60 harsher bandpass
- AGC: 500 ms
- VELDEF: STACKING, MODIFY, VELMALW2
- Pick mutes: HANDMUTE2
- Note: Two sets of vels/mutes picked: VELMALW1/HANDMUTE1 (preferred higher velocities) and VELMALW2/HANDMUTE2 (preferred lower velocities).

954_stack.dat

- DSIN: 954-2.CDPS

- GAIN: SHOT, TOPTION -2 (remove t^2 gain applied in preproc)
- GAIN: SHOT, VOPTION 2 (adds v^2 gain, best after testing), read vels from VELMALW2
- NMO: apply, VELMALW2
- MUTE: RESTORE WBT (seafloor mute), ramplen = 20 ms
- MUTE: 30% stretch mute, ramplen=20 ms (eliminates stretch missed by hand picking)
- MUTE: HANDMUTE2 (hand-picked mutes), ramplen=20 ms
- STACK
- DSOUT: 954-2.STACK2
- Observations: V^2 gain and all 3 mutes together yield the best results. Lower velocities (VELMALW2) appear to bring out shallow structures better.

954_fkmig.dat

- Poststack time migration
- Run once, commenting MUTE and HEADPUT
- re-pick seafloor on the migrated section (SFMIG, TIME) as dips will have changed from migrating
- re-run with MUTE and HEADPUT uncommented
- DSIN: Best stack (954-2.STACK2)
- MIGDMO: 1500 m/s velocity
- HEADPUT: ATTRI – assign SFMIG horizon to CDP headers as integer WBTMIG (comment first time through)
- MUTE: RESTORE WBTMIG (water-bottom mute, comment first time through)

DSOUT: 954.FKMIG

E.2 RESULTS AND FUTURE WORK

Line 954 of survey L378EG has been completely processed to poststack time migration (Fig. E.1). Results show notable improvements from the stack publicly available through the USGS (Fig. E.2; www.usgs.gov). Major processing improvements include a deconvolution, which eliminates a "ringing" seafloor, and better imaging of shallow sediments. Future work includes implementing a multiple reduction (likely surface-related multiple attenuation due to relatively short offsets) and processing other lines in the L378EG survey. Line 954 is the only line that has been completely processed by UTIG as of 3/9/2016, with ongoing efforts by both UTIG and USGS to process the other survey lines.

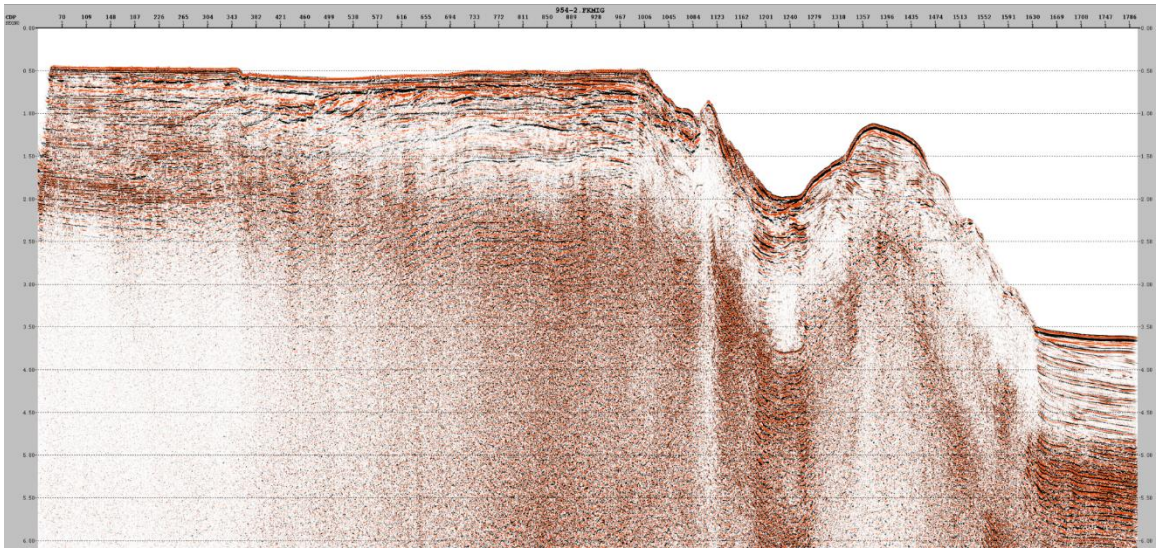

Figure E.1. Poststack time migration of Line 954 completed at UTIG. Vertical axis is in TWTT. CDP spacing is 12.5 m. No automatic gain control (AGC) has been applied to this image.

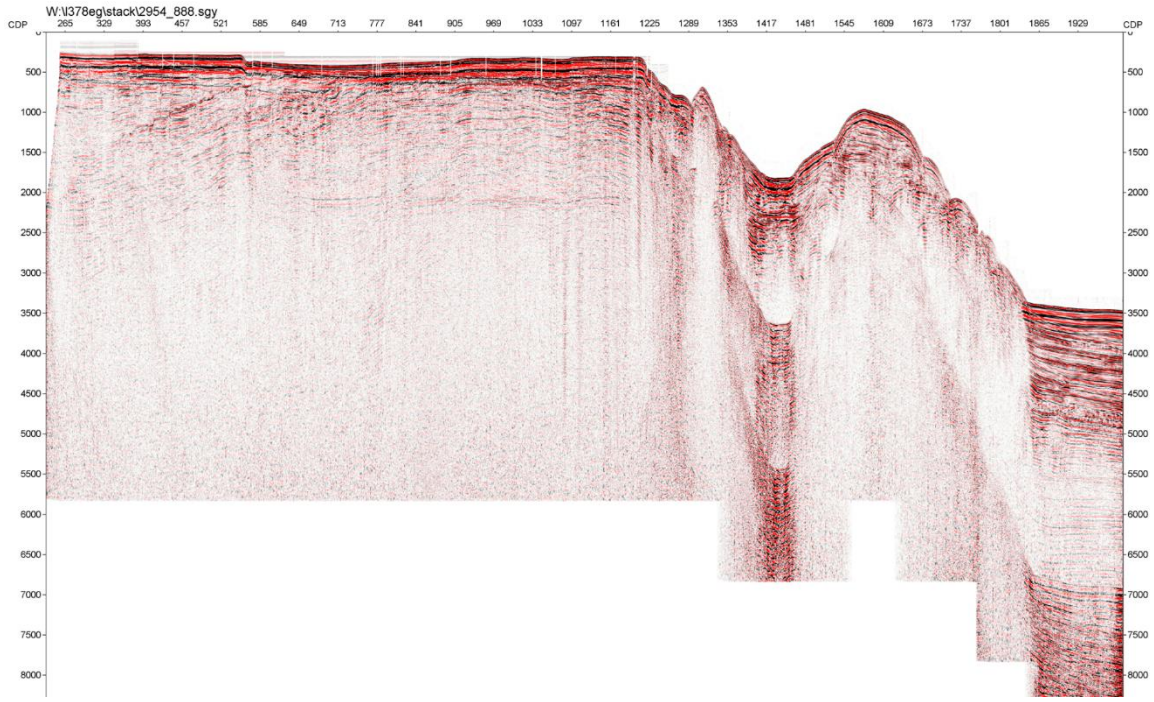

Figure E.2. Original stack of Line 954 available through the USGS. Vertical axis is in TWTT. CDP spacing is 12.5 m.

Appendix F: Inputs for tomographic inversion

F.1 TOMODD STARTING VELOCITY MODEL

The starting 1D velocity model is based on von Huene et al. (1979), which was originally developed using a series of small-scale seismic refraction and gravity profiles. A 1D starting velocity model is common in the type of analysis we employ here (e.g. Froment et al., 2014; McGuire et al., 2015). Values represent the top of the layer and are linearly interpolated where an explicit layer value is not provided by von Huene et al. (1979)'s model. Vp values are reported here. Vs values were calculated based on a constant 1.73 Vp/Vs ratio. The tomoDD starting velocity model file (MOD) is a formatted version of the model here. As of 3/10/2016, the complete tomoDD starting velocity model (MOD) is located in /disk/staff/sean/alaska/obs_craig_rapid/QCFtomoDD2/MOD_FINAL/

Depth (km)	Vp (km/s)
0	2.0
2.5	2.5
5.0	5.78
7.5	6.45
10.0	6.81
15.0	7.37
20.0	7.93
26.5	8.49

Table F.1. Table representation of tomoDD starting velocity model based on von Huene et al. (1979).

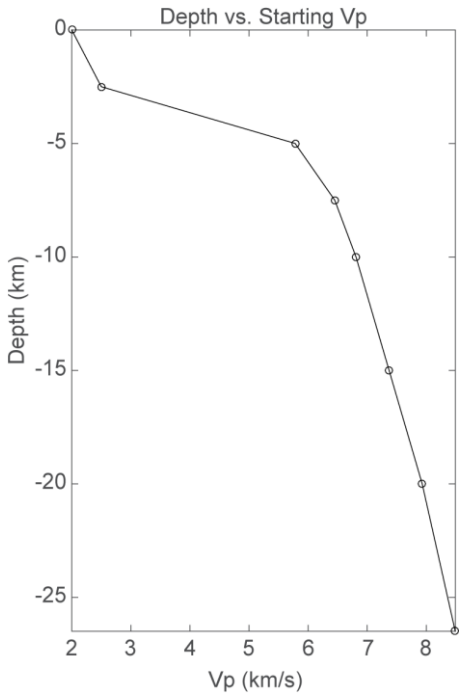

Figure F.1. Graphical representation of tomoDD starting velocity model based on von Huene et al. (1979).

F.2 TOMODD.INP

The tomoDD software requires user inputs, which include data files and various weighting and smoothing parameters. Below is the tomoDD input file (tomoDD.inp) in its entirety for our preferred final model.

```
---------------------
*--- input file selection
*cross correlation diff times:
./dt.cc
*
*catalog P diff times:
./dt.ct
*
*catalog absolute times
./both.absolute
*
*event file:
./both.event
*
*station file:
./craig2.sta.input
*
*--- output file selection
*original locations:
craig2.loc
```

```
*relocations:
craig2.reloc
*station information:
craig2.stainfo
*residual information:
craig2.res
*source paramater information:

*Output velocity
craig2.vel
*Vp model
Vp_model_craig2.dat
*Vs model
Vs_model_craig2.dat
*
*--- data type selection:
* IDAT:  0 = synthetics; 1= cross corr; 2= catalog; 3= cross & cat
* IPHA: 1= P; 2= S; 3= P&S
* DIST:max dist [km] between cluster centroid and station
* IDAT   IPHA   DIST
  3     3      500
*
*--- event clustering:
* OBSCC:    min # of obs/pair for crosstime data (0= no clustering)
* OBSCT:    min # of obs/pair for network data (0= no clustering)
```

```
* OBSCC  OBSCT  CC_format
   0      0      1
*
*--- solution control:
* ISTART:       1 = from single source; 2 = from network sources
* ISOLV:        1 = SVD, 2=lsqr
* NSET:         number of sets of iteration with specifications following
*  ISTART  ISOLV  NSET weight1 weight2 weight3 air_depth
   2        2     1    100      100      100    -0.1
* i3D delt1 ndip iskip scale1 scale2 iuses
  2    0    9     1     0.5   1.00    2
* xfac   tlim     nitpb(1) nitpb(2) stepl
 1.3   0.0005    50       50       0.2
* lat_Orig lon_Orig Z_Orig iorig rota
 55.625686 -135.178953  0  1  -27
*
*--- data weighting and re-weighting:
* NITER:                last iteration to used the following weights
* WTCCP, WTCCS:         weight cross P, S
* WTCTP, WTCTS:         weight catalog P, S
* WRCC, WRCT:           residual threshold in sec for cross, catalog data
* WDCC, WDCT:           max dist [km] between cross, catalog linked pairs
* WTCD:   relative weighting between absolute and differential data
* THRES: Scalar used to determine the DWS threshold values
* DAMP:                 damping (for lsqr only)
```

```
*       ---  CROSS DATA ----- ----CATALOG DATA ----
  10    0.3   0.3     8   -9    0.6    0.6     8   -9   1  500  1  0.2
* 12    0.8   1.0     8   -9    0.4    0.4     8   -9  10  200  1  0.2
*  1    0.1   0.1     7   -9    0.1   0.08     8   -9  10   45  0  0.2
*  1    0.1   0.1     7   -9    0.1   0.08     7   -9  10   75  1  0.2
*  1    0.1   0.1     7   -9    0.1   0.08     7   -9  10   45  0  0.2
*  1    0.1   0.1     7   -9    1.0    0.8     7   -9  .1   75  1  0.2
*  1    0.1   0.1     7   -9    1.0    0.8     7   -9  .1   45  0  0.2
*  1    0.1   0.1     7   -9    1.0    0.8     6   -9  .1   75  1  0.2
*  1    0.1   0.1     7   -9    1.0    0.8     6   -9  .1   45  0  0.2
*  1     1     1     6   -9    0.1    .08     6   -9   1   75  1  0.2
*  1     1     1     6   -9    0.1    .08     6   -9   1   45  0  0.2
*  1     1     1     6   -9    0.1    .08     6   -9   1   75  1  0.2
*  2     1     1     6   -9    0.1    .08     6   -9   1   45  0  0.2
*
*--- event selection:
* CID:  cluster to be relocated (0 = all)
* ID:   cuspids of event to be relocated (8 per line)
* CID
    1
* ID
```

F.3 Evidence for CG11 station drift

Teleseismic arrivals were used to assess systematic errors in station clocks. Only one teleseismic arrival was pickable on 6 OBS stations (Fig. F.2; Table F.2). Expected travel times for this teleseismic event were calculated using TauP software (www.seis.sc.edu/TauP/). These predicted arrival times should be similar to the actual arrival times of the P-wave at the 6 OBS stations. We find that station CG11, and potentially station CG06, exhibit travel times as much as ~2.5 seconds different from the teleseismic arrivals at the other OBS stations (Table F.3). Given that this observation is constrained by only one teleseismic event, however, with uncertainty inherent in both picks and travel time calculations, we did not correct any stations in our tomographic inversions.

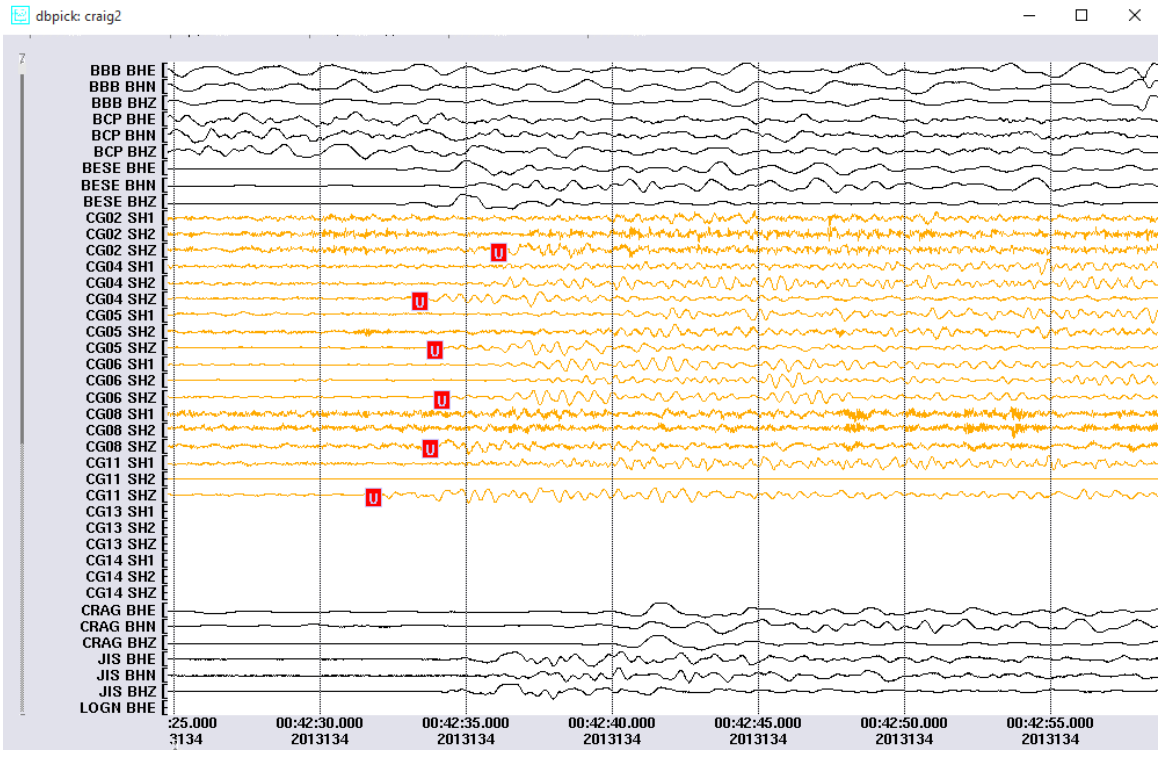

Figure F.2. Antelope software screenshot showing P-wave picks for the teleseismic event described in Table F.2. This event is the only pickable teleseism in the OBS aftershock dataset.

Date	J day	Time	Lat	Lon	Depth	Mag	Magt	SRC	Event ID
5/14/2013	134	0:32:26	18.7280	145.2870	602.30	6.80	Mw	NEI	201305142003

Table F.2. Teleseismic event details from ANSS (www.quake.geo.berkeley.edu/anss). See Fig. F.2 for P-wave picks for this event.

Station	Lat (deg)	Long (deg)	Location	Dist (deg)	Depth (km)	Phase	Travel time (s)	Predicted arrival	Actual arrival	Diff from prediction
CG02	55.3022	-134.5513	LAND	69.14	602.3	P	607.19	0:42:33.2	0:42:36.7	3.50
CG04	55.4577	-135.3319	OCEAN	68.69	602	P	604.48	0:42:30.5	0:42:33.9	3.40
CG05	55.5062	-134.7322	LAND	69.03	602	P	606.51	0:42:32.5	0:42:34.4	2.20
CG06	55.0620	-134.5859	ON FAULT	69.13	602.3	P	607.15	0:42:33.2	0:42:34.3	1.10
CG08	55.8578	-135.2473	ON FAULT	68.72	602	P	604.67	0:42:30.7	0:42:33.7	3.00
CG11	55.3057	-135.1912	OCEAN	68.78	602	P	605	0:42:31	0:42:31.9	0.90

Table F.3. Predicted travel times for the teleseismic event at 6 OBS stations. The final column shows the difference between predicted (using TauP software) and actual arrival times of the teleseism at each station. CG11 and CG06 exhibit the largest variation from the mean column value of 2.35 seconds. See Fig. F.2 for P-wave picks.

Appendix G: Preferred tomographic model

G.1 TOMODD LOG FILE

The tomoDD software writes a log file as it progresses through iterative hypocenter relocations and velocity inversions. The log file summarizes the inputs (tomoDD.inp; see Appendix F.2), data summary, and iteration details. The information below is the portion of the tomoDD.log output file containing the summary of data included in the inversion.

The full, final tomoDD.log file is located in (as of 3/10/2016):

/disk/staff/sean/alaska/obs_craig_rapid/QCFtomoDD2/FINAL_RUNS/run15/

```
----------------------
Relocate cluster number           1
Relocate all events
no clustering performed.


~ Reading data ...   Fri Feb 19 19:15:05 2016_
# stations total =     21
# stations < maxdist =     13
# cross corr P dtimes =   23912 (no org. time corr. for      0 event pairs)
# cross corr S dtimes =  439537 (no org. time corr. for      0 event pairs)
# catalog P dtimes =  228237
# catalog S dtimes =  208757
# Absolute catalog P dtimes =   15848
# Absolute catalog S dtimes =   14415
# dtimes total =   930706
# events after dtime match =       2345
# stations =     11
```

G.2 VELOCITIES

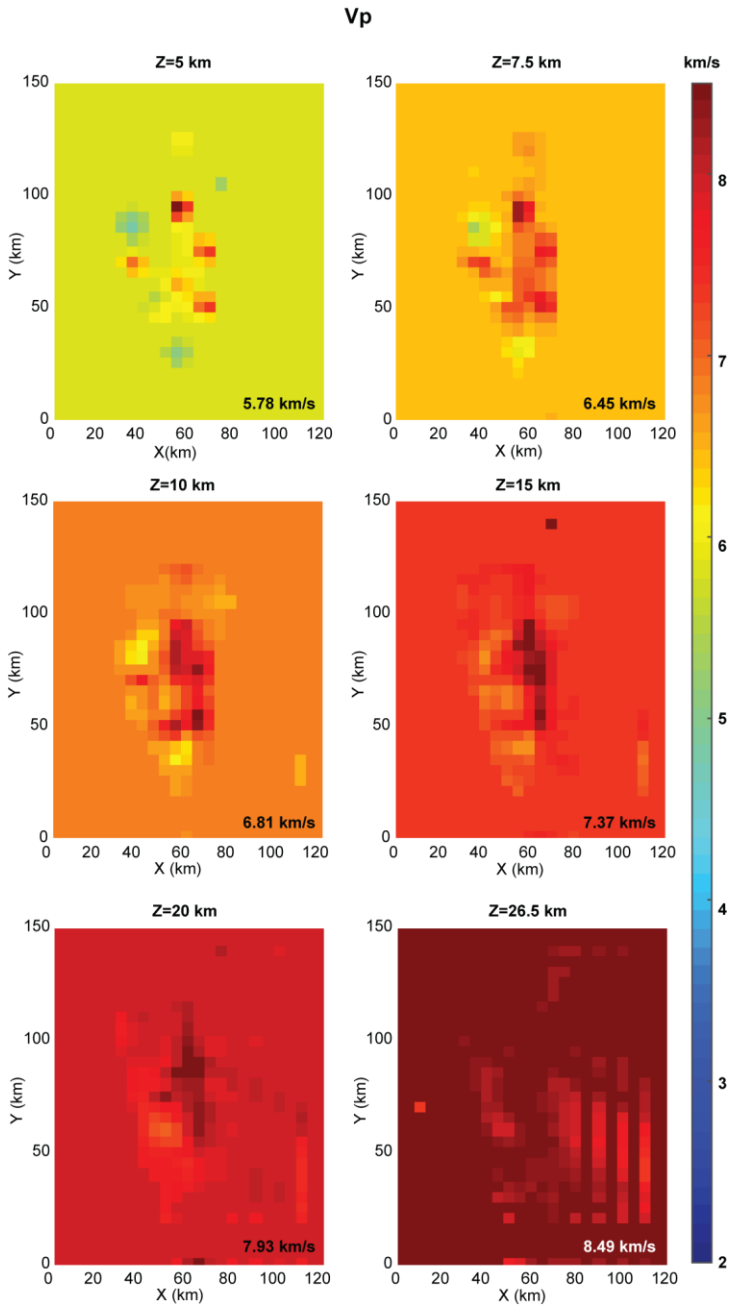

Figure G.1. Vp at 5, 7.5, 10, 15, 20, and 26.5 km depth slices. Values shown correspond with DWS>20. Starting velocity shown in the bottom right of each slice.

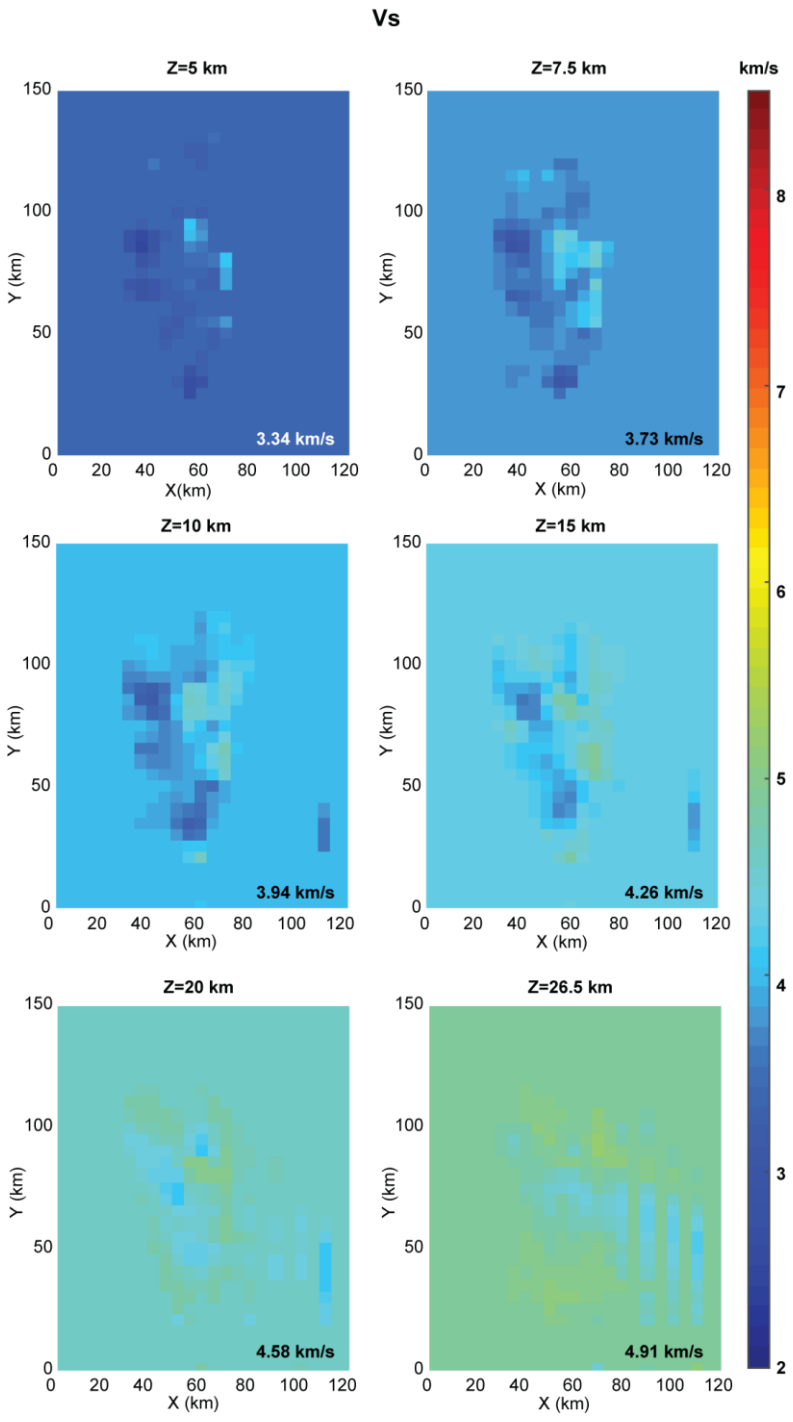

Figure G.2. Vs at 5, 7.5, 10, 15, 20, and 26.5 km depth slices. Values shown correspond with DWS>20. Starting velocity shown in the bottom right of each slice.

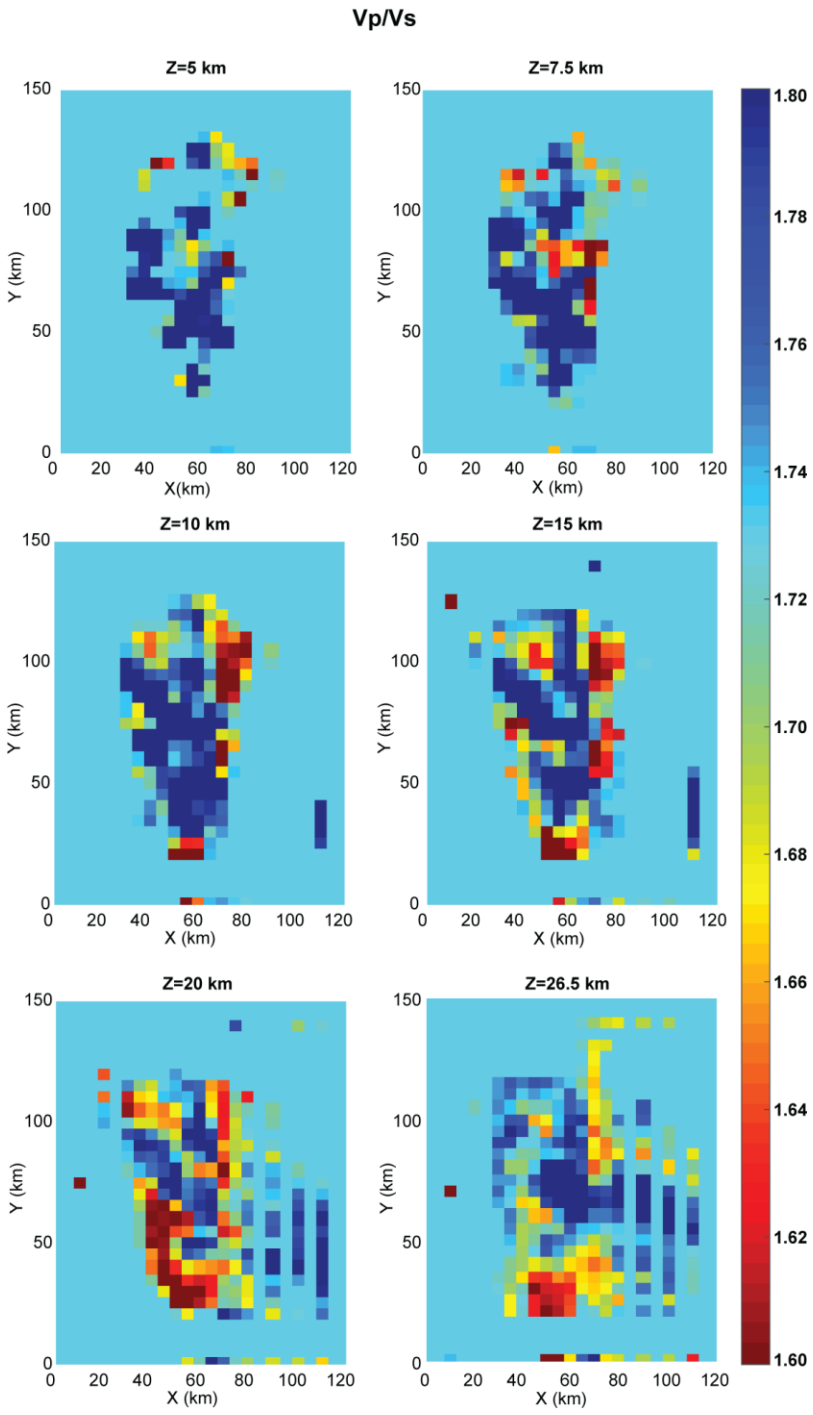

Figure G.3. Vp/Vs ratio at 5, 7.5, 10, 15, 20, and 26.5 km depth slices. Generated using Vp and Vs values where DWS >20. Starting model value was 1.73.

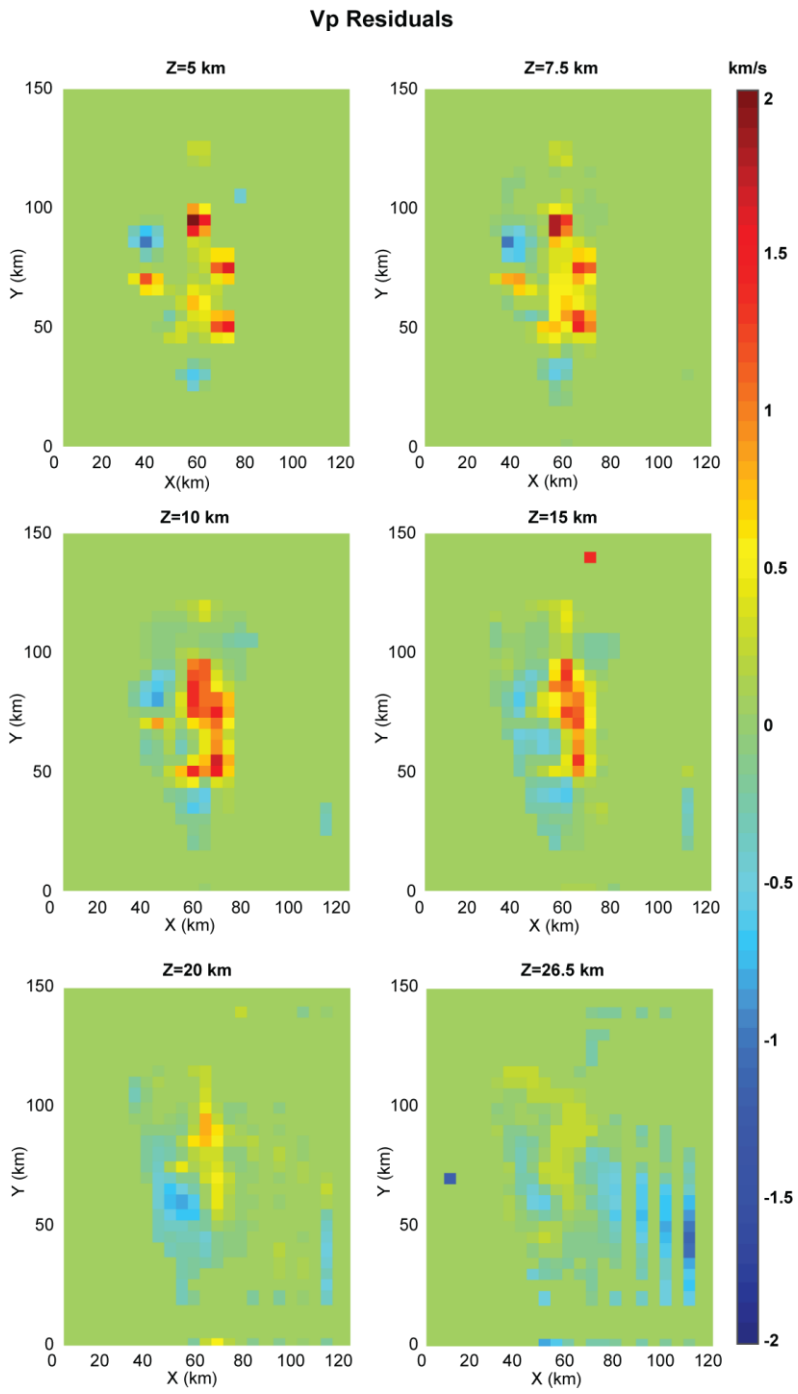

Figure G.4. Residual Vp at 5, 7.5, 10, 15, 20, and 26.5 km depth slices. Generated using Vp values where DWS >20. Positive values show velocities higher than starting model, negative values show velocities lower than starting model.

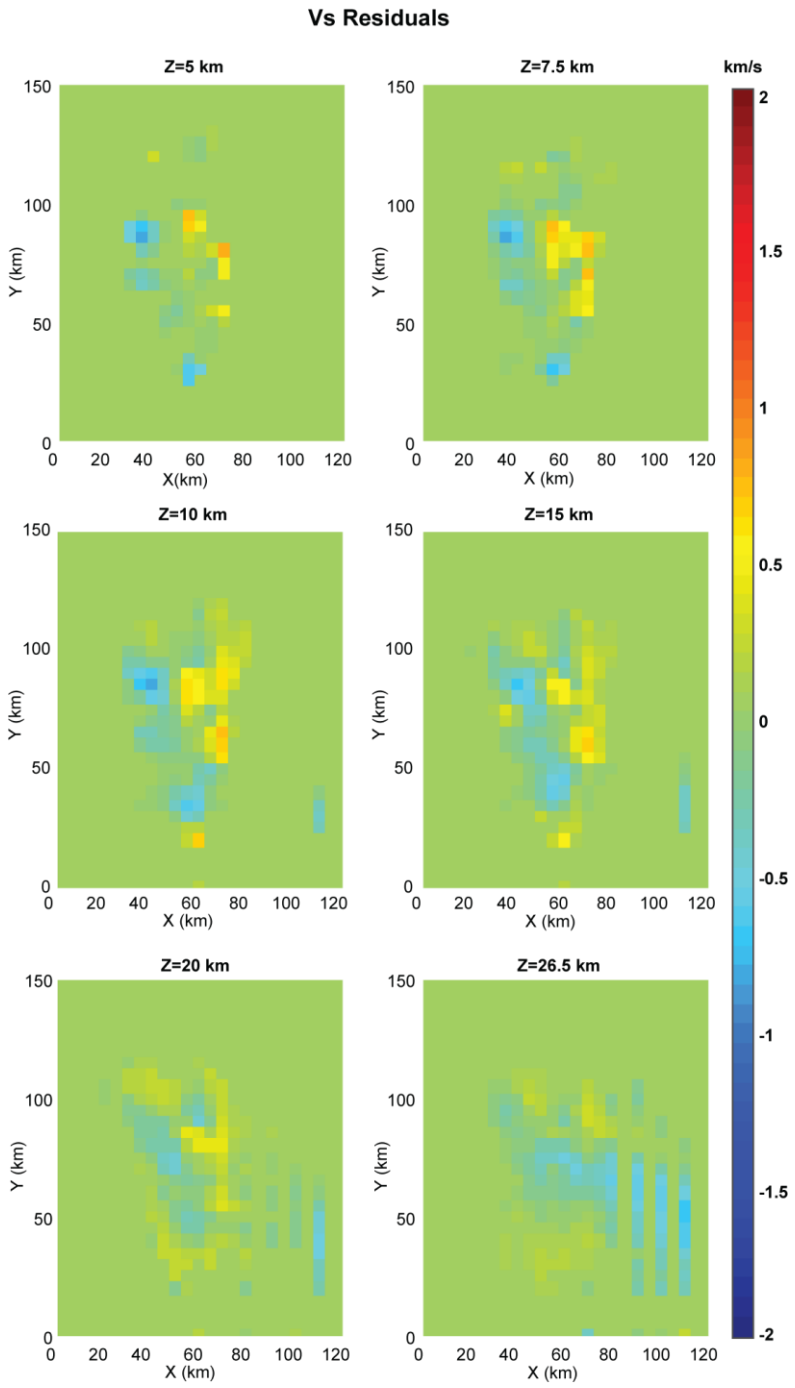

Figure G.5. Residual Vs at 5, 7.5, 10, 15, 20, and 26.5 km depth slices. Generated using Vs values where DWS >20. Positive values show velocities higher than starting model, negative values show velocities lower than starting model.

Appendix H: Preferred tomographic model evaluation

H.1 Derivative weight sum (DWS)

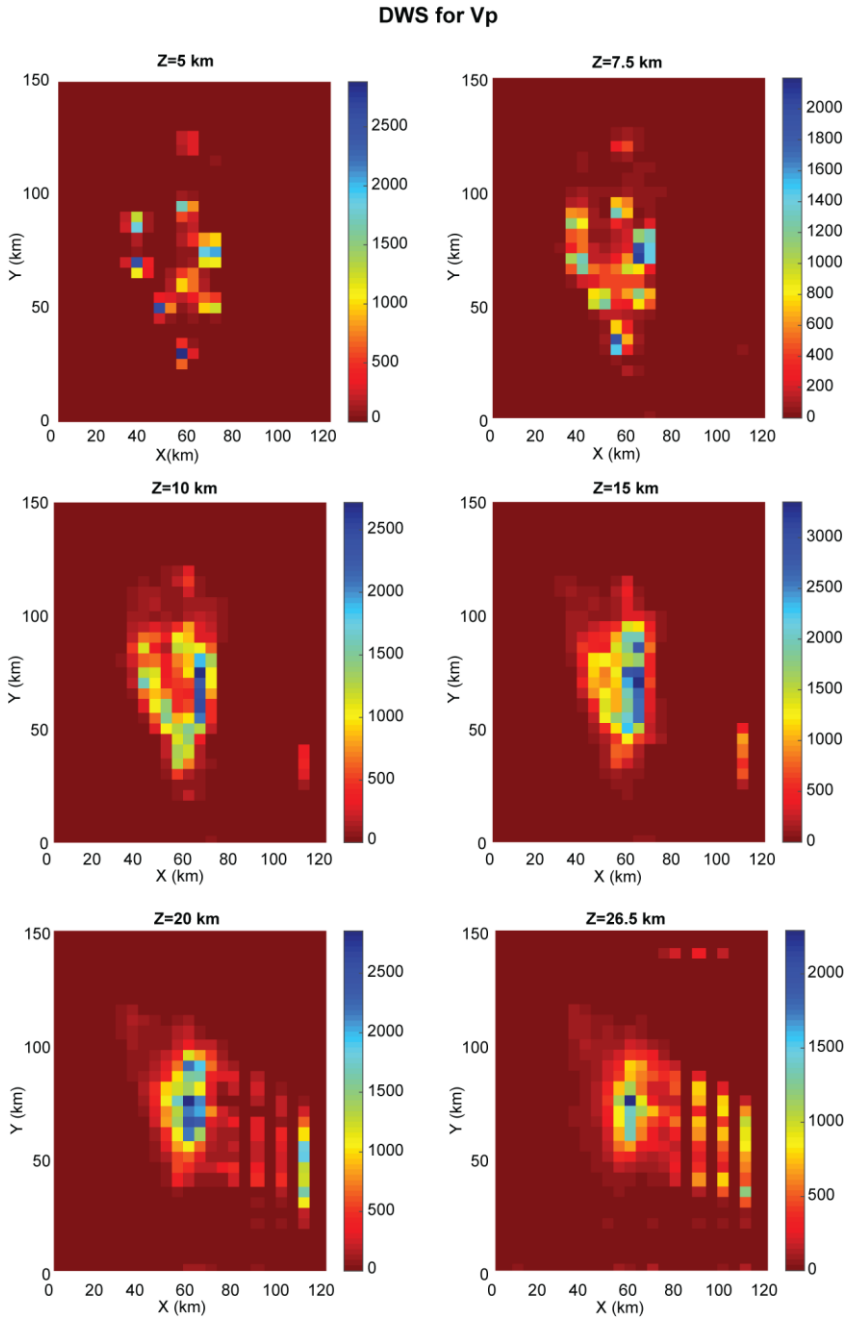

Figure H.1. Vp DWS at 5, 7.5, 10, 15, 20, and 26.5 km depth slices.

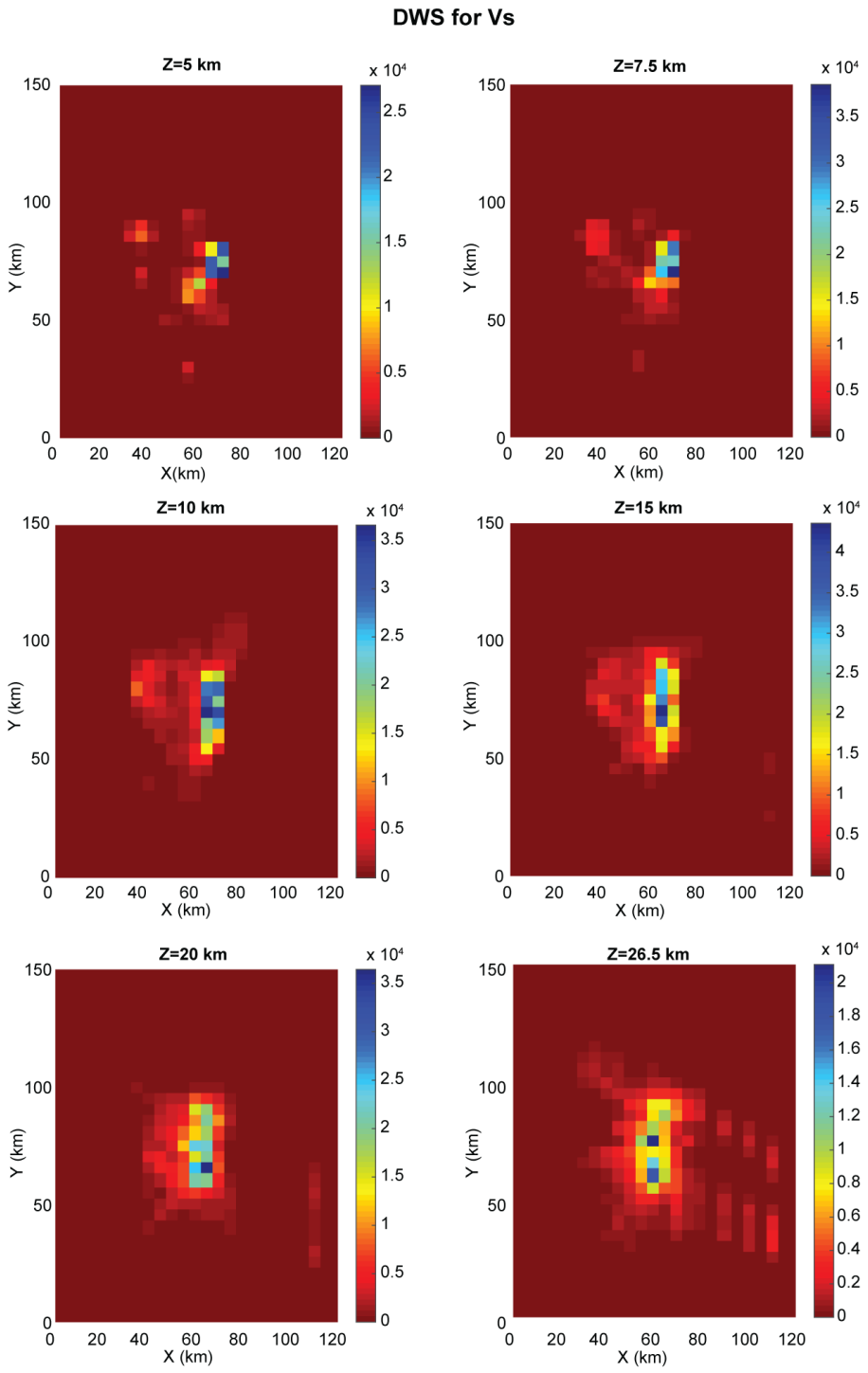

Figure H.2. Vs DWS at 5, 7.5, 10, 15, 20, and 26.5 km depth slices.

H.2 RESOLUTION TEST RESULTS

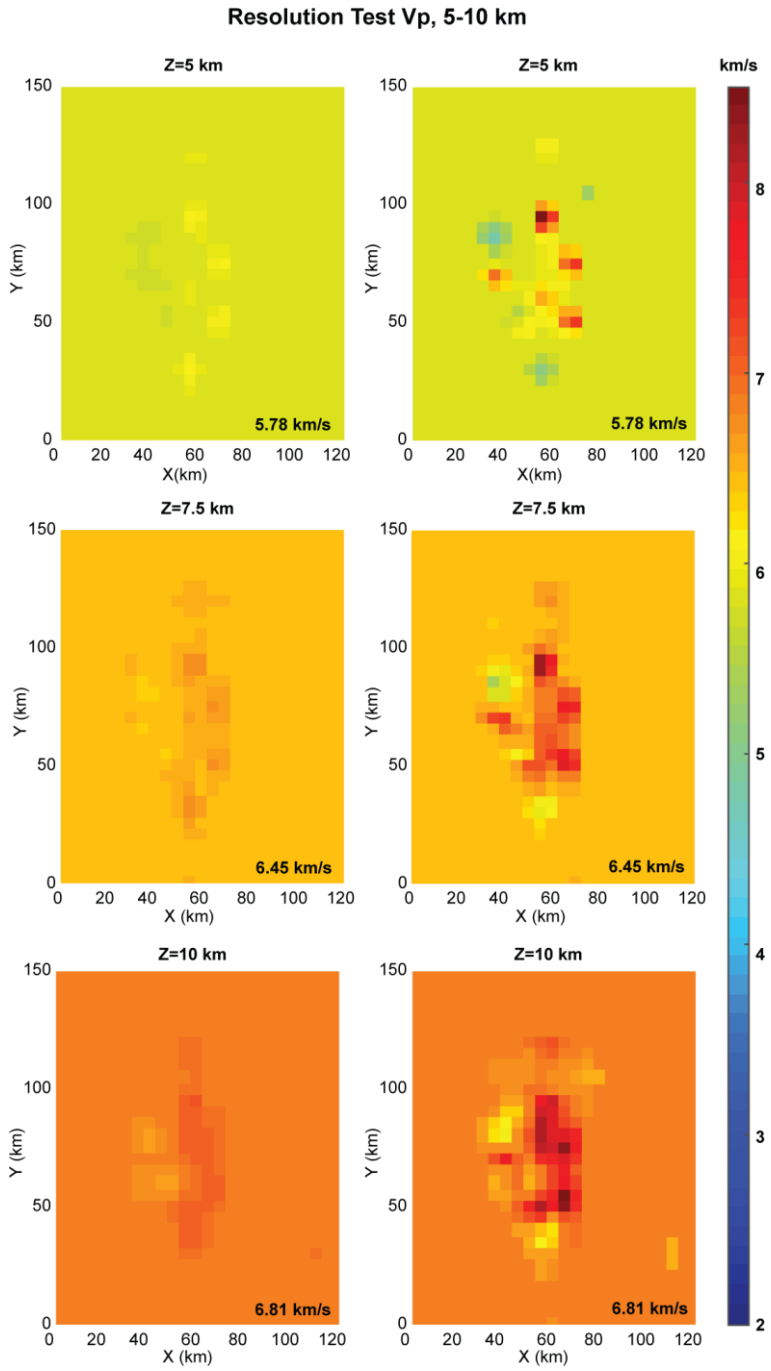

Figure H.3. Vp resolution test results at 5, 7.5, and 10 km depth slices. Resolution test shown in left panels, original model shown in right panels for comparison.

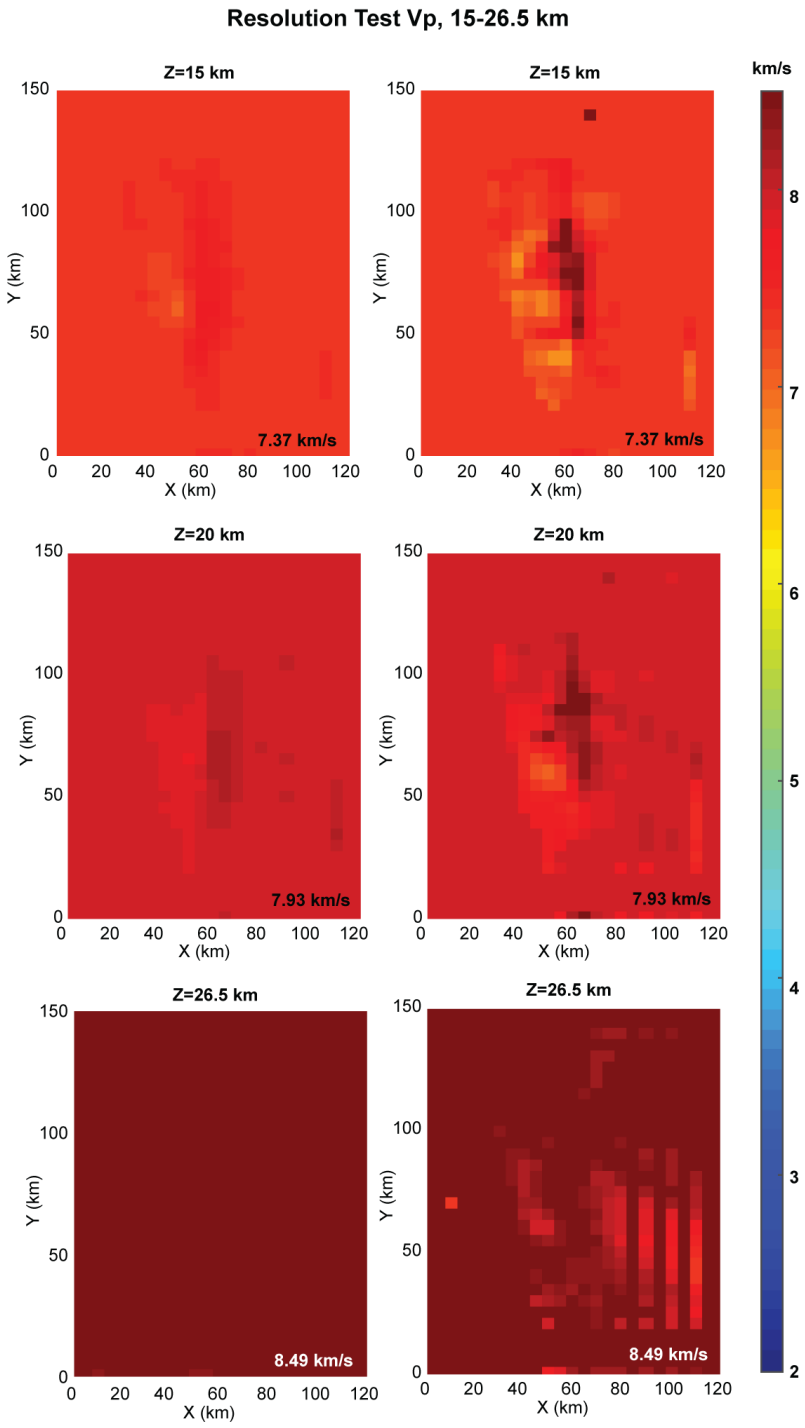

Figure H.4. Vp resolution test results at 15, 20, and 26.5 km depth slices. Resolution test shown in left panels, original model shown in right panels for comparison.

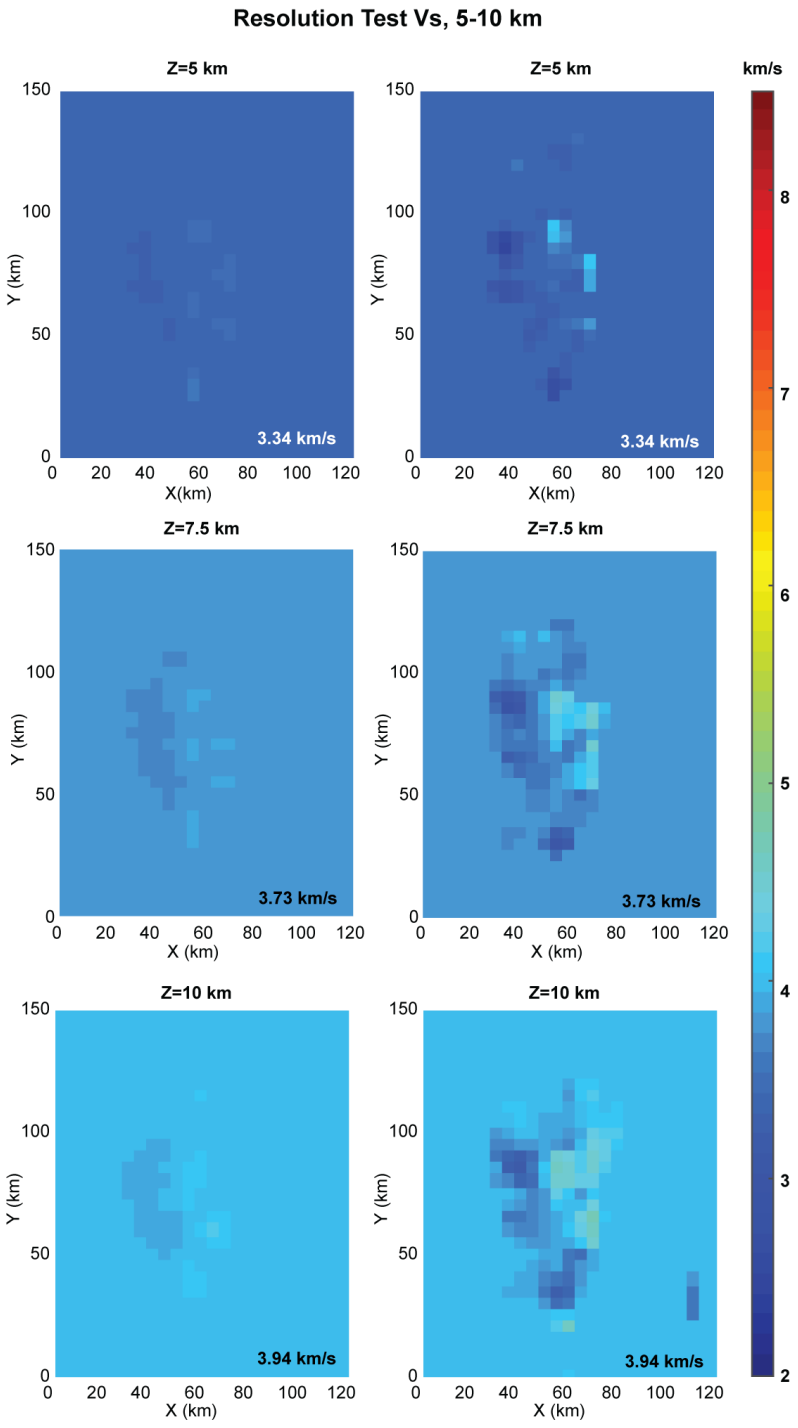

Figure H.5. Vs resolution test results at 5, 7.5, and 10 km depth slices. Resolution test shown in left panels, original model shown in right panels for comparison.

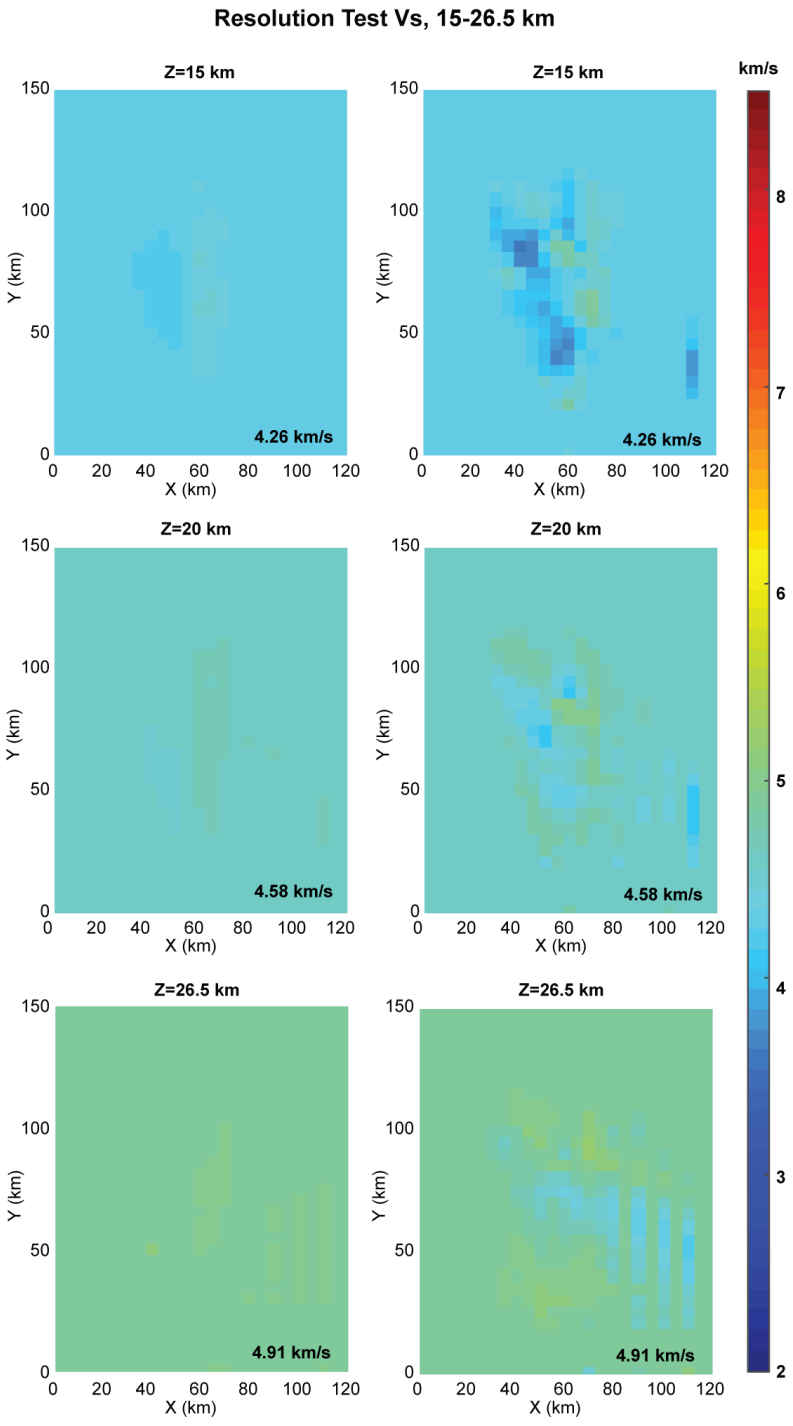

Figure H.6. Vs resolution test results at 15, 20, and 26.5 km depth slices. Resolution test shown in left panels, original model shown in right panels for comparison.

H.3 RESIDUAL TRAVEL TIMES

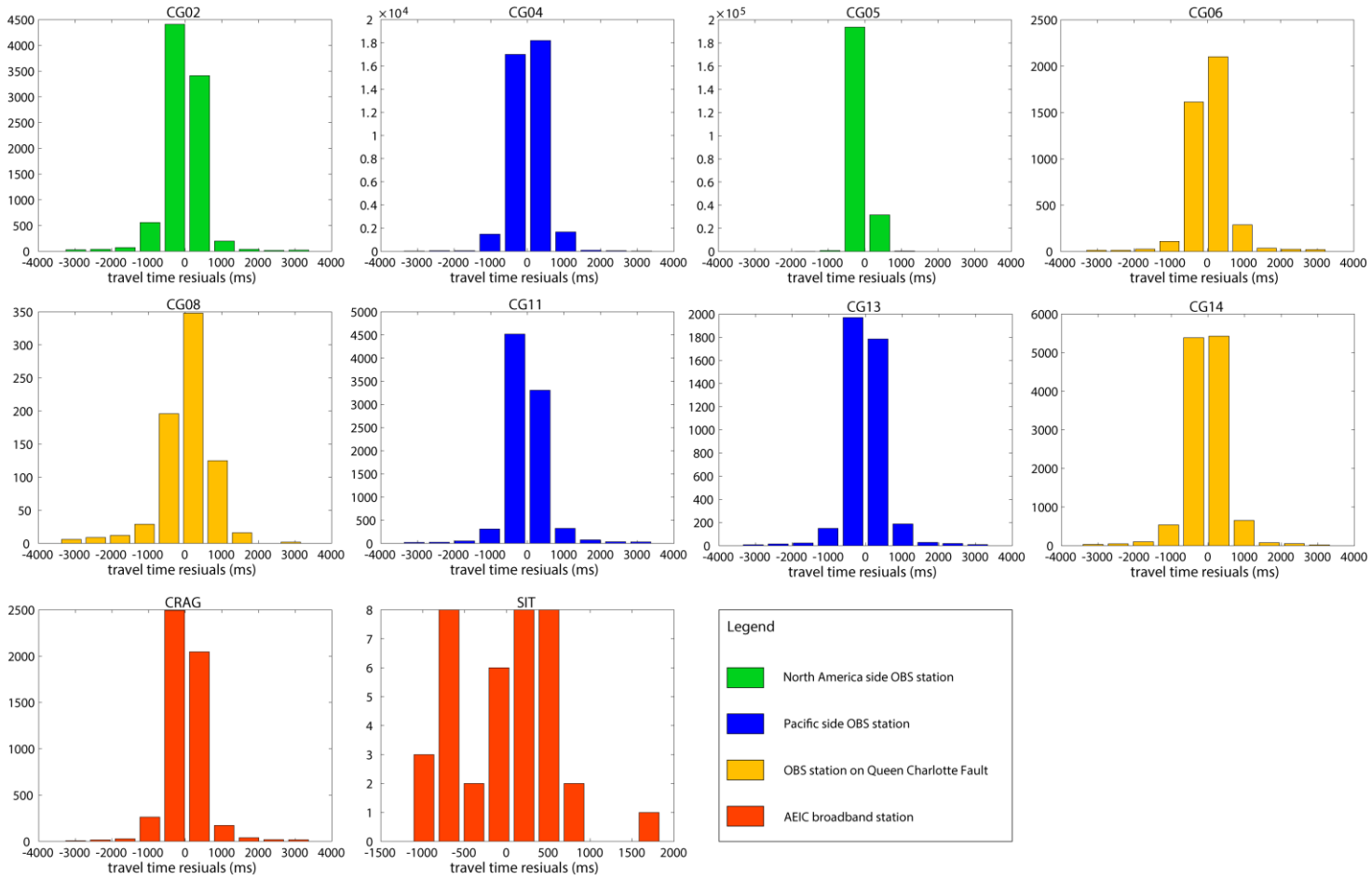

Figure H.7. Residual travel times by station for the 8 OBS stations and 2 AEIC land stations. Vertical axis indicates occurrence of residual values in the dataset. Bins vary but are generally ~500 ms.

Appendix I: Quaternary Fault and Fold Database products

Quaternary faults in southeast Alaska were mapped at UTIG using backscatter data, seafloor bathymetry, and publicly available seismic reflection data (see Appendix A). Maps were distributed to the U.S. Geological Survey (USGS) for use in the Quaternary Fault and Fold Database (QFFD). Major fault systems mapped include the Queen Charlotte Fault, Chatham Strait Fault, and offshore Fairweather Fault. New mapping was integrated with and informed by previous databases and mapping (von Huene et al., 1979; Carlson et al., 1985; Carlson et al., 1988; Bruns et al., 1992; Plafker, 1994; Reed et al., 2005). Example seismic images of each mapped fault were also included in the submission to the QFFD.

I.1 Polyline/fault shapefile attributes

FIELDNAME (description) [field properties]

OBJECTID (e.g. 1; required field)

Shape (e.g. polyline; required field)

NAME (e.g. Queen Charlotte Fault) [string, length 80]

NUM (e.g. 5527; determined from AK fault ID table) [string, length 6]

SEISNUM (e.g. 5527-01; matches with seismic crossing in point file) [long, precision 8]

ACODE (e.g. 2; translates to an age category) [long, precision 9]

SLIPCODE (e.g. 1; translates to a slip rate category) [long, precision 9]

SLIPSENSE (e.g. SS for strike-slip) [string, length 5]

DIPDIRECTION (e.g. C for center or NE for northeast) [string, length 15]

FCODE (e.g. 2; category describing continuity of fault) [long, precision 9]

MAPPEDSCALE (e.g. 1:250000; determined from…) [string, length 8]

SecondarySlipSense (e.g. R for reverse) [string, length 5]

Shape_Length (e.g. 27; calculated in km) [double, precision 0, scale 0]

STRIKE (e.g. 338; calculated in degrees clockwise from N) [short, precision 3]

COLLABORAT (e.g. The University of Texas Institute for Geophysics) [string, length 50]

OTHER_DATA (e.g. also inferred from bathymetry) [string, length 50]

I.2 POINT/PALEOSITE/SEISMIC CROSSING SHAPEFILE ATTRIBUTES

FIELDNAME (description) [field properties]

FIELDNAME (description) [field properties]

OBJECTID (e.g. 1; required field)

Shape (e.g. point; required field)

NAME (e.g. Queen Charlotte Fault) [string, length 80]

NUM (e.g. 5527; determined from…) [string, length 6]

SEISNUM (e.g. 5527-01; matches with fault crossing in polyline file) [long, precision 8]

SURVEY (e.g. EW9412; USGS identifier if available) [string, length 10]

SURVEYTYPE (e.g. MCS for multi-channel seismic) [string, length 10]

YEAR (e.g. 1994) [short; precision 4]

IMAGE_LINK (link to a seismic image file associated with this point, not populated as of 3/15/2016) [string, length 100]

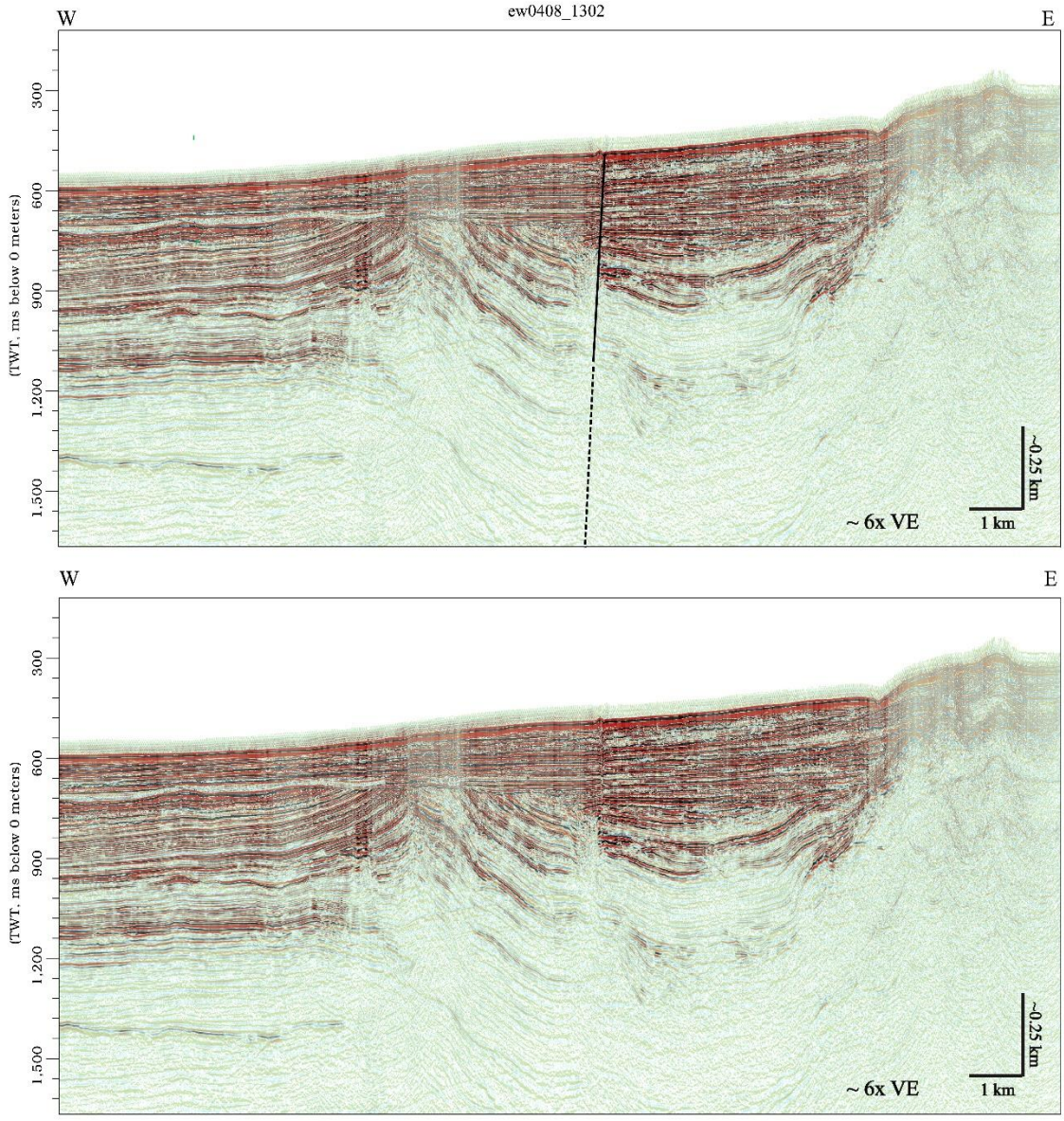

Figure I.1. Example of seismic image file associated with a fault crossing a seismic line. Locations of all such crossings are defined by a point/paleosite.

Appendix J: U.S. Extended Continental Shelf products

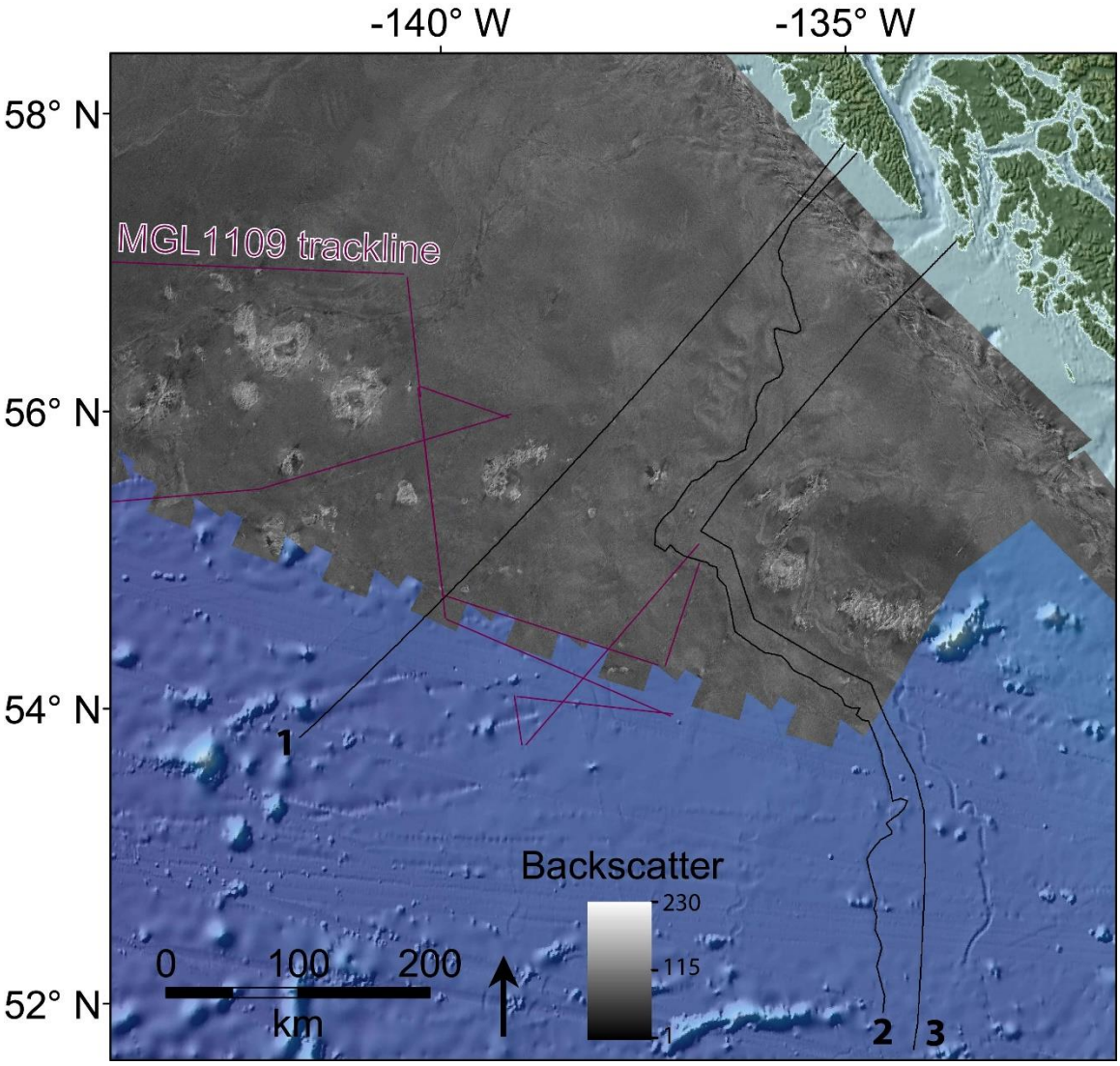

Figure J.1. Image of the southeast Gulf of Alaska showing bathymetry, GLORIA backscatter data, the MGL1109 trackline, and the locations of three sample profiles analyzed for bathymetry and gradient changes.

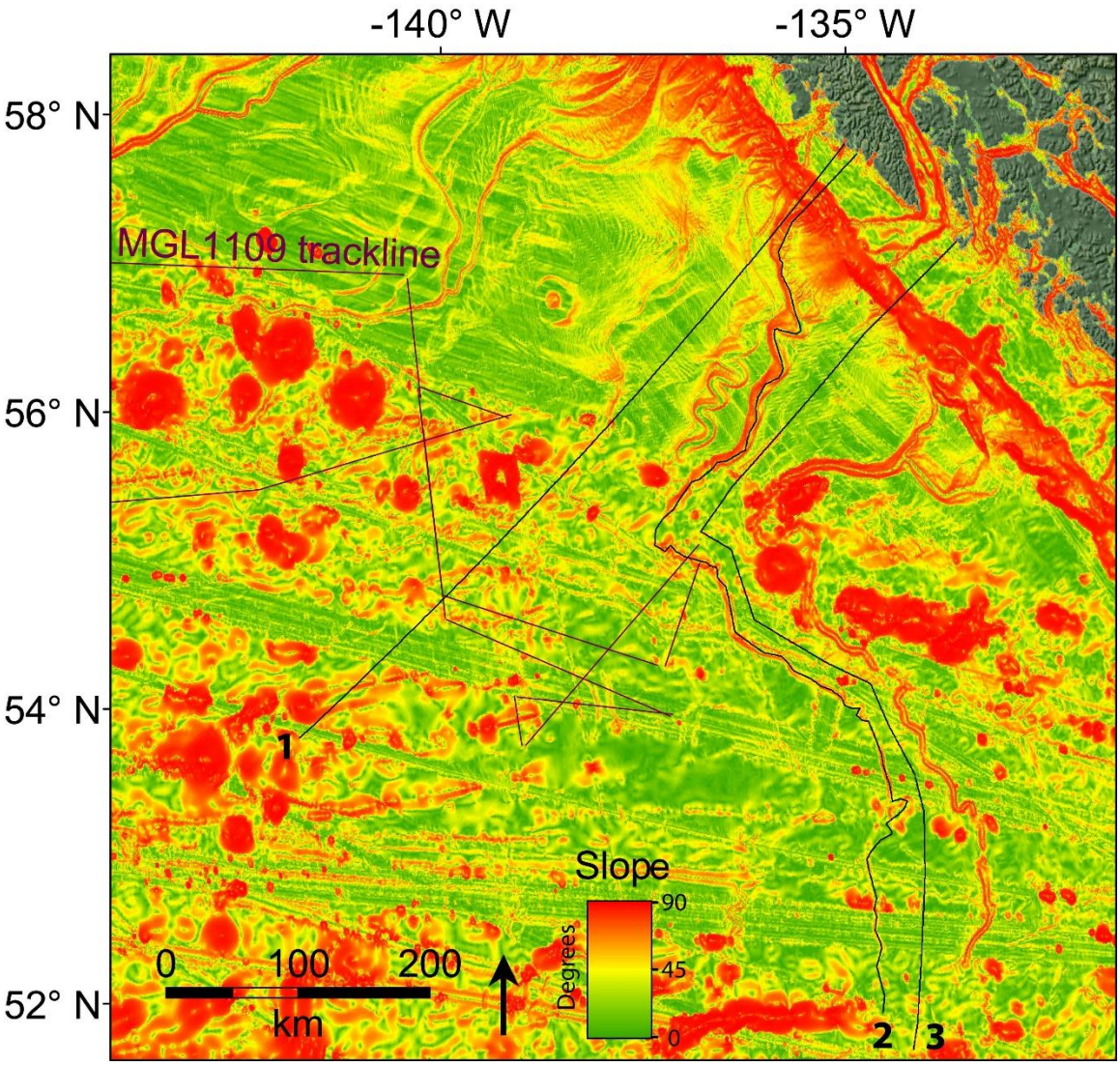

Figure J.2. Slope/gradient map of the southeast Gulf of Alaska generated from bathymetry. Map shows MGL1109 trackline and the locations of three sample profiles analyzed for bathymetry and gradient changes.

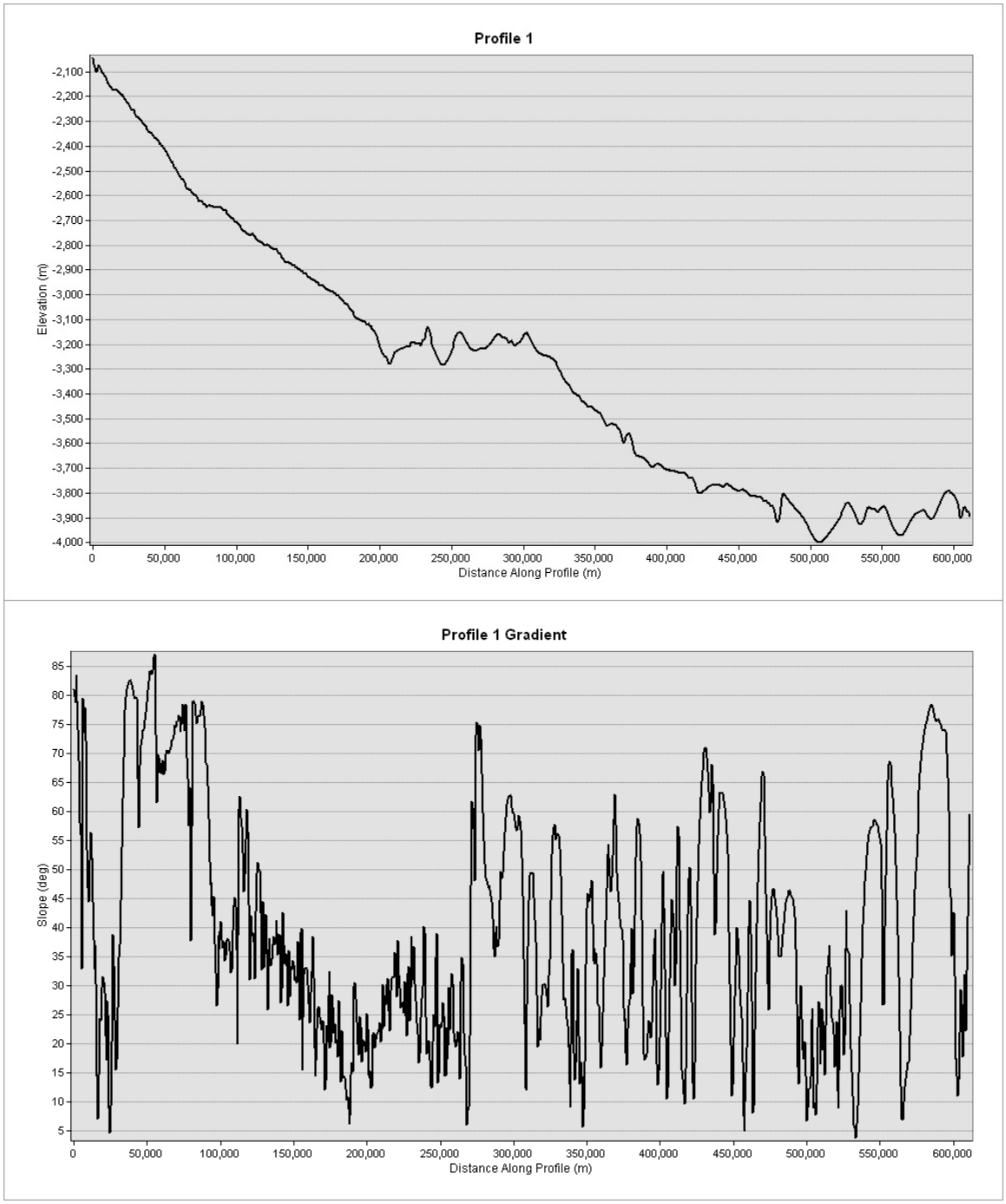

Figure J.3. Bathymetry (top) and gradient (bottom) along profile 1. See profile location in Figs. J.1 and J.2.

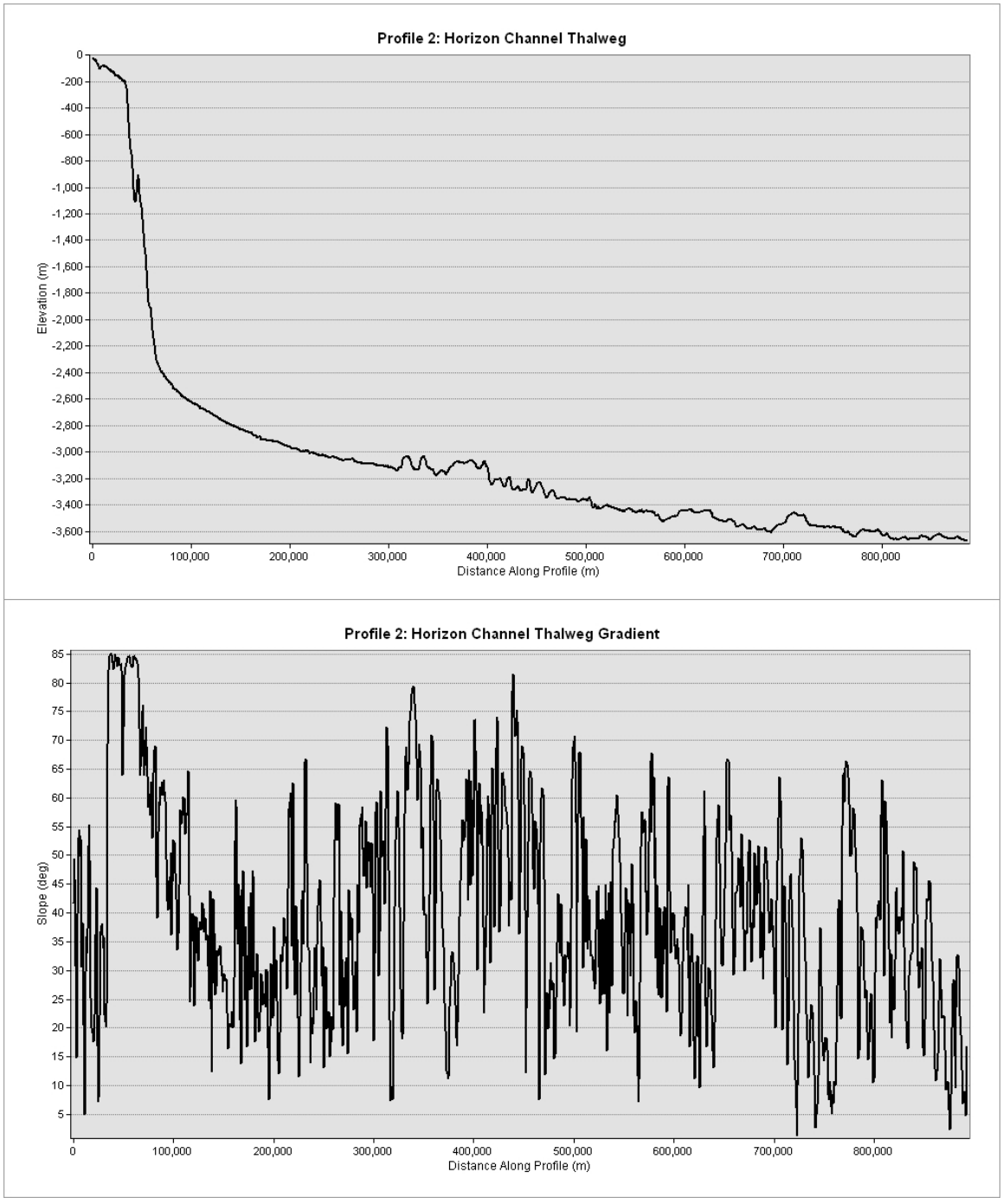

Figure J.4. Bathymetry (top) and gradient (bottom) along profile 2, the Horizon Channel thalweg. See profile location in Figs. J.1 and J.2.

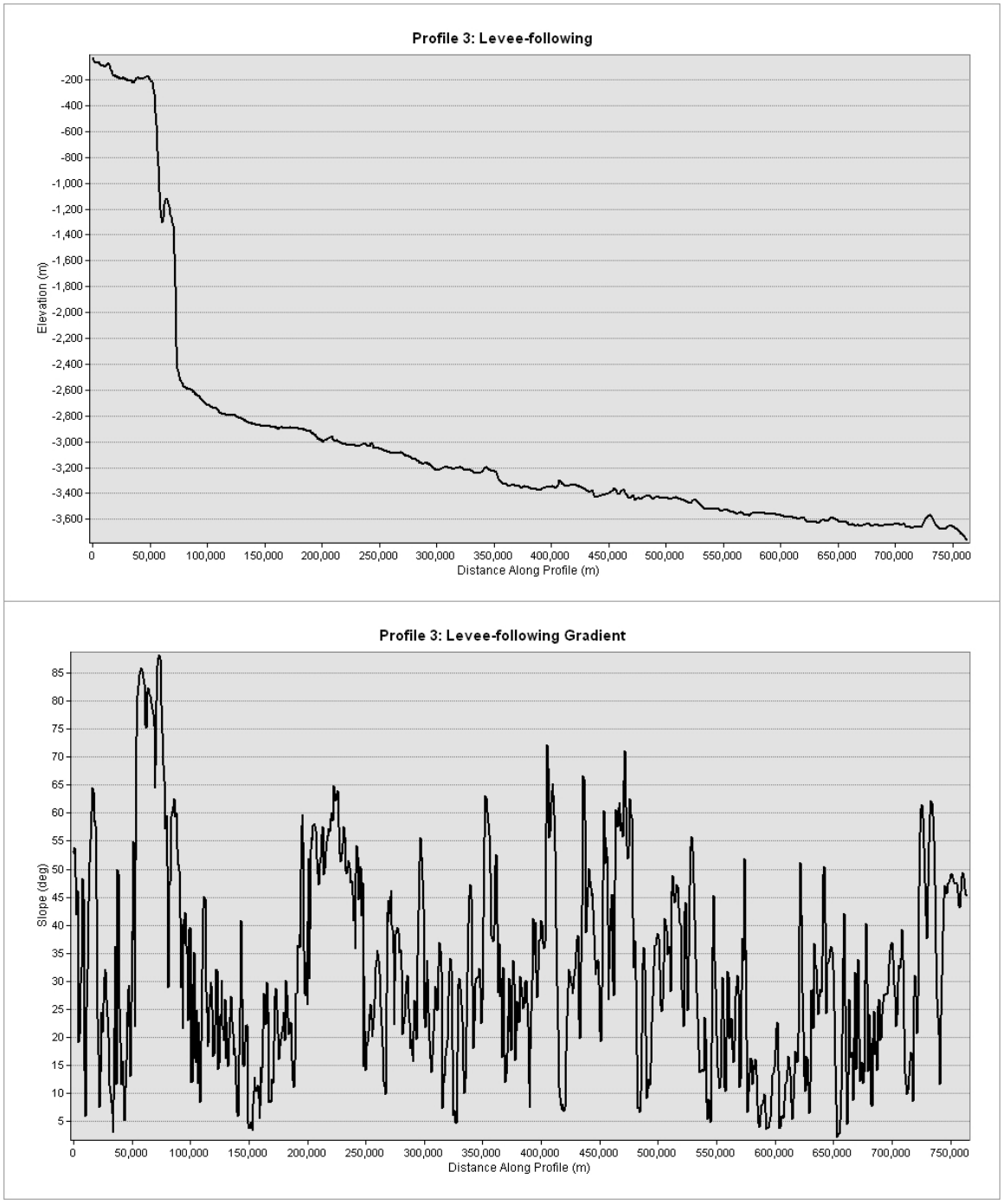

Figure J.5. Bathymetry (top) and gradient (bottom) along profile 3, following levee deposits near the Horizon Channel. See profile location in Figs. J.1 and J.2.

Appendix K: Landmark seismic import cookbook

The navigation and seismic import cookbooks below were developed at UTIG for Landmark DecisionSpace Desktop software. Slight updates might be required for newer versions of Landmark. Information is current as of 3/5/2014.

K.1 LANDMARK NAVIGATION IMPORT COOKBOOK

1) Start OpenWorks menu
2) Data -> Import -> Data import wizard, select project and interp ID
3) "Data type" tab
    a. Import data type: "Seismic 2D line" (unless you are importing different data)
    b. Select file to import (one line at a time, or you may have a file that has different seismic lines separated by specific string).
    c. You can now choose whether to define a new import format. Definitely do this ("interactively define a new format") if you need to import a lot of files that are formatted similarly. Once you've defined and saved a format, you can use your saved format to save yourself a lot of steps later on. Usually, "scanning the data file to automatically discover the format" option is ineffective, but it may be worth a try if you have industry data.
    d. Click "continue" at the bottom.
4) "Format" tab
    a. In the left panel, if it's not already there, you can add "Seis 2D Line" as a data category using the + symbol
    b. "File layout" subtab

i. Input data fields are: fixed width or delimited, depending on your data – fixed width has a bit more flexibility but is more tedious
ii. (optional) select your delimeter
iii. Usually comment defaults are ok. Update this if you have non-traditional comments or want certain lines of your data ignored

c. "File section" subtab
i. If you are just importing nav for one seismic line, select "Indicated by" and "one"
ii. If you are importing multiple lines from one nav file, select "multiple" and enter the line separator

d. "Data items" subtab – very important!!
i. Under "undefined data items", select each item you'd like to define in turn. You MUST define each item with an *, as well as latitude, longitude, shotpoint, and trace
ii. The rightmost panel is where you actually define values by either selecting a delimited column (if you selected delimited data earlier) or by highlighting the data in the first line that it appears (if you selected fixed width earlier). For both options, you'll select these values from your previewed data in the bottom panel.

5) "2D Navigation" tab
a. Use first shotpoint
b. Check "calculate missing trace ranges from the input data"

6) "Conversions" tab
a. Be sure to select the input datum under "cartographic reference system"
b. Measurement system should be "SPE Preferred Metric"

7) “Import Data” tab
    a. Click the green running man
    b. Once the import is completed, you can see any errors under the “Import Log” and “Error” tabs

K.2 LANDMARK 2D SEISMIC IMPORT COOKBOOK (POSTSTACK/PAL METHOD)

1) Start OpenWorks menu, select project
2) Applications -> Seismic processing -> PostStack/PAL
    a. Select 2D and PostStack
    b. Launch
    c. If there’s an informational message, just click OK
    d. Select interp ID
3) In the session window…
    a. Make sure there is an empty process (add a process if there isn’t, Edit -> Add)
    b. Input data -> SEGY -> parameters
    c. Click OK on any informational messages
4) In the SEG-Y Data Input window…
    a. Disk -> analyze
5) In the SEGY Analyzer window…
    a. File -> select to pick the segy files you want to import
    b. Press “start” at the top and segy information should populate the table

c. Select the lines containing info for segy files you would like to import, and click “send selected” at the bottom. If you want to import all the files, click “send all.”
d. Keep this window open in case you need to import more files later

6) Back to the SEGY data input window…
    a. Select “Enter Linenames”
    b. The top line (should say “line 1”) is extra. Select the top line, go to edit -> delete rows to remove it.
    c. Under “prefix,” enter in what you would like the prefix of your line to be (commonly, it’ll be the survey name with an underscore e.g. ew0408_). If you have multiple lines you’re importing, you can save yourself some steps by selecting all of the lines in the table and going to edit -> prefix linename to set a prefix for all of these lines.
    d. Under “linename,” enter the specific linename you would like to use (typically just a number like 05, 24, etc).
    e. Hint: the prefix and the linename put together should match the common and unique linenames you entered when importing navigation data.
    f. Once you finish entering linenames, you can close out of the window file -> close.
7) Click OK on SEGY Data Input window, OK on smaller Input Data window
8) Back to Session window…
    a. Output data -> vertical -> parameters
9) In Vertical File Parameters window…
    a. Select “List,” then search for a 32-bit dataset
    b. Format is floating point

c. Click “Basemap Info” at the bottom
    i. Select the appropriate survey and input cartographic system
    ii. Decimate shotpoints at 20 m
    iii. Duplicate shotpoints, skip line
    iv. Click close

10) Click OK on Vertical File Parameters, OK on the informational message, and OK on smaller Output Data window
11) Click Run
12) If you finish normally, great. If you finish with error, you can check out a detailed error message by going to the top of the Session window and clicking Job -> View.
13) Once you have a 32-bit dataset, you’ll most likely need to convert it to 8 bit in order to more efficiently work with it in Landmark. It’s a very similar process.
14) In Session window…
    a. Input Data -> SeisWorks Seismic -> Parameters
15) In Seisworks Input window…
    a. Select “list” at the top and choose the 32 bit dataset to which you just imported your segy files
    b. Select the other “list” in the Seisworks window, choose the specific lines you would like to convert
    c. Click OK
16) Click OK on the small Input Data window
17) Back to the Session window….
    a. Output data -> vertical -> parameters
18) In Vertical File Parameters window…
    a. Select “List,” then search for an 8-bit dataset you’d like to output to

b. Format is 8 bit, scaling is Automatic
c. Check “Scale each line independently,” 98 and 98 are fine for trace and dataset percentiles
d. Click “Basemap Info” at the bottom
    i. Select the appropriate survey and input cartographic system (remember that you are inputting data from within the project now so it’ll have the project datum)
    ii. Decimate shotpoints at 20 m
    iii. Duplicate shotpoints, skip line
    iv. Click close

19) Click OK on Vertical File Parameters, OK on the informational message, and OK on smaller Output Data window
20) Click Run
21) If you finish normally, great. If you finish with error, you can check out a detailed error message by going to the top of the Session window and clicking Job -> View
22) Check out your lines in DecisionSpace Desktop and/or the Seismic Data Manager

Appendix L: Focus to Echos upgrade cookbook

This manual was written at UTIG for upgrading Focus 5.4 projects to Echos 2011.3. Current as of 10/14/2015.

To upgrade project:

1) File location
    - All (or most) of Sean Gulick's upgraded Echos projects will go into /disk/staff/sean/Epos4
    - Subfolders database, seismic, and applications contain upgraded Echos project files
2) Launch Echos 2011.3 (most machines have 2011 installed)
3) Launch Epos 4 Project/Survey Upgrade (PSU)
    - Can be accessed from the Data Input/Output tab in 2011 version
    - In 2014 version can only be accessed by opening an Echos Shell (Options -> Shell) and typing >> PSU
4) Upgrade Parameters tab
    - If project is working in 5.4, it's a registered study, so make sure to select registered study (note we *may* be able to select unregistered if it's not in Focus but has not been tested… need all data paths for this)
    - Click folder next to Study Name, type utig2 in Host Name, and click the arrows to the right to populate the table below
    - Projects and Surveys in this list should be ok to upgrade. Click the project you want to upgrade, should take you back to the PSU window.

- Under the Upgrade area, type the name of the survey (e.g. sumut) in the Survey(s) box
- On the Database Path tab under Host Name, select the folder next to *Database Path and navigate to /disk/staff/sean/Epos4/database directory
- Click the Seismic Data Paths tab, check Seismic Data box, select Copy All Files
- Click Add, then Browse, and navigate to /disk/staff/sean/Epos4/seismic directory
- On the Applications Output Paths tab, click the folder and navigate to /disk/staff/sean/Epos4/applications directory

5) Additional Data tab
    - Check Copy Focus Data box
6) Click Upgrade

<u>To upgrade 2D velocities:</u>

1) Method 1: Use Epos utility
    - After upgrading project, open Echos terminal window (options -> shell)
    - >>sdb2vf -sdbtype vels -surveylist your-suvey-name
    - Will bring up utility showing velocities
    - Select velocity functions of interest
    - Click “Start” under “Perform Conversion(s)”
    - Check on velocities using Velocity utility or Vertical Function Data Manager
2) Method 2 (Steffen Saustrup’s method): Modify old Focus jobs and import velocities line by line

- Skip the first step if you already have a text (i.e *.dat) file of your VELDEF job. This first step is for exporting velocity jobs from the FOCUS database.
- COPY (not move) all of your VELDEF job files into a brand new directory for this conversion, to avoid doing any harm to your original VELDEF jobs.
- The second part of this workaround, which involves some text changes in the file, can be a bit tedious if you have a lot of definitions. I've written a very simple script to do all of these text substitutions for all velocity files in a directory.
- velupdate.csh looks like this:

```
#!/bin/csh
foreach file ( *veldef.dat )
  set root = $file:r
  set new = $root\_echos.dat
  echo "Converting $file to $new now."
  sed s/VELDEF/VFNDEF/ $file | sed s/HANDVEL/'vfunc  '/ - > $new
end
```

- You may need to change the foreach line to match all of your VELDEF jobs.
- You should ONLY run this script in the directory containing all of your copied VELDEF jobs !!!!! Your original VELDEF jobs are very important, don't do anything that could possibly compromise them.
- After making the text substitutions, either manually or using the script, you'll need to bring each job into an ECHOS Production window. Remove DSIN and all other modules except for VELDFN. Add a DUMIN module to the top. Make the FTYPE, FSTYPE, and VFLABEL changes as

described in the workaround document. VFLABEL is what gives the velocity function a name in the ECHOS database.

- You don't need to run the job. Click the checkmark icon in the Production Window to check the job. This will import the velocity file into ECHOS. You may get errors, but the file seems to import anyway.
- Check the velocity using the ECHOS Velocity Tool.

Appendix M: UTIG network file organization

1. PhD dissertation files, located in */disk/staff/sean/alaska/walton_phd_files/* and generally organized by project.
    a. *Baranof*. Contains MGL1109 documents, *Geosphere* paper submission and drafts, presentations and figures from various meetings, notes on related literature and from meetings, miscellaneous data (Landmark exports, volume calculations), and miscellaneous figures.
    b. *dissertation*. Contains appendices figures, chapter drafts and figures (updated and formatted for dissertation), complete dissertation drafts, and final dissertation submission files. */proposal* subfolder contains drafts, figures, and presentations used for the dissertation proposal and qualifying examination.
    c. *EndNote*. Contains master EndNote file and associated library. Many of the PDFs in the library have been annotated.
    d. *IcyBay*. Contains bathymetry, DEM, and ifSAR data from various sources and miscellaneous figures related to the Taan-Tyndall project. */proposal* subfolder contains the EHP Icy Bay proposal drafts, figures, and final submission, as well as documents associated with the Taan-Tyndall proposal.
    e. *SEAK_OBS*. Contains miscellaneous data (teleseismic arrivals), re-processing details for the L378EG and EW9412 surveys, notes on OBS processing and related literature, Illustrator, GIS, and Matlab figures used for paper and presentations, paper/dissertation chapter drafts, several presentations, and Rapid Response survey proposal and related documents.
    f. *SEAK_tectonics*. Contains earthquake data (figures, Google Earth files) for the Craig and Haida Gwaii events, Illustrator, GIS, and seismic figures used for

BSSA paper and presentations, miscellaneous notes and figures, *BSSA* paper drafts and submissions, Tréhu et al. (2015) *BSSA* paper drafts and figures, presentations (posters and talks), and Quaternary Fault and Fold Database (QFFD) documents.

g. *software.* Contains help, cookbook files, and executables for CARIS, Focus, Echos, Knudsen Chirp software, Landmark, and miscellaneous OBS programs. Also contains Fledermaus .scene and .sd files, GMT code and output files, gplates files, and MATLAB code and output files. Note that some MATLAB code is duplicated in */disk/staff/sean/alaska/obs_craig_rapid/MATLAB.*

h. *YakutatBay.* Contains data from the 2012 cruise, GPS data from various publications, digitized Plafker and Thatcher (2008) data, fault data, Illustrator, GIS, Matlab, and seismic figures, Julie Zurbuchen's thesis drafts and G^3 paper, the 2011 NEHRP proposal, notes on literature, paper text and figure drafts, and various talks and poster presentations.

2. GIS files, located in */disk/staff/sean/alaska/GIS/maps_maureen*. Top level contains maps, supfolders contain grids and shapes. Some of the more common grids and shapes have been duplicated in folders within *../GIS* for easier access.

   a. *AK_boundaries*. Shapefiles for common Alaska terranes and geographic features (e.g. coastline, Kodiak-Bowie Seamounts).

   b. *Baranof*. Shapefiles related to Baranof Fan study.

   c. *bathy.* Various bathymetry grids and DEMs used as background images.

   d. *EasyCalculate50*. GIS code used for calculating distances, angles, etc.

   e. *ECS*. Extended Contintental Shelf project maps and calculations.

   f. *faults*. Fault databases and mapped faults for all of Alaska. Also contains Quaternary Fault and Fold Database shapefiles.

g. *IcyBay*. Taan Fjord and Icy Bay bathymetry and shapefiles.

h. *OBS*. Shapefiles related to OBS study, including faults, OBS stations, and earthquake events.

i. *SEAK*. Southeast Alaska shapefiles and grids related to *BSSA* publication.

j. *seismic_dsd*. MCS trackline shapefiles exported from Landmark's DecisionSpace Desktop.

k. *usgs_NAgeol*. Database of North American geology shapefiles and maps.

l. *Yakutat.* Bathymetry, shapefiles, GPS, and geology data for the Yakutat Bay region.

3. OBS files, located in */disk/staff/sean/alaska/obs_craig_rapid*

   a. *day_volumes.* Raw OBS data.

   b. *examples*. hypoDD and tomoDD example data and code.

   c. *Matlab*. Code and output files used for OBS imaging. Note that many files are duplicated in */disk/staff/sean/alaska/walton_phd_files/software/matlab.*

   d. *notes.* Contains miscellaneous notes on Antelope software. Duplicated in */disk/staff/sean/alaska/walton_phd_files/SEAK_OBS/notes/antelope.*

   e. *QCFdb*.* Antelope database files and phase data for Craig OBS data. Working database is QCFdb2 (larger catalog of events than QCFdb1).

   f. *QCFhypoDD*.* HypoDD data files for Craig OBS data. Working folder is QCFhypoDD2.

   g. *QCFtomoDD**. TomoDD files for Craig OBS data. Working folder is QCFtomoDD2. Organization is similar to Matlab subfolder. *QCFtomoDD_synth* contains resolution testing results.

   h. *UWJan15_maureen_firstrun*. Contains files from initial trials during visit to the University of Washington in January 2015.

Appendix N. List of supplemental files

1. *BaranofMovie.mp4*. Animation showing 8 m.y. tectonic reconstruction of Baranof deep-sea fan channel development.
2. *tomoDD_input.zip.* Select tomoDD input files from preferred model, including tomoDD.inp, starting velocity model (MOD), input stations (craig2.sta.input), and original 2345 events (both.event).
3. *tomoDD_output.zip.* Select tomoDD output files from preferred tomographic model, including detailed velocity output (craig2.vel), parsed Vp and Vs models (*_model_craig2.dat), parsed DWS values for Vp and Vs models (craig2.dws_*), relocated events (craig2.reloc), residual travel times (craig2.res), and tomoDD.log.
4. *OBS_matlab*. Select MATLAB code used for visualizing tomoDD output models (plt2D_all_local.m), velocity models (avg_vel_local.m), and relocated aftershocks (*_events_local.m).

References

Abe, K., and S. Noguchi (1983), Revision of magnitudes of large shallow earthquakes, 1897–1912, *Phys. Earth Planet. In.*, *33*(1), 1-11.

Abers, G. A. (2008), Orogenesis from subducting thick crust and evidence from Alaska, *Active Tectonics and Seismic Potential of Alaska*, 337-349.

Abreu, V., M. Sullivan, C. Pirmez, and D. Mohrig (2003), Lateral accretion packages (LAPs): an important reservoir element in deep water sinuous channels, *Marine and Petroleum Geology*, *20*(6-8), 631-648.

Aderhold, K., and R. Abercrombie (2015), Seismic Rupture on an Oceanic–Continental Plate Boundary: Strike-Slip Earthquakes along the Queen Charlotte–Fairweather Fault, *Bull. Seismol. Soc. Am.*, *105*(2b), 1129-1142.

Aiken, C., J. P. Zimmerman, Z. Peng, and J. I. Walter (2015), Triggered seismic events along the eastern Denali fault in northwest Canada following the 2012 M_w 7.8 Haida Gwaii, 2013 M_w 7.5 Craig, and two M_w> 8.5 teleseismic earthquakes, *Bull. Seismol. Soc. Am.*.

Amante, C., and B. W. Eakins (2009), *ETOPO1 1 arc-minute global relief model: procedures, data sources and analysis*, U.S. Department of Commerce, National Oceanic and Atmospheric Administration, National Environmental Satellite, Data, and Information Service, National Geophysical Data Center, Marine Geology and Geophysics Division.

Ammon, C. J., T. Lay, H. Kanamori, and M. Cleveland (2011), A rupture model of the 2011 off the Pacific coast of Tohoku Earthquake, *Earth, Planets and Space*, *63*(7), 693-696.

Ammon, C. J., C. Ji, H.-K. Thio, D. Robinson, S. Ni, V. Hjorleifsdottir, H. Kanamori, T. Lay, S. Das, and D. Helmberger (2005), Rupture process of the 2004 Sumatra-Andaman earthquake, *Science*, *308*(5725), 1133-1139.

Ampuero, J.-P., and Y. Ben-Zion (2008), Cracks, pulses and macroscopic asymmetry of dynamic rupture on a bimaterial interface with velocity-weakening friction, *Geophys. J. Int.*, *173*(2), 674-692.

Atwater, T. (1970), Implications of plate tectonics for the Cenozoic tectonic evolution of western North America, *Bull. Geol. Soc. Am.*, *81*(12), 3513-3536.

Babonneau, N., A. Cattaneo, B. Savoye, G. Barjavel, J. Déverchère, and K. Yelles (2012), The Kramis Deep-Sea Fan off Western Algeria: Role of Sediment Waves in Turbiditic Levee Growth, *SEPM Special Publication*, *99*, 293-308.

Barnes, N. E., and W. R. Normark (1985), Diagnostic parameters for comparing modern submarine fans and ancient turbidite systems, in *Submarine Fans and Related*

Turbidite Systems, edited by A. H. Bouma, W. R. Normark and N. E. Barnes, New York, Springer-Verlag.

Barrie, J. V., K. W. Conway, and P. T. Harris (2013), The Queen Charlotte Fault, British Columbia: seafloor anatomy of a transform fault and its influence on sediment processes, *Geo-Mar. Lett.*, 1-8.

Bart, P. J., M. De Batis, and W. Jokat (1999), Interglacial collapse of Crary Trough-Mouth Fan, Weddell Sea, Antarctica: Implications for Antarctic glacial history, *Journal of Sedimentary Research*, *69*(6), 1276-1289.

Berger, A. L., S. P. Gulick, J. A. Spotila, P. Upton, J. M. Jaeger, J. B. Chapman, L. A. Worthington, T. L. Pavlis, K. D. Ridgway, and B. A. Willems (2008), Quaternary tectonic response to intensified glacial erosion in an orogenic wedge, *Nature Geoscience*, *1*(11), 793-799.

Berggren, W. A., D. V. Kent, J. J. Flynn, and J. A. Van Couvering (1985), Cenozoic geochronology, *Bull. Geol. Soc. Am.*, *96*(11), 1407-1418.

Bérubé, J., G. C. Rogers, R. M. Ellis, and E. O. Hasselgren (1989), A microseismicity study of the Queen Charlotte Islands region, *Can. J. Earth Sci.*, *26*(12), 2556-2566.

Bostwick, T. K. (1984), A Re-examination of the August 22, 1949 Queen Charlotte Earthquake (M.S. thesis), 126 pp, The University of British Columbia.

Botros, M., and H. P. Johnson (1988), Tectonic evolution of the Explorer-Northern Juan de Fuca Region from 8 Ma to the present, *J. Geophys. Res.*, *93*(B9), 10421-10437.

Bouchon, M., H. Karabulut, M.-P. Bouin, J. Schmittbuhl, M. Vallée, R. Archuleta, S. Das, F. Renard, and D. Marsan (2010), Faulting characteristics of supershear earthquakes, *Tectonophysics*, *493*(3), 244-253.

Bruhat, L., Z. Fang, and E. M. Dunham (2016), Rupture complexity and the supershear transition on rough faults, *J. Geophys. Res.*

Bruhn, R. L., T. L. Pavlis, G. Plafker, and L. Serpa (2004), Deformation during terrane accretion in the Saint Elias orogen, Alaska, *Bull. Geol. Soc. Am.*, *116*(7-8), 771-787.

Bruhn, R. L., J. Sauber, M. M. Cotton, T. L. Pavlis, E. Burgess, N. Ruppert, and R. R. Forster (2012), Plate margin deformation and active tectonics along the northern edge of the Yakutat Terrane in the Saint Elias Orogen, Alaska, and Yukon, Canada, *Geosphere*, *8*(6), 1384-1407.

Bruns, T. R. (1982), Structure and petroleum potential of the continental margin between Cross Sound and Icy Bay, northern Gulf of Alaska, 64 pp, U.S. Geological Survey Open-File Report 82-929.

Bruns, T. R., D. M. Mann, and R. W. Sliter (1987), Multichannel seismic-reflection profiles collected in 1978 in the eastern Gulf of Alaska, U.S. Geological Survey Open-File Report 2331-1258.

Bruns, T. R., A. J. Stevenson, and M. R. Dobson (1992), *GLORIA Investigation of the Exclusive Economic Zone in the Gulf of Alaska and Off Southeast Alaska: M/V Farnella Cruise F7-89-GA, June 14-July 13, 1989*, U.S. Department of the Interior, U.S. Geological Survey.

Bruns, T., R. Von Huene, P. Carlson, and G. Keller (1984), The eastern Gulf of Alaska transcurrent plate boundary and the migration of terranes, *Ann. Soc. Geol. Nord*, *103*, 325-331.

Bustin, A., R. Hyndman, H. Kao, and J. Cassidy (2007), Evidence for underthrusting beneath the Queen Charlotte Margin, British Columbia, from teleseismic receiver function analysis, *Geophys. J. Int.*, *171*(3), 1198-1211.

Carbotte, S. M., J. M. Dixon, E. Farrar, E. E. Davis, and R. P. Riddihough (1989), Geological and geophysical characteristics of the Tuzo Wilson Seamounts: implications for plate geometry in the vicinity of the Pacific – North America – Explorer triple junction, *Can. J. Earth Sci.*, *26*(11), 2365-2384.

Carlson, P. R., G. Plafker, and T. R. Bruns (1985), *Map and selected seismic profiles of the seaward extension of the Fairweather Fault, eastern Gulf of Alaska*, U.S. Geological Survey.

Carlson, P. R., T. R. Bruns, and G. Plafker (1988), Late Cenozoic offsets on the offshore connection between the Fairweather and Queen Charlotte faults off southeast Alaska, *Mar. Geol.*, *85*(1), 89-97.

Carlson, P. R., T. R. Bruns, B. F. Molnia, and W. C. Schwab (1982), Submarine valleys in the northeastern Gulf of Alaska: Characteristics and probable origin, *Mar. Geol.*, *47*(3–4), 217-242.

Carlson, P. R., A. J. Stevenson, T. R. Bruns, D. M. Mann, and Q. Huggett (1996), Sediment pathways in the Gulf of Alaska from beach to abyssal plain, in *Geology of the United States Seafloor: The View from GLORIA*, edited by J. V. Gardner, M. E. Field and Twichell, pp. 255-277, Cambridge University, Cambridge.

Chapman, J. B., T. L. Pavlis, R. L. Bruhn, L. L. Worthington, S. P. Gulick, and A. L. Berger (2012), Structural relationships in the eastern syntaxis of the St. Elias orogen, Alaska, *Geosphere*, *8*(1), 105-126.

Chase, R., and D. Tiffin (1972), Queen Charlotte Fault zone, British Columbia, *Marine Geology & Geophysics*, *8*, 17-27.

Christensen, N., and W. Mooney (1995), Seismic velocity structure and composition of the continental crust: A global view, *J. Geophys. Res.*, (100), 9761-9788.

Christeson, G. L., S. P. S. Gulick, H. van Avendonk, R. S. Reece, and L. L. Worthington (2010), The Yakutat Terrane: Dramatic change in crustal thickness across the Transition fault, Alaska, *Geology*, *38*(10), 895-898.

Church, J. A., and N. J. White (2011), Sea-level rise from the late 19th to the early 21st century, *Surveys in Geophysics*, *32*(4-5), 585-602.

Clark, P. U., D. Archer, D. Pollard, J. D. Blum, J. A. Rial, V. Brovkin, A. C. Mix, N. G. Pisias, and M. Roy (2006), The middle Pleistocene transition: characteristics, mechanisms, and implications for long-term changes in atmospheric PCO2, *Quaternary Science Reviews*, *25*(23-24), 3150-3184.

Clift, P. D., N. Shimizu, G. D. Layne, J. S. Blusztajn, C. Gaedicke, H. U. Schluter, M. K. Clark, and S. Amjad (2001), Development of the Indus Fan and its significance for the erosional history of the Western Himalaya and Karakoram, *Bull. Geol. Soc. Am.*, *113*(8), 1039-1051.

Coffman, J. L., C. A. Von Hake, and C. W. Stover (1982), Earthquake history of the United States *Rep.*, U.S. Department of Commerce, National Oceanic and Atmospheric Administration; U.S. Department of the Interior, Geological Survey.

Coney, P. J., D. L. Jones, and J. W. Monger (1980), Cordilleran suspect terranes, *Nature*, *288*(5789), 329-333.

Cossu, R., and M. G. Wells (2010), Coriolis forces influence the secondary circulation of gravity currents flowing in large-scale sinuous submarine channel systems, *Geophys. Res. Lett.*, *37*(17), L17603.

Cotton, M. M., R. L. Bruhn, J. Sauber, E. Burgess, and R. R. Forster (2014), Ice surface morphology and flow on Malaspina Glacier, Alaska: Implications for regional tectonics in the Saint Elias orogen, *Tectonics*, *33*(4), 581-595.

Covault, J. A., B. W. Romans, A. Fildani, M. McGann, and S. A. Graham (2010), Rapid Climatic Signal Propagation from Source to Sink in a Southern California Sediment-Routing System, *The Journal of Geology*, *118*(3), 247-259.

Covault, J., W. Craddock, B. Romans, A. Fildani, and M. Gosai (2013), Spatial and temporal variations in landscape evolution: Historic and longer-term sediment flux through global catchments, *The Journal of Geology*, *121*(1), 35-56.

Cowan, E. A., P. R. Carlson, and R. D. Powell (1996), The marine record of the Russell Fiord outburst flood, Alaska, USA, *Annals of Glaciology*, *22*, 194-199.

Crouch, J. K., S. B. Bachman, and J. T. Shay (1984), Post-Miocene compressional tectonics along the central California margin, *Tectonics and Sedimentation Along the Central California Margin, Annu. Meet. Pap.*, *38*, 37-54.

Cunningham, W., and P. Mann (2007), Tectonics of strike-slip restraining and releasing bends, *Geological Society, London, Special Publications*, *290*(1), 1-12.

Damuth, J., and R. Flood (1983), Morphology, sedimentation processes, and growth pattern of the Amazon Deep-Sea Fan, *Geo-Mar. Lett.*, *3*(2-4), 109-117.

Davis, E. E., and D. A. Seemann (1981), A compilation of seismic reflection profiles across the continental margin of western Canada *Rep.*, Geological Survey of Canada, Open File 751.

Dehler, S. A., and R. M. Clowes (1988), The Queen Charlotte Islands refraction project. Part I. The Queen Charlotte Fault Zone, *Can. J. Earth Sci.*, *25*(11), 1857-1870.

DeMets, C., R. G. Gordon, and D. F. Argus (2010), Geologically current plate motions, *Geophys. J. Int.*, *181*(1), 1-80.

Deptuck, M. E., G. S. Steffens, M. Barton, and C. Pirmez (2003), Architecture and evolution of upper fan channel-belts on the Niger Delta slope and in the Arabian Sea, *Marine and Petroleum Geology*, *20*(6), 649-676.

Ding, K., J. T. Freymueller, Q. Wang, and R. Zou (2015), Coseismic and early postseismic deformation of the 5 January 2013 Craig Mw 7.5 earthquake from static and kinematic GPS solutions, *Bull. Seismol. Soc. Am.*, *105*(2b), 1153-1164.

Dobson, M. R., D. O'Leary, and M. Veart (1998), Sediment delivery to the Gulf of Alaska: source mechanisms along a glaciated transform margin, *Geological Society, London, Special Publications*, *129*(1), 43-66.

Doser, D. I. (2006), Relocations of earthquakes (1899–1917) in south-central Alaska, *Pure and Applied Geophysics*, *163*(8), 1461-1476.

Doser, D. I., and H. Rodriguez (2011), A seismotectonic study of the Southeastern Alaska Region, *Tectonophysics*, *497*(1), 105-113.

Doubrovine, P. V., and J. A. Tarduno (2008), A revised kinematic model for the relative motion between Pacific oceanic plates and North America since the Late Cretaceous, *J. Geophys. Res.*, *113*(B12).

Dowdeswell, J. A., N. H. Kenyon, A. Elverhøi, J. S. Laberg, F. J. Hollender, J. Mienert, and M. J. Siegert (1996), Large-scale sedimentation on the glacier-influenced polar North Atlantic Margins: Long-range side-scan sonar evidence, *Geophys. Res. Lett.*, *23*(24), 3535-3538.

Dunham, E. M., and R. J. Archuleta (2004), Evidence for a supershear transient during the 2002 Denali fault earthquake, *Bull. Seismol. Soc. Am.*, *94*(6B), S256-S268.

Eberhart-Philips, D., D. H. Christensen, T. M. Brocher, R. Hansen, N. A. Ruppert, P. J. Haeussler, and G. A. Abers (2006), Imaging the transition from Aleutian subduction to Yakutat collision in central Alaska, with local earthquakes and active source data, *J. Geophys. Res.*, *111*(B11), 31.

Ekström, G., M. Nettles, and A. Dziewoński (2012), The global CMT project 2004–2010: centroid-moment tensors for 13,017 earthquakes, *Phys. Earth Planet. In.*, *200*, 1-9.

Elliott, J., J. T. Freymueller, and C. F. Larsen (2013), Active tectonics of the St. Elias orogen, Alaska, observed with GPS measurements, *J. Geophys. Res.*, *118*(10), 5625-5642.

Elliott, J. L., C. F. Larsen, J. T. Freymueller, and R. J. Motyka (2010), Tectonic block motion and glacial isostatic adjustment in southeast Alaska and adjacent Canada constrained by GPS measurements, *J. Geophys. Res.*, *115*(B9), B09407.

Elmore, C. R., S. P. Gulick, B. Willems, and R. Powell (2013), Seismic stratigraphic evidence for glacial expanse during glacial maxima in the Yakutat Bay Region, Gulf of Alaska, *Geochem. Geophys. Geosys.*, *14*(4), 1294-1311.

Enkelmann, E., P. G. Valla, and J.-D. Champagnac (2015), Low-temperature thermochronology of the Yakutat plate corner, St. Elias Range (Alaska): bridging short-term and long-term deformation, *Quaternary Science Reviews*, *113*, 23-38.

Enkelmann, E., P. K. Zeitler, T. L. Pavlis, J. I. Garver, and K. D. Ridgway (2009), Intense localized rock uplift and erosion in the St Elias orogen of Alaska, *Nature Geosci*, *2*(5), 360-363.

Estabrook, C. H., J. L. Nábělek, and A. L. Lerner-Lam (1992), Tectonic model of the Pacific-North American Plate Boundary in the Gulf of Alaska from broadband analysis of the 1979 St. Elias, Alaska, earthquake and its aftershocks, *J. Geophys. Res.*, *97*(B5), 6587-6612.

Farahbod, A. M., and H. Kao (2015), Spatiotemporal distribution of events during the first week of the 2012 Haida Gwaii aftershock sequence, *Bull. Seismol. Soc. Am.*, *105*(2b), 1231-1240.

Farley, K. A., M. E. Rusmore, and S. W. Bogue (2001), Post–10 Ma uplift and exhumation of the northern Coast Mountains, British Columbia, *Geology*, *29*(2), 99-102.

Fildani, A., and W. R. Normark (2004), Late Quaternary evolution of channel and lobe complexes of Monterey Fan, *Mar. Geol.*, *206*(1), 199-223.

Fildani, A., W. R. Normark, S. Kostic, and G. Parker (2006), Channel formation by flow stripping: Large-scale scour features along the Monterey East Channel and their relation to sediment waves, *Sedimentology*, *53*(6), 1265-1287.

Finn, S. P., L. M. Liberty, P. J. Haeussler, and T. L. Pratt (2015), Landslides and Megathrust Splay Faults Captured by the Late Holocene Sediment Record of Eastern Prince William Sound, Alaska, *Bull. Seismol. Soc. Am.*.

Fletcher, H. J., and J. T. Freymueller (2003), New constraints on the motion of the Fairweather Fault, Alaska, from GPS observations, *Geophys. Res. Lett.*, *30*(3), 1139.

Freymueller, J. T., M. H. Murray, P. Segall, and D. Castillo (1999), Kinematics of the Pacific–North America plate boundary zone, northern California, *J. Geophys. Res.*, *104*(B4), 7419-7441.

Froment, B., J. J. McGuire, R. Hilst, P. Gouédard, E. C. Roland, H. Zhang, and J. A. Collins (2014), Imaging along-strike variations in mechanical properties of the Gofar transform fault, East Pacific Rise, *J. Geophys. Res.*, *119*(9), 7175-7194.

Gardner, J. V., L. A. Mayer, and A. Armstrong (2006), Mapping supports potential submission to U.N. Law of the Sea, *EOS Trans. AGU*, *87*, 157-160.

Gardner, M., S. Bergman, G. Cushing, E. MacKevett, G. Plafker, R. Campbell, C. Dodds, W. McClelland, and P. Mueller (1988), Pennsylvanian pluton stitching of Wrangellia and the Alexander terrane, Wrangell Mountains, Alaska, *Geology*, *16*(11), 967-971.

Gehrels, G. E. (1990), Late Proterozoic-Cambrian metamorphic basement of the Alexander terrane on Long and Dall Islands, southeast Alaska, *Bull. Geol. Soc. Am.*, *102*(6), 760-767.

Goff, J. A., D. E. Lawson, B. A. Willems, M. Davis, and S. P. Gulick (2012), Morainal bank progradation and sediment accumulation in Disenchantment Bay, Alaska: Response to advancing Hubbard Glacier, *J. Geophys. Res. (2003–2012)*, *117*(F2).

Gulick, S. P. S., L. A. Lowe, T. L. PavIis, J. V. Gardner, and L. A. Mayer (2007), Geophysical insights into the Transition fault debate: Propagating strike slip in response to stalling Yakutat block subduction in the Gulf of Alaska, *Geology*, *35*(8), 763-766.

Gulick, S., R. Reece, G. Christeson, H. van Avendonk, L. Worthington, and T. Pavlis (2013), Seismic images of the Transition fault and the unstable Yakutat–Pacific–North American triple junction, *Geology*, *41*(5), 571-574.

Gulick, S., R. Powell, J. Jaeger, E. Cowan, L. Mayer, A. Mix, B. Finney, N. Pisias, F. Prahl, and J. Stoner (2004), Glacial advances and retreats in tectonic southeast Alaska during the little Ice Age and last glacial maximum: Preliminary results from EW0408, paper presented at AGU Fall Meeting Abstracts.

Gulick, S. P., J. M. Jaeger, A. C. Mix, H. Asahi, H. Bahlburg, C. L. Belanger, G. B. Berbel, L. Childress, E. Cowan, and L. Drab (2015), Mid-Pleistocene climate transition drives net mass loss from rapidly uplifting St. Elias Mountains, Alaska, *Proceedings of the National Academy of Sciences*, *112*(49), 15042-15047.

Haeussler, P. J., D. C. Bradley, R. E. Wells, and M. L. Miller (2003), Life and death of the Resurrection plate: Evidence for its existence and subduction in the northeastern Pacific in Paleocene–Eocene time, *Bull. Geol. Soc. Am.*, *115*(7), 867-880.

Haeussler, P. J., P. A. Armstrong, L. M. Liberty, K. M. Ferguson, S. P. Finn, J. C. Arkle, and T. L. Pratt (2015), Focused exhumation along megathrust splay faults in Prince William Sound, Alaska, *Quaternary Science Reviews*, *113*, 8-22.

Harris, R. A., and P. Segall (1987), Detection of a locked zone at depth on the Parkfield, California, segment of the San Andreas fault, *J. Geophys. Res.*, *92*(B8), 7945-7962.

Harris, R. N., and D. S. Chapman (1994), A comparison of mechanical thickness estimates from trough and seamount loading in the southeastern Gulf of Alaska, *J. Geophys. Res.*, *99*(B5), 9297-9317.

Hayes, G. P. (2011), Rapid source characterization of the 2011 M w 9.0 off the Pacific coast of Tohoku Earthquake, *Earth, planets and space*, *63*(7), 529-534.

Holtkamp, S., and N. Ruppert (2015), A High Resolution Aftershock Catalog of the Magnitude 7.5 Craig, Alaska, Earthquake on 5 January 2013, *Bull. Seismol. Soc. Am.*, *105*(2b), 1143-1152.

Horn, J., R. Clowes, R. Ellis, and D. Bird (1984), The seismic structure across an active oceanic/continental transform fault zone, *J. Geophys. Res.*, *89*(B5), 3107-3120.

Howell, D. G., and K. A. McDougall (1978), *Mesozoic paleogeography of the western United States*, Pacific Section, Society of Economic Paleontologists and Mineralogists.

Hyndman, R., and R. Ellis (1981), Queen Charlotte Fault zone: microearthquakes from a temporary array of land stations and ocean bottom seismographs, *Can. J. Earth Sci.*, *18*(4), 776-788.

Hyndman, R., and T. Hamilton (1993), Queen Charlotte area Cenozoic tectonics and volcanism and their association with relative plate motions along the northeastern Pacific margin, *J. Geophys. Res.*, *98*(B8), 14257-14277.

Hyndman, R., T. Lewis, J. Wright, M. Burgess, D. Chapman, and M. Yamano (1982), Queen Charlotte Fault zone: heat flow measurements, *Can. J. Earth Sci.*, *19*(8), 1657-1669.

James, T., G. Rogers, J. Cassidy, H. Dragert, R. Hyndman, L. Leonard, L. Nykolaishen, M. Riedel, M. Schmidt, and K. Wang (2013), Field studies target 2012 Haida Gwaii earthquake, *EOS Trans. AGU*, *94*(22), 197-198.

Kao, H., S.-J. Shan, and A. M. Farahbod (2015), Source Characteristics of the 2012 Haida Gwaii Earthquake Sequence, *Bull. Seismol. Soc. Am.*, *105*(2b).

Keevil, G. M., J. Peakall, J. L. Best, and K. J. Amos (2006), Flow structure in sinuous submarine channels: Velocity and turbulence structure of an experimental submarine channel, *Mar. Geol.*, *229*(3-4), 241-257.

King, G., and J. Nábělek (1985), Role of fault bends in the initiation and termination of earthquake rupture, *Science*, *228*(4702), 984-987.

Koehler, R. D., R. Farrell, P. Burns, and R. Combellick (2012), *Quaternary Faults and Folds in Alaska: A Digital Database*, Alaska Division of Geological & Geophysical Surveys.

Laberg, J. S., and T. O. Vorren (1996), The glacier-fed fan at the mouth of Storfjorden trough, western Barents Sea: A comparative study, *Geol. Rundsch.*, *85*(2), 338-349.

Lagoe, M. B., C. H. Eyles, N. Eyles, and C. Hale (1993), Timing of Late Cenozoic tidewater glaciation in the far North Pacific, *Bull. Geol. Soc. Am.*, *105*(12), 1542-1560.

Larsen, C. F., R. J. Motyka, J. T. Freymueller, K. A. Echelmeyer, and E. R. Ivins (2005), Rapid viscoelastic uplift in southeast Alaska caused by post-Little Ice Age glacial retreat, *Earth and Planetary Science Letters*, *237*(3), 548-560.

Lay, T., L. Ye, H. Kanamori, Y. Yamazaki, K. F. Cheung, K. Kwong, and K. D. Koper (2013), The October 28, 2012 M_w 7.8 Haida Gwaii underthrusting earthquake and tsunami: Slip partitioning along the Queen Charlotte Fault transpressional plate boundary, *Earth Planet. Sci. Lett.*, *375*, 57-70.

Leonard, L., and J. Bednarski (2014), Field Survey Following the 28 October 2012 Haida Gwaii Tsunami, *Pure and Applied Geophysics*, 1-16.

Lieser, K., I. Grevemeyer, D. Lange, E. Flueh, F. Tilmann, and E. Contreras-Reyes (2014), Splay fault activity revealed by aftershocks of the 2010 M_w 8.8 Maule earthquake, central Chile, *Geology*, *42*(9), 823-826.

Lopez, M. (2001), Architecture and depositional pattern of the Quaternary deep-sea fan of the Amazon, *Marine and Petroleum Geology*, *18*(4), 479-486.

Ma, S., and G. C. Beroza (2008), Rupture dynamics on a bimaterial interface for dipping faults, *Bull. Seismol. Soc. Am.*, *98*(4), 1642-1658.

Mackie, D., R. Clowes, S. Dehler, R. Ellis, and P. Morel-À-l'Huissier (1989), The Queen Charlotte Islands refraction project. Part II. Structural model for transition from Pacific Plate to North American plate, *Can. J. Earth Sci.*, *26*(9), 1713-1725.

Mammerickx, J., and E. L. Winterer (1970), Morphology of the Aleutian abyssal plain, *Bull. Geol. Soc. Am.*, *81*(11), 3457-3464.

Manley, P., and R. D. Flood (1988), Cyclic sediment deposition within Amazon deep-sea fan, *AAPG Bulletin*, *72*(8), 912.

Masson, D. (1991), Fault patterns at outer trench walls, *Mar. Geophys. Res.*, *13*(3), 209-225.

Mathews, W., and G. E. Rouse (1963), Late Tertiary volcanic rocks and plant-bearing deposits in British Columbia, *Bull. Geol. Soc. Am.*, *74*(1), 55-60.

Maus, S., et al. (2009), EMAG2: A 2–arc min resolution Earth Magnetic Anomaly Grid compiled from satellite, airborne, and marine magnetic measurements, *Geochem. Geophys. Geosys.*, *10*(8), Q08005.

McGuire, J. J., R. B. Lohman, R. D. Catchings, M. J. Rymer, and M. R. Goldman (2015), Relationships among seismic velocity, metamorphism, and seismic and aseismic fault slip in the Salton Sea Geothermal Field region, *J. Geophys. Res.*, *120*(4), 2600-2615.

Meng, X., X. Yu, Z. Peng, and B. Hong (2012), Detecting Earthquakes around Salton Sea Following the 2010 M_w7.2 El Mayor-Cucapah Earthquake Using GPU Parallel Computing, *Procedia Computer Science*, *9*, 937-946.

Mohrig, D., and J. G. Marr (2003), Constraining the efficiency of turbidity current generation from submarine debris flows and slides using laboratory experiments, *Marine and Petroleum Geology*, *20*(6), 883-899.

Morley, J., K. Potter, Y. Iwabuchi, and D. Elvers (1972), Bathymetry of three deep-sea channels in the northeast and central Tufts Abyssal Plain, *Journal of Oceanography*, *28*(4), 153-160.

Morozov, I. B., S. B. Smithson, L. S. Hollister, and J. B. Diebold (1998), Wide-angle seismic imaging across accreted terranes, southeastern Alaska and western British Columbia, *Tectonophysics*, *299*(4), 281-296.

Müller, R. D., W. R. Roest, J.-Y. Royer, L. M. Gahagan, and J. G. Sclater (1997), Digital isochrons of the world's ocean floor, *J. Geophys. Res.*, *102*(B2), 3211-3214.

Mutti, E., and W. R. Normark (1987), Comparing examples of modern and ancient turbidite systems: problems and concepts, in *Marine clastic sedimentology*, edited, pp. 1-38, Springer.

Mutti, E., and W. R. Normark (1991), An integrated approach to the study of turbidite systems, in *Seismic facies and sedimentary processes of submarine fans and turbidite systems*, edited, pp. 75-106, Springer.

Ness, G. E., and L. D. Kulm (1973), Origin and development of Surveyor deep-sea channel, *Bull. Geol. Soc. Am.*, *84*, 3339-3354.

Normark, W. (1998), Late Pleistocene channel–levee development on Monterey submarine fan, central California, *Geo-Mar. Lett.*, *18*(3), 179-188.

Normark, W. R., and D. J. W. Piper (1991), Initiation processes and flow evolution of turbidity currents: implications for the depositional record.

Normark, W. R., and P. R. Carlson (2003), Giant submarine canyons: Is size any clue to their importance in the rock record?, *Special Papers-Geological Society of America*, 175-190.

Normark, W. R., D. J. Piper, H. Posamentier, C. Pirmez, and S. Migeon (2002), Variability in form and growth of sediment waves on turbidite channel levees, *Mar. Geol.*, *192*(1), 23-58.

Nykolaishen, L., H. Dragert, K. Wang, T. James, and M. Schmidt (2015), GPS Observations of Crustal Deformation Associated with the M_w 7.7 2012 Haida Gwaii Earthquake, *Bull. Seismol. Soc. Am.*, *105*(2b).

Parsons, T., E. L. Geist, H. F. Ryan, H. J. Lee, P. J. Haeussler, P. Lynett, P. E. Hart, R. Sliter, and E. Roland (2014), Source and progression of a submarine landslide and

tsunami: The 1964 Great Alaska earthquake at Valdez, *J. Geophys. Res.*, *119*(11), 8502-8516.

Pavlis, T. L., C. Picornell, L. Serpa, R. L. Bruhn, and G. Plafker (2004), Tectonic processes during oblique collision: Insights from the St. Elias orogen, northern North American Cordillera, *Tectonics*, *23,* (3).

Pavlis, T. L., J. B. Chapman, R. L. Bruhn, K. Ridgway, L. L. Worthington, S. P. Gulick, and J. Spotila (2012), Structure of the actively deforming fold-thrust belt of the St. Elias orogen with implications for glacial exhumation and three-dimensional tectonic processes, *Geosphere*, *8*(5), 991-1019.

Piper, D. J., and W. R. Normark (2001), Sandy fans--from Amazon to Hueneme and beyond, *AAPG bulletin*, *85*(8), 1407-1438.

Piper, D. J., and W. R. Normark (2009), Processes that initiate turbidity currents and their influence on turbidites: a marine geology perspective, *Journal of Sedimentary Research*, *79*(6), 347-362.

Plafker, G. (1969), *Tectonics of the March 27, 1964, Alaska earthquake*, U.S. Government Printing Office.

Plafker, G. (1987), Regional geology and petroleum potential of the northern Gulf of Alaska continental margin, in *Geology and resource potential of the continental margin of western North America and adjacent ocean basins*, edited by D. W. Scholl, A. Grantz and J. G. Vedder, pp. 229-268, Circum-Pacific Council for Energy and Mineral Resources, Houston, Texas.

Plafker, G., and W. Thatcher (2008), Geological and geophysical evaluation of the mechanisms of the great 1899 Yakutat Bay earthquakes, *Geophysical monograph*, *179*, 215-236.

Plafker, G., W. Nokleberg, and J. Lull (1989), Bedrock geology and tectonic evolution of the Wrangellia, Peninsular, and Chugach Terranes along the Trans-Alaska Crustal Transect in the Chugach Mountains and Southern Copper River Basin, Alaska, *J. Geophys. Res., 94*(B4), 4255-4295.

Plafker, G., J. C. Moore, and G. R. Winkler (1994), Geology of the southern Alaska margin, in *The geology of Alaska*, edited by G. Plafker and H. C. Berg, pp. 389-449, Geological Society of America, Boulder, Colorado.

Plafker, G., L. M. Gilpin, and J. C. Lahr (1994), Neotectonic map of Alaska, *The Geology of North America*, *1*, 389-449.

Plafker, G., T. Hudson, T. Bruns, and M. Rubin (1978), Late Quaternary offsets along the Fairweather Fault and crustal plate interactions in southern Alaska, *Can. J. Earth Sci.*, *15*(5), 805-816.

Posamentier, H. W. (2003), Depositional elements associated with a basin floor channel-levee system: case study from the Gulf of Mexico, *Marine and Petroleum Geology*, *20*(6-8), 677-690.

Prims, J., K. Furlong, K. Rohr, and R. Govers (1997), Lithospheric structure along the Queen Charlotte margin in western Canada: constraints from flexural modeling, *Geo-Mar. Lett.*, *17*(1), 94-99.

Rabinovich, A. B., R. E. Thomson, V. V. Titov, F. E. Stephenson, and G. C. Rogers (2008), Locally generated tsunamis recorded on the coast of British Columbia, *Atmosphere-Ocean*, *46*(3), 343-360.

Raymo, M. E. (1994), The initiation of Northern Hemisphere glaciation, *Ann. Rev. Earth Planet. Sci.*, *22*, 353-383.

Rea, D. K., and H. Snoeckx (1995), Sediment fluxes in the Gulf of Alaska: paleoceanographic record from site 887 on the Patton-Murray seamount platform, in *Proceedings of the Ocean Drilling Program, Scientific Results*, edited by D. K. Rea, I. A. Basov, D. W. Scholl and J. F. Allan, pp. 247-256, Ocean Drilling Program, College Station, Texas.

Reece, R. S., S. P. S. Gulick, B. K. Horton, G. L. Christeson, and L. L. Worthington (2011), Tectonic and climatic influence on the evolution of the Surveyor Fan and Channel system, Gulf of Alaska, *Geosphere*, *7*(4), 830.

Reece, R. S., G. L. Christeson, S. P. S. Gulick, G. A. Barth, and H. J. A. Van Avendonk (2012), The effect of plate structure on intraplate volcanism, Kodiak-Bowie Seamount Chain, Gulf of Alaska, Abstract T31B-2592 presented at 2012 Fall Meeting, AGU, San Francisco, Calif., 2593-2597 Dec.

Reed, J. C., J. O. Wheeler, and B. E. Tucholke (2005), *Decade of North American Geology: Geologic Map of North America: Perspectives and Explanation*, Geological Society of America.

Ristau, J., G. C. Rogers, and J. F. Cassidy (2007), Stress in western Canada from regional moment tensor analysis, *Can. J. Earth Sci.*, *44*(2), 127-148.

Rogers, G. C. (1986), Seismic gaps along the Queen Charlotte Fault, *Earthquake Pred. Res.*, *4*(1-2), 1-11.

Rohr, K. M. M. (2015), Plate boundary adjustment of the southernmost Queen Charlotte fault, *Bull. Seismol. Soc. Am.*, *105*(2b), 1076-1089.

Rohr, K. M., and K. P. Furlong (1995), Ephemeral plate tectonics at the Queen Charlotte triple junction, *Geology*, *23*(11), 1035-1038.

Rohr, K. M. M., M. Scheidhauer, and A. M. Trehu (2000), Transpression between two warm mafic plates- The Queen Charlotte Fault revisited, *J. Geophys. Res.*, *105*(B4), 8147-8172.

Roland, E., D. Lizarralde, J. J. McGuire, and J. A. Collins (2012), Seismic velocity constraints on the material properties that control earthquake behavior at the Quebrada-Discovery-Gofar transform faults, East Pacific Rise, *J. Geophys. Res., 117*(B11).

Sandwell, D., E. Garcia, K. Soofi, P. Wessel, M. Chandler, and W. H. Smith (2013), Toward 1-mGal accuracy in global marine gravity from CryoSat-2, Envisat, and Jason-1, *The Leading Edge*, *32*(8), 892-899.

Savage, J., M. Lisowski, and W. Prescott (1986), Strain accumulation in the Shumagin and Yakataga seismic gaps, Alaska, *Science*, *231*(4738), 585-587.

Scheidhauer, M. (1997), Crustal structure of the Queen Charlotte transofrm fault zone from multichannel seismic reflection and gravity data (M.S. thesis), 184 pp, Oregon State University.

Scheidhauer, M., A. M. Trehu, and K. M. M. Rohr (1999), Multichannel seismic reflection survey over the northern Queen Charlotte Fault, *Geological Survey of Canada Open File 3779*.

Schell, M. M., and L. J. Ruff (1989), Rupture of a seismic gap in southeastern Alaska: the 1972 Sitka earthquake (*Ms* 7.6), *Phys. Earth Planet. In.*, *54*(3), 241-257.

Seton, M., R. Müller, S. Zahirovic, C. Gaina, T. Torsvik, G. Shephard, A. Talsma, M. Gurnis, M. Turner, and S. Maus (2012), Global continental and ocean basin reconstructions since 200Ma, *Earth Sci. Rev.*, *113*(3), 212-270.

Shennan, I., R. Bruhn, and G. Plafker (2009), Multi-segment earthquakes and tsunami potential of the Aleutian megathrust, *Quaternary Science Reviews*, *28*(1-2), 7-13.

Shi, Z., and Y. Ben-Zion (2006), Dynamic rupture on a bimaterial interface governed by slip-weakening friction, *Geophys. J. Int.*, *165*(2), 469-484.

Shor, G. G. (1962), Seismic refraction studies off the coast of Alaska: 1956-1957, *Bull. Seismol. Soc. Am.*, *52*(1), 37-57.

Silver, E. A., R. von Huene, and J. K. Crouch (1974), Tectonic significance of the Kodiak-Bowie seamount chain, northeastern Pacific, *Geology*, *2*(3), 147-150.

Smith, W. H. F., and D. T. Sandwell (1997), Global sea floor topography from satellite altimetry and ship depth soundings, *Science*, *277*(5334), 1956-1962.

Smith, A., R. Hyndman, J. Cassidy, and K. Wang (2003), Structure, seismicity, and thermal regime of the Queen Charlotte Transform Margin, *J. Geophys. Res.*, *108*(B11).

Snavely, P. D., H. D. Wagner, D. H. Tompkins, and D. L. Tiffin (1981), Preliminary geologic interpretation of a seismic reflection profile across the Queen Charlotte Island fault system off Dixon Entrance, Canada-United States *Rep.*, Geological Survey of Canada, Open File 81-299.

Sømme, T. O., W. Helland-Hansen, O. J. Martinsen, and J. B. Thurmond (2009), Relationships between morphological and sedimentological parameters in source-to-sink systems: a basis for predicting semi-quantitative characteristics in subsurface systems, *Basin Research*, *21*(4), 361-387.

Staff, E.-S. S. (1991), *Atlas of the U.S. Exclusive Economic Zone, Bering Sea*, U.S. Geological Survey.

Stevenson, A. J., and R. Embley (1987), Deep-sea fan bodies, terrigenous turbidite sedimentation, and petroleum geology, Gulf of Alaska, in *Geology and resource potential of the continental margin of western North America and adjacent ocean basins*, edited by D. W. Scholl, A. Grantz and J. Vedder, pp. 503-522, Circum-Pacific Council for Energy and Material Resources, Houston, Texas.

Stevenson, A. J., D. W. Scholl, and T. L. Vallier (1983), Tectonic and geologic implications of the Zodiac fan, Aleutian Abyssal Plain, northeast Pacific, *Bull. Geol. Soc. Am.*, *94*(2), 259-273.

Sykes, L. R. (1971), Aftershock zones of great earthquakes, seismicity gaps, and earthquake prediction for Alaska and the Aleutians, *J. Geophys. Res.*, *76*(32), 8021-8041.

Tarr, R. S., and L. Martin (1912), *The Earthquakes at Yakutat Bay, Alaska, in September, 1899*, U.S. Gov't. Print. Off.

Tobin, D. G., and L. R. Sykes (1968), Seismicity and tectonics of the northeast Pacific Ocean, *J. Geophys. Res.*, *73*(12), 3821-3845.

Tocher, D. (1960), The Alaska earthquake of July 10, 1958: Movement on the Fairweather Fault and field investigation of southern epicentral region, *Bull. Seismol. Soc. Am.*, *50*(2), 267-292.

Toda, S., R. S. Stein, V. Sevilgen, and J. Lin (2011), Coulomb 3.3 graphic-rich deformation and stress-change software for earthquake, tectonic, and volcano research and teaching-user guide *Rep. 2331-1258*, U.S. Geological Survey.

Tréhu, A. M., M. Scheidhauer, K. M. M. Rohr, B. Tikoff, M. A. L. Walton, S. P. S. Gulick, and E. Roland (2015), An abrupt transition in the mechanical response of the upper crust to transpression across the Queen Charlotte Fault, *Bull. Seismol. Soc. Am.*, *105*(2b).

Turner, D., R. Jarrard, and R. Forbes (1980), Geochronology and origin of the Pratt-Welker Seamount Chain, Gulf of Alaska: A new pole of rotation for the Pacific Plate, *J. Geophys. Res.*, *85*(B11), 6547-6556.

Van Avendonk, H. J. A., S. P. S. Gulick, G. L. Christeson, L. L. Worthington, T. L. Pavlis, and K. D. Ridgway (2013), Subduction and accretion of sedimentary rocks in the Yakutat collision zone, St. Elias orogen, Gulf of Alaska, *Earth and Planetary Science Letters*, *381*(0), 116-126.

von Huene, R., and L. D. Kulm (1973), Tectonic summary of Leg 18, in *Initial Reports of the Deep Sea Drilling Project, Volume 18*, edited by L. D. Kulm and R. von Huene, pp. 961-976, U.S. Government Printing Office, Washington, D.C.

von Huene, R., G. G. Shor Jr, and J. Wageman (1979), Continental margins of the eastern Gulf of Alaska and boundaries of tectonic plates, *Geological and geophysical investigations of continental margins: American Association of Petroleum Geologists Memoir*, *29*, 273-290.

Vorren, T. O., and J. S. Laberg (1997), Trough mouth fans - Palaeoclimate and ice-sheet monitors, *Quaternary Science Reviews*, *16*(8), 865-881.

Vorren, T. O., E. Lebesbye, K. Andreassen, and K. B. Larsen (1989), Glacigenic sediments on a passive continental margin as exemplified by the Barents Sea, *Mar. Geol.*, *85*(2–4), 251-272.

Vorren, T. O., G. Richardsen, S.-M. Knutsen, and E. Henriksen (1991), Cenozoic erosion and sedimentation in the western Barents Sea, *Marine and Petroleum Geology*, *8*(3), 317-340.

Wald, D. J., B. C. Worden, V. Quitoriano, and K. L. Pankow (2005), ShakeMap manual: technical manual, user's guide, and software guide *Rep. 2328-7055*.

Walter, J. I., X. Meng, Z. Peng, S. Y. Schwartz, A. V. Newman, and M. Protti (2015), Far-field triggering of foreshocks near the nucleation zone of the 5 September 2012 (M_w 7.6) Nicoya Peninsula, Costa Rica earthquake, *Earth and Planetary Science Letters*, *431*, 75-86.

Walton, M. A. L., S. P. S. Gulick, P. J. Haeussler, E. Roland, and A. M. Tréhu (2015), Basement and regional structure along strike of the Queen Charlotte Fault in the context of modern and historical earthquake ruptures, *Bull. Seismol. Soc. Am.*, *105*(2b).

Walton, M. A. L., S. P. S. Gulick, R. S. Reece, G. A. Barth, G. L. Christeson, and H. J. A. Van Avendonk (2014), Dynamic response to strike-slip tectonic control on the deposition and evolution of the Baranof Fan, Gulf of Alaska, *Geosphere*, *10*(4), 680-691.

Wang, K., and S. L. Bilek (2011), Do subducting seamounts generate or stop large earthquakes?, *Geology*, *39*(9), 819-822.

Wang, K., J. He, F. Schulzeck, R. Hyndman, and M. Riedel (2015), Thermal Condition of the 27 October 2012 M_w 7.8 Haida Gwaii Subduction Earthquake at the Obliquely Convergent Queen Charlotte Margin, *Bull. Seismol. Soc. Am.*, *105*(2b).

Wells, D. L., and K. J. Coppersmith (1994), New empirical relationships among magnitude, rupture length, rupture width, rupture area, and surface displacement, *Bull. Seismol. Soc. Am.*, *84*(4), 974-1002.

Wesnousky, S. G. (2006), Predicting the endpoints of earthquake ruptures, *Nature*, *444*(7117), 358-360.

Wilson, D. S. (2002), The Juan de Fuca plate and slab: Isochron structure and Cenozoic plate motions *Rep.*, 9-12 pp, U.S. Geological Survey Open-File Report 02-328.

Woodcock, N. H., and M. Fischer (1986), Strike-slip duplexes, *Journal of structural geology*, *8*(7), 725-735.

Worthington, L., S. Gulick, and T. Pavlis (2010), Coupled stratigraphic and structural evolution of a glaciated orogenic wedge, offshore St. Elias orogen, Alaska, *Tectonics*, *29*(TC6013), 27.

Worthington, L. L., H. J. A. Van Avendonk, S. P. S. Gulick, G. L. Christeson, and T. L. Pavlis (2012), Crustal structure of the Yakutat terrane and the evolution of subduction and collision in southern Alaska, *J. Geophys. Res.*, *117*(B1), B01102.

Xia, K., A. J. Rosakis, H. Kanamori, and J. R. Rice (2005), Laboratory earthquakes along inhomogeneous faults: Directionality and supershear, *Science*, *308*(5722), 681-684.

Yorath, C. (1987), *Petroleum geology of the Canadian Pacific continental margin*.

Yue, H., T. Lay, J. T. Freymueller, K. Ding, L. Rivera, N. A. Ruppert, and K. D. Koper (2013), Supershear rupture of the 5 January 2013 Craig, Alaska (M_w 7.5) earthquake, *J. Geophys. Res., 118*(11), 5903-5919.

Zhang, H., and C. Thurber (2003), User's manual for tomoDD1. 1 (double-difference tomography) for determining event locations and velocity structure from local earthquakes and explosions, Department of Geology and Geophysics, University of Wisconsin-Madison, Madison, WI.

Zurbuchen, J. M., S. P. Gulick, M. A. Walton, and J. A. Goff (2015), Imaging evidence for Hubbard Glacier advances and retreats since the last glacial maximum in Yakutat and Disenchantment Bays, Alaska, *Geochem. Geophys. Geosys.*, *16*(6), 1962-1974.

Vita

Maureen LeVoir Walton was born in Minnesota in 1988. She attended K-8 school at St. Charles Borromeo in St. Anthony Village, Minnesota, and high school at Totino-Grace High School in Fridley, Minnesota. In high school, Maureen was involved with show choir, band, theater, volleyball, softball, National Honor Society, and numerous AP and honors courses. She also worked as a lifeguard, water safety instructor, and sales associate. Maureen graduated high school in May of 2007, having received AP college credit in English Literature and Music Theory.

Maureen went on to major in Geology at the University of Colorado at Boulder beginning in the fall of 2007. During her undergraduate studies, Maureen worked as a singer, geology tutor, and undergraduate research assistant at the National Geophysical Data Center (NGDC). She was voted Outstanding Junior in geological sciences and Outstanding Senior in geological sciences her second and third years at CU-Boulder, respectively. Maureen completed an undergraduate honors thesis under the supervision of Dr. Karl Mueller and graduated *summa cum laude* with a B.A. in Geology after 3.5 years of study in December of 2010. Her final semester at CU, Maureen presented her honors thesis work at the Geological Society of America (GSA) Annual Meeting and the American Geophysical Union (AGU) Fall Meeting. After graduation, Maureen completed a 6-month internship at NGDC working on the General Bathymetric Chart of the Oceans (GEBCO) Gazetteer of Undersea Feature Names, which has since been integrated into Google Ocean.

Maureen sailed aboard the R/V *Marcus Langseth* in June of 2011 to kick off her graduate work at the University of Texas at Austin Institute for Geophysics, where she began her PhD later that year. Maureen's research at UT-Austin focused on using seismic reflection data to study tectonic problems in southeast Alaska. She was involved in the

acquisition of several seismic reflection datasets during her five years at UT-Austin as well as a passive-source ocean-bottom seismometer (OBS) dataset. She presented her work at numerous conferences, including the annual AGU Fall Meeting and the Seismological Society of America (SSA) Annual Meeting. Maureen has received multiple awards and fellowships during her time at UT-Austin, including the AGU Outstanding Student Paper Award (OSPA), the SSA Student Presentation Award, the GeoPRISMS AGU Student Prize Honorable Mention, and two UTIG Ewing/Worzel Fellowships. During her time at UT-Austin, Maureen served as a research assistant, teaching assistant, and GK-12 teaching fellow. Maureen was also involved with the Jackson School of Geoscience's Graduate Student Executive Committee (GSEC), helping to organize numerous social and philanthropic events benefitting the Jackson School.

Maureen met David Walton in Boulder, Colorado in 2011, and they married in Dripping Springs, Texas in 2013. They have a dog named Fenrir.

Email address: maureenlwalton@gmail.com

This dissertation was typed by Maureen L. Walton.